SYNTHESIS AND CHARACTERIZATION OF SILVER AND GOLD BASED – NANOPARTICLES AND THEIR EFFICIENCY FOR SOME DRUGS DETERMINATION

BY

Mutasem M. Al-Shalalfeh

A Thesis Presented to the
DEANSHIP OF GRADUATE STUDIES

KING FAHD UNIVERSITY OF PETROLEUM & MINERALS

DHAHRAN, SAUDI ARABIA

In Partial Fulfillment of the
Requirements for the Degree of

MASTER OF SCIENCE

In

CHEMISTRY

APRIL 2016

KING FAHD UNIVERSITY OF PETROLEUM & MINERALS
DHAHRAN- 31261, SAUDI ARABIA

DEANSHIP OF GRADUATE STUDIES

This thesis, written by **MUTASEM M. AL-SHALALFEH** under the direction his thesis advisor and approved by his thesis committee, has been presented and accepted by the Dean of Graduate Studies, in partial fulfillment of the requirements for the degree of **MASTER OF SCIENCE IN CHEMISTRY**

Dr. Tawfik Abdo Saleh
(Advisor)

8/5/2016

Dr. Abdulaziz A. Al-Saadi
Department Chairman

Dr. Abdulaziz A. Al-Saadi
(Member)

Dr. Salam A. Zummo
Dean of Graduate Studies

Prof. Mohammed A. Wazeer
(Member)

12/5/16

Date

To my Parents, Brothers, Sisters, & my Lovely Fiancée

ACKNOWLEDGMENTS

I humbly employ this medium to appreciate everyone who has contributed directly or indirectly to the completion of my MS degree in King Fahd University of Petroleum and Minerals (KFUPM), Saudi Arabia. First off, my sincere appreciation goes to all the lecturers that have taught me; Dr.Abdulkibash, Dr Musa Musa, Dr Hassan Badawi, Dr Fettouhi, Dr M. Aziz, and others. They have all contributed immensely into improving my general background and professional knowledge of chemistry.

I also wish to appreciate my dear advisor, Dr Tawfik A. Saleh. I could not have dreamt of a better supervisor as he is both supportive and brotherly. I have gained so much in terms of theoretical and practical knowledge, laboratory skills and also the general speed of completing tedious tasks. He is truly a role model and I am very lucky to have him.

I also want to thank my co-advisers. Dr Abdulaziz A. Al-Saadi taught me computational methods, which I have applied in my study. He was also very supportive and his advices helped me greatly. I learned from him a lot. I would like to thank Dr Mohammed A. Wazeer for his valuable comments and suggestions. Which further helped me understand the basics of Nuclear Magnetic Resonance Spectroscopy (NMR), and also helped me in my work.

I want to appreciate the chemistry department of KFUPM, both faculty and staff for their support and help when they were most needed. I also want to thank all my friends and colleagues.

I want to extend my appreciation to my family in Palestine, especially my father and mother. They were supportive in prayers and encouragement. So much that this whole write-up is not enough to list how much they have been helpful.

Finally, I want to appreciate my fiancée, Islam Shalalfeh, who was with me all through the journey. She has supported me in every possible way, so much that this whole write-up is not enough to list how much she has been helpful.

TABLE OF CONTENTS

ACKNOWLEDGMENTS .... **V**

TABLE OF CONTENTS .... **VII**

LIST OF TABLES .... **XII**

LIST OF FIGURES .... **XIII**

LIST OF SCHEME .... **XVI**

LIST OF ABBREVIATIONS .... **XVII**

ABSTRACT(ENGLISH) .... **XVIII**

ABSTRACT(ARABIC) .... **XX**

CHAPTER 1 : INTRODUCTION **1**

1.1 METHODOLOGY **4**

- 1.1.1. Experimental 4
- 1.1.2. Computation 6

1.2. REFERENCES **7**

CHAPTER 2 : ELECTROCHEMICAL INVESTIGATION OF GOLD NANOPARTICLES MODIFIED GLASSY CARBON ELECTRODE AND ITS APPLICATION FOR KETOCONAZOLE DETERMINATION **8**

2.1 INTRODUCTION **8**

2.2 EXPERIMENTAL **13**

- 2.2.1. Reagents 13
- 2.2.2. Preparations of gold nanoparticles (AuNP) 13

2.2.3. Working Electrode Preparation 14
2.2.4. Apparatus 14

2.3. RESULTS AND DISCUSSION 15

2.3.1. Characterization AuNP 15
2.3.2. Electrochemical behavior of KCZ on GC electrode 16
2.3.3. Electrochemical behavior of KCZ on GC/AuNP 17
2.3.4. Effect of Pre-treatment potential 19
2.3.5. Effect of Pre-adsorption time 21
2.3.6. Effect of pH 22
2.3.7. Effect of stirring 24
2.3.8. Calibration curve 25

2.4. CONCLUSION 27

2.5. REFERENCES 28

CHAPTER 3 : SPHERICAL SILVER NANOPARTICLES AS SERS SUBSTRATE FOR ENHANCED DETECTION OF KETOCONAZOLE 29

3.1. INTRODUCTION 29

3.2. EXPERIMENTAL 32

3.2.1. Chemicals and Materials 32
3.2.2. Synthesis silver of nanoparticles (Ag/NPs) 32
3.2.3. Characterization 33
3.2.4. Surface-enhanced Raman spectroscopy (SERS) 33
3.2.5. Computational details 34

3.3. RESULTS AND DISCUSSION 34

3.3.1. Characterization of Ag/NP 34
3.3.2. Density Functional Theory (DFT) 36
3.3.3. Vibrational Assignments of KCZ 40
3.3.4. SERS results of KCZ on Ag/NP 45
3.3.5. Calibration curves and detection limit 47

3.4. CONCLUSION 48

3.5. REFERENCES 49

CHAPTER 4: SILVER COLLOID AND FILM SUBSTRATES IN SURFACE-ENHANCED RAMAN SCATTERING FOR 2-THIOURACIL DETECTION.......... 51

4.1. INTRODUCTION.......... 51

4.2. EXPERIMENTAL.......... 53

4.2.1. Chemicals and Materials.......... 53
4.2.2. Synthesis of silver nanoparticles (Ag/NPs).......... 53
4.2.3. Surface-Enhanced Raman Scattering (SERS).......... 55
4.2.4. Computational details.......... 55

4.3. RESULTS AND DISCUSSION.......... 56

4.3.1. Characterization NPs.......... 56
4.3.2. Density Functional Theory (DFT).......... 58
4.3.3. Vibrational Assignments.......... 61
4.3.4. SERS results of 2-TU on Ag/NPs.......... 69

4.4. CONCLUSION.......... 77

4.5. REFERENCES.......... 78

CHAPTER 5: SILVER NANOPARTICLE-DECORATED GRAPHENE: A SUBSTRATE FOR SURFACE-ENHANCED RAMAN SCATTERING BASED DETECTION OF 2-THIOURACIL.......... 80

5.1. INTRODUCTION.......... 80

5.2. EXPERIMENTAL SECTION.......... 83

5.2.1. Chemicals and Materials.......... 83
5.2.2. Preparation of graphene oxide.......... 83
5.2.3. Preparation of silver/graphene nanocomposites (Ag/G).......... 84
5.2.4. Instruments.......... 85

5.3. RESULTS AND DISCUSSION.......... 86

5.3.1. Solid-state 13C NMR characterization.......... 86
5.3.2. FT-IR analysis.......... 88
5.3.3. UV-vis Analysis.......... 89

5.3.4. SEM and TEM analysis ... 90
5.3.5. XPS analysis ... 92
5.3.6. Raman Spectroscopy analysis ... 95
5.3.7. Vibrational Assignments ... 97
5.3.8. Detection of 2-TU ... 99

5.4. CONCLUSION ... 103

5.5. REFERENCES ... 104

CHAPTER 6: SURFACE-ENHANCED RAMAN SCATTERING BASED ON COLLOIDAL AG AND AU NANOPARTICLES FOR DETECTION OF METHIMAZOLE ... 106

6.1. INTRODUCTION ... 106

6.2. EXPRIMENTAL ... 108

6.2.1. Chemicals and Materials ... 108
6.2.2. Synthesis of nanomaterials ... 109
6.2.3. Surface-Enhanced Raman Scattering (SERS) ... 110

6.3. RESULTS AND DISCUSSION ... 111

6.3.1. Characterization NPs ... 111
6.3.2. Density Functional Theory (DFT) ... 121
6.3.3. SERS results of MTZ on different nanomaterials ... 131

6.4. CONCLUSION ... 139

6.5. REFERENCES ... 140

CHAPTER 7: GRAPHENE DENDRIMER-STABILIZED SILVER NANOPARTICLES FOR DETECTION OF METHIMAZOLE USING SURFACE-ENHANCED RAMAN SCATTERING WITH COMPUTATIONAL ASSIGNMENT ... 141

7.1. INTRODUCTION ... 141

7.2. EXPRIMENTAL ... 144

7.2.1. Chemicals and Materials 144
7.2.2. Synthesis of graphene dendrimer silver composite 144

7.3. RESULTS AND DISCUSSION 148

7.3.1. Structure analysis 148
7.3.2. Vibrational Assignments 152
7.3.3. SERS spectra of MTZ with AgG dendrimer 154
7.3.4. SERS enhancement factor of MTZ with AgG dendrimer 156
7.3.5. SERS spectra of methimazole at different concentrations 157

7.4. CONCLUSION 159

7.5. REFERENCES 160

VITAE 161

LIST OF TABLES

Table 2.1: Comparison of linear concentration ranges and detection limits of different modified electrodes. 27
Table 3.1: Bond length (Å) for Optimized geometrical of KCZ. 37
Table 3.2: Angles (^{0}) for Optimized geometrical of KCZ. 38
Table 3.3: Mulliken atomic charges of KCZ using B3LYP /6-311++G (d, p) basis sets........ 39
Table 3.4: Experimental and calculated B3LYP/6-311++G (d, p) level vibrational frequencies (cm^{-1}) FT-IR and Raman of KCZ. 44
Table 4.1: Optimized bond lengths (Å), bond angle (^{0}), and dihedral angle (^{0}) of 2-TU at the DFT with B3LYP/6-311++G(d,p). 59
Table 4.2: Mulliken atomic partial charges of 2-TU. 60
Table 4.3: Infrared (IR) and Raman Experimental and calculated vibrational frequencies (cm^{-1}) of the 2-TU using DFT method. 67
Table 4.4: Experimental Raman shift compared with the calculated Raman shift of 2-TU complex 68
Table 4.5: SERS enhancement factor of MTZ on gold and silver colloids. 72
Table 4.6: Regression equations between Raman intensities and concentrations of 2-TU and their correlation coefficients. 77
Table 5.1: XPS data of various core level present in GO, and Ag/G nanocomposites. 95
Table 5.2: Calculation and Observed Vibrational Frequencies (cm-1) at the B3LYP/6-311++G (d, p) for 2-TU. 97
Table 5.3: SERS enhancement factor of MTZ on gold and silver colloids. 101
Table 6.1: XPS data of various core level present in GO, and GO/Au nanocomposites. 120
Table 6.2: Optimized bond lengths (Å), bond, and dihedral angles (^{0}) of methimazole at the DFT B3LYP/6-311++G(d,p). 122
Table 6.3: IR and Raman Experimental and calculated vibrational frequencies (cm^{-1}) of the MTZ using DFT methods. 127
Table 6.4: Experimental Raman shift compared with the calculated Raman shift of MTZ complex 130
Table 6.5: SERS enhancement factor of MTZ on gold and silver colloids 135
Table 6.6: Regression equation between Raman intensities and concentrations of MTZ and their correlation coefficients. 139
Table 7.1: Infrared (IR) and Raman Experimental and calculated vibrational frequencies (cm^{-1}) of the MTZ using DFT methods. 152
Table 7.2: SERS enhancement factor of MTZ on AgG dendrimer 156
Table 7.3: Regression equation between Raman intensities and concentrations of MTZ and their correlation coefficients. 159

LIST OF FIGURES

Figure 2.1: (a) TEM bright field image of the AuNPs, (b) UV-vis absorption spectrum of AuNPs.. 15

Figure 2.2: CVs with bare GC electrode, (a) in blank phosphate buffer solution (PH=4), (b) in presence of 10^{-3} M KCZ, (c) in blank buffer solution (pH= 4) after pre-treatment at -1.6 V for 60 s and (d) in presence of 10^{-3} M KCZ after pre-treatment at -1.6 V for 60 s....................................... 17

Figure 2.3: CVs with GC/AuNP electrode, (a) in blank phosphate buffer solution (PH=4), (b) in presence of 10^{-3} M KCZ and (c) in presence of 10^{-3} M KCZ after pre-treatment at -1.6 V for 120s 19

Figure 2.4: (a) CVs with GC/AuNP electrode in presence of 10^{-3}M KCZ in phosphate buffer solution (pH= 4) after pre-treatment at different applied potentials for 60s, (b) Corresponding linear calibration plot of maximum oxidation peak currents for different applied potentials for KCZ pre-deposition... 20

Figure 2.5: (a) CVs with GC/AuNP electrode in presence of 10^{-3}M KCZ in phosphate buffer solution (pH= 4) after pre-treatment at an applied potential of -1.6 V for different times, (b) Corresponding linear calibration plot of maximum oxidation peak currents for KCZ different pre-deposition time. 22

Figure 2.6: (a) CVs with GC/AuNP electrode at different pH values, in presence of 10^{-3} M KCZ in phosphate buffer solution after pre-treatment at an applied potential of -1.6 V and 120 s, (b) Corresponding linear calibration plot of maximum oxidation peak currents for KCZ at different pH values. 23

Figure 2.7:CVs with GC/AuNP electrode showing the effect of stirring duringpre-treatment of electrode at -1.6 V for 120 sec. 24

Figure 2.8: (a) CVs with GC/AuNP electrode for successive additions of KCZ (20-100 µM) at optimized conditions, (b)Corresponding linear calibration plot of maximum oxidation peak currents for KCZ 26

Figure 3.1: (a) UV-Vis absorption spectra of Ag/NPs, (b) TEM image of Ag/NPs together with particle size distribution histogram of AgNPs solution........... 35

Figure 3.2: The optimized KCZ structure.. 36

Figure 3.3: Theoretical (a) FT-IR, (b) Raman spectra of KCZ.................................... 41

Figure 3.4: Experimental (a) FT-IR, and (b) Raman spectra of KCZ........................... 43

Figure 3.5: (a) Raman spectrum of aqueous KCZ solution at different Concentrations, (b) SRES spectrum of 1× 10^{-5} M of KCZ with and without Ag/NPs. Laser ʎ=633nm, acquisition time; 200 sec, and objective; 10x.. 46

Figure 3.6: (a) SERS spectra of KCZ at different concentrations; (b) Calibration curve of the band at 1041 cm^{-1}. Laser ʎ=633nm, acquisition time; 200 sec, and objective; 10x.. 48

Figure 4.1: UV-Vis absorption spectra of silver nanoparticles (a) for Type I, and (b) for Type II.. 57

Figure 4.2: (a) A typical TEM image of silver NPs (Type I) prepared with $NaBH_4$, (b) TEM image of silver NPs (Type II) prepared with $C_6H_5Na_3O_7\cdot 2H_2O$, c) SEM image of silver NPs aggregates on the glass microscope slide, (d) magnified SEM image. 57

Figure 4.3: The optimized structure of 2- Thiouracil. 58

Figure 4.4: Theoretical (a) FT-IR spectrum and (b) Raman spectrum of 2-TU 62

Figure 4.5: (a) Experimental IR spectrum, (b) Raman spectrum of 2-TU, and (c) Raman spectrum of 1.0M saturated solution of 2-TU 65

Figure 4.6: The optimized structure of 2-TU-sliver complex (a) silver atom bind through the S atom, and (b) silver atom bind through the N atom. 66

Figure 4.7: (a) Normal Raman spectrum of pure solid 2-TU, (b) Raman spectrum of 10^{-3} M solution of 2-TU, and (c) The SERS spectrum of 10^{-3} M 2-TU, Laser ʎ=633nm, acquisition time; 20 sec, and objective; 10x. 70

Figure 4.8: (a) SERS spectra of 2-TU at different concentrations using Ag/NPs type I,(b) calibration curve of the band at 1164 cm^{-1}, (c) calibration curve of the band at 921 cm^{-1}. Laser ʎ=633nm, acquisition time; 20 sec, and objective; 10x. 74

Figure 4.9: (a) SERS spectra of 2-TU at different concentrations using Ag film type II, (b) calibration curve of the band at 1164 cm^{-1} , and (c) Calibration curve of the band at 921 cm^{-1}. Laser ʎ=633nm, acquisition time; 20 sec, and objective; 10x. 76

Figure 5.1: (a) ^{13}C MAS spectrum of GO obtained at 4 kHz, and 5000 scans, (b) ^{13}C{H} cross magic angle spinning polarization (CPMAS) spectrum of GO sheets recorded at 4 kHz spin rate and 5000 scans, and .(c) ^{13}C-{1H} cross magic angle spinning polarization (CPMAS) spectrum of Ag/G sheets recorded at 4 kHz spin rate and 5000 scans 87

Figure 5.2: FT-IR spectra of GO and Ag/G nanocomposites. 89

Figure 5.3:UV-vis absorption spectra of dispersion GO, and Ag/G nanocomposite. 90

Figure 5.4: The SEM images of GO (a), and Ag/G (b); TEM images of GO (c), and Ag/G (d); energy-dispersive X-ray spectroscopy (EDS) mappings of GO (e) and Ag/G (f). 91

Figure 5.5: (a)XPS survey spectra of GO and Ag/G nanocomposites, (b) the C 1s core level XPS spectra of GO, (c) the C 1s core level XPS spectra of Ag/G and (d) XPS analysis spectra of Ag 3d in Ag/G. 94

Figure 5.6: Raman spectra of GO (blue line), and Ag/G nanocomposites (red line). 96

Figure 5.7: Raman spectra of pure solid 2-TU (a), and 2-TU with Ag/G (b). Laser ʎ=633nm, acquisition time; 30 sec, and objective; 10x. 100

Figure 5.8: (a) SERS spectra of 2-TU with different concentration,(b) calibration curve of the band at 815 cm^{-1}. Laser ʎ=633nm, acquisition time; 30 sec, and objective; 10x. 102

Figure 6.1: The typical TEM images of gold NPs (a), silver NPs (b),and of Au/G composite (c), The SEM image of GO decorated with AuNPs (d). 112

Figure 6.2: Absorption spectra of AuNPs, AgNPs, and Au/GO nanocomposites 113

Figure 6.3: IR spectra of Au, and Ag nanoparticles. b) FT-IR spectra of GO, and Au-GO nanocomposites 114

Figure 6.4: (a) Raman spectra of gold, and silver nanoparticles, and (b) Raman spectra of GO, and Au/G nanocomposites. 116
Figure 6.5: (a) XPS survey spectra of GO, and Au/G nanocomposites, (b) the C 1s core level XPS spectra of GO, (c) the C 1s core level XPS spectra of Au/G, and (d) XPS analysis spectra of Au 4f in Au/G. 119
Figure 6.6: The optimized structure of MTZ 121
Figure 6.7: Theoretical (a) FT-IR spectrum and (b) Raman spectrum of MTZ 125
Figure 6.8: (a) Experimental IR spectrum, (b) Raman spectrum of MTZ, and (c) Raman spectrum of 1.0M saturated solution of MTZ 127
Figure 6.9: The optimized structures of the, (a) MTZ-silver, and (b) MTZ-gold complex... 129
Figure 6.10: (a)SERS spectra of 1×0^{-5} M MTZ with AuNPs, and GO/NPs, (b) SERS spectra of 1×0^{-5} M MTZ with AgNPs. Laser ʎ; 633nm, acquisition time; 30 sec, and objective; 10x. 134
Figure 6.11: (a) SERS spectra of MTZ with different concentration using AuNPs, (b) calibration curve of the band at 1367 cm^{-1} using AuNPs. Laser ʎ=633nm, acquisition time; 30 sec, and objective; 10x. 137
Figure 6.12: (a) SERS spectra of MTZ with different concentration using AgNPs, (b) calibration curve of the band at 1363 cm^{-1}, using AgNPs. Laser ʎ=633nm, acquisition time; 30 sec, and objective; 10x. 138
Figure 7.1:UV-Vis absorption spectra of graphene dendrimer and Ag/G dendrimer .. 149
Figure 7.2: FT-IR spectra of G dendrimer and Ag/G dendrimer................................. 149
Figure 7.3: Typical SEM images of (a) G dendrimer and (b) Ag/G dendrimer; 151
Figure 7.4: Raman spectra of GO and Ag/G dendrimers.. 151
Figure 7.5: Raman spectrum of pure solid MTZ and SERS spectrum of 10^{-5} M MTZ with AgG dendrimer as a substrate, Laser ʎ=633nm, acquisition time; 20 sec, and objective; 50x. 155
Figure 7.6: (a)SERS spectra ofMTZ with different concentration using Ag/G dendrimer, (b)calibration curve of the band at 1359 cm^{-1} using AuNPs. Laser ʎ=633nm, acquisition time; 20 sec, and objective; 50x.................... 158

LIST OF Scheme

Scheme 2.1: Structure of KCZ 9
Scheme 4.1: process of the drying-mediated condensation effect for a drop of silver nanoparticles and 2-TU solution on the glass slides 54
Scheme 4.2: The proposed geometry of 2-thiouracil adsorbed on a silver film 72
Scheme 5.1: Illustration explaining the synthesis steps of the Ag/G nanocomposites. .. 84
Scheme 6.1: Structures of Methimazole Forms 106
Scheme 6.2: Explaining the steps of the SERS measurements. 110
Scheme 7.1: Illustration explaining the synthesis steps of the Ag/G dendrimer........... 146
Scheme 7.2: Proposed mechanism of the stabilization of the AgNPs on the GO-G-PAMAM for the preparation of Ag/G dendrimer. 147

LIST OF ABBREVIATIONS

AgNPs	:	Silver Nanoparticles
AuNPs	:	Gold Nanoparticles
CV	:	Cyclic Voltammetry
DFT	:	Density Functional Theory
FT-IR	:	Fourier Transform Infrared
GCE	:	Glassy Carbon Electrode
GO/NPs	:	Graphene Oxide- Nanoparticles
KCZ	:	Ketocenazole
MTZ	:	Methimazole
NMR	:	Nuclear Magnetic Resonance
SEM	:	Scanning Electron Microscope
SERS	:	Surface Enhanced Raman Scattering
TEM	:	Transmission Electron Microscope
2-TU	:	2-Thiouracil
XPS	:	X-ray Photoelectron Spectrometer

ABSTRACT

Full Name : Mutasem Mohammad Al-Shalalfeh

Thesis Title : Synthesis and Characterization of Silver and Gold Based Nanoparticles and Their Efficiency for Some Drugs Determination

Major Field : Chemistry

Date of Degree : April, 2016

In this work, various types of nanomaterials including silver, gold, graphene decorated with silver nanoparticles were successfully synthesized. The size, morphology, functional groups and optical properties were characterized using transmission electron microscopy, scanning electron microscopy, X-ray photoelectron spectroscopy, nuclear magnetic resonance spectroscopy, and Raman spectroscopy. As an application, the cyclic voltammetric (CV) behavior of Ketoconazole was investigated by modifying a glassy carbon electrode with gold nanoparticles. The CV responses of Ketoconazole were obtained up to a concentration of 100 µM.

More important, the structural stability, geometrical parameters, and vibrational frequencies of 2- Thiouracil, Methimazole, and Ketoconazole were predicted by the computational study using the DFT/B3LYP method with the 6-311++G (d, p) basis set. The FT-IR and Raman theoretical spectra of the compounds were calculated at the DFT level of theory, which gave excellent agreement with experimental spectra. SERS detection of 2- Thiouracil, Methimazole and Ketoconazole were carried out using the prepared silver colloid, gold colloid, and graphene oxide decorated with nanoparticles. SERS spectra of Methimazole were obtained up to a concentration of 10^{-7} M for the gold nanoparticles, up to concentration 10^{-12} for the silver nanoparticles, and up to concentration 10^{-11} for the silver-graphene dendrimer nanocomposites. SERS spectra of 2- Thiouracil were obtained up to a concentration of 10^{-6} M, and 10^{-8} M for the silver colloid, and graphene oxide-silver nanocomposites, respectively. Moreover, the SERS detection as low as 10^{-9} M was obtained from the aqueous solution of Ketoconazole through silver colloids.

ملخص الرسالة

الاسم الكامل : معتصم محمد عبد المنعم الشلالفه

عنوان الرسالة : تحضير وتوصيف مواد نانوية من الفضة والذهب وكفاءتها لتعيين بعض المركبات الدوائية

التخصص : الكيمياء

تاريخ الدرجة العلمية : أبريل , 2016

تستخدم المواد النانوية النبيلة على نطاق واسع في مطياف رامان ذات السطح المحسن والدراسات الكهروكيميائية لتوصيف وتعيين بعض المركبات الصيدلانية. حيث تم تحضير المواد النانوية مثل جسيمات الفضة النانوية، جسيمات الذهب النانوية، وجسيمات الفضة والذهب النانوية على سطح أكسيد الجرافين وجسيمات الفضة المزخرفة على جزيء ديندريمر المتفرع باستخدام طريقة الاختزال الكيميائية. كما تم في هذه الدراسة توصيف المواد النانوية المحضرة باستخدام تقنيات متعددة منها جهاز الرامان، الأشعة فوق البنفسجية، والميكروسكوب الالكتروني الماسح لدراسة حجم وشكل وتركيب المواد المحضرة. تمت أيضا دراسة الثبات التركيبي للمركبات الدوائية باستخدام طريقة الكثافة الوظيفية والاهتزاز بالمجموعة الحسابية النظرية المناسبة. حيث تمت دراسة الحسابات لمطيافية ترددات ذبذبات الاشعة تحت الحمراء ومطيافية رامان من الناحية النظرية ومقارنتها بالنتائج العملية. تمت أيضا الدراسة العملية لمطيافية رامان لمركبات صيدلانية مختلفة مثل الكيتوكونازول، والثيوراسيل والميثيمازول باستخدام أسطح المواد النانوية المحضرة كأسطح اسناد وادمصاص. وقد تم الحصول على أطياف سطح تعزيز رامان في المحاليل العضوية المائية. وقد تم الوصول الى تعيين تراكيز ضئيلة جدا من هذه المركبات

CHAPTER 1

INTRODUCTION

This research focused on the synthesis nanomaterials and investigated the detection of selected pharmaceutical compounds (Thiouracil, Methimazole and Ketoenazole). The Surface Raman enhanced Scattering (SERS), and electrochemical techniques are extensively used in determination of several the drugs. These have wide applications in many nanotechnology, bioscience, Forensics, and pharmaceutical industry fields [1]. SERS is a very promising method for investigating the pharmaceutical compounds, due to it’s an ability to provide information about chemical structural and physical properties and identifies substances from the characteristic spectra [2]. The major advantage of SERS over other spectroscopic techniques is that SERS is a molecularly specific technique producing spectra, which has sharp peaks, whereas, for example, fluorescence spectra is broad, overlapping, and less specific for a particular molecule [3]. Average enhancement factor of Raman signals by SERS has been recorded in excess of 10^{10} for detection of analyte on the surface of nanomaterials, which is related to the excitation of surface plasmon resonance on substrates as a result of the interactions between adsorbents and metals. [4].

There are two major mechanisms of enhancement reported in the literature, chemical enhancement (CE), and electromagnetic enhancement (EME). The chemical effects is contributing the minor part of the enhancement magnitude, while the electromagnetic effect is dominant of the SERS signal [5, 6]. The EME is dependent on the roughness that present metal surface, which is related to the surface Plasmon resonance of the metal surface. The EME involves excites surface Plasmon on the metal, due to the incident laser irradiates on the metal surface. This excitation surface Plasmon leads to generate a strong electromagnetic field on the metal surface that magnifies the incident laser and the Raman scattering. The EME is generally of the order of 10^6-10^8 [7].

While the CE is dependent on charge transfer excitation between the adsorbent and metal surface through their bonds, which can occur by transfer one electron from the highest occupied to the Fermi level (EF) of the metal, or by transfer one electron from the Fermi level (EF) of the metal to the lowest unoccupied molecular orbital (LOMO). These charge transfers cause a change in the polarizability of the molecule. The CE can be normally achieved up to 10^2 -10^3 [8].

The knowledge of molecular structure, vibrational properties, and energetic data analysis, in the gas phase of a molecule, is very important for the pharmaceutical compounds, and food science. Theoretical studies can be assisted to get deeper understanding the physical and chemical properties of molecules. Also, it is important to study the interaction mechanism of drug molecules on the metal surfaces [9-10]. Recently, many of pharmaceutical compounds have been reported. The Density Functional Theory (DFT) calculations were reported to provide the structural and vibrational properties of the antimalarial drug Halofantrine, using B3LYP/6-31++G (d, p) level of theory [11]. The DFT method has been reported to predict the conformations of Thiouracil derivatives, and adsorption behavior on gold substrates using SERS method, with B3LYP/6-31++G (d, p) basis set [12]. SERS involves adsorption of molecules onto the substrate surface. SERS enhancement has influence on the type of metallic substrates. Most common metals used are gold, silver, and copper. Among them, the silver metal is the most common type used as SERS substrates, due to its stability in the air [13], and very strong surface Plasmon resonance in UV-vis, and near IR range. The silver metal at the nanoscale (10-100) nm display localized surface Plasmon's resonance that can be excited with visible light, causing a high enhancement compared with all the metals [14]. However, silver nanoparticles have a strong tendency to aggregate over storage time, which leads to low detection reproducibility and reliability [15].

Recently, the electrochemical methods have been the common techniques for study enzymatic catalysis, solar energy conversion, and environmental monitoring [16]. Electrochemical methods have many advantages like, easy handling, short analysis time, very sensitive, no use of organic solvent, the ability to detect multiple analytes without separation steps, the ability to analyze targets within biological matrices, including sweat or urine when compared with other techniques [17]. Electrochemical methods have been shown to be excellent in the pharmaceutical formulation, and for the determination of the drug in bulk structure. Therefore, many of the studies have been reported to pharmaceutical analysis, including the voltammetric determination of antiamoebic, capecitabine, sedatives, antiadrenergic, ketoconazole, clotrimazole, and piperazine [18]. Moreover, the electrochemical methods are very helpful techniques to study the reaction mechanism. Redox properties of a pharmaceutical compound can give insights into its metabolic fate or pharmaceutical activity [19]. The important idea in electrochemical studies is based on modifying working electrodes by nanomaterials like silver, and gold nanoparticles, which provide high surface area, electronic and mechanical properties, increase the rate of electron transfer [20].

1.1 METHODOLOGY

1.1.1. Experimental

(a) Synthesis of nanoparticles

The nanomaterials were synthesized using chemical reduction methods. Chemical method has been the most common method used for the synthesis of nanoparticles due to its very cheap cost, fewer instruments required, as well the accuracy process, which is a part of preparation process carried out under normal environmental conditions. Silver nanoparticles (AgNPs) were synthesized by reduction of sodium nitrate $AgNO_3$ (precursor and source of silver metal) by sodium borohydride ($NaBH_4$) or sodium citrate ($Na_3C_6H_5O_7$) as reducing agents and stabilizing agents in the preparation process. On the other hand, gold nanoparticles (AuNPs) were synthesized by reduction of the chloroauric acid ($HAuCl_4$) through pamoic acid, and sodium citrate as reducing and stabilizing agents.

(b) Electrochemical study

The cyclic voltammetric (CV) response of ketoconazole was studied using electrochemical work station (CHI1140A, CH Instruments Inc, Austin, TX, USA). The electrochemical cell consists of; glassy carbon electrode as a working electrode, an Ag/AgCl as a reference electrode, and the platinum electrode as a counter electrode. The working electrode was modified with 50µl of gold nanoparticles, and dried at 70 ^{0}C using an oven for 20 min. The best cyclicvoltammetric responses were recorded at optimum conditions. The pre-adsorption -1.6 V, deposition time 120 sec, stirring the solution during the measurements, and pH = 4.0 were chosen for ketoconazole investigation.

(c) FT –IR and Raman spectra

The infrared spectra of 2-Thiouracil, Methimazole and Ketoconazole in solid and solution samples were recorded using Thermo Nicolet Nexus 470 FT IR Spectrometer equipped with a global source, a KBr beam spiltter, and a DTGS KBr detector in the range of 400 cm^{-1} - 4000 cm^{-1}. The Raman spectroscopy system (Lab Ram HP Evolution Raman spectrometer, HORIBA Scientific^{TM}) was used to collect the Raman spectra in the regain 50 cm^{-1} – 4000 cm^{-1} of pharmaceutical compounds, The Helium – Neon laser source operating at approximately 17mW (visible wavelength, 633 nm) was used for sample excitation, with 10x objective or focus and collection of Raman scattered light.

1.1.2. Computation

(a) DFT calculations.

The GAUSSIAN 09 program was used to implement the DFT/B3LYP calculations. The 6-311++G(d, p) basis set was employed to optimize the structures of the compounds, and predict the Mulliken atomic partial charges the atoms of molecules, and predict important parameters of optimized geometry such as bond length, bond angles, and dihedral angles. The potential energy distributions (PEDs) for the normal modes among the symmetry coordination of the pharmaceutical compounds were calculated by Veda program. Complete vibrational assignments of the normal modes for the 2-Thiouracil, Methimazole and Ketoconazole were made on the basis of the calculated PED values, FT-IR signal intensities, Raman line activity, and SERS peaks with the help of Gauss-View 5.0 graphical animation for all the compounds.

(b) Theoretical FT –IR and Raman spectra

The theoretical Infrared and Raman spectra of compounds were extracted from the Gaussian 09 outputs. The calculated wavenumber was scaled using the scaling factor 0.961 for frequency region ≥ 2000 cm^{-1}, and scaling factor 0.985 for frequency region > 2000 cm^{-1}.

1.2. REFERENCES

[1] S. Schlücker. Angew. Chem. Int. Ed. 2014, 53, 4756.

[2] S. Abalde-Cela, P. Potel, C. Mateo, L. Rodríguez-Lorenzo, R.A.Puebla, L.M. LizMarzán. J. R. Soc. Interface. 2010, 7, 435.

[3] E. C. Le Ru, E. Blackie, M. Meyer. J. Phys. Chem. C. 2007, 111, 13794.

[4] R. Gupta, W.A. Weimer. Chemical Physics Letters. 2003, 374, 302.

[5] Shicai Xua, Shouzhen Jiang, Jihua Wang, Jie Wei , Weiwei Yue , Yong Ma. Sensors and Actuators B. 2016, 222, 1175.

[6] Kartopu, G. Es-Souni, M. Sapelkin, A. V. Dunstan. Journal of Nanoscience and Nanotechnology. 2008, 4, 931.

[7] Nicholas Valley, Nathan Greeneltch, Richard P. Van Duyne, and George C. Schatz. J. Phys. Chem. Lett. 2013, 4, 2599.

[8] Stiles, P.L., et al. Ann. Rev. Anal. Chem. 2008, 1(1), 601.

[9] S. Cınta Pınzaru, I. Pavel, N. Leopold and W. Kiefer. 2004, 35, 338.

[10] Asha Raj, Y. Sheena Mary, C. Yohannan Panicker, K. Raju. Molecular and Biomolecular Spectroscopy. 2013, 113, 28.

[11] Frosch T, Popp J. Journal of Biomedical Optics. 2010, 5.

[12] Wenpeng Yang, Yongjun Hu Spectrochimica Acta Part A. 2015, 134, 399.

[13] Steven M. Asiala and Zachary D. Schultz. Anal. Chem. 2014, 86, 2625.

[14] Cyril M, M. Leona, and J. R. Lombardi Anal. Chem. 2016, 88, 152.

[15] Xuefeng Yan, Lingzhi Wang, Dianyu Qi, Juying Lei, Bin Shen, Tapas Sen and Jinlong Zhang. RSC Adv. 2014, 4, 57743.

[16] L.G. Martinez, P.C. Falco, A.S. Cabeza. J. Pharm. Biomed. Anal. 2002, 29, 405.

[17] Ozkan S, Uslu B, Dogan B. Microchim Acta. 2006, 153, 27.

[18] Vinod K. Gupta, Rajeev Jain, Keisham Radhapyari, Nimisha Jadon, Shilpi Agarwal. 2011, 408, 179.

[19] S. S. Kalanur, J. Seetharamappa, G. P. Mamatha, M. D. Hadagali , P.B. Kandaga. Int. J. Electrochem. Sci. 2008, 3, 756.

[20] L. Aguı, P. Y. Sedeno, Jose M. P. analytica chimica acta. 2008, 622, 11.

CHAPTER 2

Electrochemical Investigation of Gold Nanoparticles Modified Glassy Carbon Electrode and its Application for Ketoconazole Determination

2.1 INTRODUCTION

Ketoconazole (KCZ) is an extensively used anti-fungal compound used to treat skin and systemic mycoses. Due to its excellent anti-fungal properties, KCZ is also an active ingredient of anti-scaling shampoos and pomades [1]. KCZ is an effective drug against many gram-positive microorganisms KCZ is a synthetic piperazine, belongs to the family of imidazoles and its chemical name is (cis-1-acetyl-4-{4-[[2-(2,4-dichloro-phenyl)-2-(1H-imidazol-1-ylmethyl)-1,3-dioxolan-4-yl]-methoxy] phenyl} and its structure is shown in Scheme 2.1 [2, 3]. Despite its low toxicity and many advantages over other anti-fungal drugs, it has side effects including the inhibition of cytochrome (P-450) and Phase II enzymes, suppression of testosterone hormone, cortisol synthesis in human body and inhibition of gonadal and adrenal steroids [4]. Some adverse effects can lead to conditions such as utricaria, leukopenia, nausea and haemolytic anemia [3].

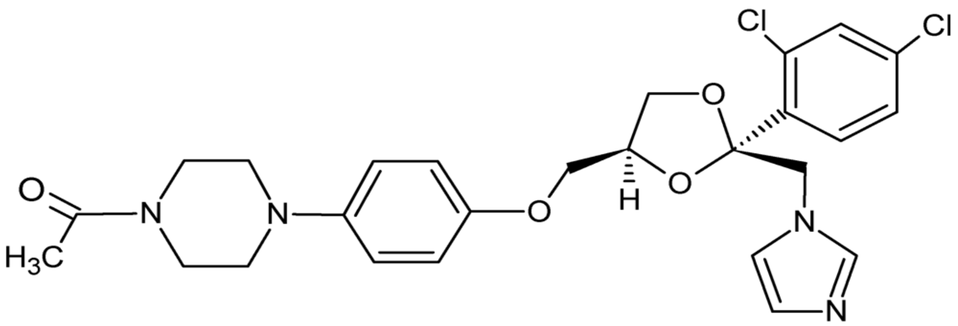

Scheme 2.1: Structure of KCZ

Due to its presence in a wide range of pharmaceutical formulations and body fluids, determination of KCZ is significant area of interest. Conventionally, concentration of KCZ is determined with modern chromatographic techniques involving extraction with chloroform and determination with UV detector or diode array detector [4, 5, 6]. Other traditional techniques for KCZ determination include several spectrometric methods and electrophoresis. Although these methods produce satisfactory results but are expensive, need pre-extraction procedures and are laboratory based. Electrochemical methods, on the other hand, have advantages over conventional spectrophotometric methods, such as, cost effectiveness, in-situ and continuous monitoring, easily portable and simple instrumentation and minimum or no need of sample pre-treatment. KCZ is an electrochemically active compound but to date very few studies have been carried out for its direct electrochemical detection. Fijalek et al., in 1992 [8] used a hanging mercury electrode for determination of KCZ in phosphate buffer solution with a detection limit close to 1 ppm. Shamsipur and Farhadi [3, 9] explored the use platinum, gold and glassy carbon electrodes for KCZ determination through several electrochemical techniques including volatammetry, amperometry and chronocoulometry. A possible mechanism for the KCZ oxidation was also proposed. Shamsipur and Farhadi [10] also used carbon paste electrode with adsorptive stripping voltammetry for KCZ determination in many pharmaceautical preparations and urine samples. A linear concentration range of $2.4 \times 10^{-8} – 4.8 \times 10^{-7}$ was achieved for KCZ determination with differential pulse technique.

In many subsequent direct electrochemical studies, reduction of KCZ had been used at the electrode surface. Arranz et al. [11] used hanging mercury drop electrode and used adsorptive stripping differential pulse voltammetry to study KCZ in aqueous solution of Britton- Robinson buffer (BR- buffer). A pre- concentration step was used for KCZ determination. With differential pulse polarography a detection limit of 0.07 μM was achieved. The method was successfully used for KCZ determination in gel formulation samples and spiked urine samples. Peng et. al., [12] studied electrochemical dtermination of KCZ with abare GC electrode. A pre-concentration step was necessary for KCZ determination. Differential pulse voltammetry was used to study the adsorptive and stripping behavior of KCZ. A detection limit of 0.004 nM was achieved.

Most of the electrodes used in the above studies face the problem of poisoning with KCZ adsorption at the electrode surface and thus need regeneration procedures. To avoid this problem Dantas et al., [1] fabricated a silver solid amalgum electrode for voltammetric KCZ determination. Solid amalgam electrodes were prepared by mixing fine powders of Ag, Cu, Au, Bi, Sn and Zn with liquid Mercury. Reduction of KCZ was studies at – 1.46 V vs Ag/AgCl electrode. The electrode was used for KCZ determination in spiked tablet, shampoo, and cream samples. Although the method showed robustness and specificity for analytical purposes a pH of 12 was necessary for adequate performance of this silver solid amalgum electrode.

Borowiec et al., [3] modified GC electrode surface with multi-walled carbon nanotubes (MWCNTs) and used for KCZ determination. Presence of MWCNTs significantly enhanced the electrochemical response for KCZ with differential pulse voltammetry technique. A linear concentration range of 1.0 ─ 30 μM was achieved with a detection limit of 0.44 μM was achieved.

To the best of our knowledge, not any other nanostructures modified electrodes have been reported yet for KCZ determination. Gold nanoparticles (AuNP) are one of the most commonly used nanostructures for the preparation of electrochemical sensors and biosensors. The reason for their frequent use is their bio-compatibility, ease of synthesis, control on size and improved efficacy [13]. Although, Au is a well-known inert metal, Au nanostructures, particularly of less than 10 nm in diameter, are widely used as catalysts in a variety of chemical reactions [14]. The catalytic activity of AuNP varies significantly with their size and dimensions. The catalytic properties of AuNP are not only due to their high surface area but many other effects are also intrinsically induced depending on the size and shape of the Au nanostructures [15]. These effect include quantum size effects, charge transfer to and from the support surface (if any), surface plasmon effect [16], oxidation state of Au atoms, crystalline facet/plane, and very low coordinated Au atoms present at the surface and edges of Au nanostructures [17]. Thus, electrodes modified with different types of AuNP give a much better and enhanced response [18]. Among several methods developed for the preparation of AuNP refluxing the aqueous solution of citrate and Au precursor is popular due to rigid size controlling and good catalytic properties of the resulting AuNP [15]. Recently, we developed a very simple method for the chemical synthesis of AuNP at room temperature with an excellent control over size and shape of the resulting AuNP. We used $HAuCl_4$ as gold precursor and pamoic acid both as a stabilizer and reducing agent at the same time [19]. The AuNP prepared by pamoic acid method showed good florescent properties but this is the first time that these AuNP have been employed for an electrocatalytic study, which is essential to explore a wide range of applications of these newly synthesized AuNP.

In this paper, we modified glassy GC electrode with AuNP synthesized by a simple method using pamoic acid and sodium hydroxide. The resulting a GC/AuNP electrode was used for KCZ determination. KCZ was first accumulated at the GC/AuNP electrode by applying negative potentials, followed by CV experiments. The performance of GC/AuNP was improved by optimizing experimental parameters such as pH, applied potential used for accumulation step, time required for accumulation and pH of the measurement solution.

2.2 EXPERIMENTAL

2.2.1. Reagents

Ketoconazole ((±)-cis-1-Acetyl-4-(4-[(2-[2,4-dichlorophenyl]-2-[1H-imidazol-1 ylmethyl]-1,3-dioxolan-4-yl)-methoxy]phenyl) piperazine), sodium acetate, acetic acid, 0.02 µm alumina alumina powder, pamoic acid (PA) and sodium hydroxide were purchased from Sigma-Aldrich. Buffer powder packets for pH 7 (Prod No 33190) and pH 4 (Prod No 33189) were obtained from BDH Ltd, Pool, England. All solutions were prepared with ultrapure water obtained from a water purification system (LaboStar™ and Ultra Clear™ Lab Water Systems, Siemens Water Technologies USA (www.water.siemens.com). The buffer were prepared by dissolving the supplied buffer powder in 100 ml ultrapure water to obtain pH 4 or 7. The buffers of other pHs were prepared by adding acid or base to the above buffer.

2.2.2. Preparations of gold nanoparticles (AuNP)

The 10.8 nm PA-capped AuNP were synthesized according to our earlier reports [19, 20, 21] Briefly, a clear solution of 2 mM disodium salt of PA (Na_2-PA) was prepared by sonication of 7.9 mg of PA and 40 µl of 1.0 M NaOH (aq.) in 10 ml water. Next, excess 100 µl of 1.0 M NaOH was added to the clear solution and subsequently sonicated for 1 min. Afterwards, 10 ml of 1.34 mM $HAuCl_4$ (aq.) was added to the above solution under sonication, and the sonication was continued for 15 min. After 60 min keeping at undisturbed at RT, the reaction mixture was centrifuged at 12000 rpm for 60 min to remove unbounded pamoic acid. Then the precipitated AuNPs were re-dispersed in the ultrapure water, which is called purified AuNPs solution.

2.2.3. Working Electrode Preparation

Glassy carbon electrode was polished with 0.02 µm alumina slurries and washed with ultrapure water prior to each use. Then, 50 µl of the purified AuNPs solution was added on the surface of the glassy electrode and successively dried at 70 ^{0}C using an oven for 20 min.

2.2.4. Apparatus

All electrochemical experiments were performed using an electrochemical work station (CHI1140A, CH Instruments Inc, Austin, TX, USA). The Ag/AgCl (in 3M.L^{-1} KCl CHI111, CH Instruments Inc). The electrochemical cell consisted of a bare or AuNP-modified GCE disk working electrode, a Pt counter electrode, and an Ag/AgCl (3 M .L^{-1}KCl) reference electrode. All CV experiments were carried out at room temperature. A scan rate of 0.1mV /s was employed between 0 -1.2 V , unless described otherwise.

2.3. RESULTS AND DISCUSSION

2.3.1. Characterization AuNP

The TEM image was taken using the JEM -2100F Field Emission Electron Microscope, JEOL- USA) at 200 kV acceleration voltage. . Figure 2.1a illustrates the bright field Transmisson Electron Microscopy (TEM) image of these chemically synthesized AuNP. AuNP appear dark against the liquid's bright background. AuNP are homogeneously dispersed with an excellent control over their size and shape. The Ultraviolet –visible (UV-vis) absorption spectrum of AuNPs is shown in Figure 2.1b. The characteristic absorption maximum of gold nanoparticles was found at $\lambda_{\max}$ ~ 510 nm, due to surface Plasmon resonance of AuNPs.

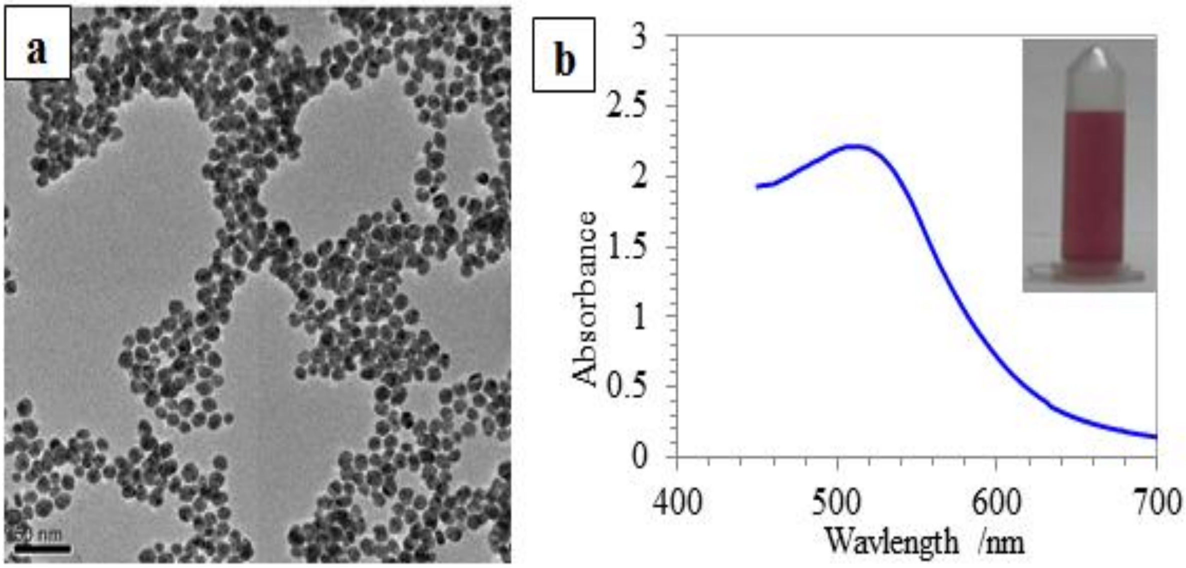

Figure 2.1 : (a) TEM bright field image of the AuNPs, (b) UV-vis absorption spectrum of AuNPs.

2.3.2. Electrochemical behavior of KCZ on GC electrode

Figure 2.2 represents CVs with bare GC electrode with and without pre-adsorption step both in the absence and presence of 10^{-3}M KCZ at pH 4.0. No redox peaks were observed in the absence of KCZ with GC electrode. In Figure 2.2 two well-defined redox couples could be observed without pre-adsorption step for KCZ with oxidation peak currents much higher than reduction peak currents showing the quasi-reversible nature of KCZ redox couples. First anodic peak, which appeared at 0.697 V was representative of the oxidation of methoxy group of KCZ resulting in the formation of KCZ^{+} radical cation while the second peak at 0.983 V was due the oxidation of piperazine rings of KCZ as had been reported earlier for oxidation of the piperazine rings of trazodone [2, 9] and doxazosin [22]. Figure 2.2 is also showing CV responses of KCZ after pre-adsorption of KCZ at -1.6 V for 60 s. It was evident that in presence of KCZ the current for anodic peak at 0.697 was about 4.5 higher than that was without pre-adsorption step, while the second anodic peak was not visible due to the solvent evolution at the same voltage. Thus, pre-adsorption step clearly enhanced the oxidation peak current signal for KCZ and was considered a necessary step for KCZ determination in the samples.

As, described earlier by Buckley *et al.*, [23] it is difficult to determine the detailed mechanism because of the variety of possible functional groups and the complex nature of the carbon surface. Likewise, during cathodic treatment, oxygen containing functional groups are reduced. We believe that the GCE surface has been activated during the polarization at -1.6 V, which lead to decrease the over-potential of the oxygen evolution reaction.

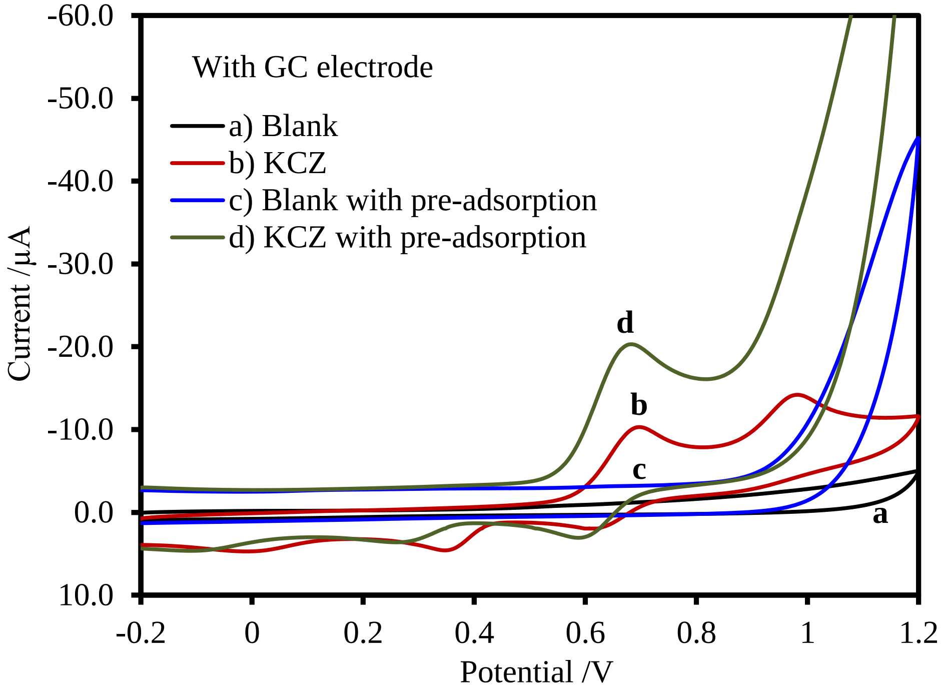

Figure 2.2: CVs with bare GC electrode, (a) in blank phosphate buffer solution (PH=4), (b) in presence of 10^{-3} M KCZ, (c) in blank buffer solution (pH= 4) after pre-treatment at -1.6 V for 60 s and (d) in presence of 10^{-3} M KCZ after pre-treatment at -1.6 V for 60 s.

2.3.3. Electrochemical behavior of KCZ on GC/AuNP

Figure 2.3 represents the CVs with GC/AuNP with and without pre-adsorption step. A significant increase in the oxidation peak current could be observed compared to bare GC electrode without a pre-adsorption of KCZ. Overall, oxidation peak current for KCZ was 2-3 times higher than that of bare GC electrode showing excellent catalytic activity of (GC/AuNP) electrode. It is interesting to observe that only one oxidation peak appeared for KCZ at the GC/AuNP electrode while KCZ displayed two oxidation peaks on bare GC electrode (Figure 2.2). Although, the mechanism of KCZ oxidation is very complex. There is one oxidation peak at GC/AuNP electrode and no reduction peak, which infers that oxidation is irreversible. Perhaps, AuNP reduced the over-potential both oxidation processes i.e., oxidation of piperazine rings and methoxy group of KCZ. This phenomena leads to oxidize the piperazine rings and methoxy group in same region. As result, one oxidation peak is appeared on AuNP/GCE in anodic segment. Beside, the experimental result revealed that the product, which was generated oxidation, cannot be reduced in subsequent reversed cycle on AuNP/GCE as only one peaks was appeared which is related to reduction of oxidized gold.

Figure 2.3 also shows KCZ response after pre-treatment of GC/AuNP in KCZ solution at -1.6 V for 120 s. Again a significant rise in the anodic peak current could be observed after pre-treatment. In fact, anodic peak current was approximately 2.5 times higher than that carried out without pre-adsorption step. Thus, prior to utilization of GC/AuNP electrode for KCZ determination, optimization of several experimental parameters was carried out to acquire the best possible analytical response for KCZ oxidation. For this purpose, applied potential and time for pre-adsorption of KCZ, pH and effect of stirring during pre-adsorption step were optimized.

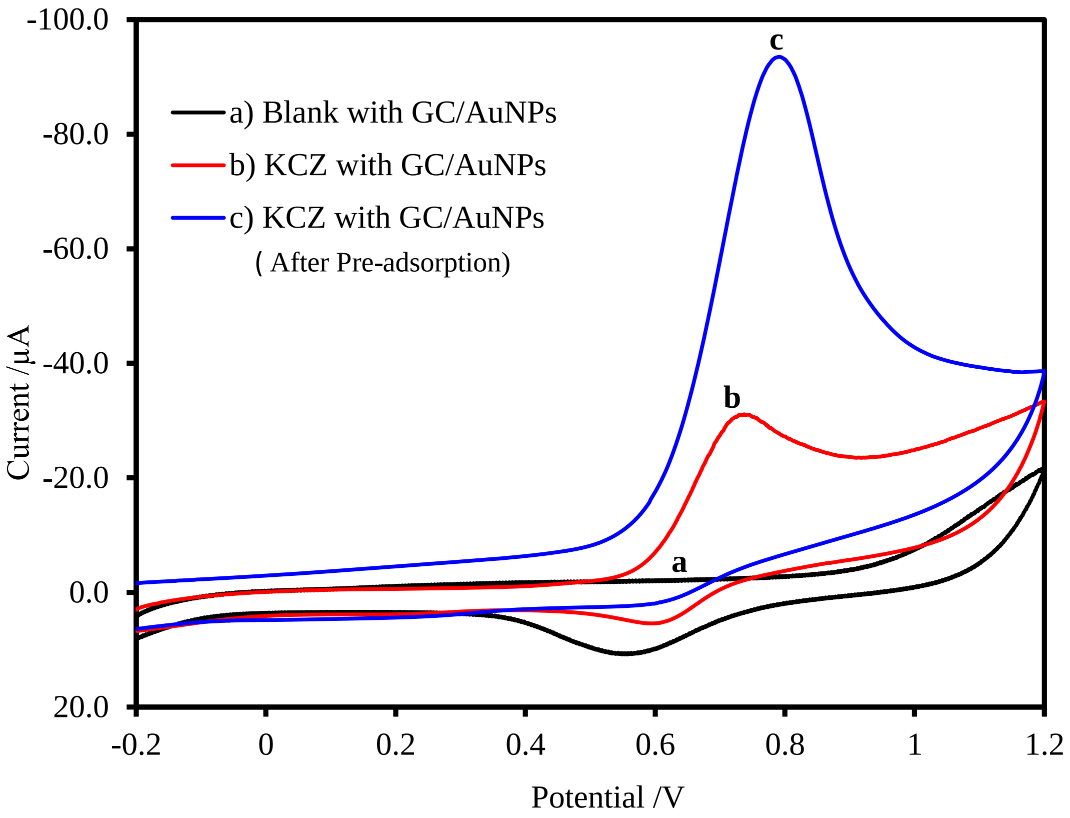

Figure 2.3: CVs with GC/AuNP electrode, (a) in blank phosphate buffer solution (PH=4), (b) in presence of 10^{-3} M KCZ and (c) in presence of 10^{-3} M KCZ after pre-treatment at -1.6 V for 120s

2.3.4. Effect of Pre-treatment potential

Figure 2.4 shows the effect of applied potential used for KCZ adsorption at the GC/AuNP electrode surface. A fixed adsorption time of 60 s was used while applied potential was varied from -0.2 ─ -1.8 V. It can be clearly seen in Figure 2.4a that oxidation peak current was increasing with decreasing applied potential reaching a maximum at -1.6 V. Figure 2.4b shows that oxidation peak had a linear relationship with applied potential down to -1.6 V and remained nearly constant after that. Thus, an applied potential of -1.6 V was chosen for pre-adsorption of KCZ at GC/AuNP electrode in all subsequent experiments.

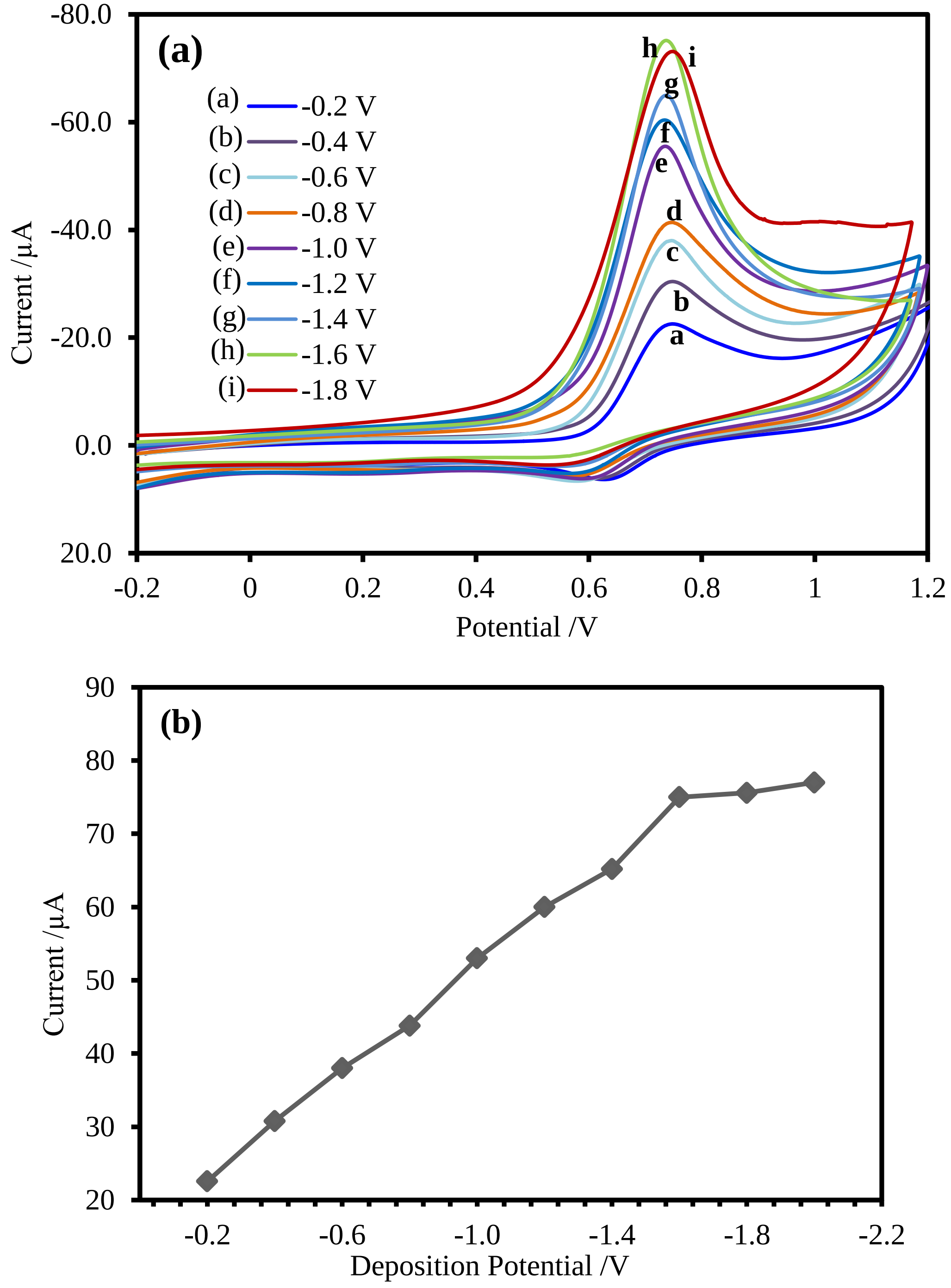

Figure 2.4: (a) CVs with GC/AuNP electrode in presence of 10^{-3}M KCZ in phosphate buffer solution (pH= 4) after pre-treatment at different applied potentials for 60s, (b) Corresponding linear calibration plot of maximum oxidation peak currents for different applied potentials for KCZ pre-deposition.

2.3.5. Effect of Pre-adsorption time

Next at a fixed applied potential of -1.6 V, adsorption time was varied from 10 – 180 s and change in oxidation peak current was studied in the subsequent CV experiments. Figure 2.5a shows the CVs obtained with a GC/AuNP electrode for 10^{-3} M KCZ solution when time applied for pre-adsorption was varied from 10 – 180 s. It was evident that time employed for KCZ pre-adsorption had a significant influence on the oxidation peak current. Figure 2.5b shows that oxidation peak current increased almost linearly with the increase in pre-adsorption time up to 120 s. Beyond 120 s, oxidation peak current remained almost constant. Thus, a pre-adsorption time of 120 s was chosen as optimum time for KCZ pre-adsorption and used in all subsequent experiments.

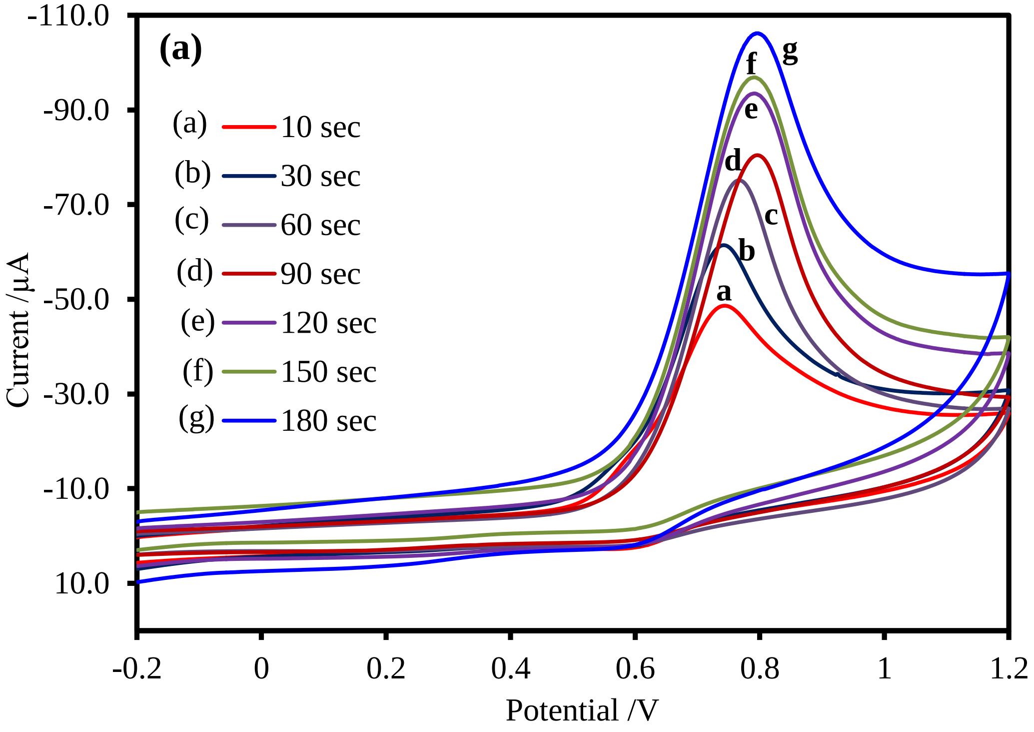

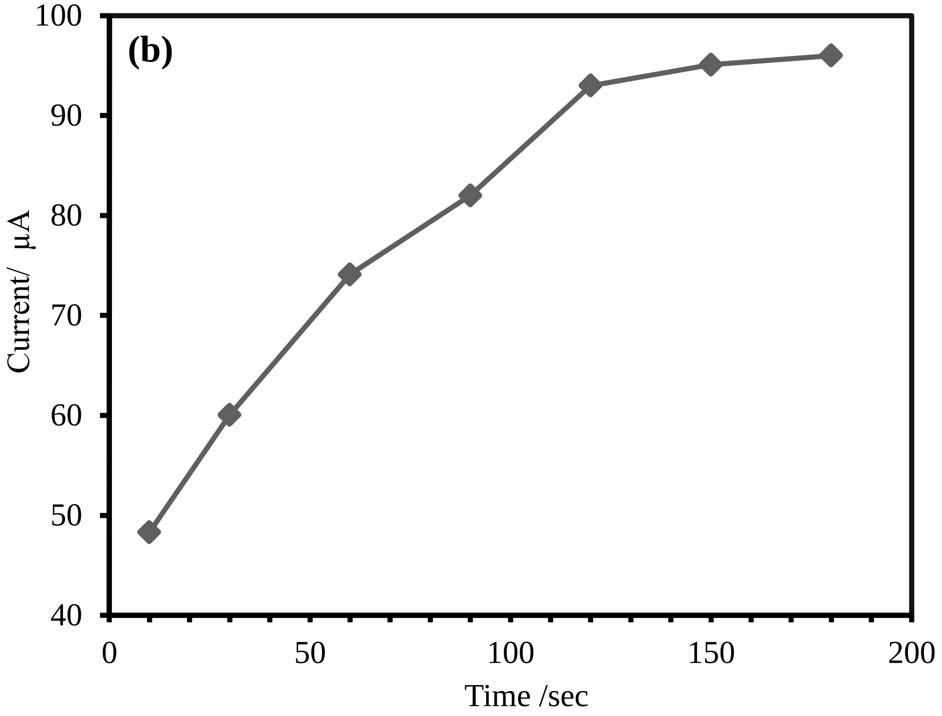

Figure 2.5: (a) CVs with GC/AuNP electrode in presence of 10^{-3}M KCZ in phosphate buffer solution (pH= 4) after pre-treatment at an applied potential of -1.6 V for different times, (b) Corresponding linear calibration plot of maximum oxidation peak currents for KCZ different pre-deposition time.

2.3.6. Effect of pH

One of the key factor, which can influence the electrochemical response is the pH of the solution used for KCZ measurement. Fig. 6A shows that oxidation peak currents for KCZ increased significantly with increase in pH with a maximum peak current at pH 4. Fig. 6B shows that beyond pH 4, up to pH 7, oxidation peak current for KCZ decreased rapidly possibly due to less efficient adsorption of KCZ at the electrode surface and difficulty in the oxidation of KCZ functional groups at pH higher than 4. A shift in peak position can also be observed with the change in pH which might be due to the involvement of proton exchange between buffer solution and the KCZ molecule, however, due to the complex nature of the KCZ molecule and carbon surface it is difficult to determine the detailed mechanism. Nevertheless, these results demonstrate that GC/AuNP electrode can ideally be used at pH 4 for KCZ determination.

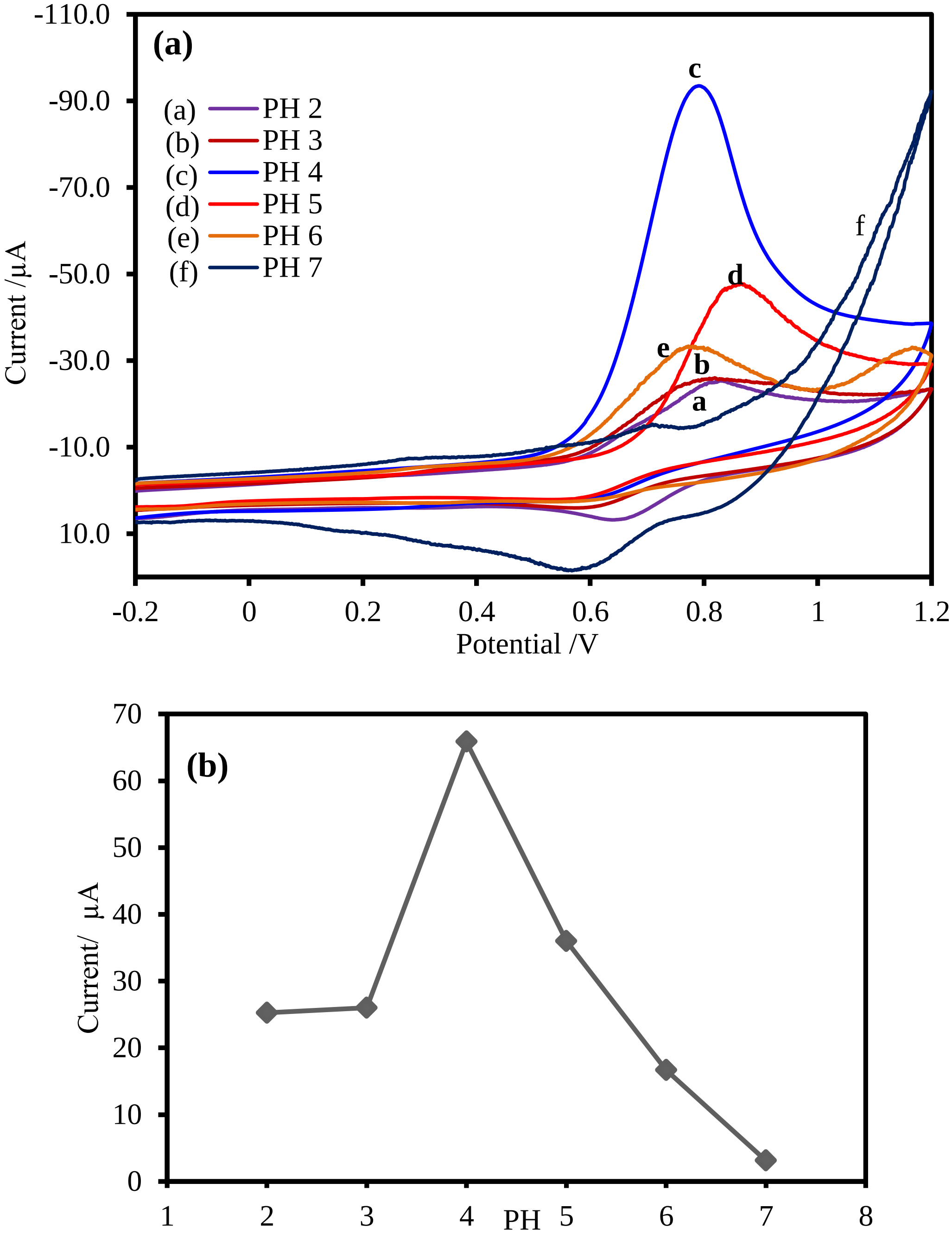

Figure 2.6: (a) CVs with GC/AuNP electrode at different pH values, in presence of 10^{-3} M KCZ in phosphate buffer solution after pre-treatment at an applied potential of -1.6 V and 120 s, (b) Corresponding linear calibration plot of maximum oxidation peak currents for KCZ at different pH values.

2.3.7. Effect of stirring

Stirring of the KCZ solution during pre-adsorption step has also significant effect of KCZ's oxidation peak current and is represented in Fig. 7. When stirring was employed during the pre-adsorption step, the maximum oxidation peak current increased from 92 μA without stirring to approximately 118 μA (Fig. 7) in the subsequent CV experiments. This means during pre-adsorption step stirring assisted the mass transfer for KCZ from solution to the GC/AuNP electrode surface and allowed adsorption of maximum amount of KCZ at the working electrode surface. Thus, a pre-adsorption time of 120 s, an applied voltage of – 1.6 V, pH 4 and stirring of the solution during pre-adsorption were chosen as optimum parameters for measurement of KCZ.

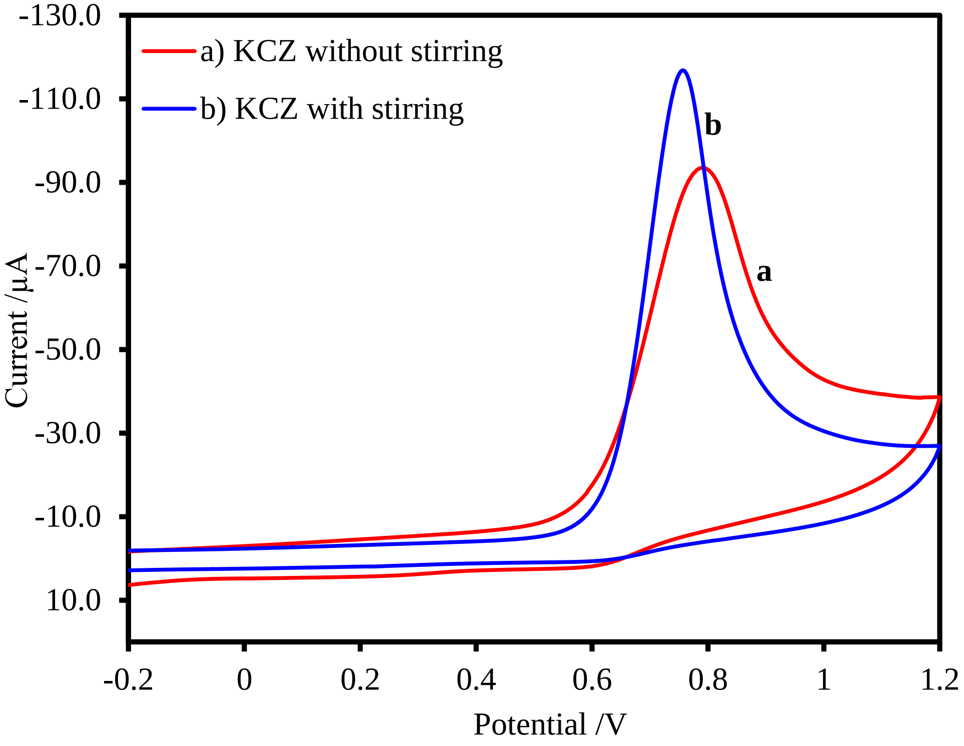

Figure 2.7: CVs with GC/AuNP electrode showing the effect of stirring during pre- treatment of electrode at -1.6 V for 120 sec.

2.3.8. Calibration curve

Figure 2.8a shows CVs obtained with GC/AuNP electrode for successive addition of KCZ to the measurement buffer solution. Evidently, the oxidation peak current increased with increasing concentration of KCZ. Figure 2.8b shows a linear calibration curve of oxidation peak currents for increasing KCZ concentrations. GC/AuNP electrode gave a linear response for 20- 100 μM (R^2 = 0.9986) of KCZ. A detection limit of 2.3 μM (3σ) was achieved. Table 2.1 shows a comparison of GC/AuNP electrode performance for KCZ determination with unmodified GC electrode and other reported methods. This comparison shows that under similar experimental conditions GC/AuNP electrode showed almost 4 times higher oxidation peak current response than a bare GC electrode. Furthermore, GC/AuNP electrode gave a linear concentration range and detection limit comparable or better than many of the reported methods.

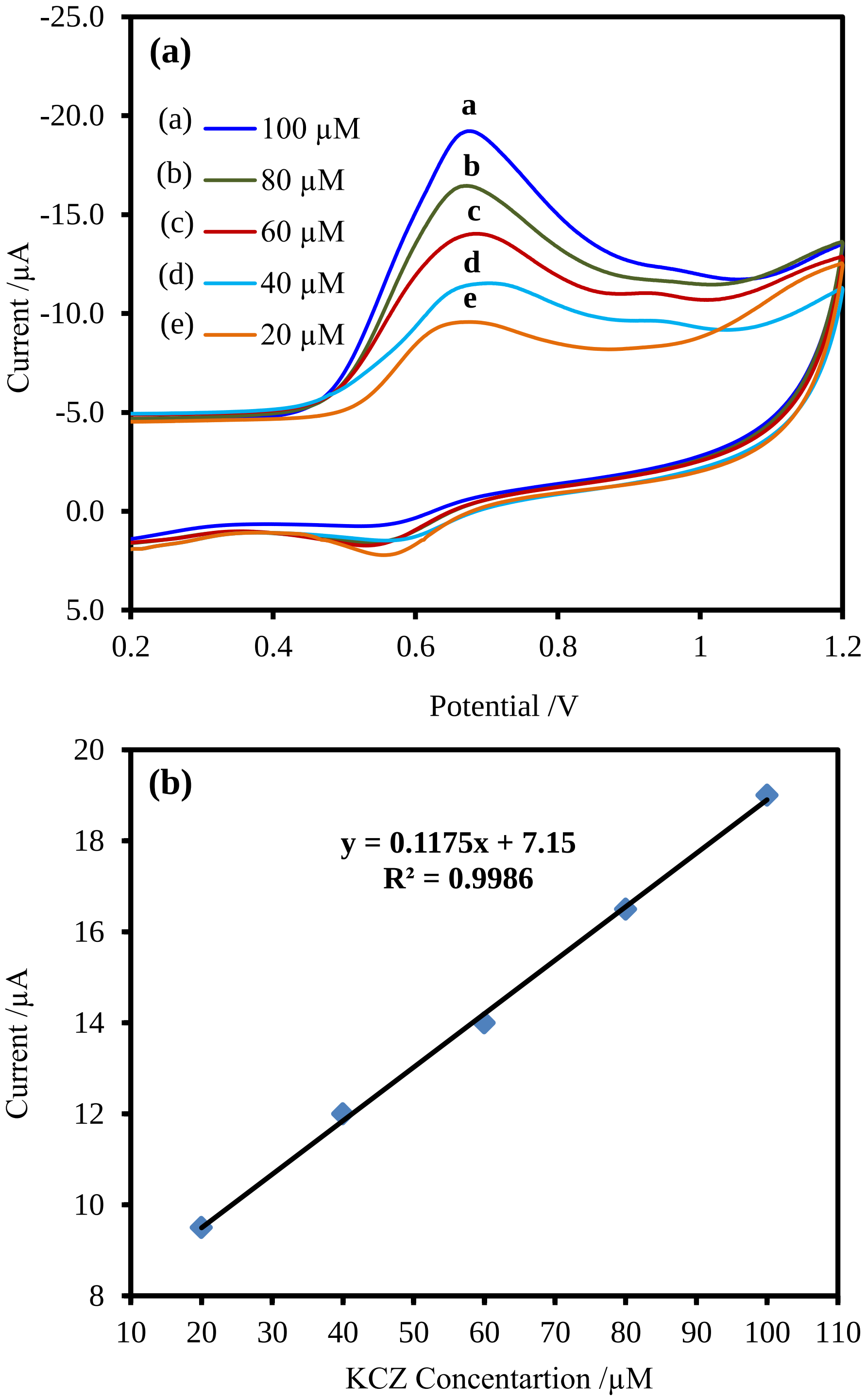

Figure 2.8: (a) CVs with GC/AuNP electrode for successive additions of KCZ (20-100 µM) at optimized conditions, (b)Corresponding linear calibration plot of maximum oxidation peak currents for KCZ

Table 2.1: Comparison of linear concentration ranges and detection limits of different modified electrodes

Method*	**Working electrode**	**Media, pH**	**Linear range (μM)**	**Limit of detection (μM)**	**Standard deviation (SD)**	**Ref.**
CV	GEC modified with AuNP	0.1M acetate buffer (pH 4)	20 – 100	2.3	0.35	Present work
DPV	GCE modified with β cyclodextrin (CDGCE)	0.04 M of Britton–Robins buffer (pH 9)	8 – 80	10.54	0.562	[4]
SWV	glassy carbon electrode (GC)	0.1M NH3-NH4Cl buffer (pH 9)	0.0317 - 0.32	0.0747	1.0	[22]
SWV	polished silver solid amalgam electrode (p-AgSAE)	0.1M Britton Robinson buffer (PH 12)	0.497 – 4.30	0.12	0.3457	[1]
DPV	multi-walled carbon nanotubes (MWCNTs)-modified glassy carbon (GC) electrode	0.2 M phosphate buffer solution (PBS) (pH 7)	1.0 – 30	0. 44	-----	[3]
SWV	a boron-doped diamond electrode (BDD)	0.2M NH3–NH4Cl buffer (pH 9.42)	0.287 – 3.13	0.0829	0.37	[23]

*Cyclic voltammetry (CV), Differential pulse voltammograms (DPV), Square wave voltammetric (SWV).

2.4. CONCLUSION

A simple GC/AuNP electrode was fabricated by the simple chemical reduction method. PA capped AuNP of 10.8 nm were synthesized at the GC electrode surface. A pre-adsorption step was necessary for optimum KCZ determination. The resulting GC/AuNP electrode was used for KCZ determination at pH 4. Analytical parameters such as deposition voltage, deposition time, and pH for analytical measurements were optimized. The GC/AuNP electrode gave a linear concentration range and detection limit comparable or better than many of the reported methods.

2.5. REFERENCES

[1] A. N. d. S. Dantas, D. De Souza, J. E. Soares. Electrochim Acta. 2010. 55. 9083

[2] M. Shamsipur, K. Farhadi. Electroanalysis. 2000, 12, 429.

[3] J. Borowiec, L. Wei, L. Zhu, J. Zhang. Anal Methods. 2012, 4, 444.

[4] M. A. El Ries, M. F. Abdel Ghany, L. A. Hussin, F. M. El-Anwar, A. M. Mohamed. Bulletin of Faculty of Pharmacy, Cairo University. 2013, 51, 49.

[5] E. M. Moety, F. I. Khattab, K. M. Kelani,A. M. AbouAl-Alamein. Farmaco. 2003, 57, 931.

[6] E. M. Koves. J Chromatogr A. 1995, 692, 103.

[7] K. Farhadi, R. Maleki. J Pharm Biomed Anal. 2002, 30, 1023.

[8] Z. Fijałek, J. Chod kowski, M. Warowna. Acta PolPharm. 1992, 49, 1.

[9] M. Shamsipur, K. Farhadi. Chem Anal . 2001, 46, 387.

[10] M. Shamsipur, K. Farhadi. Analyst. 2000, 125, 1639.

[11] P. Arranz, A. Arranz, J. M. Moreda, A. Cid, J. F. Arranz. J Pharm Biomed Anal. 2003, 33, 589.

[12] T. z. Peng, Q. Cheng, C. F. Yang. Fresenius' J Anal Chem. 2001, 370, 1082.

[13] J. M. Pingarrón, P. Sedeño, A. Cortés. Electrochim Acta. 2008, 53, 5848.

[14] P. Rodriguez, D. Plana, D. J. Fermin, M. T. M.Koper. J Catal. 2014, 311, 182.

[15] M. Grzelczak, J. Juste, P. Mulvaney, L. Marzan. Chem Soc Rev. 2008, 37, 1783.

[16] M. Tahir, B. Tahir, N. A. S. Amin. Appl Surf Sci. 2015, 356, 1289.

[17] T. K. Sau, C. J. Murphy. J Am Chem Soc. 2004, 126, 8648.

[18] M. R. Akanda, M. Sohail, M. A. Aziz, A.-N. Kawde. Electroanalysis. 2015.

[19] M. A. Aziz, J.-P. Kim, M. N. Shaikh. Gold Bulletin. 2015, 48, 85.

[20] M. A. Aziz, J.-P. Kim, M. Oyama. Gold Bulletin. 2014, 47, 127.

[21] M. A. Aziz, M. Sohail, M. N. Shaikh, M. Oyama. Electroanalysis. 2016.

[22] K. Łukasiewicz, H. Tarasiewicz, A. Niedzielko. Anal Lett. 2011, 44, 955.

[23] K. Mielech-Lukasiewicz, K. Roginska. Anal Methods. 2014, 6, 7912.

[24] A. Bourke, M. A. Miller et al.. J Electrochem Soc. 2015, *162*, A1547.

CHAPTER 3

Spherical Silver Nanoparticles as SERS Substrate for Enhanced Detection of Ketoconazole

3.1. INTRODUCTION

Surface Enhanced Raman Spectroscopy (SERS), is an important technique for identification and detection of solid, liquid, and gas sample. SERS is highly sensitive and selective method compared with Raman spectroscopy [1]. It is used to investigate and study the molecular vibration at low concentrations. Its principle requires excitation of a localized surface Plasmon resonance (LSPR) resulting from an incident of electromagnetic waves [2]. Recently, it has been used in many important research areas such as medical applications, analytical chemistry, and physical application [3, 4]. SERS has been studied both theoretically and experimentally. The first study by Fleischmann in 1974, was performed by using pyridine absorbed at the surface of silver electrode [5].

SESR is used to study the interaction between the nanoparticles and the surface of the analyte with high sensitivity and low detection limits [6]. SERS is commonly referring to the phenomenon where the Raman-signals from adsorbates on suitable surfaces are enhanced several times due to the excitation of Surface Plasmon Resonance (SPR) on the surface of metals like silver, gold, and copper. The enhancement of SERS signal can be of order factor 10^8 to 10^{10} [7-8]. The enhancement can be explained by two mechanisms, electromagnetic and chemical enhancement. The electromagnetic enhancement considers the dominant effect due to SPR [9-11].

Nanotechnology is of interest in several important fields such as medicine, industrial, biosensors, drug delivery, and catalysis [12-14]. Metal nanoparticles like Ag/NPs and Au/NPs have been widely used in SERS due to their unique properties such as size and shape [15]. Silver colloids are the most common type of SERS substrate which exhibits the large enhancement, strong surface plasmon polarization mode in the visible light range, and relatively stable. There are several methods to synthesize metal nanoparticles (NPs), including chemical method, such as chemical reduction, thermal decomposition [16], and physical method such as chemical vapor deposition, and microwave irradiation [17]. The reduction methods are the most used for the synthesis of Ag/NPs. The reduction method requires three main components, (i) precursor like metal salt (ii) reducing agent like trisodium citrate, ethylene glycol, and sodium borohydride, (iii) stabilizing agent like vinyl pyrrolidone, dodecanoic acid, and oleylamine [18-21]. Ag/NPs have been known to be used in several applications like physical and pharmaceutical application, those related to optical, electrical, and thermal properties [22-26]. Ag/NPs have been used for treating various human diseases, due to the high surface area resulting from the ability of Ag/NPs to coordinate with a large number of legend.

The computational method is widely useful to investigate the design of new drugs and materials that are difficult to find or very expensive; further, it is useful to study the properties of molecules and the assignment of IR and Raman bands [27]. This method is based on mathematical algorithms, statistics, and databases to integrate chemical theory [28]. Ab initio, semiempirical and molecular mechanics numerical techniques were used to determine the geometry optimizations, potential energy surface calculations, and frequency calculation, as seen in the calculations [29-34].

The main goals of this study were to employ silver nanoparticles as substrate to evaluate their behaviour and to establish an alternative environmentally friendly SERS methodology for the determination of ketoconazole. With regard to the Raman technique, SERS was employed due to its extreme sensitivity in the detection of organic molecules. In addition, SERS provides valuable information concerning the enhancement mechanism when paired with well-developed DFT calculations

3.2. EXPERIMENTAL

3.2.1. Chemicals and Materials

Ketoconazole (KCZ) named as ((±) -*cis*-1-Acetyl-4-(4-[(2-[2, 4-dichlorophenyl] -2-[1H-imidazol-1-ylmethyl] -1,3-dioxolan-4-yl) -methoxy] phenyl) piperazine) ≥98% purity was purchased from Sigma-Aldrich. Silver nitrate ($AgNO_3$), CAS No 7761-88-8, was purchased from BDH ACS. Sodium borohydride (NaBH4) 90% purity and Potassium Bromide (KBr) ≥99% purity were purchased from Sigma-Aldrich. All solutions were prepared with ultrapure water obtained from a water purification system (Ultra Clear™ Lab Water Systems, Siemens Water Technologies USA)

3.2.2. Synthesis silver of nanoparticles (Ag/NPs)

Nanoparticles of Ag/NPs were prepared by the chemical reduction method [24, 25]. First, 50 ml of aqueous 0.0010 M $AgNO_3$ solution was prepared as a precursor of the Ag nanoparticles. Then, 150 ml aqueous solution 0.0020M $NaBH_4$ was prepared as a stabilizing and reducing agent (the $NaBH_4$ solution was prepared fresh), by dissolving 11.34 mg in distilled water. The sodium borohydride was placed on ice for 20 min to cool; then the $AgNO_3$ solution was added to $NaBH_4$ solution at rate 1 drop/sec under continuous stirring.

When the silver nitrate was added the color of the mixture turned to dark yellow; this color indicates the formation of nanoparticles.

Mechanism of Ag/NPs formation [26]:

$$AgNO_3 + NaBH_4 \rightarrow Ag + 1/2H_2 + 1/2B_2H_6 + NaNO_3$$

3.2.3. Characterization

The nanomaterials were characterized by various methods including; SEM techniques to determine the particle size, morphology, and particle distributions of nanomaterials.

The UV-Visible spectra of colloids were recorded on a genesis 10S UV-Vis spectrophotometer (Thermo Scientific), using standard quartz cuvette at room temperature between 200-700 nm range. The colloid samples were prepared by dilution the stock solution 4x with distilled water.

FT-IR spectra of samples were recorded using a Perkin-Elmer IR spectrophotometer using potassium bromide (KBr) pellets, the pellet was designed through blending the sample and potassium bromide with a ratio (1:100), the FT-IR measurement was scanned at a range of wavelength from (400 to 4000) cm^{-1}. The He-Ne laser source operating at 0.5 W was utilized for sample excitation

3.2.4. Surface-enhanced Raman spectroscopy (SERS)

The SERS spectra of KCZ were obtained by using Raman spectroscopy system Lab Ram HP Evolution Raman spectrometer equipped with an internal He-Ne 17mW laser at a 633 and 532 nm excitation wavelengths. SERS samples were prepared by using a 3: 1 volume ratio of the KCZ solutions to the colloid. The parameters of the instrument were optimized for all measurements as, laser wavelength at 633nm, acquisition time larger than 200 sec, and objective x10 vi's. The SERS spectra were obtained in the range from 400-1200 cm^{-1}.

3.2.5. Computational details

The DFT calculations were employed to investigate the structural and spectroscopic properties of KCZ compound. The GAUSSIAN 09 program running on an IBM RS/6000 model S85 Unix server was used to carry out the DFT/B3LYP calculations. The 6-311++G (d, p) triple basis set was employed to optimize the structure of the KCZ compound. The Gauss –View program was used to collect the vibrational assignment, Raman line activity, and infrared band intensities of the KCZ compound.

3.3. RESULTS AND DISCUSSION

3.3.1. Characterization of Ag/NP

Several techniques were used to characterize Ag/NPs including ultraviolet-visible spectroscopy (UV-vis) absorbance, SEM, and TEM [35].

Figure 3.1a shows the absorption spectra of the yellow silver colloids prepared by sodium borohydride reduction. The absorption characteristic maximum of the silver nanoparticles was found at 400 nm, which corresponds upon the surface plasmon resonance of silver nanoparticles indicating the presence of spherical Ag nanoparticles, and TEM imaging confirmed this. Figure 3.1b depicts the TEM image of Ag/NPs, which indicates that the average size of the synthesized spherical silver nanoparticles is about 15 nm.

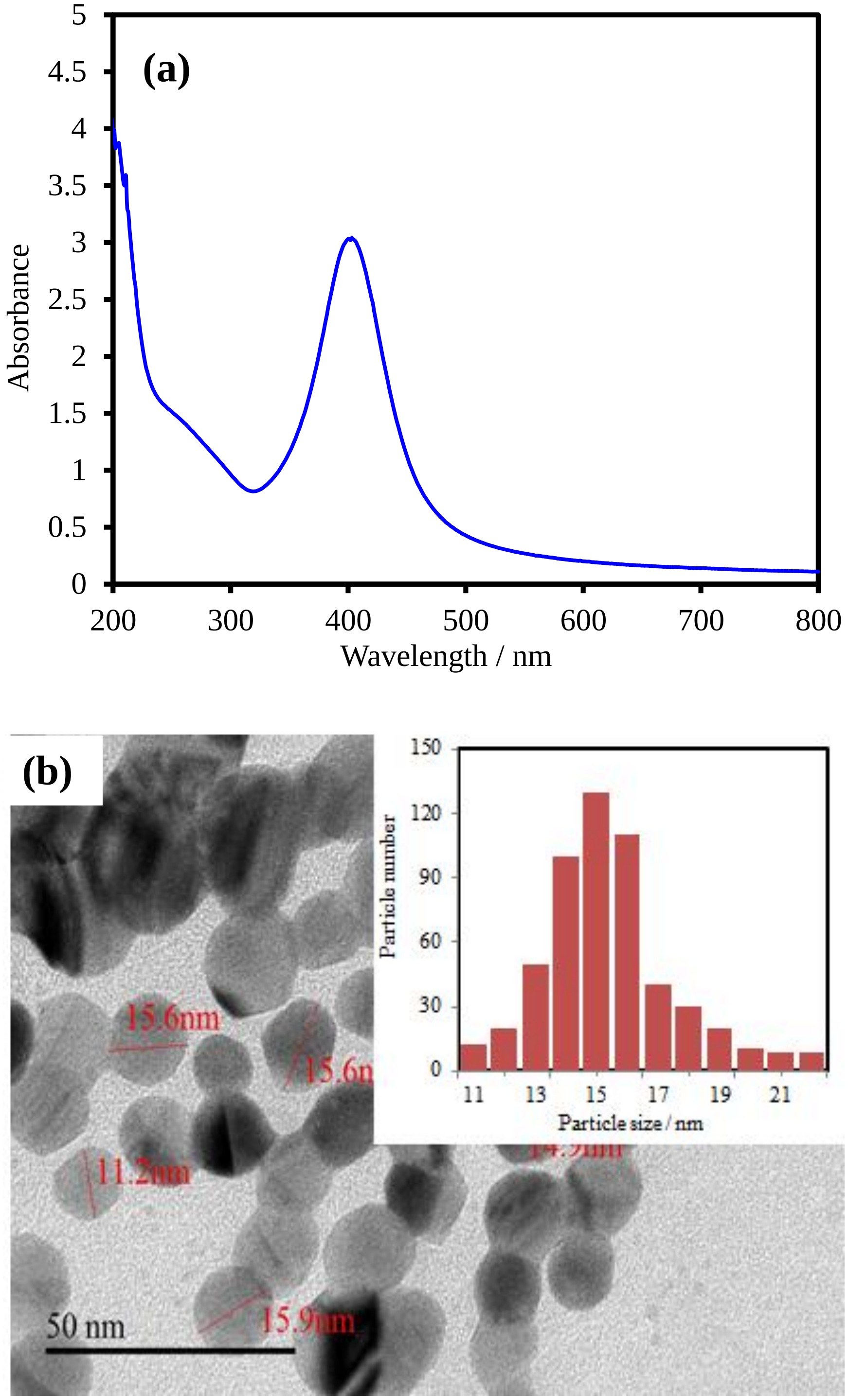

Figure 3.1: (a) UV-Vis absorption spectra of silver nanoparticles, (b) TEM image of silver nanoparticles together with particle size distribution histogram of AgNPs solution

3.3.2. Density Functional Theory (DFT)

3.3.2.1. Molecular geometry of KCZ

Density Functional Theory (DFT) works using Becke's three-parameter hybrid exchange functional with the Lee-Yang-Parr correlation functional, of the density functional theory. And 6-311++G (d, p) basis set were chosen to optimize the structure and to calculate the electronic properties of drug molecule [36]. Geometry optimization of KCZ structure, shown in Figure 3.2, was achieved by minimizing potential energy, using DFT calculation with B3LYP/6-311++G (d, p) method.

The important parameters of the optimized geometry such as bond length, and bond angles, are presented in Table (3.1), and Table (3.2), repressively.

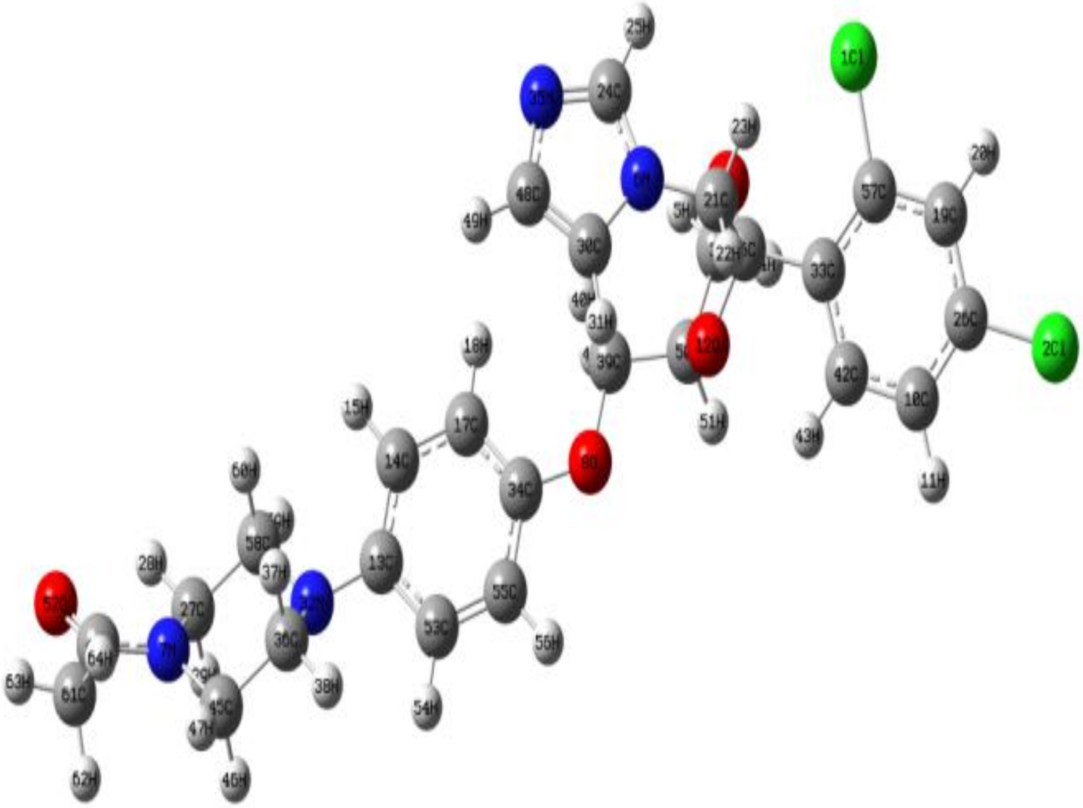

Figure 3.2: The optimized KCZ structure

Table 3.1: Bond length (Å) for Optimized geometrical of KCZ.

Atoms	Bond length\Å	Atoms	Bond length\Å	Atoms	Bond length\Å
R (1,57)	1.7609	R (14,15)	1.082	R (35,48)	1.3784
R (2,26)	1.7538	R (14,17)	1.4001	R (36,37)	1.1046
R (3,4)	1.0953	R (16,21)	1.5436	R (36,38)	1.09
R (3,5)	1.0901	R (16,33)	1.5428	R (36,45)	1.5291
R (3,9)	1.4259	R (17,18)	1.0817	R (39,40)	1.0955
R (3,50)	1.5402	R (17,34)	1.3912	R (39,41)	1.0992
R (6,21)	1.4488	R (19,20)	1.0811	R (39,50)	1.5192
R (6,24)	1.3703	R (19,26)	1.389	R (42,43)	1.082
R (6,30)	1.383	R (19,57)	1.3934	R (44,52)	1.2238
R (7,27)	1.4615	R (21,22)	1.0907	R (44,61)	1.5216
R (7,44)	1.3749	R (21,23)	1.0897	R (45,46)	1.0991
R (7,45)	1.4588	R (24,25)	1.0792	R (45,47)	1.088
R (8,34)	1.3719	R (24,35)	1.3127	R (48,49)	1.0788
R (8,39)	1.4198	R (27,28)	1.0882	R (50,51)	1.0937
R (9,16)	1.411	R (27,29)	1.098	R (53,54)	1.0838
R (10,11)	1.0821	R (27,58)	1.5276	R (53,55)	1.3835
R (10,26)	1.3893	R (30,31)	1.0768	R (55,56)	1.0836
R (10,42)	1.3904	R (30,48)	1.3695	R (58,59)	1.0919
R (12,16)	1.4203	R (32,36)	1.4667	R (58,60)	1.1042
R (12,50)	1.4399	R (32,58)	1.4612	R (61,62)	1.0935
R (13,14)	1.3969	R (33,42)	1.3999	R (61,63)	1.0878
R (13,32)	1.4216	R (33,57)	1.4027	R (61,64)	1.0932
R (13,53)	1.408	R (34,55)	1.4006		

Table 3.2: Angles (^{0}) for Optimized geometrical of KCZ.

Atoms	Angles (^{0})	Atoms	Angles (^{0})	Atoms	Angles (^{0})
A (4,3,5)	109.3462	A (22,21,23)	108.0943	A (7,44,52)	121.7682
A (4,3,9)	110.6264	A (6,24,25)	121.7722	A (7,44,61)	117.5233
A (4,3,50)	111.3489	A (6,24,35)	112.1046	A (52,44,61)	120.7057
A (5,3,9)	107.6993	A (25,24,35)	126.1229	A (7,45,36)	110.4914
A (5,3,50)	113.9293	A (2,26,10)	119.9002	A (7,45,46)	109.5915
A (9,3,50)	103.7026	A (2,26,19)	119.1547	A (7,45,47)	110.271
A (21,6,24)	126.7014	A (10,26,19)	120.945	A (36,45,46)	109.1075
A (21,6,30)	126.8607	A (7,27,28)	107.9084	A (36,45,47)	109.1932
A (24,6,30)	106.3976	A (7,27,29)	109.4083	A (46,45,47)	108.1408
A (27,7,44)	119.7577	A (7,27,58)	110.7975	A (30,48,35)	110.4714
A (27,7,45)	113.7103	A (28,27,29)	108.5381	A (30,48,49)	127.959
A (44,7,45)	125.851	A (28,27,58)	110.8295	A (35,48,49)	121.5692
A (34,8,39)	118.5567	A (29,27,58)	109.3117	A (3,50,12)	103.2903
A (3,9,16)	106.736	A (6,30,31)	121.7914	A (3,50,39)	113.5744
A (11,10,26)	120.4765	A (6,30,48)	105.6891	A (3,50,51)	111.798
A (11,10,42)	120.7968	A (31,30,48)	132.515	A (12,50,39)	110.4952
A (26,10,42)	118.7267	A (13,32,36)	115.6653	A (12,50,51)	108.455
A (16,12,50)	109.6165	A (13,32,58)	117.353	A (39,50,51)	109.0202
A (14,13,32)	123.1897	A (36,32,58)	111.1637	A (13,53,54)	119.5104
A (14,13,53)	117.5032	A (16,33,42)	118.8583	A (13,53,55)	121.38
A (32,13,53)	119.281	A (16,33,57)	124.1181	A (54,53,55)	119.0899
A (13,14,15)	120.522	A (42,33,57)	117.0058	A (34,55,53)	120.442
A (13,14,17)	121.4859	A (8,34,17)	125.0165	A (34,55,56)	118.7338
A (15,14,17)	117.9907	A (8,34,55)	115.8503	A (53,55,56)	120.8112
A (9,16,12)	105.9688	A (17,34,55)	119.1319	A (1,57,19)	115.8481
A (9,16,21)	109.24	A (24,35,48)	105.3364	A (1,57,33)	122.4249
A (9,16,33)	112.2511	A (32,36,37)	110.614	A (19,57,33)	121.7266
A (12,16,21)	108.6353	A (32,36,38)	109.5557	A (27,58,32)	110.4773
A (12,16,33)	110.0764	A (32,36,45)	110.8693	A (27,58,59)	108.6473
A (21,16,33)	110.5144	A (37,36,38)	107.5926	A (27,58,60)	109.001
A (14,17,18)	118.6752	A (37,36,45)	109.1425	A (32,58,59)	108.8281
A (14,17,34)	120.0448	A (38,36,45)	108.9922	A (32,58,60)	111.8075
A (18,17,34)	121.2671	A (8,39,40)	111.0431	A (59,58,60)	107.9967
A (20,19,26)	120.7176	A (8,39,41)	109.9548	A (44,61,62)	111.6815
A (20,19,57)	120.0945	A (8,39,50)	107.6458	A (44,61,63)	107.3102
A (26,19,57)	119.1879	A (40,39,41)	109.1202	A (44,61,64)	111.9131
A (6,21,16)	113.5698	A (40,39,50)	109.9922	A (62,61,63)	108.9043
A (6,21,22)	109.0063	A (41,39,50)	109.0536	A (62,61,64)	108.0218
A (6,21,23)	109.1258	A (10,42,33)	122.4017	A (63,61,64)	108.9454
A (16,21,22)	108.0836	A (10,42,43)	119.6645		
A (16,21,23)	108.822	A (33,42,43)	117.9336		

3.3.2.2. Mulliken analysis

It is an important application in quantum mechanical, used to estimate the partial atomic charge from calculations implemented by the methods of computational chemistry [37]. Calculation charge method is based on a Linear Combination of Atomic Orbitals (LCAO) basis sets [38]. The results of atomic charge are summarized in Table (3.3). The magnitude atomic charge of carbon and oxygen atoms were found to be either positive or negative charge. All the hydrogen atoms have a positive charge, the two chloride atoms have a positive charge, the three nitrogen atoms have a positive charge, and one atom has a negative charge.

Table 3.3: Mulliken atomic charges of KCZ using B3LYP /6-311++G (d, p) basis sets.

Atoms	Charge	Atoms	Charge	Atoms	Charge
Cl	0.475547	C	-0.000423	H	0.169469
Cl	0.505318	H	0.171044	C	-0.490145
C	-0.465472	C	0.169414	H	0.149555
H	0.210114	C	-0.838386	C	0.452659
H	0.183287	H	0.225644	H	0.243471
N	0.275365	H	0.183222	O	-0.333115
N	0.101361	C	0.21838	C	0.048669
O	0.003152	H	0.155433	H	0.151941
O	0.12129	N	0.344832	C	-0.366591
C	-0.732817	C	-0.171096	H	0.171341
H	0.207985	C	-0.111502	C	-0.323615
O	0.148667	N	-0.102154	C	0.199371
C	-0.675932	C	-0.477893	H	0.175661
C	0.184236	H	0.156505	H	0.151529
H	0.192287	H	0.14859	C	-0.491926
C	-0.573548	C	-1.037709	H	0.160004
C	0.383441	H	0.162693	H	0.204973
H	0.173352	H	0.169305	H	0.153449
C	-0.047783	C	-0.17431		
H	0.237131	H	0.21031		
C	-1.000297	C	0.161183		
H	0.215746	C	-0.430243		
H	0.15137	H	0.166662		

3.3.3. Vibrational Assignments of KCZ

3.3.3.1. Vibrational Assignments Theoretically, by DFT

The vibrational frequency modes of KCZ calculated by the DFT with B3LYP 6-311++G (d, p) triple basis sets, and experimental FT-IR and Raman vibrational frequencies are given in Table (3.4). The calculated FT-IR and Raman wavenumbers were in a good correlation between the intensities of experimental vibration modes.

The calculated FT-IR vibration spectrum is shown in Figure 3.3a, and Raman spectrum is shown in Figure 3.3b. The calculated wavenumber was scaled using the scaling factor 0.961 for frequency region ≥ 2000 cm^{-1}, and scaling factor 0.985 for frequency region > 2000 cm^{-1} [39]. The Raman activities (S_i) were calculated with the Gaussian 09 program by converting to Theoretical Raman intensities, using the following relationship derived from the intensity theory of Raman scattering [40, 41].

$$I_i = \frac{f\,(\nu_0 - \nu_i)^4 S_i}{\nu_i \exp\left(\frac{-hc\nu_i}{kT}\right)},$$

where v_0 is the exciting wave number in cm^{-1}, v_i the vibrational wavenumber of i –th normal mode, h, c and k universal constants and f are a suitably chosen common normalization factor for all peak intensities

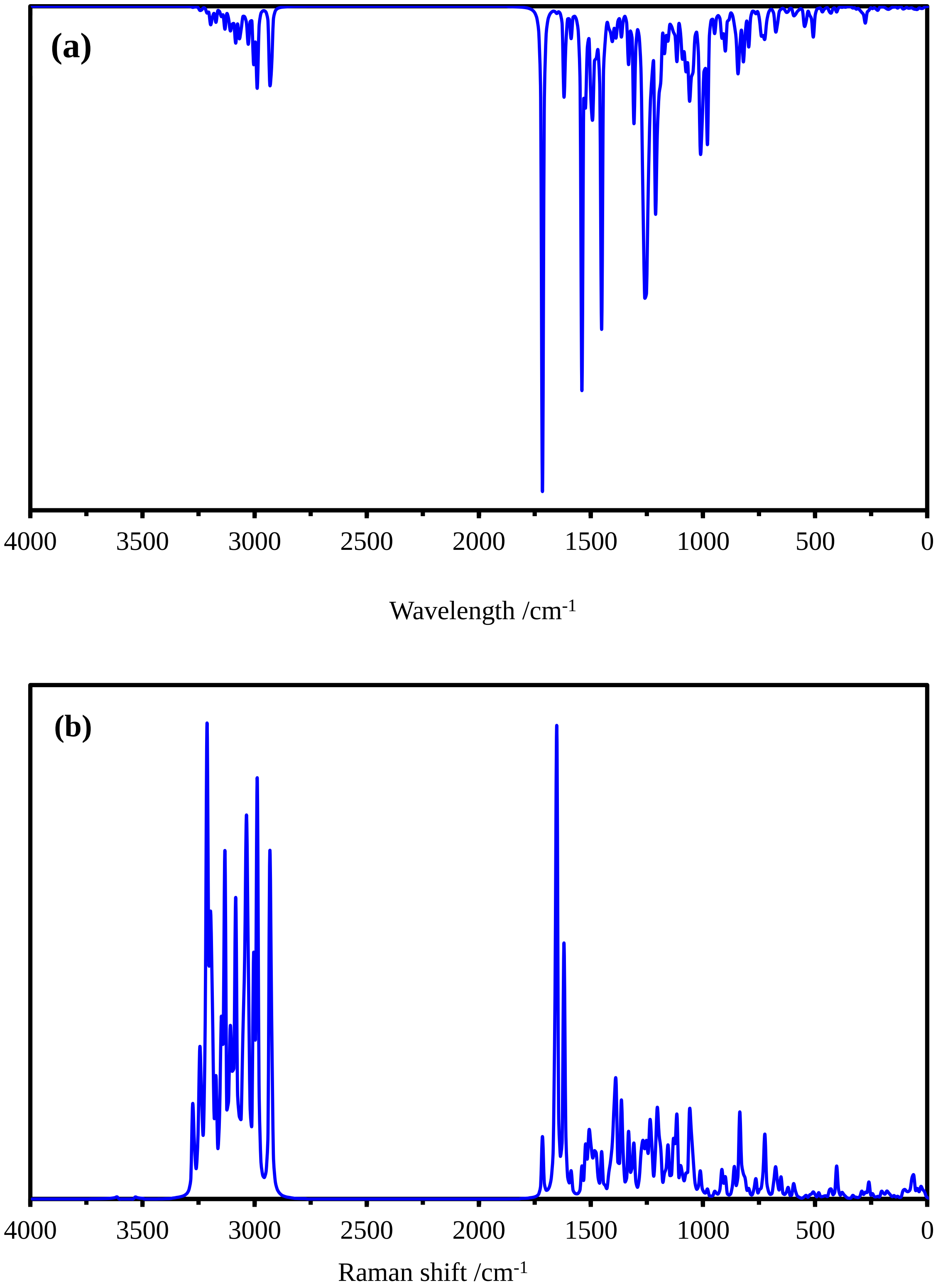

Figure 3.3: Theoretical (a) FT-IR, (b) Raman spectra of KCZ

3.3.3.2. Vibrational Assignments Experimentally

(a) FT-IR analysis

Figure 3.4a shows the IR spectra of the pure drug solid sample. The stretching, vibration C=C–H is observed at 3139 cm^{-1} with medium intensity, and peaks at 3073, 3043 cm^{-1} are for aromatic symmetry C–H stretch (medium intensity), and stretching, vibration for cyclic (epoxy) C–O at 1050 cm^{-1} (weak intensity) [42,43]. The stretching vibration of C=O is observed at 1644 cm^{-1} [44]. The stretching vibration, C–N peak can be observed at 1442, 1290, 1106, and 1050 cm^{-1}, The peaks at 1584, 1555 and 1509 cm^{-1} representative for the C=C aromatic group, and CCC bending in the plane can be seen at 1004, and 736 cm^{-1} [45]. The CCN peaks in the plane can be seen at 1333, and 703 cm^{-1} [46,47]. The peaks at 556 cm^{-1} for CCCl bending out of a plane with weak intensity, stretching vibration of C–Cl appears at 795 cm^{-1} [48 49].

(b) Raman analysis

The Figure 3.4b shows the Experimentally spectra of KCZ with pure solid, The intensity band is at 3136 cm^{-1} for =C–H stretching, vibration with medium intensity, and peaks at 3000 cm^{-1} for cyclic C–H (strong intensity). The peak of C-O is at 1048cm^{-1}, also the C–O bending peak appears at 1199 cm^{-1} (weak intensity). The peak at 1617, 1583, and 1552 cm^{-1} were detected for aromatic C=C with sharp intensity. The peak at 1639 cm^{-1} with medium intensity represents probably C=O. The peak of C–Cl was detected at 799 cm^{-1}.

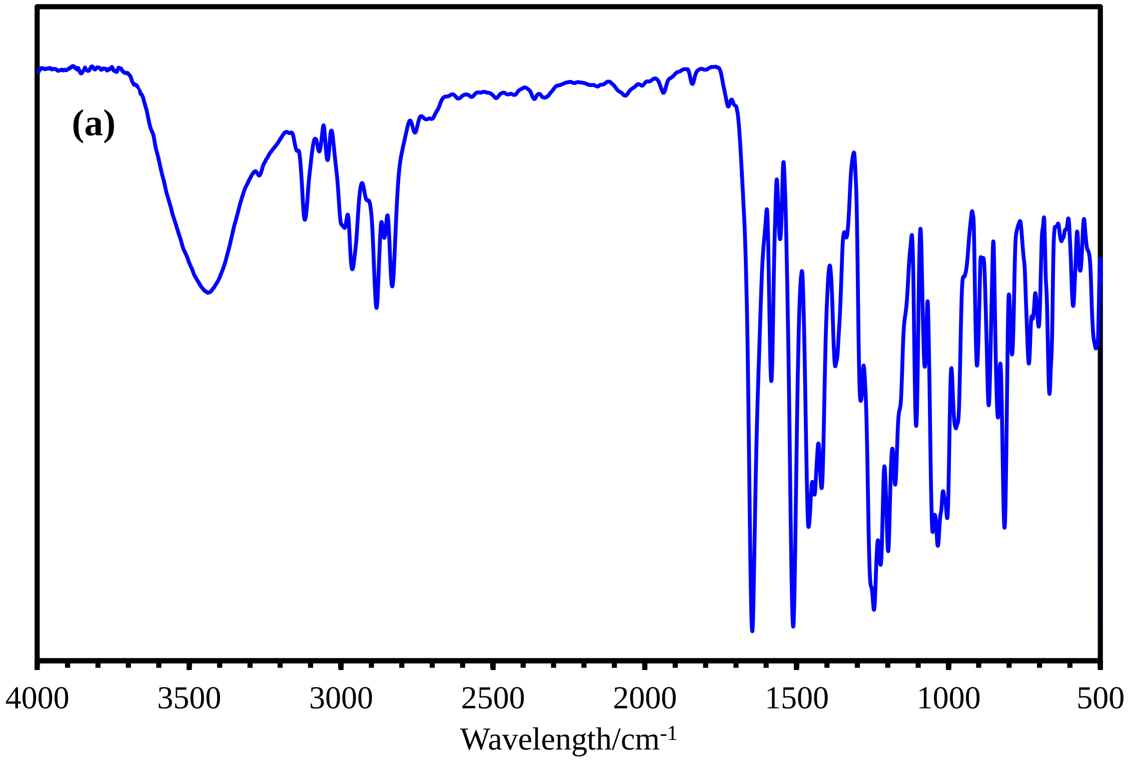

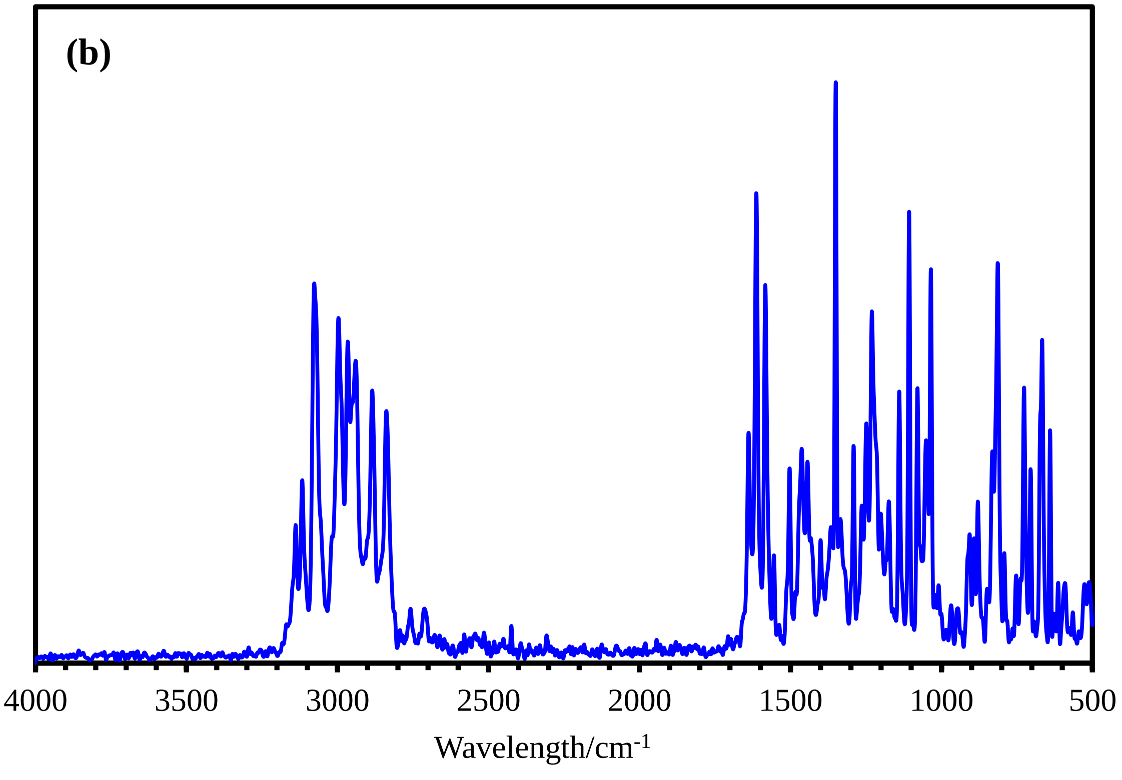

Figure 3.4: Experimental (a) FT-IR, and (b) Raman spectra of KCZ.

Table 3.4: Experimental and calculated B3LYP/6-311++G (d, p) level vibrational frequencies (cm^{-1}) FT-IR and Raman of KCZ.

Calculation IR & Raman	EXP IR	EXP Raman	SERS	Assignments
3142	3139 vw	3136 m		C=C-H str.
3119	3118 m	3116 m		N=C-H str.
3074	3073 w	3076 vs		C-H ring asym. str.
3049	3043 w			C-H ring asym. str.
3009	2997 w	3000 s		CH_2 cyclic sym. str.
2964	2963 m	2965 w		CH_2 sym. str.
2945	2940 w	2938 w		O-C-H sym. str.
2885	2885 s	2883 s		N-CH_2 sym. str.
2869	2856 w			C-CH_2 cyclic sym. str.
1679	1644 vs	1639 m	1661 m	C=O str.
1630		1617 vs	1600 w	C=C ring str.
1588	1584 v	1583 vs	1577 w	C=C ring str.
1564	1555 w	1552 w		C=C ring str.
1516	1509 vs	1503 v	1512 m	N-C=C ring str.
1468	1461 w	1462 m		CH_2 scissor
1450	1442 w	1443 w		N-CH_2 scissor, C-N str.
1396		1394 w	1399 vw	C-N str.
1379	1373 m			C-C ring str, CH bend
1366		1361 vw	1363 m	C-N str. CH_3 scissor
1339	1333 vw	1332 vw	1327 w	CH_2 wag, CNC bend in-p
1298	1290 w	1291 m		C-N str, CH_2 rock, CH bend
1213	1201 s	1199 m	1188 w	C-N bend, C-O bend, CH_2 twist
1142	1142 w	1140 m	1163 m	C-N str, ring bend
1116	1106 s	1107 vs	1102 vw	C-N str, N-CH bend
1050	1050 w	1048 m	1041 s	C-O str, C-N str,
1007	1004 w	1003 vw		CCC in-p bend, CCH in-p bend
914	906 s	904 m		CCN bend out-ph, CCH bend
843	837 m	834 m	828 s	C-N str
806	795 m	799 m		C-Cl str, ring bend
748	736 m	741 w	730 w	COC in-p bend, CCC in-p bend
711	703 m	704 m		CCN in-p bend, OCO in-p bend
670	667 s	666 s	663 vw	CNC out-p bend,
588	589 s	585 m	577 w	NCO out-p bend,
567	566 m	562 w		ring bend def, CCCl out-p bend

3.3.4. SERS results of KCZ on Ag/NP

The Raman signal can be enhanced several times by using some of the nanomaterials to adsorbed at the surface of the metal surface due to the excitation of Surface Plasmon Resonance (SPR) on substrates because of their interactions [50,51]. The silver nanoparticles were used as substrates of SERS. The KCZ solution serves as a target to study the SERS sensitivity [52].

1ml of KCZ solution was placed in a glass cell. Figure 3.5a shows the Raman spectra for KCZ of different concentration. Multi sharp peaks can be assigned to KCZ molecule. These peaks can be assigned as at 798 cm^{-1} for C-N stretching vibration, 1050 cm^{-1} for C-O vibration, peak present at 1389 cm^{-1} for C-N stretching vibration, C=C aromatic stretching vibration present at 1610 cm^{-1}, and stretching vibration C=O detect at 1635 cm^{-1}. The intensity of C-O peak increases with increasing the concentration of KCZ solution.

Figure 3.5b represents the Raman spectra of Ag/NPs and the Raman spectra of 1×10^{-5} M KCZ without Ag/NPs, and the Raman spectra of 1×10^{-5}M KCZ with Ag/NPs. It can be seen a number of bands were enhanced due to the excitation of surface Plasmon resonance of substrates which is due to the strong interaction between KCZ and Ag/NPs.

The peak intensity of KCZ at 1050 cm^{-1} in the normal Raman spectrum for C-O stretching, vibration mode with Ag/NPs highly enhances is stronger than without Ag/NPs. As shown in Figure 5b, it is shifted to 1041 cm^{-1} in SERS spectra. Also, there is a significant enhancement of the peak of C-N at 798 cm^{-1} in normal Raman spectra and it is shifted to 820 cm^{-1} in SERS spectra. The band at 1151 cm^{-1} in the normal Raman spectrum shifted to 1157 cm^{-1} in the SERS spectrum. This band shows medium enhancement factor, which is attributed to the C-N stretching. The weak modes at 1489 and 1358 cm^{-1} in the normal Raman spectrum are shifted to 1512, and 1363 cm^{-1} ,respectively in the SERS spectrum. These bands are enhanced to higher intensities in SERS spectrum than normal Raman spectrum, which are contributed to N-C=C ring stretching, and C-N stretching, respectively.

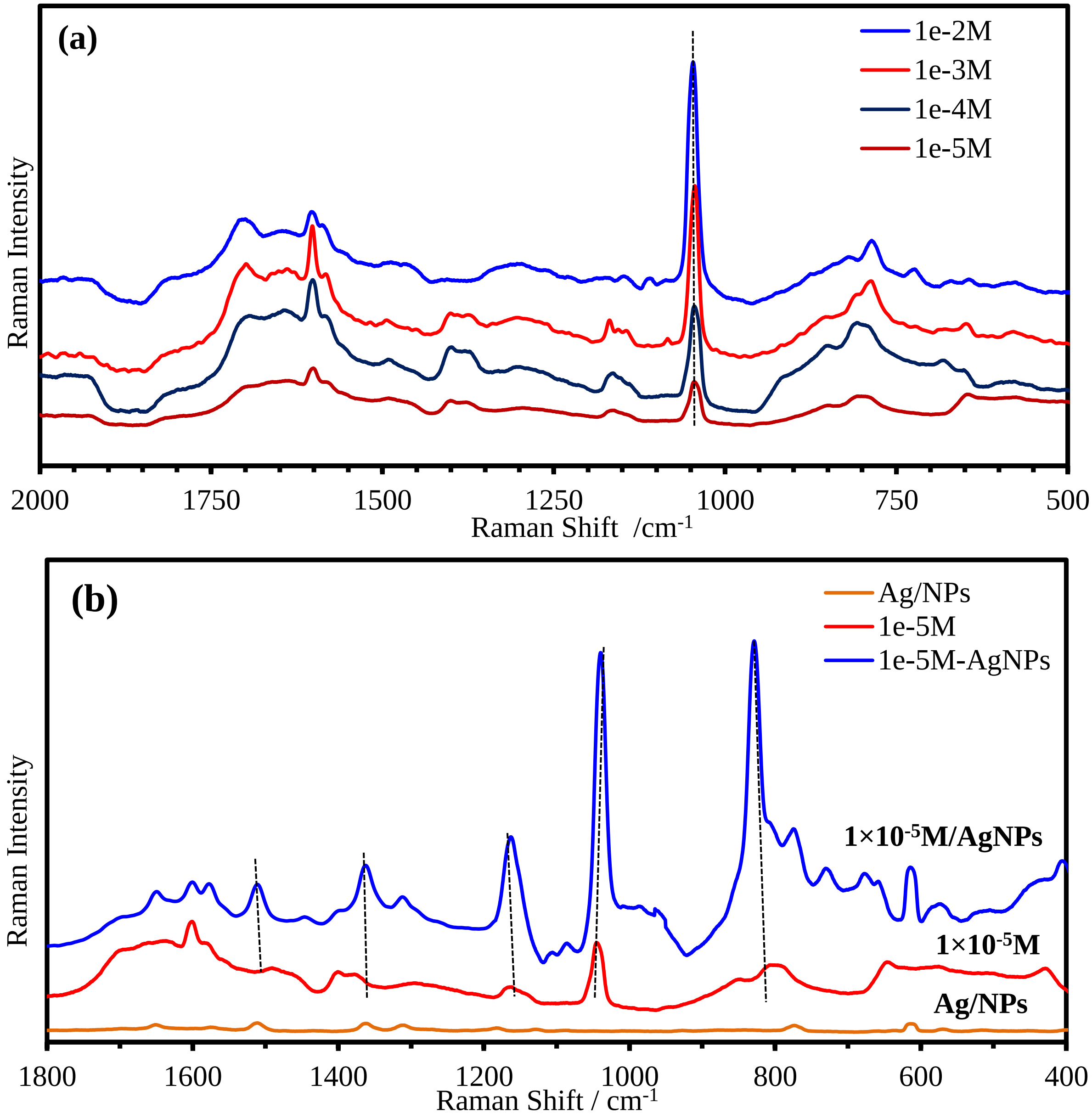

Figure 3.5: (a) Raman spectrum of aqueous KCZ solution at different Concentrations, (b) SRES spectrum of 1× 10^{-5} M of KCZ with and without Ag/NPs. Laser ʎ=633nm, acquisition time; 200 sec, and objective; 10x.

3.3.5. Calibration curves and detection limit

The concentration-dependent SERS spectra of KCZ obtained by using Ag/NPs are given in Figure 3.6a. We can see that the SERS intensity was affected by changing the concentration of KCZ. The SERS intensity increased proportionally with increased concentrations of KCZ solutions in a range from (1×10^{-5} to 1×10^{-9}) mol. L^{-1}. Figure 3.6b shows the calibration curves at bands 1041 cm $^{-1}$. The calibration curve was plotted as intensity vs log [KCZ], which was found to be linear in the range of (1×10^{-5} to 1×10^{-9}) mol. L^{-1} with the R^2 equal to 0.9956. The SERS detection limit in this report reached 9.1×10^{-10} mol. L^{-1}. We collected the SERS spectra of 9.1×10^{-10} mol. L^{-1} KCZ solution seven times and reported the average, with an SD equal to 0.63.

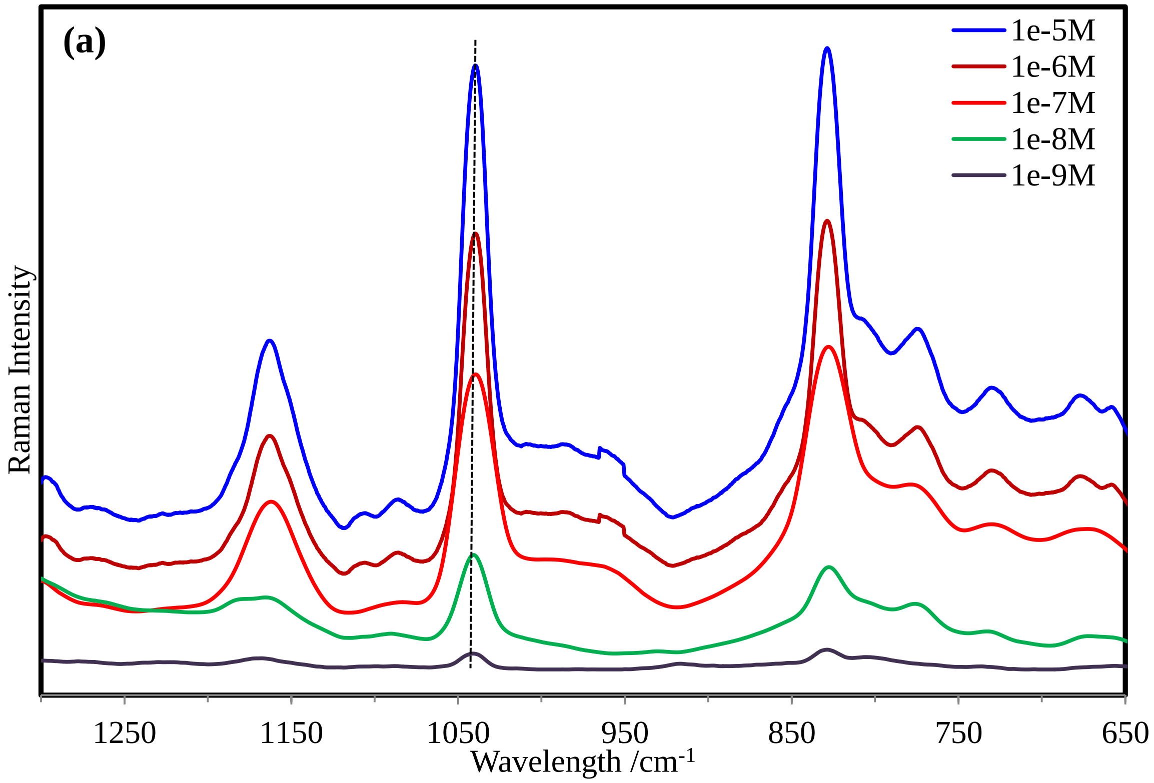

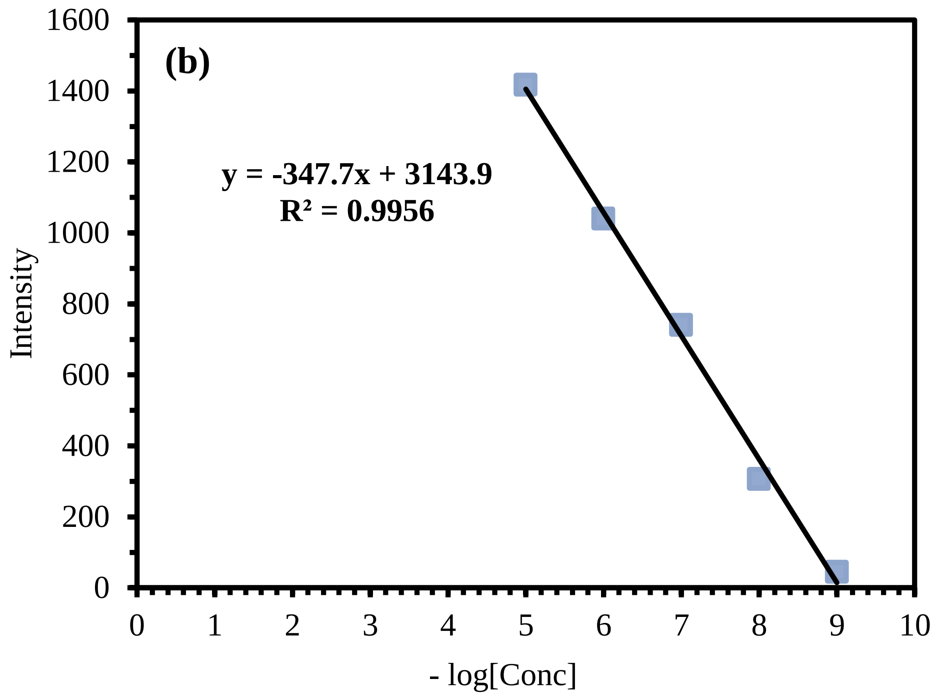

Figure 3.6: (a) SERS spectra of KCZ at different concentrations; (b) Calibration curve of the band at 1041 cm^{-1}. Laser ʎ=633nm, acquisition time; 200 sec, and objective; 10x.

3.4. CONCLUSION

The silver nanoparticles were synthesized by a reduction method, with about 15 nm particle size. The optimized conformation of KCZ on the silver surface was discussed by SERS and DFT calculation with B3LYP/6-311++G (d, p) basis set. The intensities and the wavenumber of vibration frequency bands in the theoretical spectrum are close to experimental spectra. The bands assigned to the C-O and to C-N stretching vibration modes are clearly enhanced. These results indicate that KCZ molecules are mostly chemisorbed on the silver substrates, and are significantly enhanced through the O and N atoms. The SERS determination on KCZ was studied at different concentrations; the detection limit of 9.1×10^{-10}M was obtained.

3.5. REFERENCES

[1] Wei Xie and Sebastian Schlucker. Phys. Chem. 2013, 15, 5329.

[2] Paul L. Stiles, Jon A. Dieringer, Nilam C. Shah, and Richard P. Van Duyne. Annu Rev Anal Chem. 2008, 1, 601.

[3] V. Deckert, P. Singh, Z. Zhang. Chem. Commun. 2015, 51, 3069.

[4] M. S. Wong, N. J. Halas, G. Scuseria. J. Am. Chem. Soc. 2008, 130, 16592.

[5] Qianwang Chen, Xiangkai Kong, Ran Li. Chem. Commun. 2011, 47, 11237.

[6] Peijie Wang, Duan Zhang, Lisheng Zhang, Yan Fan. Chm. Phy Letters. 2013, 556, 146.

[7] Furong Tian, Franck Bonnier, Alan Casey. Anal. Methods. 2014, 6, 9116.

[8] Nathan D. Israelsen, Cynthia Hanson, and Elizabeth Vargis. Scientific World Journal. 2015, 12, 124582.

[9] Zhijun Zhang, Bin Ren. Nanoscale. 2013, 5, 1059.

[10] Yudong Lu, Shanyuan Feng, Xueyun Liu. J. Nanomaterials. 2013, 8, 984831

[11] P. J. Vikesland, W. Lenga, S. Renneckar. Analyst. 2015, 140, 5640.

[12] H. Rivera, G. M. Herrera, A. C. Padilla. 2013, 3, 158.

[13] Kamat PV. J. Phys. Chem B. 2002, 106, 7729.

[14] Mann. S, Ozin. GA. Nature. 1996, 382, 313.

[15] Nicewarner-Pena SR, Freeman RG, Reiss BD. Science. 2001, 294, 137.

[16] Seongmin Hong and Xiao Li. Journal of Nanomaterial. 2013, 9, 790323.

[17] Lawrence, D.Ä.; Ryan, R. Catalyst Preparation. 2006, 93.

[18] Sergeev, G.B. Elsevier Science. 2006, 7, 36.

[19] Yugang Sun, Younan Xia. Materials science. 2002, 298, 2176.

[20] S. Naveen, A. Umer, M. Rafioue. Nano. 2012, 7, 5.

[21] S. Iravani, H. Korbekandi, S.V. Mirmohammadi. Research in Pharmaceutical Sciences. 2014, 9, 385.

[22] Sukumaran Prabhu and Eldho K Poulose. International Nano Letters. 2012, 2, 32.

[23] Y.Aparna, J.V.Ramana Rao, K. Venkateswara Rao. IEEE. 2011, 4, 783.

[24] N. Ramzan, S. Naveed, Asim Umer. Nano. 2012, 7, 5.

[25] Ratyakshi and R.P. Chauhan. Asian Journal of Chemistry. 2009, 21, 113.

[26] M. Emran Quayum, Md. Khairul Hassan Bhuiyan. J. Pharm. Sci. 2013, 12(1), 29.

[27] David Young. John Wiley & Sons. 2001, 123, 41.

[28] F. Jensen. John Wiley & Sons. 2007.

[29] G. H. Grant, W. G. Richards. Oxford. 1995.

[30] P. W. Atkins, R. S. Friedman. Oxford. 1997.

[31] B. L. Hammond, W. A. Lester, Jr., P. J. Reynolds. World Scientific. 1994.

[32] C. David Sherrill. School of Chemistry and Biochemistry. 2000.

[33] Foresman. J.B. and Frisch. M. Inc. Pittsburgh PA. 1996.

[34] Yildiz-Ören, Betül P. J. Fac. Pharm, Ankara, 2003, 32(3), 165.

[35] Zaheer Khan, Athar Adil Hashmi, Sunil Kumar. Adv. Mat. Lett. 2011, 2(3), 188.

[36] C. Lee, W. Yang, and R. G. Parr. Physical Review B. 1988, 37, 785.

[37] C.C.Sangeetha, R.Madivanane, V.Pouchaname. Int. J. Chem. Tech Res. 2014, 6(5), 2854.

[38] Mulliken R. S. J. Chem. Phys.1955, 23(10), 1833.

[39] Leena Sinha, Onkar Prasad, Vijay Narayan. J. At. Mol. Sci. 2012, 105.

[40] Onkar Prasad. Leena Sinha, and Naveen Kumar. J. At. Mol. Sci. 2010, 3, 201.

[41] G. Keresztury. New York. 2002, 1, 1.

[42] M. Najmuddin, AA Mohsin, T. Khan. J. Pharm. Bio and Chem. Sc. 2010, 1, 407.

[43] Arshad Bashir Khan, Chanky Saha. J Pharm Sci. 2015, 5(2), 61.

[44] M. Pandeeswaran, K.P. Elango. Spectrochimica Acta Part A. 2009, 72, 789.

[45] R.Radzuan, A.B. Abdul Majeed, M.K. Hamzah. IEEE. 2010, 10, 407.

[46] Md. R. Ali, G. Kumar, Md. A. Hussain. Am. J. Pharm Health Res. 2014, 3,2.

[47] Anandakirouchenane E, Sarath Chandiran. J. Bio & Pharm Res. 2014, 5(4), 336.

[48] B. Karolewicz, A. Go´rniak, J.Pluta. J. Therm. Anal. Calorim. 2014, 115, 2487.

[49] Joanna S Day, Howell G.M Edwards. Spectrochimica Acta Part A. 2004, 60, 1725.

[50] Lee, P.C., Meisel, D. Journal of Physical Chemistry. 1986, 86 (17), 3391.

[51] Koji Mitamura, Toyoko Imae, Nagahiro Saito, and Osamu Takai. J. Phys. Chem. B. 2007, 11, 8891.

[52] Li, H. G. and Cullum, B. M. Applied Spectroscopy. 2004, 59, 410.

CHAPTER 4

Silver Colloid and Film Substrates in Surface-Enhanced Raman Scattering for 2-Thiouracil Detection

4.1. INTRODUCTION

2-Thiouracil (2-TU) known as 4-Hydroxy-2-mercaptopyrimidine is a pyrimidine derivative, and a thio- derivative of uracil, and one of the nucleic acid bases. It plays a significant role in biological and medical applications such as an anticancer agent, antithyroid drug, antiviral agent, and anticarcinogenic agent [1]. Some forms of 2-TU have been appeared in corrosion inhibitor of steel [2], as dental adhesives [3], and in a prebiotic environment [4]. Its configuration allows forming a complex structure when 2-TU interacts with some transition metal like mine, Au, Cr, Zn, and Ag. It is used to determine the orientation of crystal growth when the complex is added as additive to the metal solution and determines the position of the molecule with the metallic surface [5].

The absorption and fluorescence spectra of 2-TU have been reported [6]. The IR spectra of 2-TU have been recorded in Ar matrices and KBr [7-8]. The band assignment of the 2-TU has been recorded by different studies based on an initial study at Hartree Fock (HF) calculation, Density functional theory (DFT) calculation [9], and coupled with Matrix Isolation [10]. Some computational methods have been used to provide structure, conformation, optimized structure, vibration frequencies and Raman, IR, NMR spectra of the molecule. The harmonic and anharmonic vibration frequencies, and geometry optimizations of 2-thiouracil and uracil were reported using DFT and PT2 calculation, at BLYP and B3LYP [11]. Surendra Babu reported the energy, the equilibrium constant, and dipole moment of 2-TU in the gas phase in a solvent with different polarities using DFT at B3LYP/6- 311++G (d, p) basis set calculations [12]. The surface-enhanced Raman spectroscopy (SERS) is the powerful technique used for the detection of a single molecule with high sensitivity, and the ability to identify the structures of drugs that are rich vibrations bond [13]. Many substances with rough surface were advanced in the SERS study like electrodes, metal film, and metallic colloids [14]. Gold (Au) and Silver (Ag) nanoparticles have been the most common of colloids due to their easy preparation, and high enhancement for the SERS detection. The particle size and geometry shape of nanoparticles affect the enchantment of SERS signals. The silver and gold NPs provide signal enhancement of the vibration signals [15]. Several methods have been used to prepare many of metal nanoparticles with specific size and shape, such as physical, biological, and chemical methods. The latter is the common one for preparing the nanoparticles due to the easy method, low cost, and high purity of yield [16]. SERS plays an important role in determining the adsorption orientation and existence forms for drugs, such as meperidine, diazepam, aspirin, and thiouracil on the surface of silver and gold metal [17, 18].

Adsorption orientations of drugs depend on the concentration, temperature, pH, and potential of the surface [19]. The common advantage of SERS is that it provides the information structure of adsorbed molecules, and, therefore, SERS is used in several fields of applications, such as biochemistry, medicinal applications, analytical applications [20-24]. In this work, we aimed to prepare Ag/NPs and investigate their efficiency as substrates for the detection of 2-TU by SERS.

4.2. EXPERIMENTAL

4.2.1. Chemicals and Materials

2-Thiouracil **“**4-Hydroxy-2-mercaptopyrimidine, Catalog number is T7750, and ≥99% purity was purchased from Sigma-Aldrich. Silver nitrate ($AgNO_3$, 99.8%) product, the number 30087, was purchased from BDH-Chemicals Ltd Poole England. Sodium borohydride ($NaBH_4$, 90%), 8mm diameter, and 7.5% $CoCl_2$ impurity were purchased from Sigma-Aldrich. Trisodium citrate dihydrate ($C_6H_5Na_3O_7{\cdot}2H_2O$, 98%) **(**catalog number S-279, and the product number 78479) was purchased from Fisher Scientific Company in U.S.A. Potassium bromide (KBr, ≥ 99%) was purchased from Sigma-Aldrich. The chemical compounds were used without any purification process. Solutions were prepared with ultrapure water obtained from a water purification system (Ultra Clear™ Lab Water Systems, Siemens Water Technologies USA)

4.2.2. Synthesis of silver nanoparticles (Ag/NPs)

4.2.2.1. Synthesis of silver nanoparticles (Ag/NPs) Type I

See section 3.2.2.

4.2.2.2. Synthesis of silver nanoparticles (Ag/NPs) Type II

Silver colloids were prepared using the Han-Qing Yua and An-Wu Xu description with a modification [25]. First, a solution of 10^{-3}M silver nitrate was prepared by dissolving 45mg of $AgNO_3$ in 250ml of deionized water, followed by heating the solution at 90 ^{o}C. Then, 10 ml of 0.5% solution of trisodium citrate dihydrate was added at a rate 1 drop/sec to the solution under stirring. After adding 5ml, the solution color turned yellow. Finally, the solution was kept at boiling for one hour; the color of the solution changed to greenish yellow.

Mechanism of formation Ag/NPs [26]:

$$4Ag^{+} + C_6H_5O_7Na_3 + 2H_2O \longrightarrow 4Ag + C_6H_5O_7H_3 + 3Na^{+} + H^{+} + O_2\uparrow$$

Scheme 4.1 shows the procedure of preparing the SERS substrate. First, 10-µL of the silver colloid solution was deposited on a glass slide and allowed to dry in air. Then, 10µL of the targeted 2-thiouracil solution was dropped on the top of the dried silver nanoparticles, which were attached to a glass slide, and allowed to dry in air.

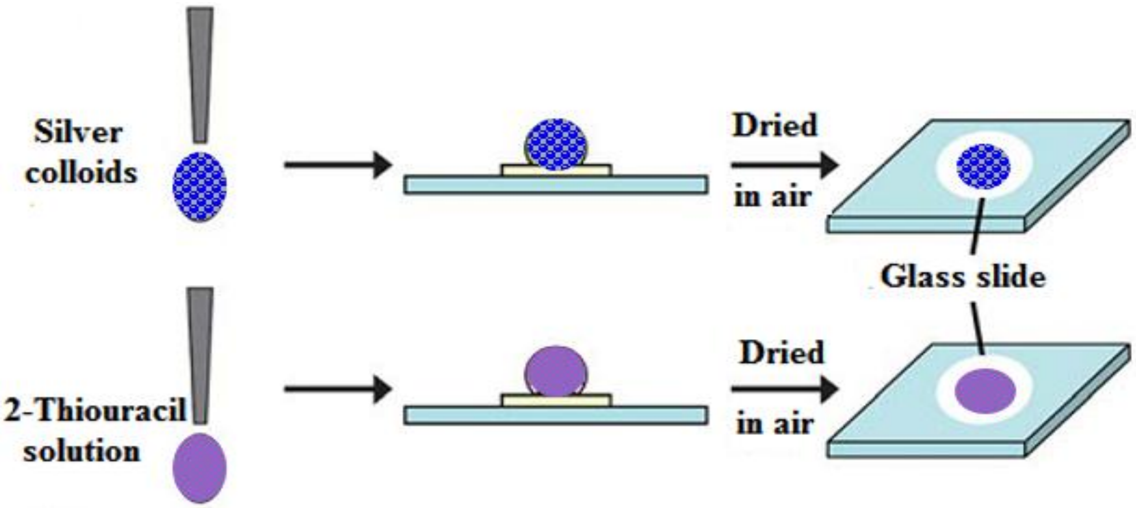

Scheme 4.1: process of the drying-mediated condensation effect for a drop of silver nanoparticles and 2-TU solution on the glass slides

4.2.3. Surface-Enhanced Raman Scattering (SERS)

The SERS spectra of 2-TU were obtained by using a Raman spectroscopy system (Lab Ram HP Evolution Raman spectrometer). One milliliter of 2-TU solution was placed in a glass cell with dimensions of 1cm in radius and 2 cm in height. The glass cell was placed in the dark room. The 633 nm radiation setting of an Argon ion laser was used as the excitation source. A 10x objective was used for focusing the laser beam on the solution. The acquisition time was 20 sec, with one accumulation for the collection of each SERS spectra. The SERS spectra were obtained in the range from 350-1350 cm^{-1}.

4.2.4. Computational details

The DFT calculations were employed to investigate the structural and spectroscopic properties of 2-TU compound. The GAUSSIAN 09 program running on an IBM RS/6000 model S85 Unix server was used to carry out the DFT/B3LYP calculations. The 6-311++G (d, p) triple basis set was employed to optimize the structure of the 2-TU compound. The B3LYP/ GEN basis set was employed to optimize the structure of 2-TU -Ag, and 2-TU-Au complex. The Gauss –View program was used to collect the vibrational assignment, Raman line activity, and infrared band intensities of the 2-TU compound.

4.3. RESULTS AND DISCUSSION

4.3.1. Characterization NPs

Figure 4.1a shows the UV-vis spectrum of the prepared silver nanoparticles (Type I). The maximum absorbance of silver nanoparticles shows the surface Plasmon resonance at λ_{max} ~ 400 nm while in Figure 4.1b the maximum absorption band is at λ_{max} ~ 420 nm, for (Type II) of the obtained silver nanoparticles. The maximum absorbance bands have a narrow width, which means the nanoparticle distribution is very narrow [27].

Ag/NPs prepared with $NaBH_4$ as a precursor is depicted in Figure 4.2a. A good dispersion nanoparticles can be observed. The size of spherical particles ranges between 13-17 nm. Figure 4.2b shows the TEM image of Type II silver NPs prepared with $C_6H_5Na_3O_7{\cdot}2H_2O$ as a precursor. The image indicates well-dispersed particles with a uniform shape. The average size of these particles is about ~ 70 nm.

The SEM images of Ag/NPs film, prepared by the addition of 200 µl of Ag/NPs of Type II to the glass slide and dried in clean conditions, are shown in Figure 4.2c and 4.2d. They show the SEM image of silver nanoparticles formed by chemical reduction of silver nitrate, and their aggregates with sizes in the range of 10 to 50 nm.

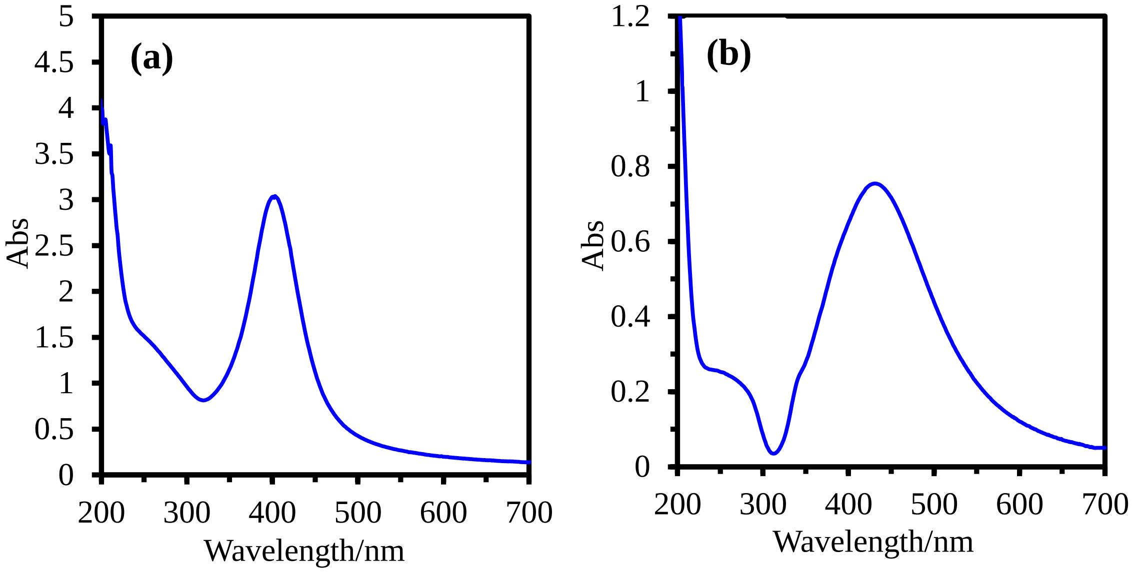

Figure 4.1: UV-Vis absorption spectra of silver nanoparticles (a) for Type I, and (b) for Type II

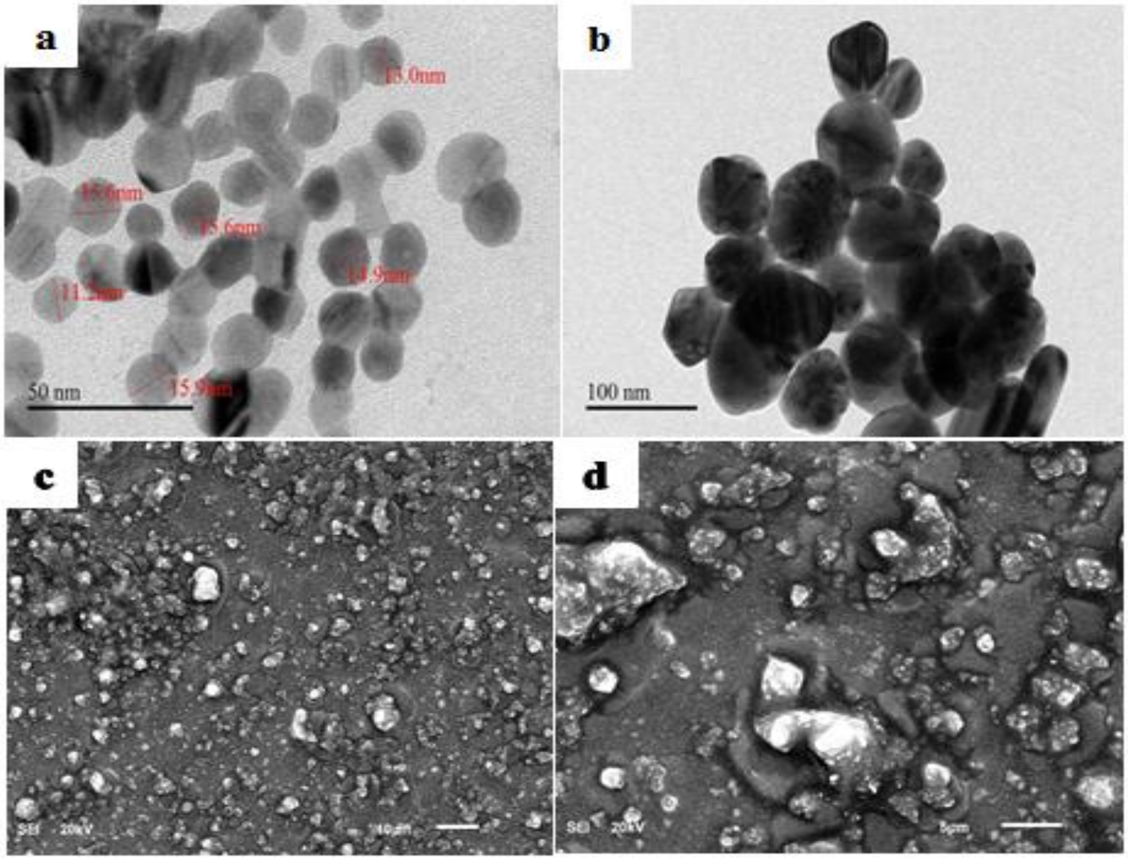

Figure 4.2: (a) A typical TEM image of silver NPs (Type I) prepared with $NaBH_4$, (b) TEM image of silver NPs (Type II) prepared with $C_6H_5Na_3O_7 \cdot 2H_2O$, (c) SEM image of silver NPs aggregates on the glass microscope slide, (d) magnified SEM image of the (c).

4.3.2. Density Functional Theory (DFT)

4.3.2.1. Molecular geometry of 2-TU

The determination of the structure of the molecule in question is the first substantial step in the theoretical calculations. The optimized structure of 2-Thiouracil was determined using the DFT calculations with B3LYP/6-311++G (d, p) basis set, as shown in Figure 4.3, with minimum surface potential energy. All measurements were derived using the Gaussian 09 program. The important parameters of the optimized geometry, such as bond length, bond angles, and dihedral angles are presented in Table 4.1. All theoretical calculations of the isolated 2-TU molecule were performed in the gaseous state while the experimental results were done in the solid state. Therefore, the theoretical parameters of the optimized structure are complementary to the experimental values.

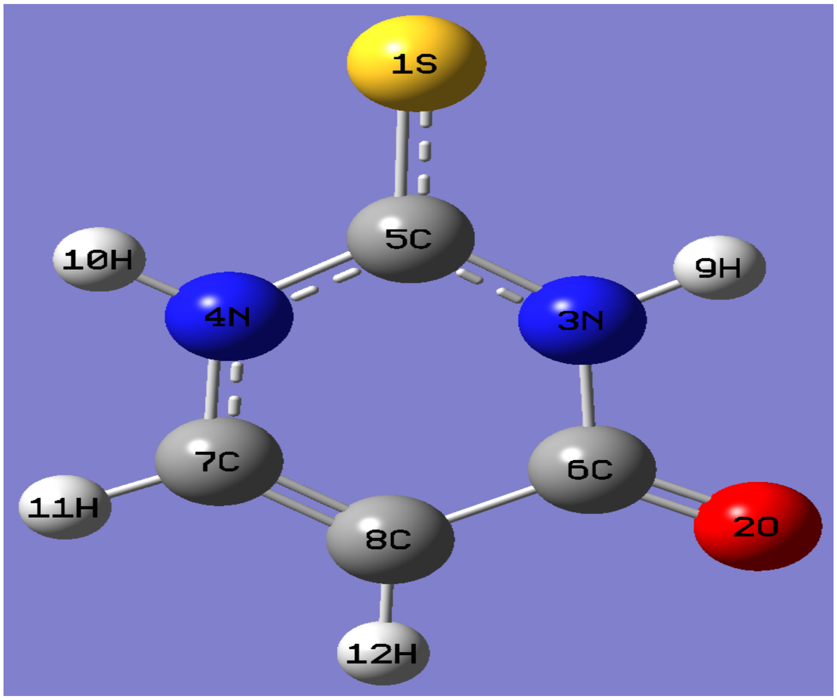

Figure 4.3: The optimized structure of 2- Thiouracil.

Table 4.1: Optimized bond lengths (Å), bond angle (^{0}), and dihedral angle (^{0}) of 2-TU at the DFT with B3LYP/6-311++G(d,p).

Atoms	**Bond length (Å)**	**Atoms**	**Angles (^{0})**	**Atoms**	**Dihedral Angle (^{0})**
S1-C5	1.6614	C5-N3-C6	128.0961	C6-N3-C5-S1	180.0007
O2-C6	1.2137	C5-N3-H9	116.147	C6-N3-C5-N4	0.0016
N3-C5	1.3699	C6-N3-H9	115.757	H9-N3-C5-S1	0.0031
N3-C6	1.4166	C5-N4-C7	123.8845	H9-N3-C5-N4	180.004
N3-H9	1.013	C5-N4-H10	115.2912	C5-N3-C6-O2	180.0102
N4-C5	1.3781	C7-N4-H10	120.8243	C5-N3-C6-C8	0.008
N4-C7	1.3741	S1-C5-N3	124.2642	H9-N3-C6-O2	0.0079
N4-H10	1.0095	S1-C5-N4	122.4821	H9-N3-C6-C8	-179.9943
C6-C8	1.4563	N3-C5-N4	113.2537	C7-N4-C5-S1	-180.0069
C7-C8	1.3479	O2-C6-N3	120.0523	C7-N4-C5-N3	-0.0077
C7-H11	1.0827	O2-C6-C8	126.5376	H10-N4-C5-S1	-0.0081
C8-H12	1.0793	N3-C6-C8	113.4101	H10-N4-C5-N3	-180.009
		N4-C7-C8	121.7707	C5-N4-C7-C8	0.0033
		N4-C7-H11	115.2528	C5-N4-C7-H11	180.0027
		C8-C7-H11	122.9765	H10-N4-C7-C8	-179.9953
		C6-C8-C7	119.585	H10-N4-C7-H11	0.004
		C6-C8-H12	118.3667	O2-C6-C8-C7	-180.0146
		C7-C8-H12	122.0483	O2-C6-C8-H12	-0.0121
				N3-C6-C8-C7	-0.0123
				N3-C6-C8-H12	-180.0097
				N4-C7-C8-C6	0.0075
				N4-C7-C8-H12	-179.9951
				H11-C7-C8-C6	180.0082
				H11-C7-C8-H12	0.0056

4.3.2.2. Mulliken analysis

A Mulliken analysis is an important application in quantum mechanics and is used to estimate the partial atomic charge from calculations implemented by the methods of computational chemistry. The calculation charge method is based on a Linear Combination of Atomic Orbitals (LCAO) basis set [28]. The Mulliken partial charges of an S1 atom and a C5 atom which connects with the S1 atom are -0.641505, and +0.222915, respectively. The Mulliken charge distributions of the O atom and the C6 atom of the neighboring O were obtained as -0.312416, and +0.1244, respectively. The H atoms have a positive charge, and the N atoms have a negative charge. Table 4.2 presents the partial atomic charge for all atoms of the 2-TU optimized structure.

Table 4.2: Mulliken atomic partial charges of 2-TU.

Atoms	Charge
S	-0.641505
O	-0.312416
N	-0.247023
N	-0.202683
C	0.222915
C	0.1244
C	0.11389
C	-0.136352
H	0.351967
H	0.328949
H	0.181523
H	0.216335

4.3.3. Vibrational Assignments

The vibrational frequency modes of 2-TU were recorded through the DFT method with B3LYP level and 6-311++G (d, p) basis sets, and the experimental FT-IR and Raman for the solid and saturated solution of 2-TU are shown in Table 4.3. The FT-IR and Raman theoretical wave numbers of the vibration modes were excellently correlated with the experimental modes. The FT-IR and Raman spectra of the theoretical and the experimental method are present in Figure 4.4, and Figure 4.5, respectively.

4.3.3.1. Vibrational Assignments Theoretically, by DFT

The FT-IR and Raman spectra are shown in Figure 4.4. Vibration frequency modes were obtained by DFT methods with B3LYP/ 6-311++G (d, p) triple basis sets. All FT-IR and Raman calculated modes are in excellent correlation with the experimental result. The calculated wave number was scaled using a scaling factor 0.961 for the frequency region ≥ 2000 cm^{-1}, and a scaling factor of 0.985 for the frequency region > 2000 cm^{-1}. For example, the NH stretching vibrational modes were assigned at 3484 and 3448 cm^{-1} in the theoretical spectra. The calculated CH stretching vibrational modes for 2-TU were assigned at 3116 and 3079 cm^{-1}. The C=O stretching band was assigned at 1745 cm^{-1} in the theoretical spectra. The sharp band at 1638 cm^{-1} in the theoretical spectra correspond to the C=C stretching vibration mode. Here, the stretching vibration of C=S was assigned at 1142 cm^{-1}, and the C=S bending band in the plane was assigned at 446 cm^{-1} in the calculated spectrum. In addition, the bands at 1375, 1214, 1184, 1065, 989, and 903 cm^{-1} are related to C-N stretching. The peaks present at 489 and 266 cm^{-1} are attributed to S-C-N bending in the plane, and the small signal at 581 cm^{-1} is assigned to C-N-H bending out of the plane. The NH bending modes (in the plane) were predicted at six different frequencies, and bending modes (out of plane) were predicted at two different frequencies, (Table 4.3).

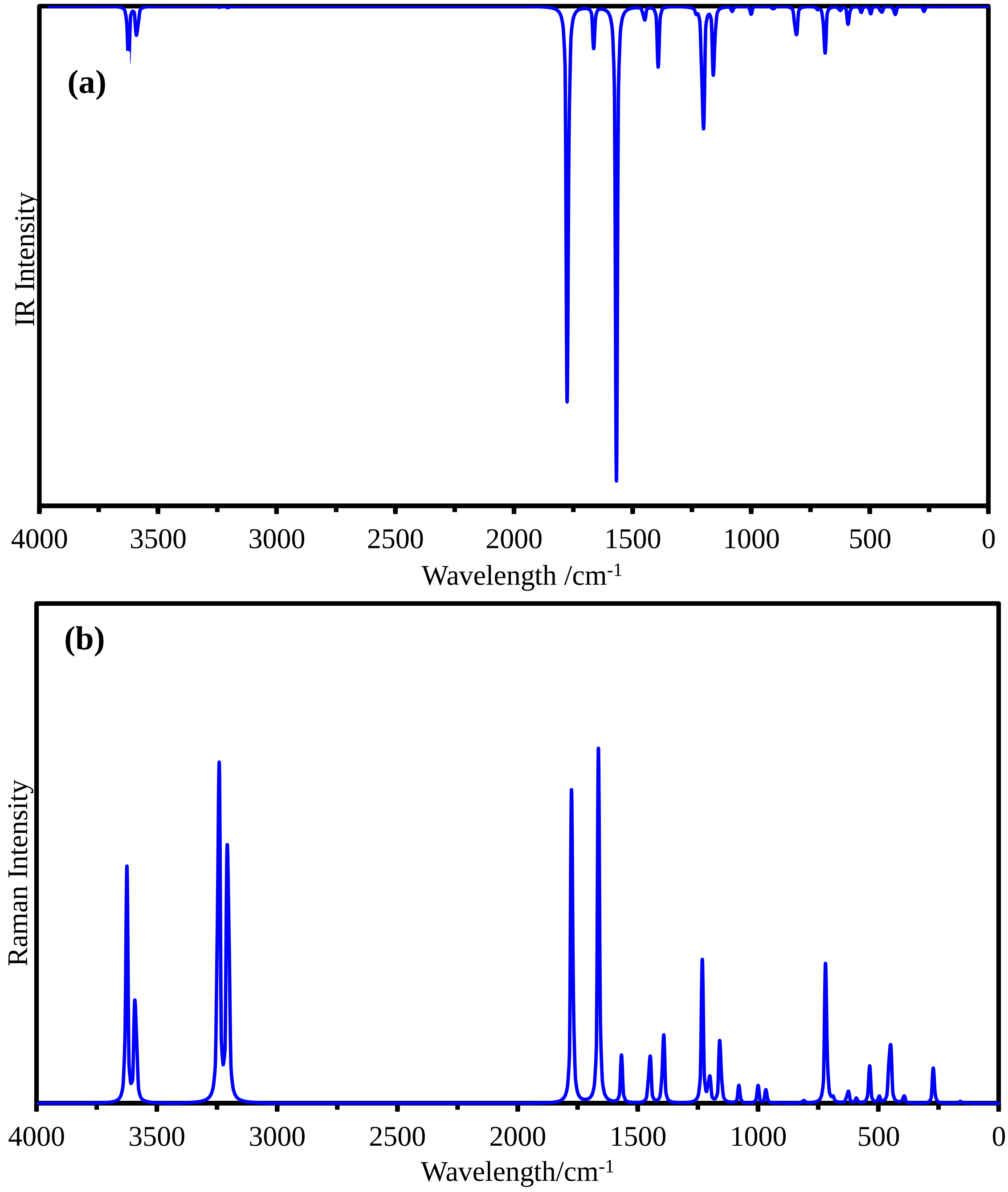

Figure 4.4: Theoretical (a) FT-IR spectrum and (b) Raman spectrum of 2-TU

4.3.3.2. Vibrational Assignments Experimentally

Figure 4.5a and Figure 4.5b are showing the FT-IR and Raman spectra of the pure solid sample of 2-TU, respectively. The C-H stretching is present at (3130 and 3080) cm^{-1} in the IR experimental spectrum, and at (3131 and 3081) cm^{-1} in the Raman experimental spectrum. The C=C peak was predicted at 1627 and 1626 cm^{-1} in the IR and Raman experimental spectrum, respectively. The C=O vibration mode generally appears at 1678 cm^{-1} in the IR experimental spectrum, and at 1679 cm^{-1} in the Raman experimental spectrum. The stretching band of C=S was predicted at 1173 and 1171 cm^{-1} in the IR and Raman experimental spectrum, respectively. This is in agreement with the previous reports [10, 29]. The C-N stretching bands were predicted at 1562, 1383, 1216, 1072, 1002, and 912 cm^{-1} in the IR experimental spectrum, and at 1554, 1377, 1220, 1071, 999, and 913 cm^{-1} in the Raman experimental spectrum. This is in agreement with the literature [29]. The N-H bending modes in the plane generally appear at 1449, 1366 cm^{-1} at the IR and at 1445, 1368 cm^{-1} at the Raman experimental spectrum, for all uracil derivatives [30]. The C-H bending bands out of the plane were predicted at 955, 794, and 735 cm^{-1} in the IR experimental spectrum, and at 957, 789, and 736 cm^{-1} in the Raman experimental spectrum. The C=S in-plane mode was detected at 452 and 453 cm^{-1} in the IR and Raman experimental spectrum, respectively. This peak is in agreement with the previous study [31].

Figure 4.5c shows the Raman spectrum of the 1.0 M 2-TU saturated solution for the 400- 3900 cm^{-1} region. The paramount bands observed in the 1.0 M solution of the 2-TU are tabulated in Table 4.3. The Raman spectra in an agreement with the normal Raman spectrum of the 2-TU solid.

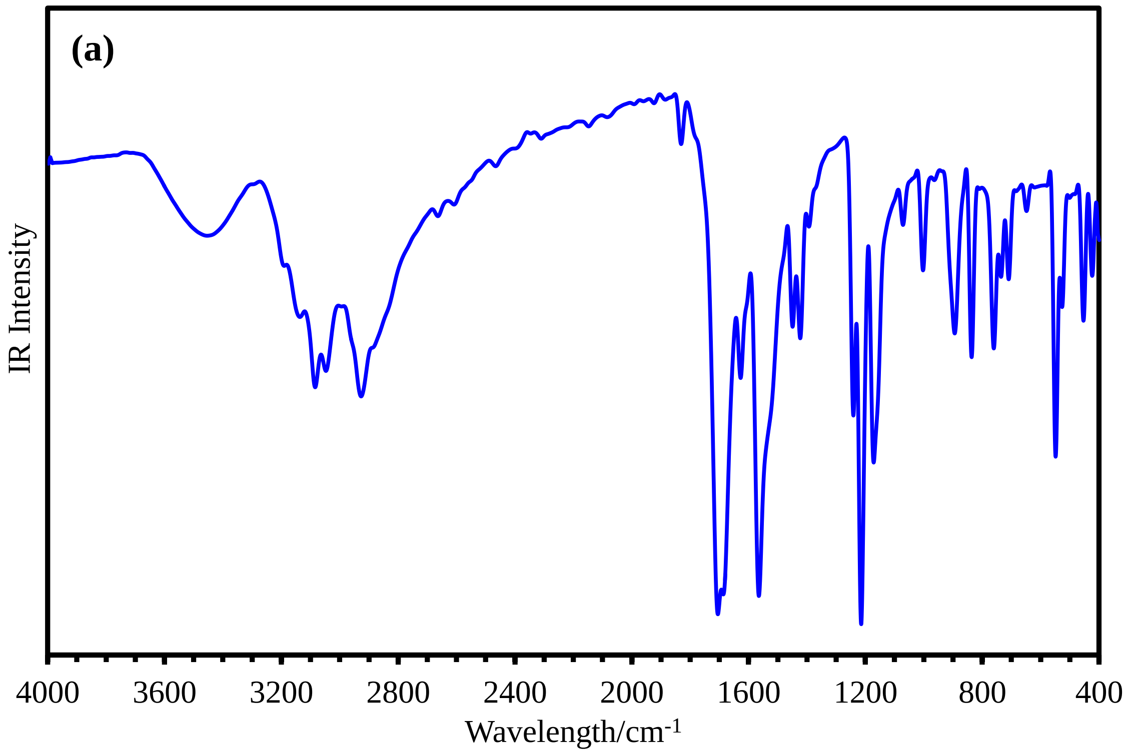
(a)
IR Intensity
4000
3600
3200
2800
2400
2000
1600
1200
800
400
Wavelength/cm-1

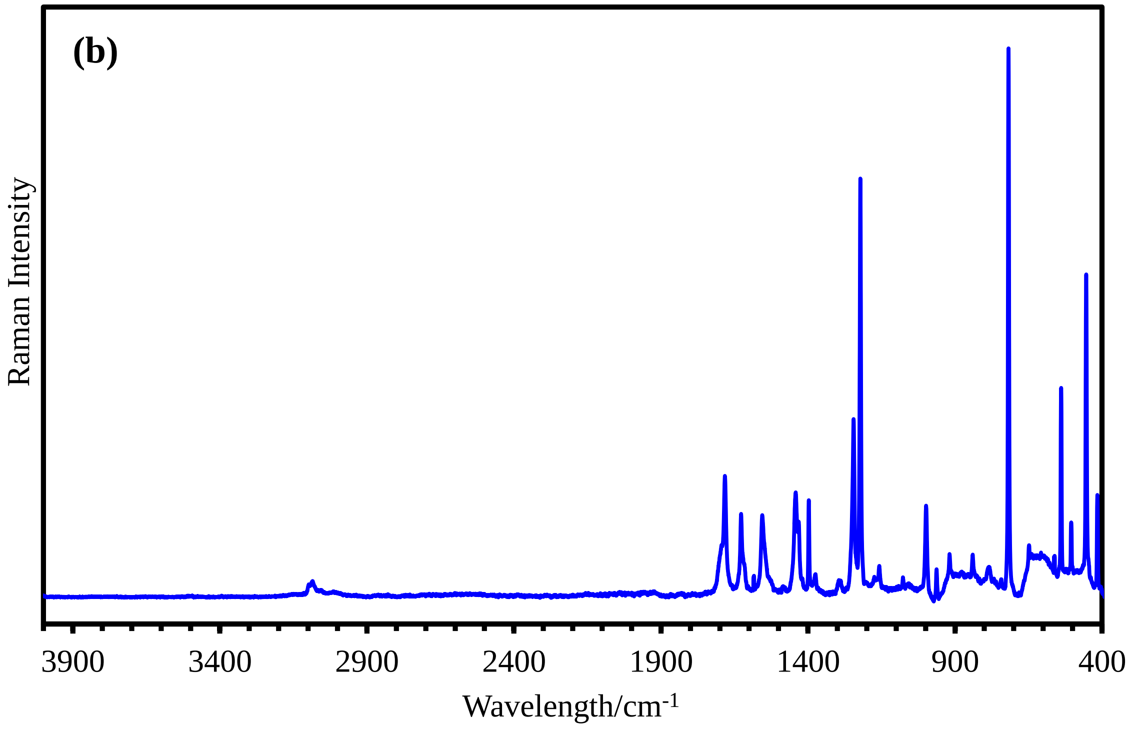
(b)
Raman Intensity
3900
3400
2900
2400
1900
1400
900
400
Wavelength/cm-1

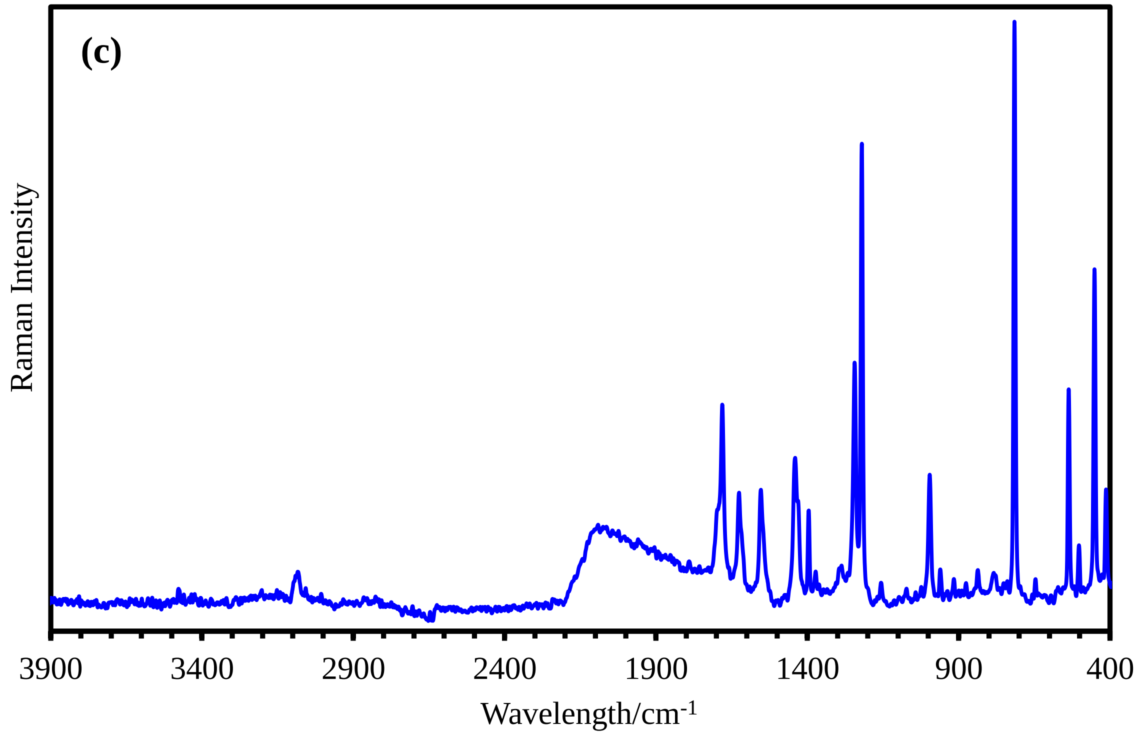

Figure 4.5: (a) Experimental IR spectrum, (b) Raman spectrum of 2-TU, and (c) Raman spectrum of 1.0M saturated solution of 2-TU

4.3.3.3. DFT calculation of 2-TU-silver complex

For a 2-TU-silver complex, various possible conformers are probable and depend on the natural silver atom. The paramount enhanced bands are attributed to the ring S atom and the N atom because the silver atom can bind through the ring S and N atoms. The optimized structures of 2-TU- silver complex were obtained using the DFT calculations with B3LYP/ GEN basis set, with minimum surface potential energy, as shown in Figure 4.6.

The vibrational frequencies of the 2-TU- silver complex were calculated through DFT with B3LYP/ GEN basis set and compared with the theoretical Raman, and the SERS of 2-TU are tabulated in Table 4.4. It can be noted that the calculated data are in an agreement with the experimental data. For example, the calculated C=S band at 1142

cm^{-1} in the 2-TU calculated is shifted to a lower frequency at 1131 cm^{-1} in the 2-TU-silver (S-Ag) calculated. In the observed case, the C=S band at 1171 cm^{-1} is shifted to a lower frequency at 1164 cm^{-1} in the SERS spectrum. The band at 1065 cm^{-1} is shifted to a lower wavenumber at 1051 cm^{-1} in the 2-TU-silver (N-Ag) theoretical and is in very good agreement with the experimental data, which is shifted from 1071 cm^{-1} to 1052 cm^{-1} in the SERS spectrum. In addition, the peak at 612 cm^{-1} is significantly shifted to 588 cm^{-1} in the theoretical case, and it is significantly shifted from 605 cm^{-1} to 572 cm^{-1} in the observed data. The other agreements between the experimental data and the theoretical data are summarized in Table 4.4.

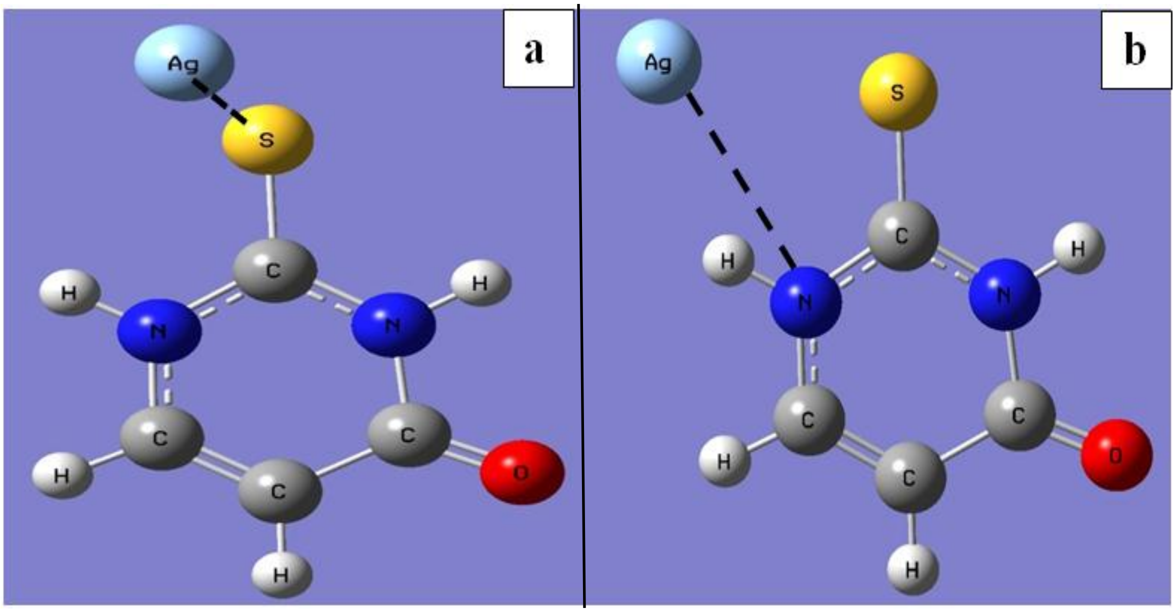

Figure 4.6: The optimized structure of 2-TU-sliver complex (a) silver atom bind through the S atom, and (b) silver atom bind through the N atom.

Table 4.3: Infrared (IR) and Raman Experimental and calculated vibrational frequencies (cm^{-1}) of the 2-TU using DFT method.

Calculated (Calc) ^{a}			Observed (Obs) ^{b}				
Scaled Freq.	**IR Int.**	**Raman Act.**	**IR**	**Raman**	**Solution**	**SERS**	**Assignment ^{c}**
3484	90.9	75.3			3477 vw		100%ν (N4-H)
3448	64.4	44.8	3453 m				100%ν(N3-H)
3116	2.1	128.1	3130 w	3131 vw	3135 vw		95% ν(C8-H)
3079	3.1	106.3	3080 w	3081 w	3083 w		96% ν (C7-H)
1745	679.6	67.5	1678 vs	1679 m	1681 m	1690 w	76% ν (C=O), 14% δ (N3-H).
1638	62.1	65.7	1627 s	1626 m	1630 m	1628 m	64% ν (C7=C8), 13% δ (C7-C8-H)
1543	687.7	8.2	1562 s	1554 m	1554 s	1562 m	13% ν (C5-N3), 54% δ (N4-H) bend
1428	27.6	11.5	1449 m	1445 m	1442 s	1451 m	23% δ (N3-H) bend, 27% δ (C7-H)
1375	7.4	12.9	1383 vw	1377 m	1379 m	1387 m	43% ν (N4-C5), 29 % δ (N3-H) bend, 48% δ (C7-H)
1366	83.6	1.4	1366 vw	1368 vw	1368 vw	1368 vw	23% δ (N3-H) bend, 10% δ (N3-C-S) bend, 11% δ (C-N3-C)
1214	6.5	22.9	1216 vs	1220 vs	1220 vs	1220 s	18% ν (N4-C7), 46% δ (C7-C8-H)
1184	269.3	5.9		1186 vw	1189 vw		38% ν (N3- C5) 54% δ (N4-H) bend
1142	127.7	12.7	1173 vs	1171vw	1170 vw	1164 s	63% ν (C=S), 25% ν (N4-C5), 11% δ (N4-H) bend
1065	7.1	2.8	1072 w	1071 vw	1073 vw	1052 s	31% ν (N4-C7), 10% ν (C7=C8), 27% δ (C7-C8-H)
989	11.9	2.7	1002 s	999 m	999 s	1002 vw	12% ν(N3- C5) 12 % ν (N4-C7), 35% δ (C-N4-C), 14 % δ (C-N3-C)
952	0.2	2.2	955 vw	957 m	959 w	954 vw	74% γ (C7- H), 13% γ (C8-C7-N4)
903	6.2	0.2	912 vw	913 m	912 vw	921 s	31% ν (N4-C5), 43% δ (C-N4-C)
799	67.4	0.5	794 vw	789 vw	793 vw		26% γ (C8-H),56 % γ (H-C7-C8-H) wag, 12% γ (C=O)
726	0.5	0.1	735 w	736 vw	737 vw		25% γ (C8-H), 10% γ (C7- H) 28% γ (C=O).
707	3.8	23.1	710 m	716 vs	716 vs	720 s	18% ν (N3-C6), 34% δ (C-N4-C), 13% δ (N-C5-N) bend .
679	83.7	0.8	680 vw	681 vw			78% γ (N3-H), 13% γ (N4-H).
612	7.9	2.3	596 vw	605 vw	603 vw	572 m	86% γ (S-C-N).
581	29.6	0.7		575 vw		653 w	81% γ (C-N-H)
531	8.9	5.3	529 w	534 s	535 vs		17% ν (N4-C5), 10% ν(C5-N3), 38% δ (C-N3-C)
489	11.2	0.8		503 w	505 m	502 w	12% δ (N3-C-S) bend, 11% δ (C-N4-C), 48% γ (C8-C7-N4)
446	14.0	13.2	450 s	452 s	451 vs	443 m	36% ν (N3-C6), 26 % δ(N-C5-N) bend, 29% δ (C=S),
391	15.9	1.2	399 w	402 m			21% γ (C8-C7-H), 12% γ (C=O).

266	8.3	4.9		282 s	281 vs	300 sh	10% ν (N4-C5), 67% δ (N3-C-S)bend
155	0.9	0.3		178 vw	182 vw		100% γ ring
122	0.5	0.1		128 m			79% γ (N4-C-S)

[a] IR intensities and Raman activities are calculated in (km/mole),(Ǎ^4/amu) respectively.
[b] vs = very strong; s = strong; m = medium; w = weak; vw = very weak, sh=shoulder.
[c] ν, stretching, vibration; δ, bending in the plane; γ, bending out of the plane.

Table 4.4: Experimental Raman shift compared with the calculated Raman shift of 2-TU complex

Calculated (Calc)			**Observed (Obs)**	
2-TU (cm^{-1})	**N-Ag (cm^{-1})**	**S-Ag (cm^{-1})**	**Solid (cm^{-1})**	**SERS (cm^{-1})**
3484	3440	3483		
3448	3265	3448		
3116	3116	3117	3131 vw	
3079	3081	3082	3081 w	
1745	1755	1748	1679 m	1690 w
1638	1630	1628	1626 m	1628 m
1543	1549	1539	1552 m	1562 m
1428	1435	1428	1445 m	1451 m
1375	1389	1383	1377 m	1387 m
1366	1379	1369	1368 vw	
1214	1215	1213	1220 vs	1220 s
1184	1190	1182	1186 vw	
1142	1134	1131	1171vw	1164 s
1065	1051	1062	1071 vw	1052 s
989	992	986	999 m	1002 vw
952	958	952	957 m	
903	916	887	913 m	921 s
799	805	799	789 vw	
726	718	713	736 vw	
707	714	706	716 vs	722 s
679	694	676	681 vw	
612	611	588	605 vw	572 m
581	642	578	575 vw	653 w
531	531	529	534 s	
489	492	489	503 w	502 w
446	443	438	452 s	443 m
391	393	391	402 m	
266	280	261	282 s	300 sh

4.3.4. SERS results of 2-TU on Ag/NPs

4.3.4.1. Silver colloids (Type I)

The silver nanoparticles can be used as a SERS substrate. The 2-TU solution served as a target molecule to study the SERS sensitivity of an Ag/NPs aggregate. 1.0 ml of the 2-TU solution was mixed with 30µl of silver, then SERS was performed. Figure 4.7a depicts the normal Raman spectra of solid 2-TU, which is in agreement with the reviewed literature [32]. The Raman spectrum of a 10^{-3}M solution of 2-TU is shown in Figure 4.7b, where four weak peaks are observed at 454, 718, 1047, 1222, and 1245 cm^{-1}. Figure 4.7c shows the SERS spectra of 2-TU in the SERS-active substrates. The SERS spectrum of 2-TU contains some of the bands with a frequency shift and some change in the intensity. A comparison between the SERS spectra and the normal Raman spectra of 2-TU shows the weak signal at 1171 cm^{-1} in the normal Raman spectrum, which is shifted to a lower wavelength at 1164 cm^{-1} in SERS spectrum. This band is related to C=S vibration stretching, which shows a significant enhancement in the SERS spectrum. This enhancement indicates the S atom interacts directly with the Ag/NPs surface to form a strong Ag-S bond. The result indicates the signals at 1071 cm^{-1} and 913 cm^{-1} in the normal Raman spectrum, with a very weak intensity, are shifted to 1052 cm^{-1} and 921 cm^{-1}, respectively. These signals are assigned to ν (N4-C7), and ν (N4-C5) vibration modes, respectively. These bands are enhanced to a higher intensity in the SERS spectrum than in a normal Raman spectrum. In addition, the small peak at 605 cm^{-1} in the normal Raman spectra, assigned to γ (S-C5-N) wagging, is shifted to lower wavelengths at 572 cm^{-1} in the SERS spectra. This band is enhanced by the high intensity in the SERS spectrum by a large factor. The small band at 581cm^{-1} in the normal Raman spectra, assigned to N-H bending out of the plane, is shifted to higher wavelengths at 653 cm^{-1} in the SERS spectra, which shows an insignificant enhancement in the SERS spectrum. The enhancement of these bands results from the adsorption of 2-TU molecules at the Ag/NPs surface, which can be explained by the excitation of a surface Plasmon resonance on substrates due to the strong interaction between 2-TU and Ag/NPs substrate [33].

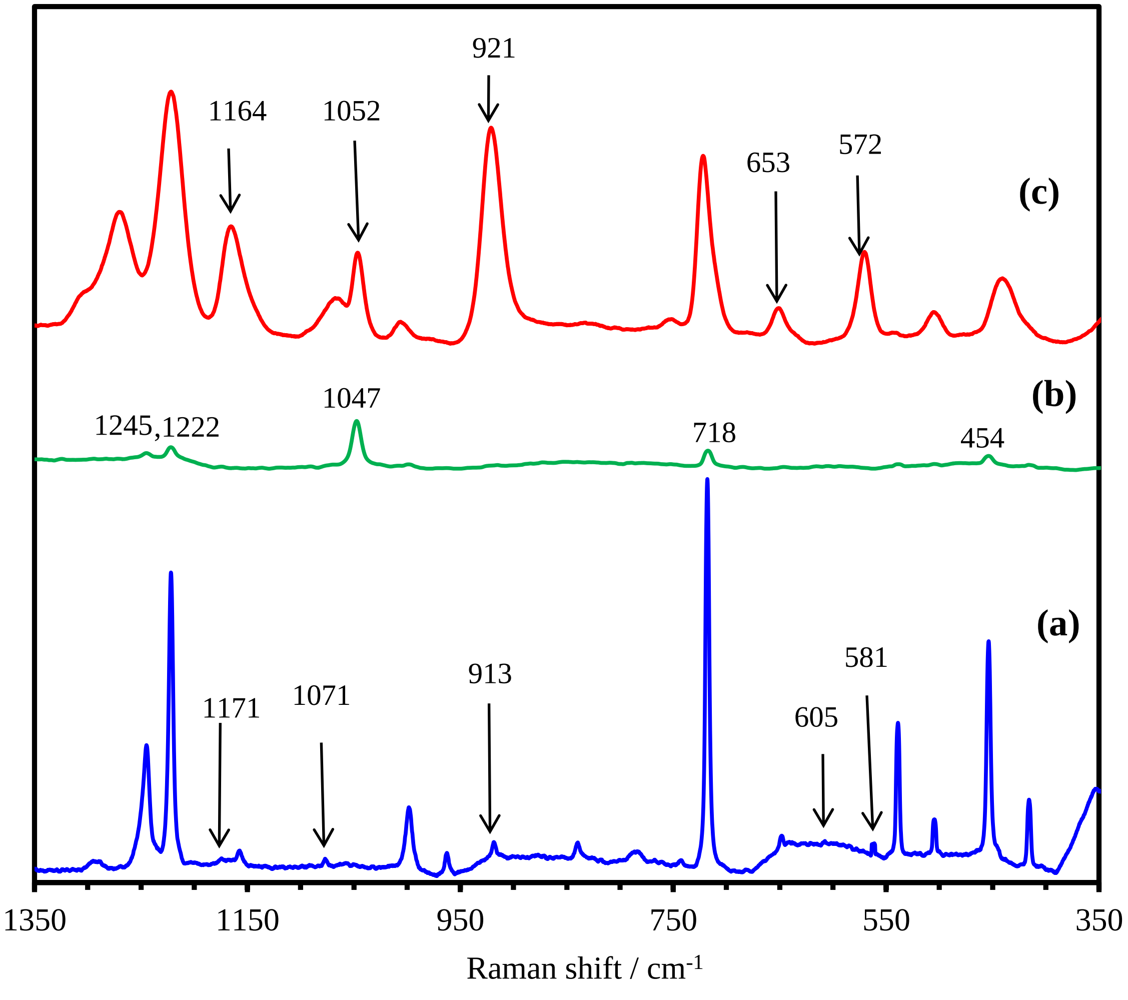

Figure 4.7: (a) Normal Raman spectrum of pure solid 2-TU, (b) Raman spectrum of 10^{-3} M solution of 2-TU, and (c) The SERS spectrum of 10^{-3} M 2-TU, Laser ʎ=633nm, acquisition time; 20 sec, and objective; 10x.

4.3.4.2. Silver film (Type II)

The changes in frequency shift and the intensity of signals at 1164, 1052, 921, 653 and 572 cm^{-1} of the SERS spectrum for 2-TU were provided from the silver film, and exhibit the same effect in the SERS spectrum as that obtained by using Ag/NPs Type I.

The SERS band's intensity of 2-TU on glass slides is lower than that on the Ag/NPs. This corresponds to the difference in the surface properties of the film from that of the colloids. A glass slide is hydrophilic; drops of the Ag/NPs solution tend to diffuse and spread over a wide glass surface area, meaning they are widely dispersed and nearly separate from each other. This makes it very complicated to detect the aggregated Ag/NPs, which is given a higher peak enhancement than the isolated nanoparticles [34].

The first report about the adsorption of 2-TU molecules by deposition on silver film was done by V. Joy, T. Srinivasan [35]. They determined that the strong peak at 3082 cm^{-1} in the normal Raman spectrum is due to the C8-H stretching mode; the C8-H bond is perpendicular and C7-H bond makes an angle 30 degrees to the surface film of silver. Also, it was determined the 2-TU molecules adsorbs as the oxothiolate ion on the surface of silver films, as shown in scheme 2. This study, based on electromagnetic theory, states that the maximum intensity of the C-H stretching-vibration bond is obtained when it is perpendicular to the surface [36].

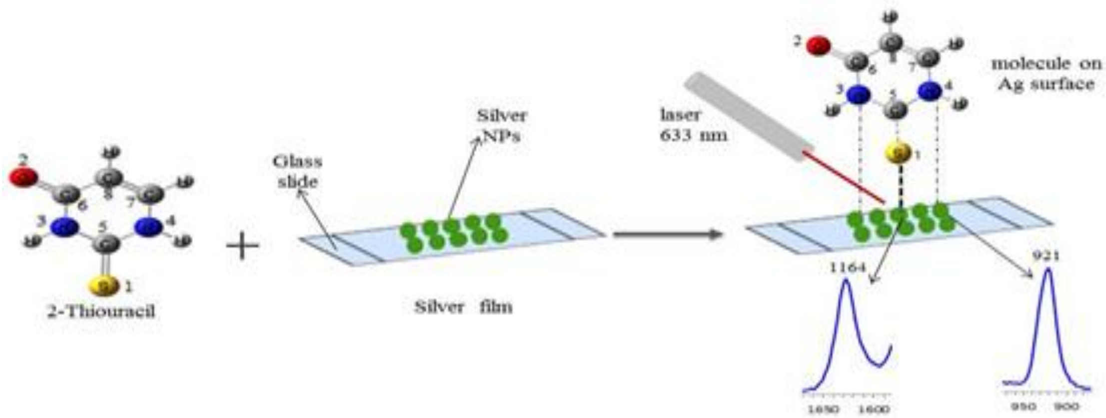

Scheme 4.2: The proposed geometry of 2-thiouracil adsorbed on a silver film

4.3.4.3. SERS enhancement factor of 2-TU

The SERS enhancement factors for the vibrations of 2-TU (1×10^{-3} M) on silver colloid and silver film to the corresponding band obtained from 1.0 M saturated solution were calculated using the following equation.

$$EFs = (\delta_{SERS} \times C_{normal}) / (\delta_{normal} \times C_{SERS})$$

Where δ and C are the Raman mode intensity and sample concentration, respectively. The EFs for the SERS peaks of 2-TU on silver colloid and silver film are given in Table 4.5. The EFs is not the same for the different SERS modes, the maximum enhancement was observed at 921 cm^{-1}.

Table 4.5: SERS enhancement factor of MTZ on gold and silver colloids.

Normal Raman spectra (cm^{-1})	SERS spectra (cm^{-1})	EFs colloid	EFs film
1171	1164	1.2×10^4	1.3×10^4
1071	1052	1.2×10^4	8.1×10^3
913	921	3.4×10^4	2.5×10^4
605	572	1.9×10^4	1.5×10^4
581	653	5.2×10^3	5.3×10^3

4.3.4.4. SERS spectra of 2-thiouracil at different concentrations

The concentrations dependent SERS spectra of 2-TU obtained by using Ag/NPs (Type I) are given in Figure 4.8a. It can be observed that the SERS intensities were affected by changing the concentration of 2-TU. The SERS intensity increased proportionally with increased concentrations of the 2-TU solution in the range from 10^{-3}M to 10^{-6} M when the 2-TU interacted with the Ag/NPs (Type I). The results show that the linear correlation obtained at 921 cm^{-1} band was better than that obtained at the 1164 cm^{-1} band. Figure 4.8b and Figure 4.8c shows the calibration curves at bands 1164 cm^{-1} and at 921 cm^{-1}, respectively. The calibration curve of the band at 921 cm^{-1} is with an R^2 of 0.9762, which is more linear than that of the calibration curves at 1164 cm^{-1}, where R^2 equal 0.9555.

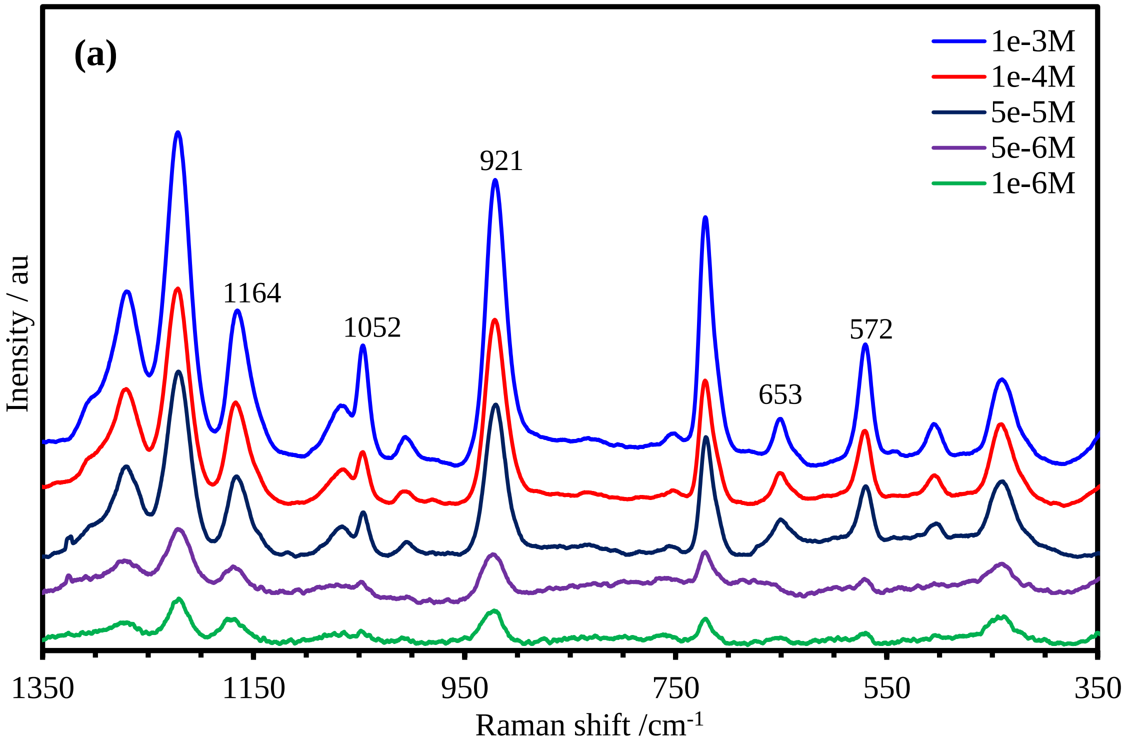

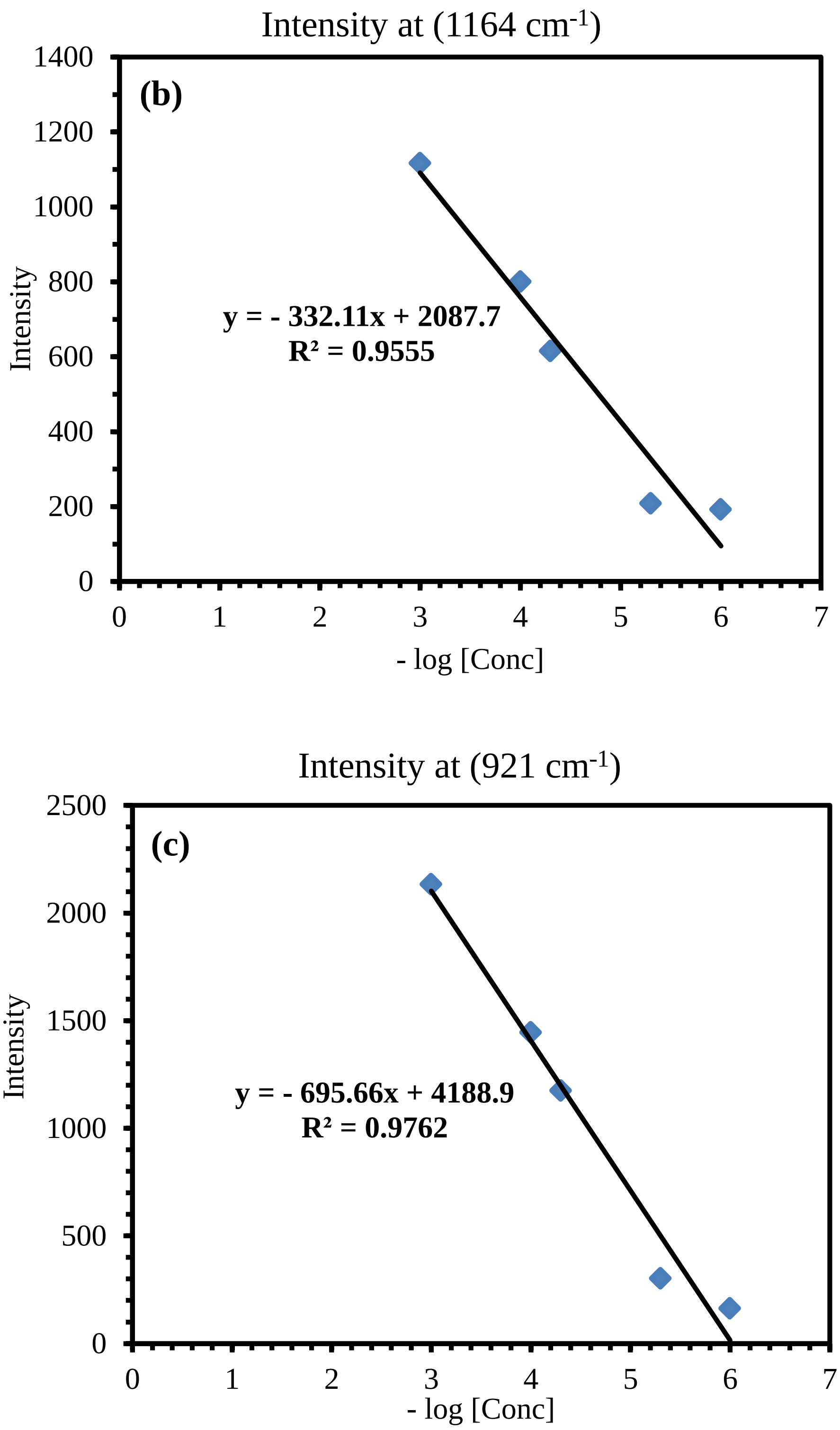

Figure 4.8: (a) SERS spectra of 2-TU at different concentrations using Ag/NPs type I,(b) calibration curve of the band at 1164 cm^{-1}, (c) calibration curve of the band at 921 cm^{-1}. Laser ʎ=633nm, acquisition time; 20 sec, and objective; 10x.

Figure 4.9a shows the concentration-dependent SERS spectra of 2-TU obtained by using silver film (Type II). The SERS intensity increases proportionally with an increase in the concentrations of the 2-TU solution in the range from 10^{-3}M to 10^{-7}M when the 2-TU interacts with the Ag film (Type II). Figure 4.9b and Figure 4.9c show the SERS and the calibration curve at band at1164 cm^{-1} and 921 cm^{-1}, respectively. The results in Figure 4.8a show that the intensities of the bands are greater than the intensities in Figure 4.9a. The calibration curve obtained using Type II more linear than the calibration curves obtained using Type I. The linear correlation and detection limit for the two silver types are summarized in Table 4.6.

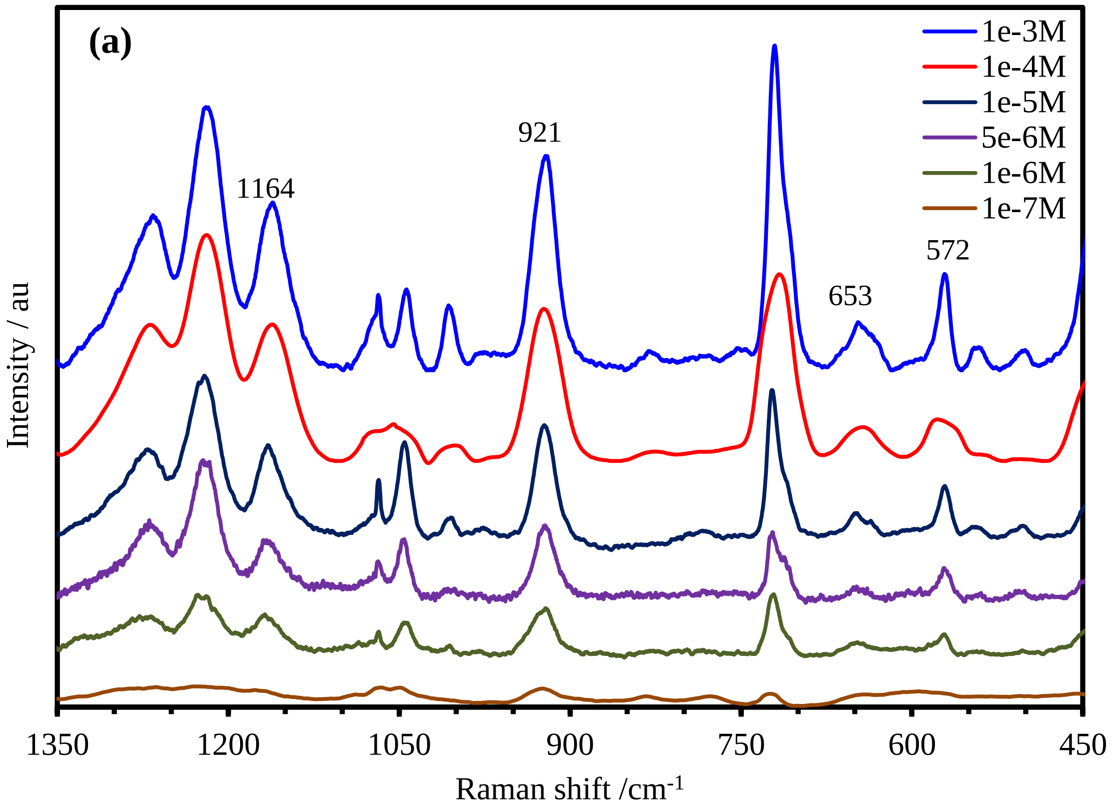

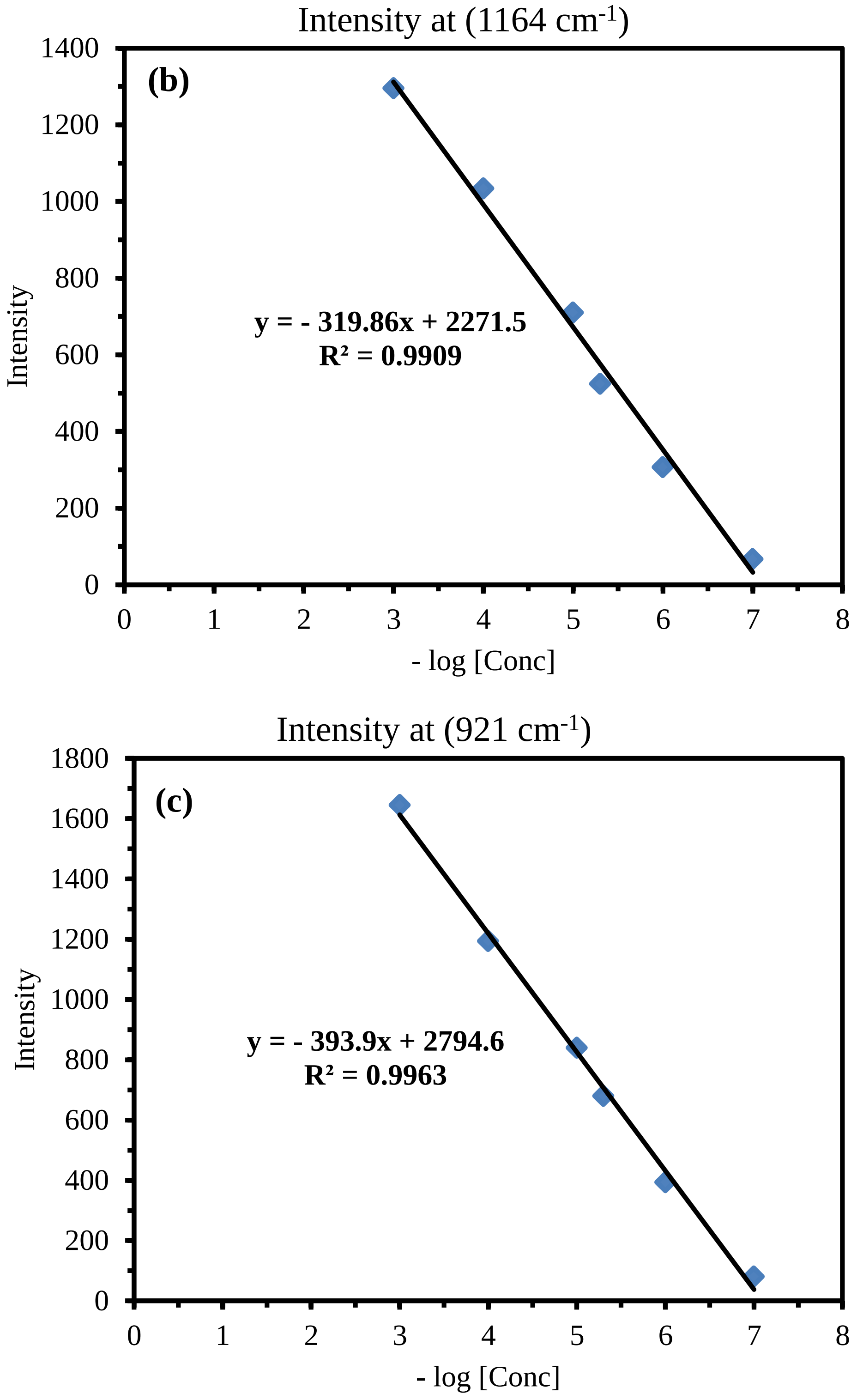

Figure 4.9: (a) SERS spectra of 2-TU at different concentrations using Ag film type II, (b) calibration curve of the band at 1164 cm^{-1} , and (c) Calibration curve of the band at 921 cm^{-1}. Laser ʎ=633nm, acquisition time; 20 sec, and objective; 10x.

Table 4.6: Regression equations between Raman intensities and concentrations of 2-TU and their correlation coefficients.

Silver Type	**Band position**	**Slope equation**	**R^2**	**Detection limit**
Silver NPs	1164 cm^{-1}	y = - 332.11x + 2087.7	0.9555	4×10^{-7} M
	921 cm^{-1}	y = - 695.66x + 4188.9	0.9762	3×10^{-7} M
Silver Film	1164 cm^{-1}	y = - 324.24x + 2289.8	0.9909	3×10^{-7} M
	921 cm^{-1}	y = - 393.9x + 2794.6	0.9963	0.2×10^{-7} M

4.4. CONCLUSION

The SERS spectrum of 2-TU was investigated in both a solid state and aqueous solution using silver nanoparticles prepared by reduction methods. The optimized conformation, and Mulliken atomic partial charges of 2-TU in solid and adsorption on the silver surface were discussed by SERS and DFT calculation with B3LYP/6-311++G (d, p) basis set. The intensities and the wave number of the vibration frequency bands in the theoretical spectra are close to the experimental spectra. The bands assigned to C=S stretching vibration, N4-C7 stretching vibration, N4-C5 stretching vibration, out-of-plane (S-C5-N) wagging, and out-of-plane (C-N-H) bending modes were enhanced. Most of the bands related to the N atom and S atom are apparently enhanced and shifted. These results confirm that 2-thiouracil molecules are adsorbed on the silver substrates through the S and N atoms. The correlation between the 2-thiouracil concentration and the SERS signal was linear and of good detection limits. Type II showed better linearity and a better detection limit when compared with Type I.

4.5. REFERENCES

[1] S. Shigeta, S. Mori, T. Kira, K. Takahashi, E. Kodama, K. Konno. Antiviral Chemistry & Chemotherapy. 1999, 10, 195.

[2] Cristina Puzzarini, Malgorzata Biczysko, Vincenzo Barone, Isabel Pen , Carlos Cabezasd and Jose´ L. Alonso. Phys. Chem. Chem. Phys. 2013, 15, 16965.

[3] Napolitano A, Palumbo A, d'Ischia M, Prota G. J. Med. Chem. 1996, 39, 5192.

[4] M.P. Robertson, M. Levy, S.L. Miller. J. Mol. Evol. 1996, 43, 543.

[5] M. Gupta, M.N. Srivastave. Synth. React. Inorg. Met Org. Chem.1996, 26, 305.

[6] Jean-Jacques Aaron, Mihaela Buna, Cyril Parkanyi, Maged Shafik Antonious, Alphonse Tine, and Lamine Cisse. Journal of Fluorescence. 1995, 5, 4.

[7] Shende. C, Inscore. F, Gift, A. Maksymiuk, P. Farquharson, S. Instrum. Eng. 2005, 6007, 165.

[8] Yadav, R. A. Yadav, P.N.S. …et al. Indian Acad. Sci. Chem. Sci. 1988, 100, 69.

[9] M. Alcolea Palafoxa, G. Tardajos , A. Guerrero-Martínez , J.K. Vats, Hubert Joe, V.K. Rastogi. Spectrochimica Acta Part A. 2010, 75, 1261.

[10] L. Lapinski, H. Rostkowska. …et al. Spectrochimica Acta Part A. 1998, 54, 685.

[11] Malgorzata Biczysko, Julien Bloino , Ivan Carnimeo , Paweł Panek , Vincenzo Barone. Journal of Molecular Structure. 2012, 1009, 74.

[12] N. Surendra Babu. American Chemical Science Journal. 2013, 3(2), 137.

[13] Farquharson, S.; Gift, A.; Shende, C …et al. J. Molecules. 2008, 13, 2608.

[14] Anderson, D. J.; Moskovits, M. J. Phys. Chem. B. 2006, 110(28), 13722.

[15] Nie, S.; Emory, S.R. Science. 1997, 275, 1102.

[16] Tomczak, M. M.; Slocik, J. M.; Naik, R. R. Biochem. Soc. Trans. 2007, 35, 512.

[17] P. Corio, M. Temperini. J. Solid State Electrochem. 2003, 7, 576.

[18] S. Sanchez-Cortes, J.V. Garcia-Ramos . R. F. Aroca, R. A. Alvarez-Puebla, N. Pieczonka. Advances in Colloid and Interface Science. 2005, 116(1-3, 45.

[19] H.B. Aguiar, A.C. Sant'Ana, M.L.A. Temperini. Vib. Spectrosc. 2006, 40, 127.

[20] Arnaudov, L. N.; de Vries, R. Biomacromolecules. 2006, 7(12), 3490.

[21] Yakutik, I. M., Shevchenko, G. P., Rakhmanov, S. K. A Physicochemical and Engineering Aspects. 2004, 242, 175.

[22] A. Nafady, H. I. Afridi, S. Sara, A. Shah, and A. Niaz. Journal of the Iranian Chemical Society. 2011, 8, 34.

[23] A. S. Goswami and G. S. Ingawele. Asian Journal of Chemistry. 2014, 7(1), 23.

[24] M. Emran Quayum, Md. Khairul Hassan Bhuiyan. J. Pharm. Sci. 2013, 12(1), 29.

[25] An-Wu Xu, Han-Qing Yu, Wen-Gang Qu. J. Mater. Chem. 2012, 22, 20986.

[26] P. C. Lee and D. Meisel. J. Phys. Chem. 1982, 86 (17), 3391.

[27] L.H. Qian, B. Das, Y. Li, Z.L. Yang. J. Mater. Chem. 2010, 20, 6891.

[28] Bae. S.J, C. Lee, I.S. Choi, C. S. Hwang, M. Gong, K. Kim, and S. W. Joo. Journal of Physical Chemistry B. 2002, 106(28), 7076.

[29] P. J. Rosy, S. Kalyanasundharam, K. Santhanalakshmi, S. Muthukumar. International Letters of Chemistry, Physics and Astronomy. 2015, 49, 74.

[30] V.K. Rastogi, M. Alcolea Palafox, R.P. Tanwar. Spectrochimica Acta Part A. 2003, 59, 2473.

[31] Wenpeng Yang, Yongjun Hu. Spectrochimica Acta Part A: Molecular and Biomolecular Spectroscopy. 2015, 134, 399.

[32] Philippe Carbonniere, Tecla Lucca, Claude Pouchan, Nadia Rega, Vincenzo Barone. Journal of Computational Chemistry. 2005, 26, 384.

[33] Li Wang, Yujing Sun, Jiku Wang. Bull. Korean Chem. Soc. 2014, 35(1), 30.

[34] Wang. Li, Sun. Yujing, Cui. Yuncheng, Wang. Jiku, Li. Zhuang. Bull. Korean Chem. Soc. 2013, 34(2), 443.

[35] V.T. Joy, T.K.K. Srinivasan. J. Raman Spectrosc. 2001, 32, 785.

[36] A.G. Brolo. Z. Jiang, D.E. Irish. J. Elec. Chem. 2003, 547, 163.

CHAPTER 5

Silver Nanoparticle-Decorated Graphene: A Substrate for Surface-Enhanced Raman Scattering Based Detection of 2-Thiouracil

5.1. INTRODUCTION

Graphene oxide (GO), a two-dimensional carbon sheet with a thickness of about 1 nm, has seized a great attention due to its high surface area, high electron mobility, planar structure, and excellent physical properties [1-4]. The most common method to obtain GO is by graphite oxidation using strong oxidizing agents [5-6]. GO sheet consists of oxygen –containing surface groups such as epoxides, alcohols, carboxylic acids, and ketones at the edges of GO [7-8]. The interlayer spacing in GO (0.625 nm) is more than that of graphite (0.335 nm) [9]. GO was first prepared by Brodie who treated graphitic powder with potassium chlorate in concentrated fuming nitric acid [10]. Hummers reported a modified method for the synthesis GO which could be utilized for preparing large graphitic films using potassium permanganate, and sodium nitrate in concentrated sulfuric acid [11].

Due to the functional groups that can serve as nucleation sites, GO is known to be an excellent substrate to the diffusion of metal nanoparticles, such as Ag, Au, Pt and Pd, [12]. These nanoparticles decorated graphene are promising candidates to study the changes in the Raman spectrum of graphene and charge transfer between metal and graphene. These changes can be related to ionization energy and electron affinity of metal particles [13]. The GO/Hydrogels/Ag composites were used as highly efficient catalysts for wastewater treatment [14]. In addition, zinc oxide nanorods and reduced graphene oxide hydrogel are mainly used for enhanced photocatalytic organic dye removal [15]. 3D porous IL–CNT–graphene gel and MnO_2–graphene gel was used as freestanding electrodes for asymmetric supercapacitors, due to their physical properties such as good rate capability, wide cell voltage, and dependable stability [16]. The GO-Metal nanoparticles show the special properties due to synergistic effects. Recently, the silver nanoparticles decorated on graphene are more prevalent in research attention due to the applications and unique properties in catalysis, chemical sensing, and electronics [17]. Ryu et al. reported on the synthesis of Ag\GO nanocomposites hybrids using microwave radiation and characterized the electrochemical performances [18]. Rangari et al. reported Ag-coated CNTs hybrid nanoparticles prepared using the sonochemical technique for antimicrobial applications [19]. Zhao et al. prepared Ag-GO using Hummers methods with glucose as reduction agent and evaluated its antibacterial activity [20]. Due to the weak intensity of Raman scattering, the characterization of low concentration sample is difficult. The surface Raman enhancement scattering (SERS) is a powerful method, which has wide application in several fields [21]. SERS used to investigate and identify the structure of the molecule with high sensitivity. SERS could provide the signal intensity of the molecules, enhanced by several orders of magnitudes on the substrate surface [22]. The SERS method has been applied to detect proteins and oligonucleotides with high selectivity and sensitivity [23].

The advantages of G/metal composites are minimum nanoparticles agglomeration, strong chemical enhancement, and high adsorption to the surface of target particles; which make them advance substrates for sensitive SERS detection [24]. Recently, graphene decorated with metal nanoparticles, serving as SERS-active substrates, have been widely employed. For example, TingYu et al. obtained high-enhanced SERS spectra of different crystal violet molecules on monolayer graphene –gold composite [25]. Shicai et al. reported G/CuNPs, TG/CuNPs and CuNPs that could serve as an SERS-active substrate, and depicting the excellent SERS enhancement activity for adenosine detection in the range 5 to 500 mM [26]. Chen et al reported on the SERS effect of Rhodamine 6G, and Rhodamine B, using Ag nanoparticle-decorated graphene oxide (GO) [27]. In addition, Liu and co-workers prepared Ag/G by reduction methods using sodium citrate as reducing agent to detect Trinitrotoluene at a very low concentration by SERS platform [28]. X. Ding and co-workers obtained the SERS performance of Hg^{2+} ions based on the AuNPs/G Heterojunctions composite [29]. He et al. has grouped synthesized gold-Graphene nanocomposites by chemical vapor deposition (CVD) as an SERS substrate for sensitive and multiplex DNA detection [30-31].

In this work, the graphene oxide was prepared and decorated with silver nanoparticles (Ag NPs) by simultaneous reduction of graphene oxide and silver ions. Herein also, a simple, and rapid SERS spectral method was proposed for detection 2-thioracile using the prepared silver/graphene nanocomposite (Ag/G).

5.2. EXPERIMENTAL SECTION

5.2.1. Chemicals and Materials

Graphite powder (99.99%) particle size ≤ 150 µm, and sodium peroxidisulfate ($Na_2S_2O_8$ ≥ 99.0%), Cat Number 71890, were purchased from Sigma-Aldrich. Hydrogen peroxide (H_2O_2, 30wt %) was purchased from Shanghai Chemical Reagent Co. Sodium nitrate ($NaNO_3$) the Cat. No. BDH4574-500G and the CAS Number 7631-99-4.

5.2.2. Preparation of graphene oxide

The modified Hummers method was applied to synthesize graphene oxide from natural graphite [11]. About 4.0 g of graphite was immersed in a mixture of 150 ml of concentrated sulfuric acid (H_2SO_4) and concentrated nitric acid (HNO_3) in the ratio 3:1; and, stirred in an ice bath for around 1h. Then, 2.0 g of $NaNO_3$ was slowly added under stirring for another 8 h at room temperature. Afterward, 8.0 g of $Na_2S_2O_8$ was added slowly to the reaction mixture. Then, the reaction mixture was kept under stirring at room temperature overnight until the mixture became pasty. Following, the system was placed in an ice bath and 150 ml of de-ionized water was added, then, stirring the solution for one day at 90 ^{o}C temperature. On the following day, the mixture was cooled to room temperature, then, about 20 ml of H_2O_2 (30%) was poured into the mixture in sequence, till turning the color of the solution from dark brown to a pale brown-yellowish. After the addition, the mixture was stirred for 3 h at room temperature. Next, the mixture was filtered, and the obtained material was washed with deionized water for several times until the solution pH was close to neutral. The black isolated solid was dried overnight at room temperature.

5.2.3. Preparation of silver/graphene nanocomposites (Ag/G)

The scheme 5.1 shows the preparation steps of silver/graphene nanocomposites (Ag/G). About 13.5 mg of the prepared GO compound was dispersed in 20 ml de-ionized water by sonication in an ultrasound bath for 30 min. Then, 10 ml of $AgNO_3$ solution (1e-3M) was mixed with previously dispersed GO. The mixture was sonicated for an additional 30 min. The reaction mixture was stirred for 30 min at room temperature before the addition of the reducing agent. The Ag NPs was synthesized using sodium borohydride ($NaBH_4$) as a reducing agent. 10 ml of a freshly prepared solution of $NaBH_4$ (1×10^{-3} mol/L) was added slowly, 1drop/sec, to the reaction mixture under stirring. The semblance of the solution turns to dark brown depending on the concentration of silver nitrate, the reaction mixture was kept under stirring at room temperature for 12 h. Next, the black product was collected by centrifugation at 10000 rpm/min for 30 min. After that, the solid product was washed with deionized water three times and dried at room temperature overnight.

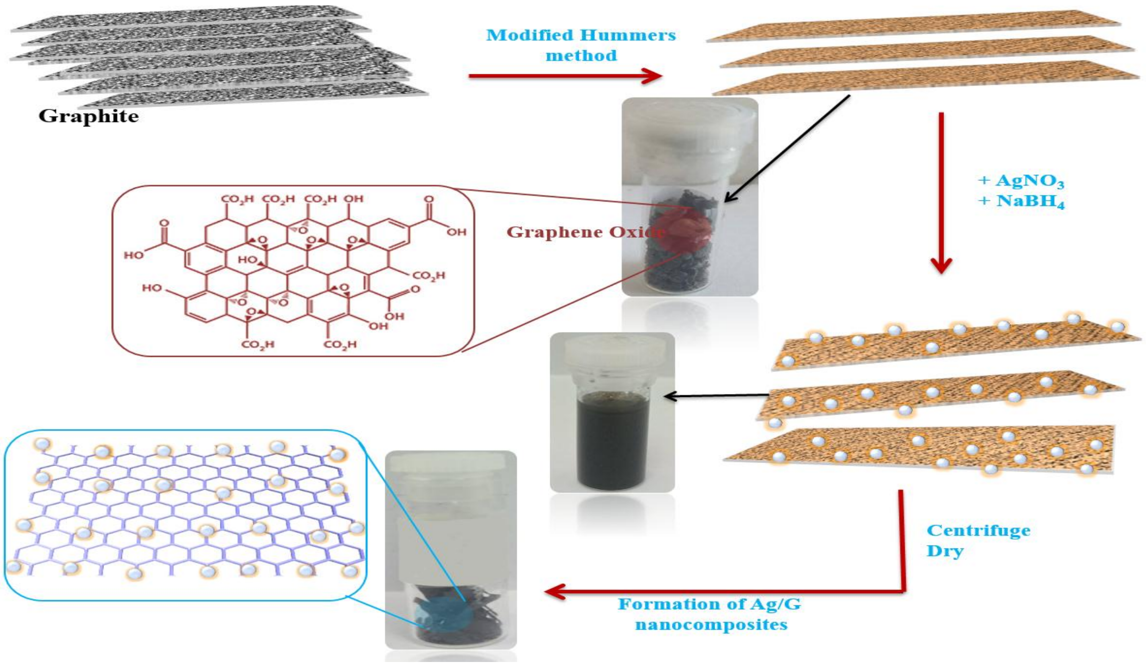

Scheme 5.1: Illustration explaining the synthesis steps of the Ag/G nanocomposites.

5.2.4. Instruments

The surface morphologies of synthesized samples were captured using scanning electron microscope (SEM) (JSM-6610LV, JEOL USA) with a range from 300kV to 20kV acceleration voltage. The morphology of nanocomposites was recorded on a transmission electron microscope (JEM -2100F Field Emission Electron Microscope, JEOL- USA) with 200 KV acceleration voltage. The chemical composition of the nanomaterial surface was analyzed using X-ray photoelectron spectrometer (XPS) microprobe (Thermo Scientific™ ESCALAB™ 250Xi) and using nuclear magnetic resonance (NMR) spectroscopy (BRUKER™ AVANCE™ III 400 MHz spectrometer). The dispersion of the prepared materials was performed with Drug PCB Ultrasonic Cleaner DR-P30 3L (220V, 37KHs, 160 w). The solid Ag/G composite was separated from filtrate with HERMEL LABOR TECHNIK (Z 36 HK, speed range 2000 rpm.min^{-1} to 10000 rpm.min^{-1}, Temp range -20 ^{0}C to 40 ^{0}C, max volume 6×250 ml). Raman spectra of the prepared solutions and materials were collected using a Raman spectroscopy; Lab Ram HP Evolution Raman spectrometer (HORIBA Scientific). It is equipped with an internal HeNe 17mW red laser at 633 nm excitation wavelength. A 10x objective was applied for focusing the laser beam to a resolution. The acquisition time was 30 sec with one accumulation for collection each SERS spectra. The SERS spectra were obtained in the range from 400-2000 cm^{-1}. A stock solution of 1 M of 2-TU in water solvent was prepared. SERS samples were prepared by using a 3 to 1 volume ratio (1.0 ml TU with 0.3 ml nanocomposites). The SERS measurements were performed by using internal HeNe 17 mW Laser at λ=633nm, acquisition time; 30 sec, and objective; 10x.

5.3. RESULTS AND DISCUSSION

5.3.1. Solid-state 13C NMR characterization

The solid-state ^{13}C NMR was used to study the chemical structure of the prepared graphene oxide. Due to the low natural abundance of ^{13}C (1.1%), the ratio of signal to noise in the measurements of samples is very low, and so long acquisition time of is ordinarily required for good quality result [47]. The magic angle spinning (MAS) ^{13}C-{1H} spectrum of GO is shown in Figure 5.1a. The spectrum consists of bands at ~ 28, 59, 71, and 132 ppm. These bands are assigned to C-H (sp^3 hybridized), epoxied (C-O-C), tertiary alcohol (C-OH), and to sp^2 unsaturated carbons (C=C), respectively. The results are in agreement with previous studies [48].

The ^{13}C-{1H} cross magic angle spinning polarization (CPMAS) spectrum is depicted in Figure 5.1b. The major signals are assigned to 27 ppm (-CH), 59 ppm (epoxide), 72 ppm (t-C-OH), and 132 ppm (sp^2 C). In this work, the detected significantly strong signals at 164, and 192 ppm are in ^{13}C-{1H} cross polarization (CP) spectrum than in the MAS ^{13}C spectrum. The signal at 164 ppm can be attributed to ester that generated from the interaction between tertiary alcohols with nearby carboxylic acid (on the same graphene sheet or neighboring sheet). The signal obtained at 192 ppm, can be assigned to ketone carbonyl groups. The spectrum is very similar to spectrum reported by Ajayan, and Leah [49-50]. The simple polycyclic aromatic ketone was assigned from 184-186 ppm. This signal most shifted to about 192 ppm, due to the adjacent epoxy and hydroxyl groups [49, 50,51]. Figure 5.1c shows the ^{13}C-{1H} cross magic angle spinning polarization (CPMAS) spectrum of Ag/G composite, the intensity of oxygenated functional groups (hydroxyl, and epoxy) decreased, which implies that the silver interact with the graphene via hydroxyl and epoxy functional groups.

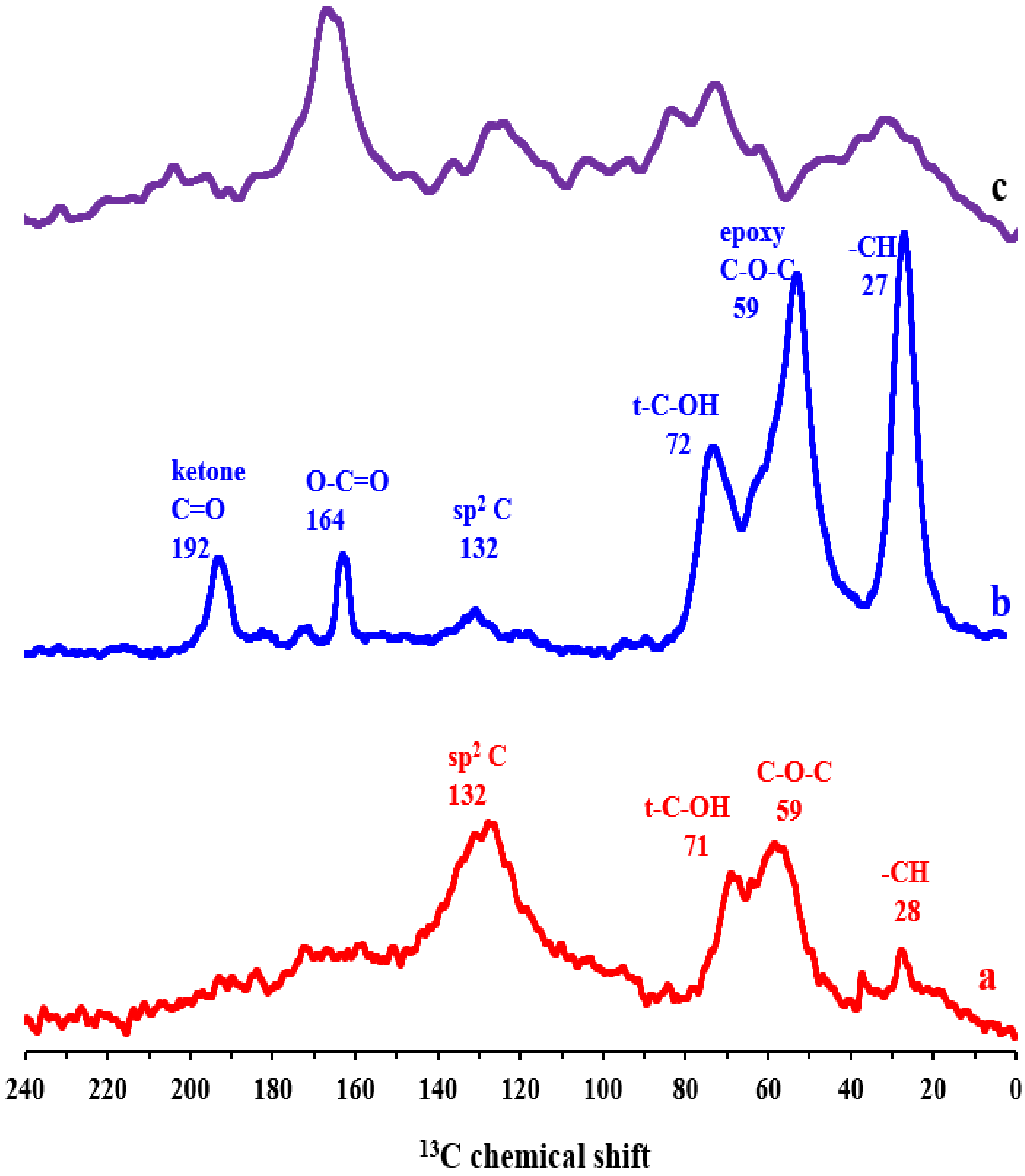

Figure 5.1: (a) ^{13}C MAS spectrum of GO obtained at 4 kHz, and 5000 scans, (b) ^{13}C{H} cross magic angle spinning polarization (CPMAS) spectrum of GO sheets recorded at 4 kHz spin rate and 5000 scans, and (c) ^{13}C-{1H} cross magic angle spinning polarization (CPMAS) spectrum of Ag/G sheets recorded at 4 kHz spin rate and 5000 scans

5.3.2. FT-IR analysis

The FT-IR was employed to confirm the chemical structure of GO and Ag/G nanocomposites. Figure 5.2 shows the FT-IR spectra of GO and Ag/G composites. The FT-IR spectrum of GO shows the broadband at ~3418 cm^{-1} corresponding to vibration stretching OH groups of water molecule adsorbed on GO surface. The absorption peaks at 2921, and at 2852 cm^{-1} are assigned to symmetric and antisymmetric stretching vibration of CH_2, respectively [34]. The two absorption peaks in the medium area at 1733 and 1637 cm^{-1} are assigned to C=O carbonyl/carboxyl and C=C aromatic groups present at the edges of GO. The absorption peaks at 1330 cm^{-1} can be attributed to C-O of carboxylic acid [35]. The absorption peaks at 1229, and at 1122 cm^{-1} are corresponding to stretching vibration of C-O of epoxide, and C-OH of alcohol groups, respectively [36]. In FT-IR spectrum of Ag/G, the peak at 3420 cm^{-1} corresponding to vibration OH group has weak intensity compared with GO. Furthermore, the band due to the C=C aromatic ring of the GO skeleton structure is clear at 1620 cm^{-1}, and the peak at 1383 cm^{-1} is attributed to the C-OH deformation [37]. The absorption peaks at 1262, and at 1057 cm^{-1} are correspond to the C-H stretching of epoxy, and stretching, vibration C-O of alkoxy groups, respectively [38-39]. There is a decrease in the absorption peaks of the oxygenated functional groups in FT-IR spectrum of Ag/G nanocomposites. This can be attributed to the existence of the Ag NPs on the GO nanosheet surface, and to the reduction of GO sheet by $NaBH_4$ during the preparation process of Ag/G nanocomposites [40].

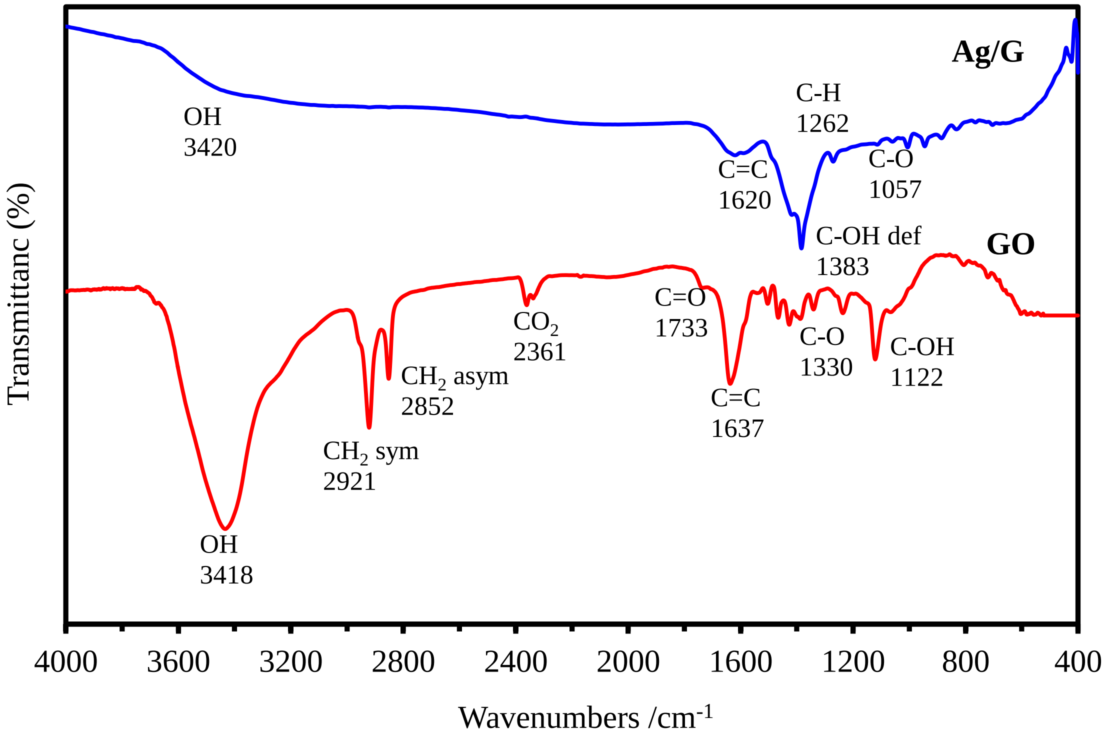

Figure 5.2: FT-IR spectra of GO and Ag/G nanocomposites.

5.3.3. UV-vis Analysis

The Ultraviolet –visible (UV-vis) absorption spectra of GO and Ag/G nanocomposites are shown in Figure 5.3. GO spectrum dispersion in water shows two characterization peaks. A maximum absorption band is at 231 nm indicating π-π* electronic transitions of C=C aromatic bonds, and a shoulder band is at 300 nm corresponding to the n-π* electronic transitions of C=O bonds [32]. Moreover, the maximum absorption band of Ag/G is at 403 nm due to Plasmon resonance of Ag/G indicating the formation Ag NPs on the surface of GO suspension. In addition, the spectrum of Ag/G shows a red shift in the π-π* C=C aromatic bonds absorption in a GO spectrum from 231nm to 261 nm. These observations can be attributed to the partial restoration of sp^2 carbon π-conjugation of graphene, during the reduction GO with $NaBH_4$ to form Ag/G [33].

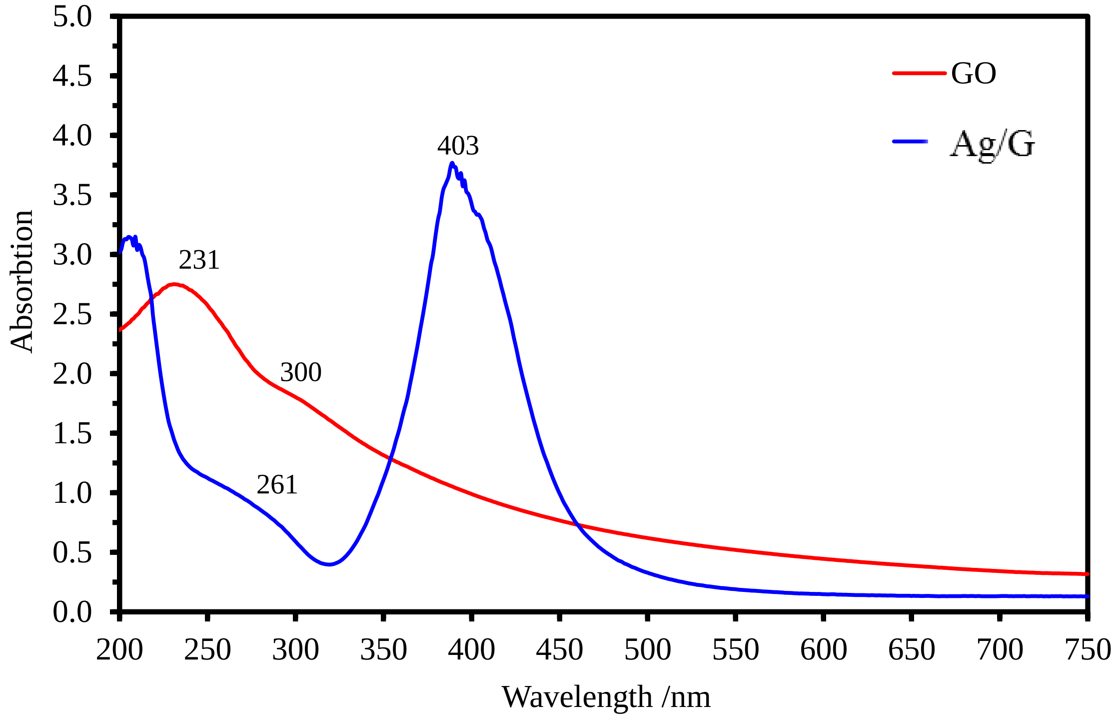

Figure 5.3: UV-vis absorption spectra of dispersion GO, and Ag/G nanocomposite.

5.3.4. SEM and TEM analysis

The morphology of the synthesized GO and Ag/G are studied by SEM and TEM. The SEM image of GO is shown in Figure 5.4a. The edges of the GO film become a bent shape, neatly stacked, and the morphology of the GO surface appears as soft carpet or waves. In addition, the GO sheet contains kinked and wrinkled areas. The SEM image of Ag/G composite is shown in Figure 5.4b. The great amount and uniform size of Ag NPs decorate the GO sheet can be observed. Estimated by TEM image of GO stable sheets are shown in Figure 5.4c. The TEM image clearly shows the GO sheets are wrinkled and thin. Figure 5.4d shows the TEM of GO after functionalization with the Ag NPs. It is observed that a great number of AgNPs are decorated onto the GO surface with homogeneous dispersion. However, some particles of AgNPs are created by agglomeration of smaller particles. That can be attributed to the higher surface energy of the silver particles, loading degree close to saturation. The attachment of Ag ion with GO sheet are attributed to physisorption, electrostatic binding or charge transfer interactions between GO sheets and nanoparticles, as the GO and silver ions with opposite charges. The energy-dispersive X-ray spectroscopy (EDS) elemental mapping was performed to confirm the silver distribution on the graphene sheets. The EDS mapping images of GO and Ag/G are depicted in Figure 5.4 e-f, which indicates that graphene sheets were well decorated with silver.

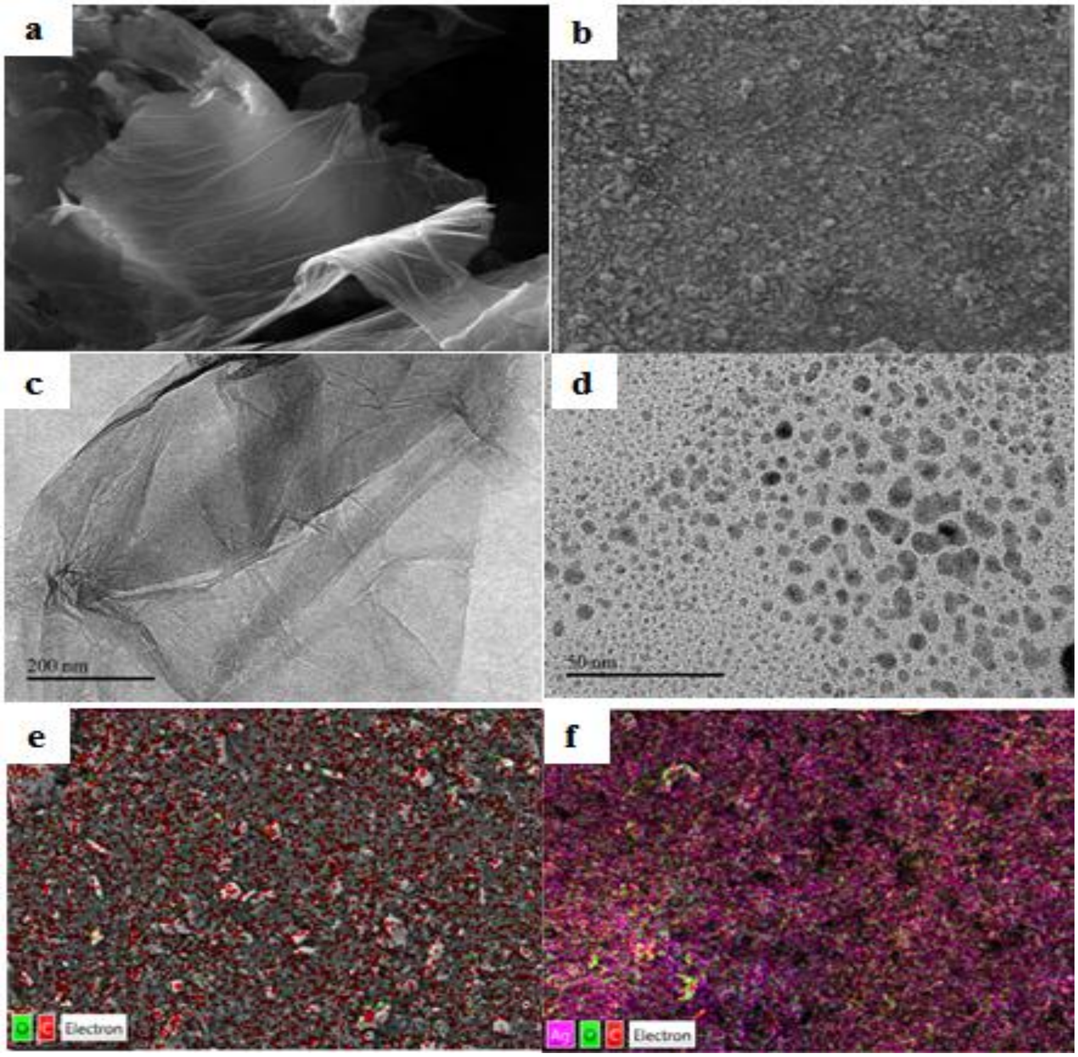

Figure 5.4 : The SEM images of GO (a), and Ag/G (b); TEM images of GO (c), and Ag/G (d); energy-dispersive X-ray spectroscopy (EDS) mappings of GO (e) and Ag/G (f).

5.3.5. XPS analysis

XPS, a surface sensitive technique, was employed to analyze the chemical composition of the graphene oxide, and graphene oxide- silver nanocomposites. Figure 5.5a shows the XPS survey spectra for GO, and Ag/G nanocomposites. The Ag 3d peaks (doublet) present in Ag/G indicate successful deposit of Ag NPs on the GO sheets. The C wt% decrease from 67.96 % to 44.08%, on GO and Ag/G, respectively, due to the chain grafting with Ag NPs on graphene.

The XPS spectra were calibrated to the position of the C-C peaks of 284.5 ± 0.2 eV [41]. Figure 5.5b and 5.5c show the C 1s signals of GO and Ag/G deconvoluted into four peaks (curve was fitted using Thermal science, Advantage 5.1 program). These signals are corresponding to carbon atoms in different functional groups, C-C (Csp^2 and Csp^3 at 284.5 eV), C-O (epoxy and hydroxyl, at 286.72 eV) C=O (carbonyl, at 287.8 eV), and O-C=O (carboxylate carbon, at 289.2 eV) [32, 41, 42]. After the GO sheets decorated with Ag NPs, the intensity of oxygenated functional groups (hydroxyl, epoxy, carbonyl, and carboxylate groups) decreased, which implies that the oxygenated functional groups (C-O, C=O, and O-C=O) might be removed by chemical reduction. The binding energies and the atomic percentage of each group of C 1s spectra peaks of GO and Ag/G are summarized in Table 5.1.

Figure 5.5d shows the XPS spectrum of Ag 3d doublet (3d$_{5/2}$, and 3d$_{3/2}$) for Ag/G. The 3d$_{5/2}$ and 3d$_{3/2}$ peaks present at 368.3 EV, and at 374.3eV, respectively, with $\Delta = 6$ eV, shifted to lower binding energy compared with standard binding energies for pure silver (368.0 and 374.0 eV) due to electron transfer from metallic silver to GO sheets. The observed data are in a good agreement with the literature [43-46].

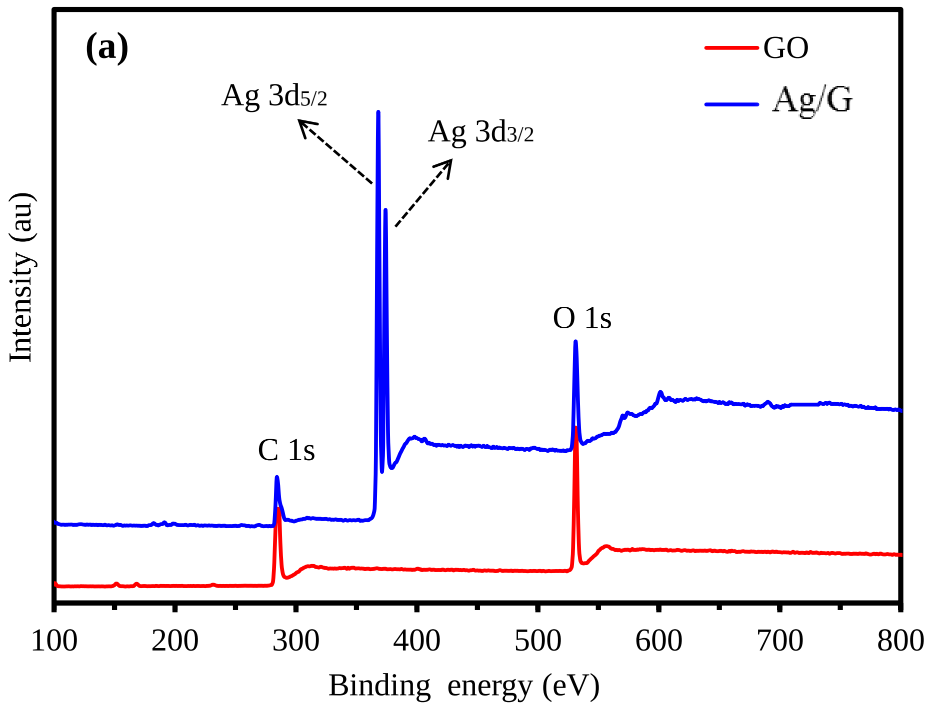
(a)
GO
Ag/G
Ag 3d5/2
Ag 3d3/2
O 1s
C 1s
Intensity (au)
100
200
300
400
500
600
700
800
Binding energy (eV)

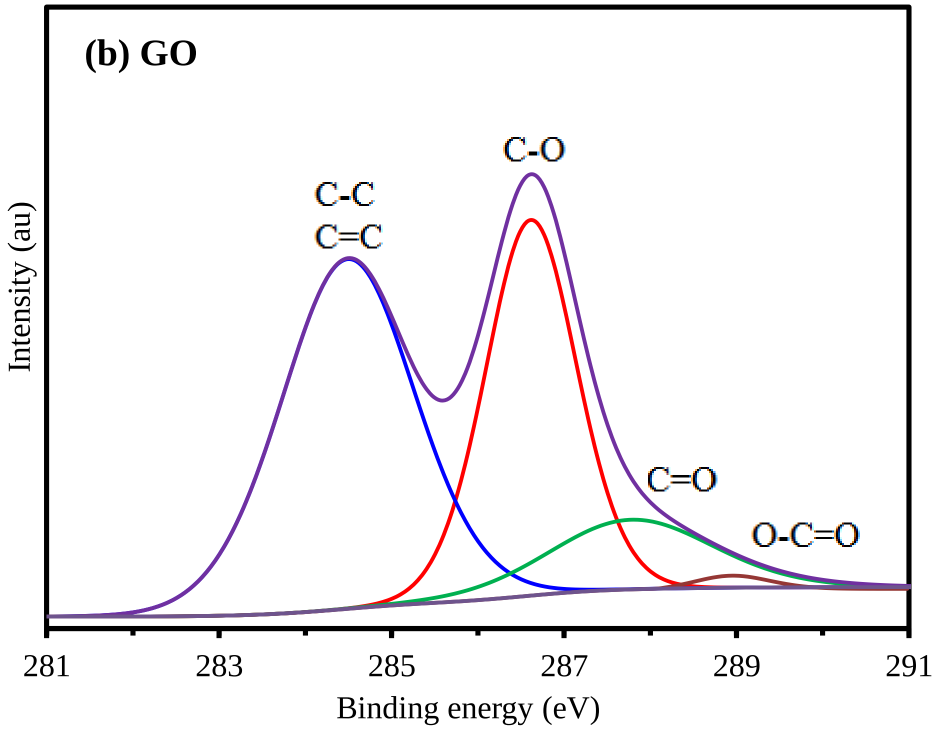
(b) GO
C-C
C=C
C-O
C=O
O-C=O
Intensity (au)
281
283
285
287
289
291
Binding energy (eV)

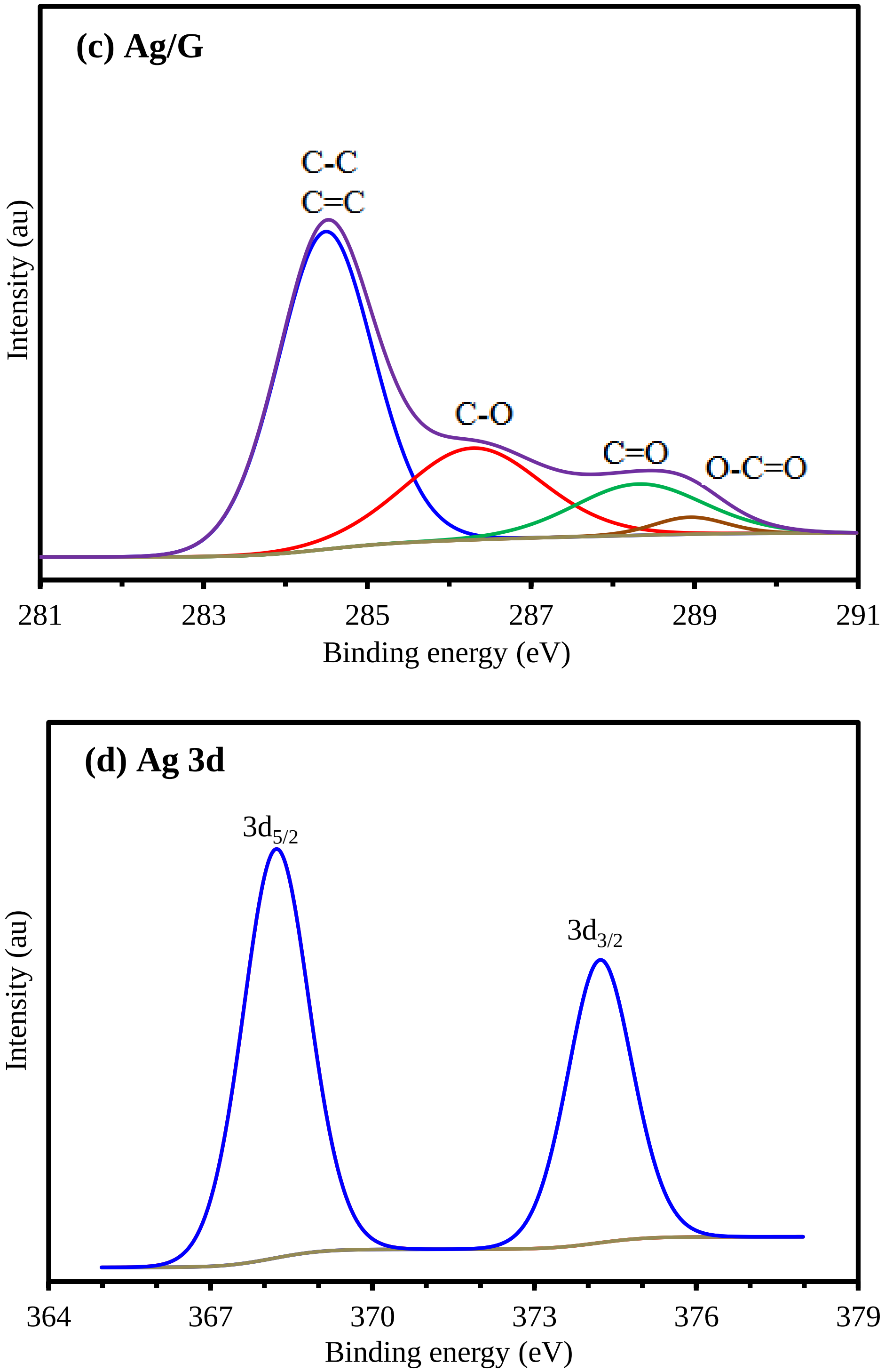

Figure 5.5: (a)XPS survey spectra of GO and Ag/G nanocomposites, (b) the C 1s core level XPS spectra of GO, (c) the C 1s core level XPS spectra of Ag/G and (d) XPS analysis spectra of Ag 3d in Ag/G.

Table 5.1: XPS data of various core level present in GO, and Ag/G nanocomposites.

Composites	Peaks	BE (eV)	Atomic %	Bond Type
Ghraphene Oxide	C1s	284.5	49.76	C-C, and C=C
		286.72	36.39	C-O (epoxy and hydroxyl groups)
		287.8	11.92	C=O (carbonyl groups)
		289.2	1.94	O-C=O (carboxylate carbon groups)
Graphene oxide – Silver nanocomposites	C1s	284.5	59.71	C-C, and C=C
		286.53	24.86	C-O (epoxy and hydroxyl groups)
		287.98	13.01	C=O (carbonyl groups)
		289.1	2.42	O-C=O (carboxylate carbon groups)
	Ag 3d	368.3	59.67	$3d_{5/2}$
		374.3	40.33	$3d_{3/2}$

5.3.6. Raman Spectroscopy analysis

The Raman scattering is a useful technique to distinguish ordered and disordered carbon structures. Figure 5.6 shows the typical Raman spectra of solid GO, and Ag/G nanocomposites. In the case of GO, the spectra displayed two prominent bands. The D band around 1350 cm^{-1}, which is related to disordered carbon sp^3 atoms and breathing mode of the k-point phonons with A_{1g} symmetry. The increased intensity indicates the formation of more sp^2 domains. The G band around 1600 cm^{-1} is corresponding to the E_{2g} phonon of order sp^2 carbon atoms [52-53]. On the other hand, the D band of Ag/G nanocomposites is assigned to 1339 cm^{-1}, it is shifted to a lower frequency about (11cm^{-1}) compared with D band in GO sample, indicating a higher level of disorder of the graphene layers and increased numbers of defects because of the partial reduction of GO by sodium borohydride during the synthesis of the Ag-GO nanocomposites [54]. The G band of the Ag/G nanocomposites at 1596 cm^{-1} is clearly downshifted by (4 cm^{-1}) with respect to that of GO.

Besides, the intensity ratio of D and G bands (I_D/I_G) increases. The I_D/I_G is used to assess the degree of disorder the average size of the sp^2 carbon atoms domains. The ratio values are 1.16 and 1.46 for graphene oxide and Ag/G nanocomposites, respectively. The I_D/I_G value of GO and Ag/G increase progressively, due to damaging the graphical structure of carbon materials, during the reduction process of graphene. This can be explained by the removing of some oxygen functional groups through reduction process, leading to form high-level fragmentation along the reactive sites of graphene [4, 51, 55].

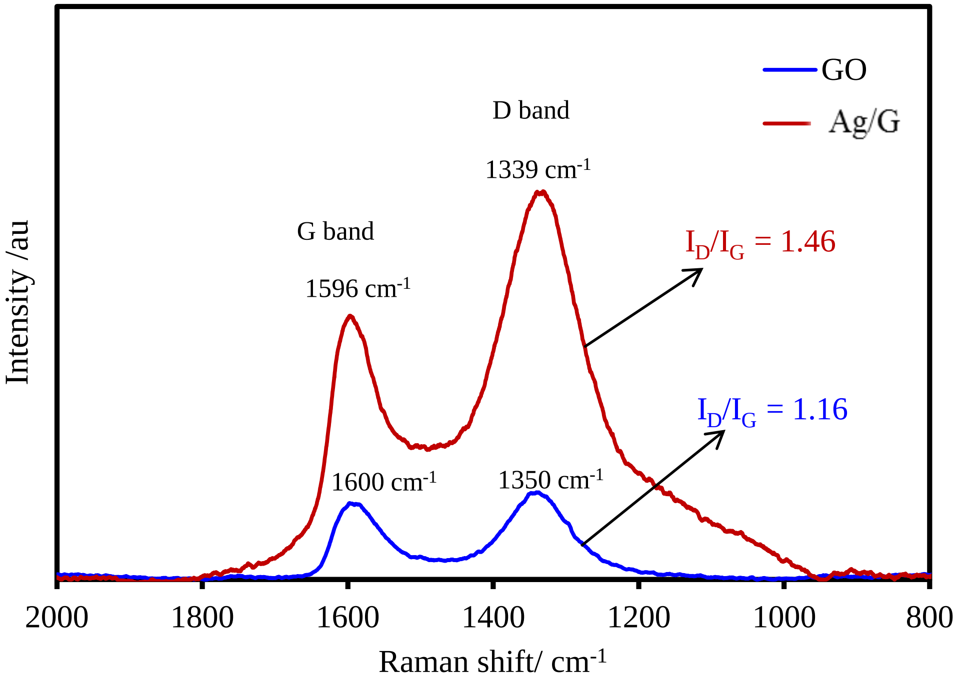

Figure 5.6: Raman spectra of GO (blue line), and Ag/G nanocomposites (red line).

5.3.7. Vibrational Assignments

The Theoretical and Experimental vibration frequency modes of 2-TU are shown in **Table 5.2**. The Wavenumbers were calculated through DFT method with B3LYP level and 6-311++G (d, p) basis sets, which excellently correlated with the experimental modes.

Table 5.2: Calculation and Observed Vibrational Frequencies (cm^{-1}) at the B3LYP /6-311++G (d, p) for 2-TU.

Calculated (Calc) [a]			**Observed (Obs)** [b]				
Scaled Freq.	**IR Int.**	**Raman Act.**	**IR**	**Raman**	**Solution**	**SERS**	**Assignment** [c]
3484	90.9	75.3			3477 vw		100%ν (N4-H)
3448	64.4	44.8	3453 m				100%ν(N3-H)
3116	2.1	128.1	3130 w	3131 vw	3135 vw		95% ν(C8-H)
3079	3.1	106.3	3080 w	3081 w	3083 w		96% ν (C7-H)
1745	679.6	67.5	1678 vs	1679 m	1681 m		76% ν (C=O)
1638	62.1	65.7	1627 s	1626 m	1630 m		64% ν (C7=C8), 13% δ (C7-C8-H) bend
1543	687.7	8.2	1562 s	1554 m	1554 s	1527 s	13% ν (C5-N3), 54% δ (N4-H) bend
1428	27.6	11.5	1449 m	1445 m	1442 s		23% δ (N3-H) bend, 27% δ (C7-H) bend
1375	7.4	12.9	1383 vw	1384 m	1383 m		43% ν (N4-C5), 29 % δ (N3-H) bend, 48% δ (C7-H) bend.
1366	83.6	1.4	1366 vw	1368 vw	1368 vw	1377 s	23% δ (N3-H) bend, 10% δ (N3-C-S) bend, 11% δ (C-N3-C) bend
1214	6.5	22.9	1216 vs	1220 vs	1220 vs	1214 m	18% ν (N4-C7), 46% δ (C7-C8-H) bend
1184	269.3	5.9		1186 vw	1189 vw		38% ν(N3- C5) 18% δ (N4-H) bend
1142	127.7	12.7	1173 vs	1171vw	1170 vw		63% ν (C=S), 25% ν(N4-C5), 11% δ (N4-H) bend
1065	7.1	2.8	1072 w	1071 vw	1073 vw	1075 w	31% ν (N4-C7), 10% ν (C7=C8), 27% δ (C7-C8-H) bend
989	11.9	2.7	1002 s	999 m	999 s	1004 w	12% ν(N3- C5) 12 % ν (N4-C7), 35% δ (C5-N4-C7) bend, 14 % δ (C-N3-C) bend
952	0.2	2.2	955 vw	957 m	959 w	951 sh	74% γ (-C8-C7- H) tiwst, 13% γ (C8-C7-N4) wgg
903	6.2	0.2	912 vw	913 m	912 vw	931 vs	31% ν (N4-C5), 43% δ (C-N4-C) bend

799	67.4	0.5	794 vw	789 vw	793 vw	815 vs	26% γ (C6-N3), 56 % γ (C7-C8-H) wag, 12% γ (C-C=O)wag
726	0.5	0.1	735 w	736 vw	737 vw	755 w	25% γ (C7-C8-H), 10% γ (C8-C7- H) twist, 8% γ (C-C=O) wag.
707	3.8	23.1	710 m	716 vs	716 vs	724 m	18% ν (N3-C6), 34% δ (C-N4-C) bend, 13% δ (N-C5-N) bend .
679	83.7	0.8	680 vw	681 vw			78% γ (N3-H) twis, 13% γ (N4-H) twist.
612	7.9	2.3	596 vw	605 vw	603 vw		86% γ (N-C5-N) wag.
581	29.6	0.7		575 vw		606 m	81% γ (C-N-H)
531	8.9	5.3	529 w	534 s	535 vs		17% ν (N4-C5), 10% ν(C5-N3), 38% δ (C-N3-C) bend
489	11.2	0.8		503 w	505 m	512 w	12% δ (N3-C-S) bend, 11% δ (C-N4-C), 62% δ (C8-C6-O)bend
446	14.0	13.2	450 s	452 s	451 vs	448 s	36% ν (N3-C6), 26 % δ(N-C5-N) bend, 29% δ (C=S),
391	15.9	1.2		402 m			48% γ (C8-C7-N4) wag, 12% γ (C=O). 21% γ(N3-C5-N4) twist
266	8.3	4.9		282 s	281 vs		10% ν (N4-C5), 67% δ (N3-C-S) bend, 14% δ (C86-C6-O)bend
155	0.9	0.3		178 vw	182 vw		100% γ ring
122	0.5	0.1		128 m			79% γ (N4-C-S) twist

[a] IR intensities and Raman activities are calculated in (km/mole),(Ǎ^{4}/amu) respectively.
[b] vs = very strong; s = strong; m = medium; w = weak; vw = very weak, sh=shoulder.
[c] ν, stretching, vibration; δ, bending in the plane; γ, bending out of the plane

5.3.8. Detection of 2-TU

5.3.8.1. SERS results of 2-TU on Ag/G

Figure 5.7 shows the normal Raman spectrum of solid 2-TU and an SERS spectrum of 2-TU with Ag/G nanocomposites. The comparison between SERS spectrum and normal Raman spectrum of 2-TU indicates that the weak band at 736 cm^{-1} in the normal Raman spectrum assigned to γ (C8-H), γ (C7-H) vibration mode, is shifted to higher frequencies at 755 cm^{-1}, with enhanced intensity. The bands at 789 and 913 cm^{-1} in the normal Raman spectrum are shifted to 815, and 931 cm^{-1}, respectively. The bands (related to γ (C6-N3),ν (C7-C8) and δ (C-N4-C8), in SERS) are enhanced to very high intensity in SERS spectrum. In addition, the small peak at 957 cm^{-1} in the normal Raman spectrum is enhanced by higher intensity, and shifted to 951cm^{-1} in SERS spectrum, which is attributed to γ (C7- H), and γ (C8-C7-N4). Moreover, the very weak band in the normal Raman spectrum about 1071 cm^{-1} is shifted to higher wavenumber in the SERS spectrum at 1075 cm^{-1}. The shift and enhanced factor are very small for this band. Finally, the two peaks at 1368 and 1554 cm^{-1} in the normal Raman spectrum are shifted to 1377 , and 1527 cm^{-1} in the SERS spectrum, respectively, with high enhancement. The peak at 1368 cm^{-1} is related to δ (N3-H) bend, δ (N3-C-S) bend, and δ (C-N3-C). On the other hand, the band at 1554 cm^{-1} is related to ν (C5-N3), and δ (N4-H).

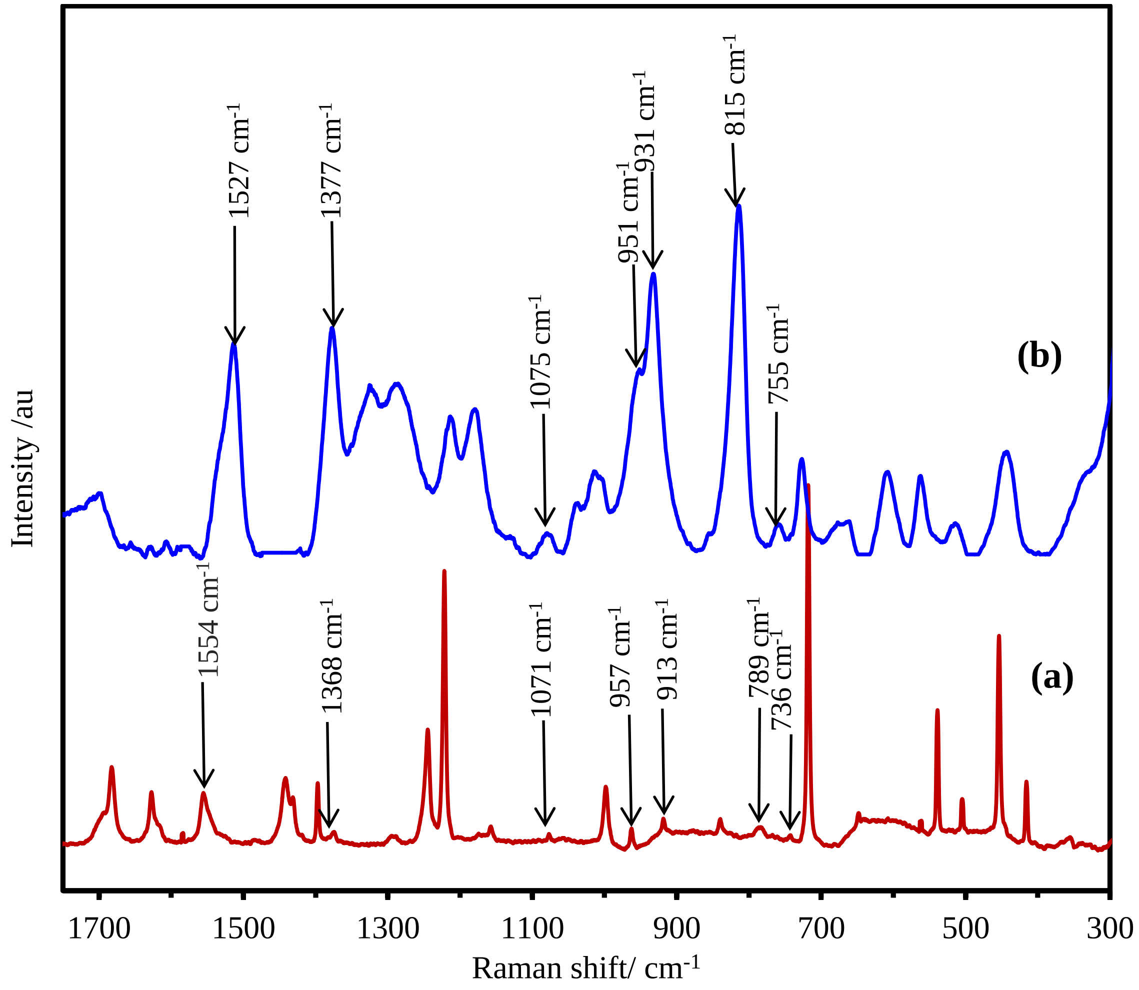

Figure 5.7: Raman spectra of pure solid 2-TU (a), and 2-TU with Ag/G (b). Laser ʎ=633nm, acquisition time; 30 sec, and objective; 10x.

5.3.8.2. SERS enhancement factor of 2-TU

The SERS enhancement factors for the vibrations of 2-TU (1×10^{-3} M) on silver-graphene composite to the corresponding band obtained from 1.0 M saturated solution were calculated using the following equation.

EFs = $(\delta_{\text{SERS}} \times C_{\text{normal}}) / (\delta_{\text{normal}} \times C_{\text{SERS}})$

Where δ and C are the Raman mode intensity and sample concentration, respectively.

The EFs for the SERS prominent peaks of 2-TU on silver- graphene composite are given in Table 5.3. The EFs is not the same for the different SERS modes, the maximum enhancement was observed at 815 cm^{-1}.

Table 5.3: SERS enhancement factor of MTZ on gold and silver colloids.

Normal Raman spectra (cm^{-1})	**SERS spectra (cm^{-1})**	**EFs**
1554	1527	4.8×10^{2}
1368	1377	1.7×10^{3}
913	931	2.7×10^{3}
789	815	2.9×10^{3}

5.3.8.3. SERS spectra of 2-TU with different concentrations

The most enhanced band at 815 cm^{-1} in SERS spectra was selected for creating a qualitative analysis of 2-TU. SERS spectra of 2-TU at different concentrations examined on the Ag/G substrate are given in Figure 5.8a. The intensities of the SERS spectra increase with increasing the concentration of 2-TU implying that the SERS intensities are proportional to the quantity of 2-TU molecules. The minimum concentration of 2-TU observed by Ag/G was lower than 10^{-8} M. Figure 5.8b shows the SERS intensity of the vibration frequency at 815cm^{-1} versus the concentration of the 2-TU solution. Considering the band at 815 cm^{-1}, the SERS response for 2-TU in solutions with a dynamic range between 10^{-7} M to 10^{-8} M was obtained with a linear coefficient (R^2) of 0.9952.

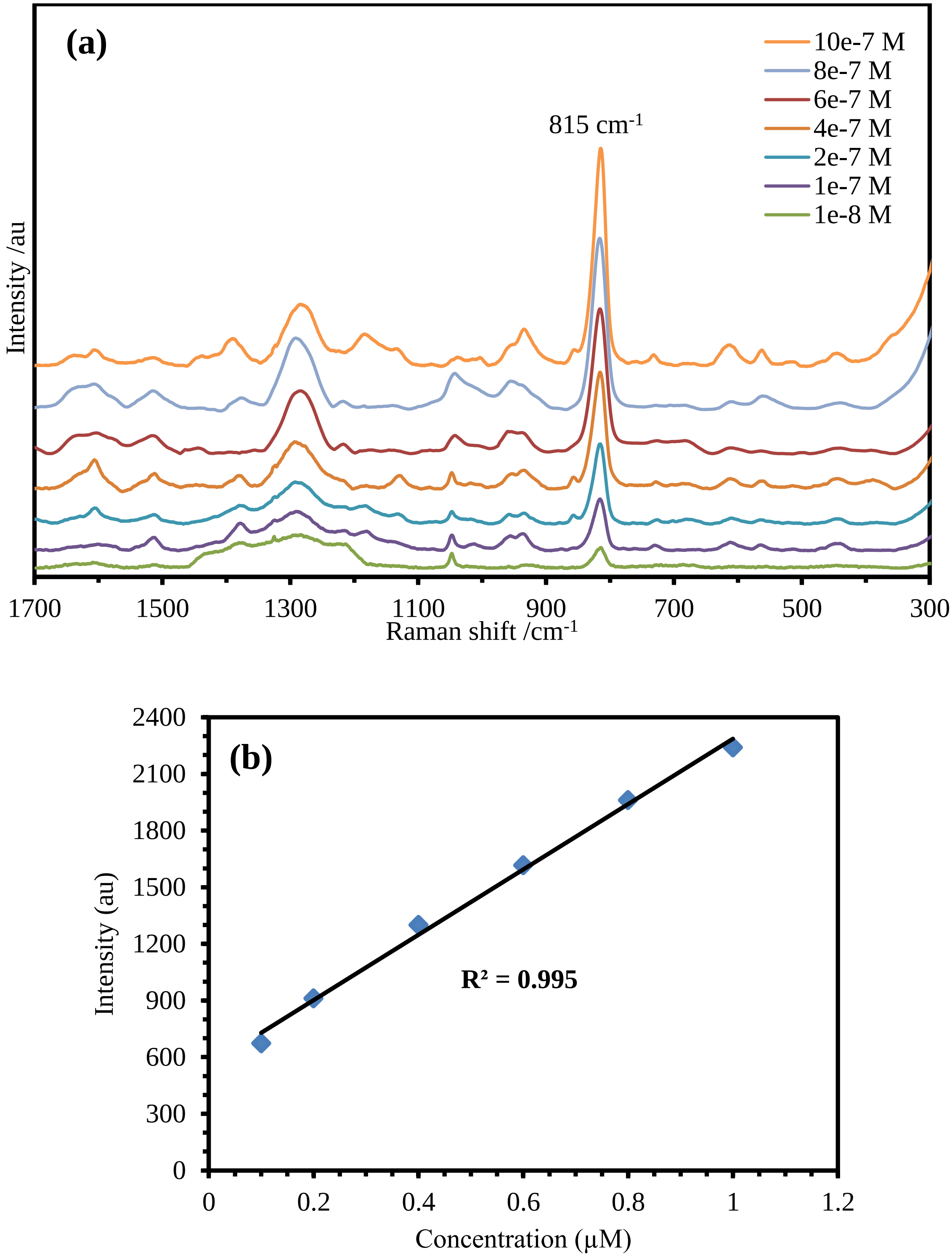

Figure 5.8: (a) SERS spectra of 2-TU with different concentration,(b) calibration curve of the band at 815 cm^{-1}. Laser ʎ=633nm, acquisition time; 30 sec, and objective; 10x.

5.4. CONCLUSION

Graphene decorated with silver nanoparticles (Ag/G) was synthesized by the reduction method using $NaBH_4$ as reducing agent. The Ag/G nanocomposites were characterized by UV-vis, FT-IR, XPS, NMR, and Raman spectroscopy, to investigate their chemical composition, and structure. All the results confirmed that Ag NPs were uniformly loaded onto the graphene sheets. However, NMR and XPS spectra indicate that the C sp^2, C sp^3, hydroxyl, epoxy, carboxylic, and ketone groups are the major functional groups presented on graphene sheets. Additionally, the Raman signals of 2-TU are greatly enhanced after deposition of Ag/G nanocomposites due to charge transport. Thus, the SERS substrates prepared by our method show excellent enhancement (LOD was 1.1×10^{-10}), and can be employed to detect 2-thiouracil.

5.5. REFERENCES

[1] X. S. Zhao, Li Li Zhang, and Rui Zhou. J. Mater. Chem. 2010, 20, 5983.

[2] M.J. McAllister, J.L. Li, … et al. Chem. Mater. 2007, 19, 4396.

[3] C. Lee, X. Wei, J.W. Kysar, J. Hone. Science. 2008, 321, 385.

[4] Huang Lin-jun, Wang Yan-xin, … et al.. Int. J. Electrochem. Sci. 2016, 11, 398.

[5] A. L. Higginbotham, J. R. Lomeda, … et al. Appl. Mater. Interfaces. 2009, 1, 2256.

[6] A. Lerf, H. He, M. Forster, J. Klinowski. J Phys Chem B. 1998, 102, 4477.

[7] F. Uhl, C. Wilkie. Polym Degrad Stab. 2004, 84, 215.

[8] D.R. Dreyer, S. Park, C.W. Bielawski, R.S. Ruoff. Chem. Soc. Rev. 2010, 39, 228.

[9] C. Hontoria- Lucas, A. Lo´ pez-Peinado, … et al. Carbon. 1995, 33, 1585.

[10] B. C. Brodie. Philos. Trans. R. Soc. London. 1859, 14, 249.

[11] W. S. Hummers, Offeman. R. E. J. Am. Chem. Soc. 1958, 80, 1339.

[12] G. Williams, B. Seger, P.V. Kamat. ACS Nano. 2008, 2, 1487.

[13] C.N.R. Rao, Swapan K. Pati, … et al. Chemical Physics Letters. 2010, 497, 70.

[14] Tifeng Jiao , Haiying Guo, Qingrui Zhang, … et al. Scientific Reports. 2015, 5, 1.

[15] Van Hoang Luan, … et al. Journal of Colloid and Interface Science. 2015, 437, 181.

[16] Yimin Sun, Yubo Cheng, Kui He, … et al. RSC Adv. 2015, 5, 10178.

[17] M.A. Shenashen, S.A. El-Safty and E.A. Elshehy. Part. Syst. Charact. 2014, 31, 293.

[18] A.M. Shanmugharaj, Sung Hun Ryu. Electrochimica Acta. 2012, 74, 207.

[19] Vijaya K Rangari , Ghouse M Mohammad , … et al. Nanotechnology. 2010, 21, 95.

[20] Jizhen Ma, J. Zhang, … et al. J. Mater. Chem. 2011, 21, 3350.

[21] S. Schlücker. Angew. Chem. Int. Ed. 2014, 53, 4756.

[22] Paula A.A.P. Marques… et al. Ciência & Tecnologia dos Materiais. 2014, 26, 102.

[23] J. Liu, I. White, D.L. DeVoe. Anal Chem. 2011, 83, 2119.

[24] Xu, W.; Mao, N.; Zhang, J. Small. 2013, 9, 1206.

[25] Caiyu Qiu. Haiqing Zhou, … et al. CARBON. 2013, 59, 487.

[26] Shicai Xu, Baoyuan Man, … et al. Appl. Mater. Interface., 2015, 7 (20), 10977.

[27] S. Chen , Xin Li , Yuanyuan Zhao , Limin Chang , Jingyao Q. CARBON. 2015, 81, 767.

[28] M. Liu, W. Chen. Biosensors and Bioelectronics. 2013, 46, 68.

[29] X. Ding, L. Kong, J. … et al. ACS Appl. Mater. Interfaces. 2013, 5 (15), 7072.

[30] S. He, K.K. Liu, S. Su, J. Yan, X. Mao, D. Wang. Anal Chem. 2012, 84 (10), 4622.

[31] M. R. Das, R. K.Sarma,… et al Colloids and surfaces. B:Biointerfaces. 2011, 83, 16.

[32] Ana carolina Mazarin de Moraes, Bruna araujo lima, … et al International Journal of Nanomedicine, 2015, 10, 6847.

[33] de Faria AF, de Moraes ACM, Marcato PD, et al. J Nanopart Res. 2014, 16, 1.

[34] Mohammad A. Aldosari, Ali A. Othman … et al. Molecules 2013, 18, 3152.

[35] sangiliyandi gurunathan,… et al. International Journal of Nanomedicine. 2015, 10, 6257.

[36] Zeng, X.; Yang, J.; Yuan, W. Eur. Polym. J. 2012, 48, 1674.

[37] Anh-Tuan Le, … et al. Journal of Alloys and Compounds .2014, 615, 843.

[38] Sarat K Swain, Deepak Sahu, … et al. Appl Sci Adv Mater Int. 2015, 1(6), 224.

[39] Soon Wei Chook, Chin Hua Chia …et al. Nanoscale Research Letters . 2012, 7, 541.

[40] Zhu C, Guo S, Fang Y, Dong S. ACS Nano. 2010, 4, 2429.

[41] S. Stankovich, D. A. Dikin, R. D. Piner, … et al. Carbon. 2007, 45, 1558.

[42] Jing Li and Chun-yan Liu. Eur. J. Inorg. Chem. 2010, 1244.

[43] S. W. Chook, C. H. Chia, S. Zakaria, … et al. Nanoscale Research Letters. 2012, 7, 541.

[44] Kai-Chih Hsu and Dong-Hwang Chen. Nanoscale Research Letters. 2014, 9, 193.

[45] B. J. Schultz, R.V. Dennis, … et al. RSC Adv. 2014, 4, 634.

[46] Hsi-Wen Tien, Yuan-Li Huang, Shin-Yi Yang, … et al. Carbon. 2011, 49, 1550.

[47] W. Cai, R.D. Piner, F.J. Stadermann, … et al. Science. 2008, 321(5897), 1815.

[48] Heyong He, T. Riedl, A. Lerf, and Jacek Klinowski. J. Phys. Chem. 1996, 100, 19954.

[49] Wei Gao,LawrenceB.Alemany, Lijie Ci, P. M. Ajayan. Nature Chemistry. 2009, 1, 403.

[50] Leah B. Casabianca, Medhat A. Shaibat, … et al . J. AM. CHEM. SOC. 2010, 132, 5672.

[51] Guangyuan Xu, Jenny Malmström, … et al. Journal of Nanomaterials. 2016.

[52] Stankovich S, Dikin DA, Piner RD… et al. Carbon. 2007, 45(7), 1558.

[53] Leila. S, A. A. Athawale. Int. J. Ren. Ene. and Env.Eng. 2014, 2(1), 58.

[54] Yazhou Zhou, Xiaonong Cheng, … et al. J. Mater. Chem. C. 2014, 2, 6850.

[55] Zhang Z, Xu FG, Yang WS, et al. Chem Commun. 2011, 47(22), 6440.

CHAPTER 6

Surface-Enhanced Raman Scattering Based on Colloidal Ag and Au Nanoparticles for Detection of Methimazole

6.1. INTRODUCTION

Methimazole (MTZ), known as 1-methylimidazole-2-thiol, exists in two forms are shown in scheme 6.1. It is used in thyroid hormone biosynthesis by preventing the organification of iodide in the thyroid [1]. MTZ as an antithyroid drug is used for the treatment of hyperthyroidism, and in Graves' disease [2]. MTZ is one of the azole derivatives that extensively used in the field of inhibition of metals from corrosion [3].

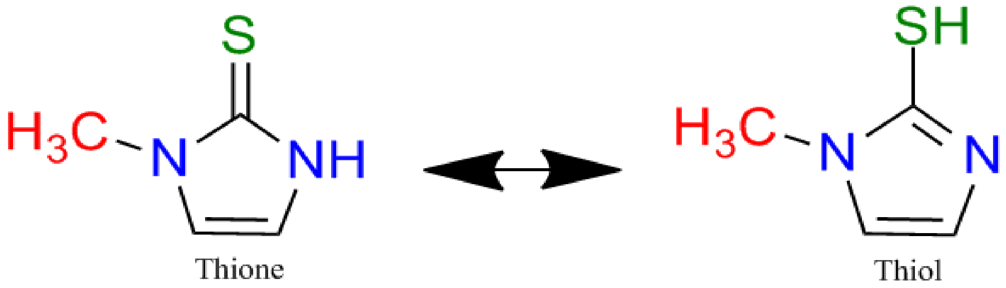

Scheme 6.1: Structures of Methimazole Forms

Due to its presence in a wide range of pharmaceutical formulations and body fluids, the determination of MTZ is a significant area of interest. MTZ has been investigated by various methods including; electrochemical techniques, high-performance liquid chromatography, gas chromatography, fluorescence probe method, and infrared and Raman spectroscopies. [4-5]. However, these techniques required additional derivatization procedure and more time-consuming [6].

Surface Enhanced Raman Scattering (SERS), an advanced method of Raman technique, has become a center of interest for molecular characterization. SERS is a promising alternative method for the analysis of the biological and pharmaceutical compounds, due to its high-sensitivity, and non-destructive nature [7]. Spectral intensities in SERS are enhanced by a high factor, for example, 10^8-10^{10} can be obtained for target molecules adsorbed on the substrate surface compared to traditional Raman spectroscopy [8]. This enhancement is arising from the two main factors, electromagnetic and chemical charge transfer enhancements. The first one contributes the major part of the enhancement magnitude, which involves excites surface Plasmon on the metal, due to the incident laser irradiates on the metal surface. The chemical mechanism involves transfer one electron from the highest occupied molecular orbital to the lowest unoccupied molecular orbital [9-10]. The most important benefits of the SERS represent for the determination of the sites through which the molecule interacts with the metal surface and the type of orientation [11]. Several studies were reported for the detection and investigation of pharmaceutical compounds in aqueous solution, through functionalization of the target analyte with metal nanoparticles [12-14].

Silver and gold nanoparticles have been extensively used as substrates for the detection of drugs, due to attractive physicochemical properties, surface plasmon resonance in the visible region and easy machining. Ma and Liang at al, reported the investigation of mercury (II) using methimazole and cyclodextrin compounds coated with silver nanoparticles [15]. Noble metals have been combined with graphene to produce nanocomposites able for SERS sensing. The graphene composites are active for use as SERS substrate, because it is a very high surface area and the metal can be grown directly on the graphene sheets via a simple solution-based approach [16].

In this work, we prepared the gold and silver nanoparticles by the chemical reduction method. The resulting was used as SERS substrate for detection the methimazole in aqueous solution by Raman technique. Moreover, the DFT calculation was carried out to obtain a detailed interpretation of the SERS spectra.

6.2. EXPRIMENTAL

6.2.1. Chemicals and Materials

Methimazole "1-Methyl-2-imidazolethiol " (analytical standard, ≥ 99% purity), the CAS number 60560, were purchased from Sigma-Aldrich. Gold(III) chloride trihydrate ($HAuCl_4 \cdot 3H_2O$, ≥ 49% Au basis), the CAS number 16961-25-4, was purchased from Acros Organics BVBA. Trisodium citrate di-hydrate ($C_6H_5Na_3O_7 \cdot 2H_2O$, 98%) **(**cat number is S-279, product number 78479) was purchased from Fisher Scientific Company in U.S.A. Silver nitrate ($AgNO_3$, 99.8%), product number 30087, was purchased from BDH-Chemicals Ltd Poole England. Potassium bromide (KBr, ≥ 99%) was purchased from Sigma Aldrich. Solutions were prepared with ultrapure water obtained from a water purification system (Ultra Clear™ Lab Water Systems, Siemens Water Technologies USA).

6.2.2. Synthesis of nanomaterials

6.2.2.1. Synthesis of gold nanoparticles

The gold nanoparticles were prepared according to the process described by Siyavash and Mahsa [17]. About, 100.0 ml of a 0.1 M aqueous $HAuCl_4$ was boiled on a hot plate, with stirring. Then, 10.0 ml of sodium citrate (0.5 M) was rapidly added to the boiling gold solution. The solution color turned gray-blue within 60 sec. After 2 min the color of mixture solution changed to red-violet. Then, the solution was kept under heating for 10 min. Finally, the heating source was removed, and the solution was allowed to cool to room temperature.

6.2.2.2. Synthesis silver nanoparticles (Ag/NPs)

Silver colloids were prepared using the Han-Qing Yua and An-Wu Xu description with modification [18]. See section 4.2.2.2.

6.2.2.3. Synthesis of graphene oxide/gold nanocomposites (GO/AuNPs)

The synthesis of graphene oxide was reported in the previous chapter. About 0.1 g of the prepared GO was dispersed in 40.0 ml de-ionized water by sonication in an ultrasound bath for 30 min. Then, the gold colloid solution was mixed with the previously dispersed GO. Then, the mixture solution was aged during 0.5 h to promote the deposition of Au/NPs with the graphene surface. The solution was stirred continuously for 2 h at room temperature.

Next, the resulted precipitation was collected by centrifugation at 10000 rpm/min for 30 min. After that, the solid product was washed with deionized water three times, and dried at room temperature overnight.

6.2.3. Surface-Enhanced Raman Scattering (SERS)

The SERS spectra of Methimazole were obtained by using Raman spectroscopy system Lab Ram HP Evolution Raman spectrometer equipped with an internal He-Ne 17mW laser at a 633 nm excitation wavelength. SERS samples were prepared by using a 3: 1 volume ratio of the methimazole solutions to the colloid. A 10x objective was used for focusing the laser beam to the solution. The data acquisition time was 30 sec with one accumulation for collection each SERS spectra. A glass cell with dimensions of 1 cm radius, 2 cm height was used as a sample cell for the Raman spectra, Scheme 6.2. The SERS spectra were obtained in the range from 400-2000 cm^{-1}.

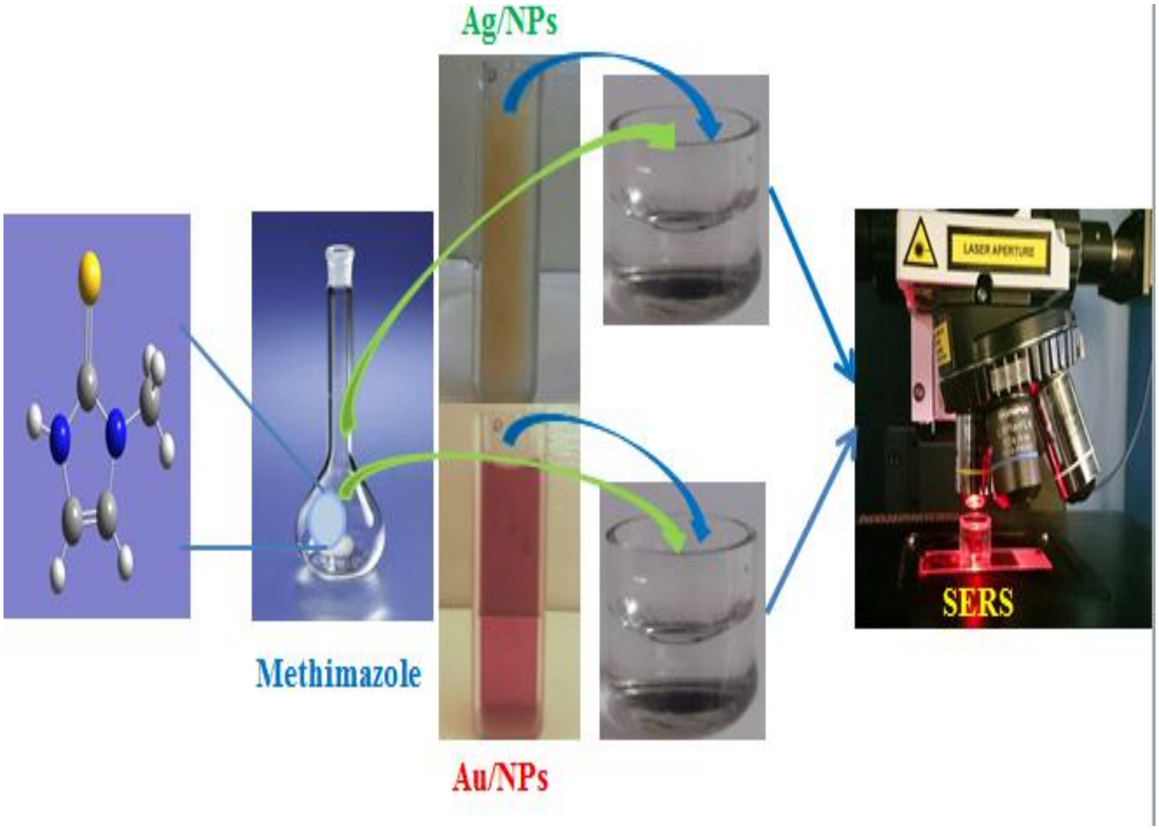

Scheme 6.2: Explaining the steps of the SERS measurements.

6.3. RESULTS AND DISCUSSION

6.3.1. Characterization NPs

Various techniques were used for characterizing AuNPs, AgNPs, and GO/AuNPs, including SEM, TEM, ultraviolet-visible spectroscopy (UV-vis), Raman, and FTIR.

6.3.1.1. SEM and TEM analysis

The TEM images were taken using the JEM -2100F Field Emission Electron Microscope, JEOL- USA) at 200 kV acceleration voltage. The TEM image of Au/NPs is depicted in Figure 6.1a. Uniform nanoparticles can be observed, with spherical shape and size ranges between 10-12 nm. Figure 6.1b shows the TEM image of Ag/NPs, which indicates uniform shape and well-dispersed particles with the average size of about ~ 60 nm as estimated by TEM scale. The great amount of Au NPs with uniform size decorated on the GO sheet can be observed in Figure 6.1c.

The SEM image of Au/G composite is shown in Figure 6.1d, which indicate that graphene sheets were well decorated with homogeneous dispersion gold nanoparticles.

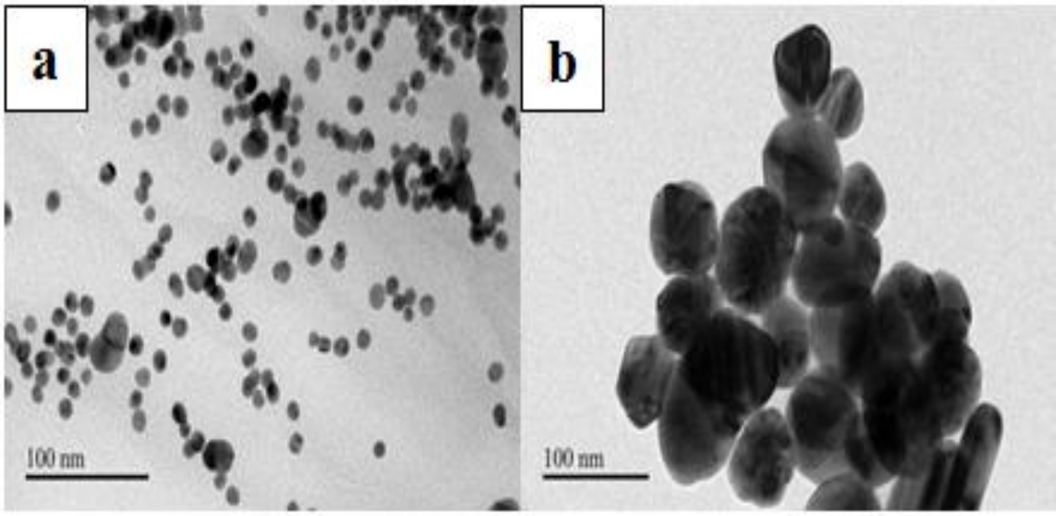

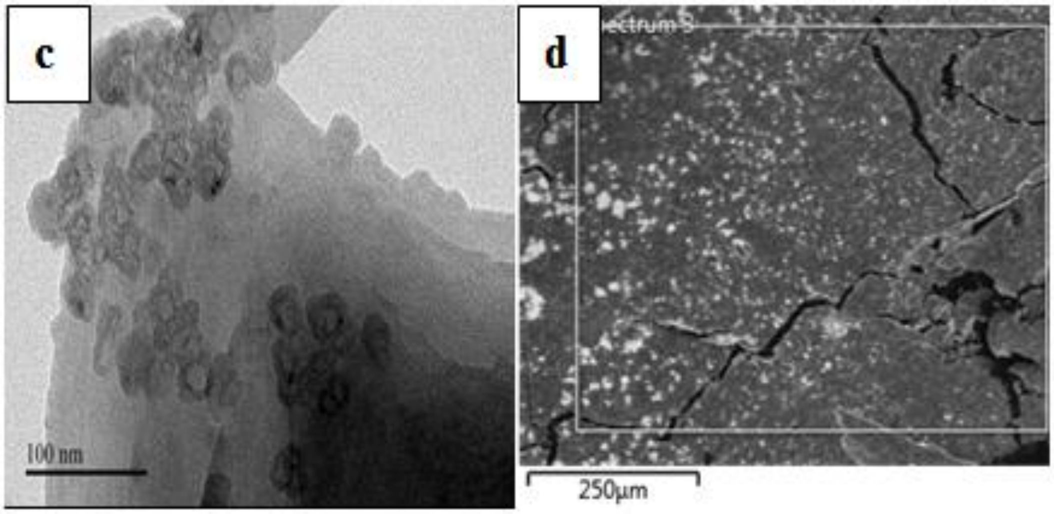

Figure 6.1: The typical TEM images of gold NPs (a), silver NPs (b), and of Au/G composite (c), The SEM image of GO decorated with AuNPs (d).

6.3.1.2. UV-vis Analysis

The Ultraviolet –visible (UV-vis) absorption spectra of AuNPs, and Au/GO nanocomposites are shown in Figure 6.2. The characteristic absorption maximum of the gold nanoparticles was found at 524 nm, due to surface plasmon resonance of AuNPs. The UV-vis spectra of silver nanoparticles showed surface plasmon resonance band at 421 nm. The UV-vis spectrum of GO decorated with AuNPs shows absorption peaks at 235 nm, which is related to π-π^* electronic transitions of C=C aromatic bonds. The band at 520 nm, which is corresponding to the absorption gold NPs, indicate successful deposition AuNPs on the GO surface sheets. This is in agreement with the reported synthesis of the GO-Au nanocomposites [19].

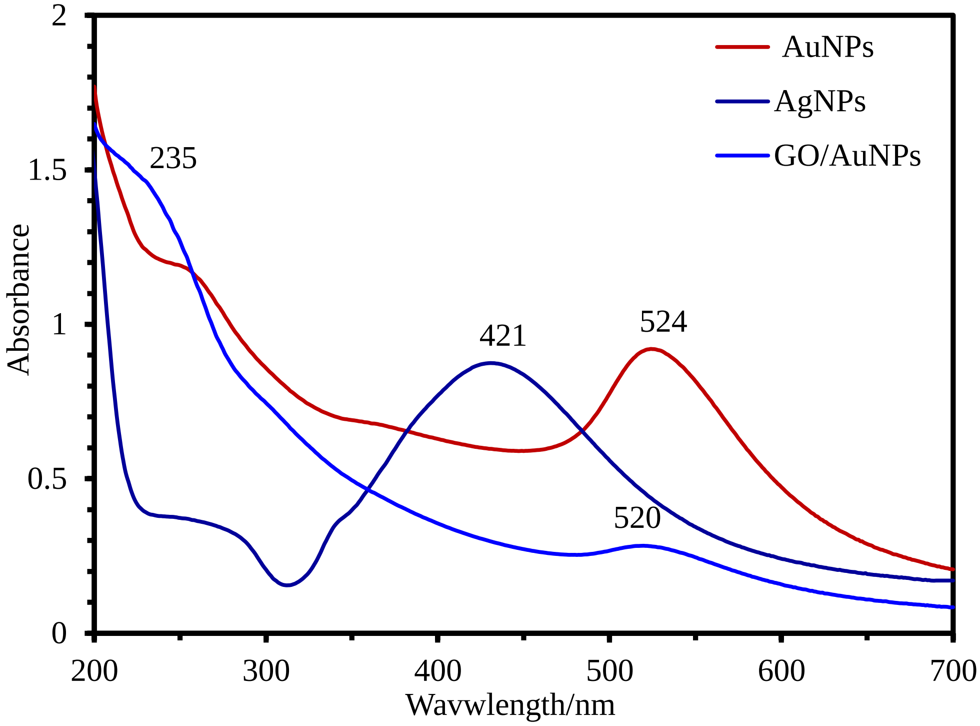

Figure 6.2: Absorption spectra of AuNPs, AgNPs, and Au/GO nanocomposites

6.3.1.3. IR Spectroscopy

The FT-IR spectra of silver and gold nanoparticles are shown in Figure 3a. Characteristic absorption peaks were obtained in the region 400 to 4000 cm^{-1} for both silver and gold nanoparticles. The spectrum shows very broad band around 3400-3600 cm^{-1}**,** a weak signal around 2060-2100 cm^{-1}, absorption relative sharp peak located at 1630 cm^{-1}, and a shoulder band around 735 - 755cm^{-1}. Figure 3b shows the FT-IR spectra of GO and G/Au composites with the absorption broad band at around 3380-3420 cm^{-1} assigned to the O-H stretching. The absorption peaks at 2921 cm^{-1}, and at 2852 cm^{-1} are attributed to symmetric and antisymmetric stretching vibration of CH, respectively. The medium band at 1637 cm^{-1} is attributed to a C=C aromatic group. The low peak intensities at 1733, 1330, 1212, and at 1122 cm^{-1} are attributed to the C=O carbonyl group, C-O carboxylic group, C-O epoxy group, and C-OH alkoxy stretching vibrations, respectively. The FT-

IR spectrum of GO/Au shows decrease in the intensity of the bands of different oxygen functionalities, due to the oxygen functionalities band experienced a chemical reduction [20].

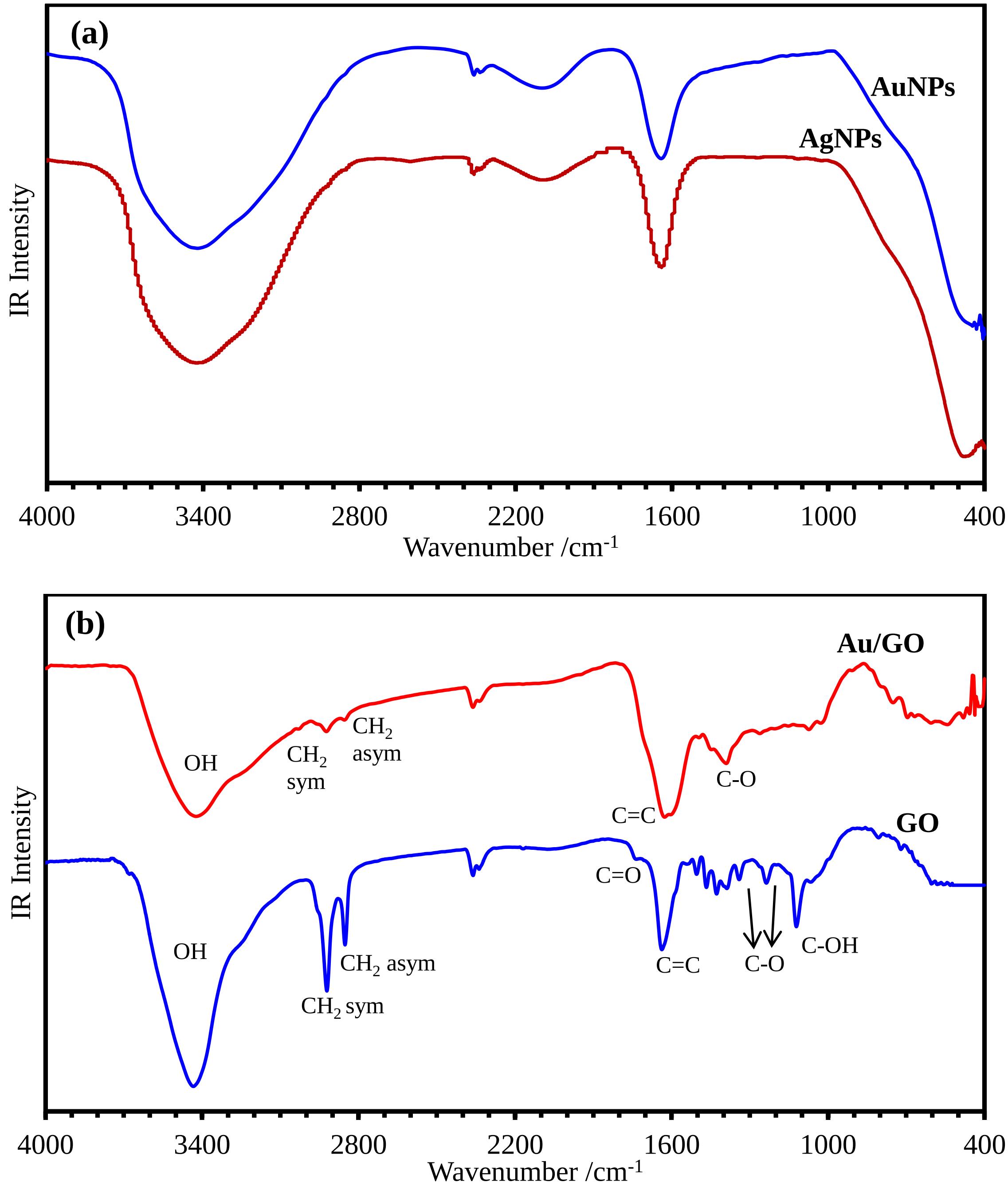

Figure 6.3: IR spectra of Au, and Ag nanoparticles. b) FT-IR spectra of GO, and Au-GO nanocomposites.

6.3.1.4. Raman Spectroscopy Analysis

The Raman spectra of silver and gold nanoparticles were given in Figure 6.4a. In the case of both gold and silver, no clear Raman bands were observed in the 200 to 3000 cm^{-1} range of the spectra. However, it can be observed the spectra show a weak broadband 1380-1420 cm^{-1} and a very small peak at 926 cm^{-1} in silver. With gold nanoparticles, a weak band is observed at around 730 – 830 cm^{-1}.

Figure 6.4b shows the typical Raman spectra of solid GO, and Au/G nanocomposites. In case of GO, the spectrum shows two prominent peaks, D (~ 1350 cm^{-1}), which attributed to disordered carbon sp^3 atoms and breathing mode, and G band at (~ 1600 cm^{-1}) corresponding to the E_{2g} phonon of order sp^2 carbon atoms. The intensity of D band higher intensity compared to that of the G band, due to higher disorder in graphene sheets [21]. In Au/G case, the D band assigned at 1342 cm^{-1} is shifted to a lower frequency about (8 cm^{-1}) compared with D band in GO sample, indicating a higher level of disorder of the graphene layers and increased numbers of defects because of the partial reduction of GO by sodium citrate during the synthesis of the Au-GO nanocomposites. The G band of Au/G nanocomposites is obtained at 1595 cm^{-1}, which is upshifted by 5cm^{-1} compared with G band in GO. This shift can be attributed to electron– phonon coupling.

Besides, the intensity ratio of D and G bands (I_D/I_G) increases. The I_D/I_G is used to assess the degree of disorder, the average size of the sp^2 carbon atoms domains, and decrease of the mean crystallite size of GO. The ratio values are 1.16 and 1.26 for graphene oxide and Au/G nanocomposites, respectively. The I_D/I_G value of GO and Au/G increase progressively, due to damaging the crystal structure of carbon materials, during the reduction process of graphene. This can be explained by the removing of some oxygen functional groups through reduction process, lead to form high-level fragmentation along the reactive sites of graphene, forming a graphene sheet more disorder. [22, 23]

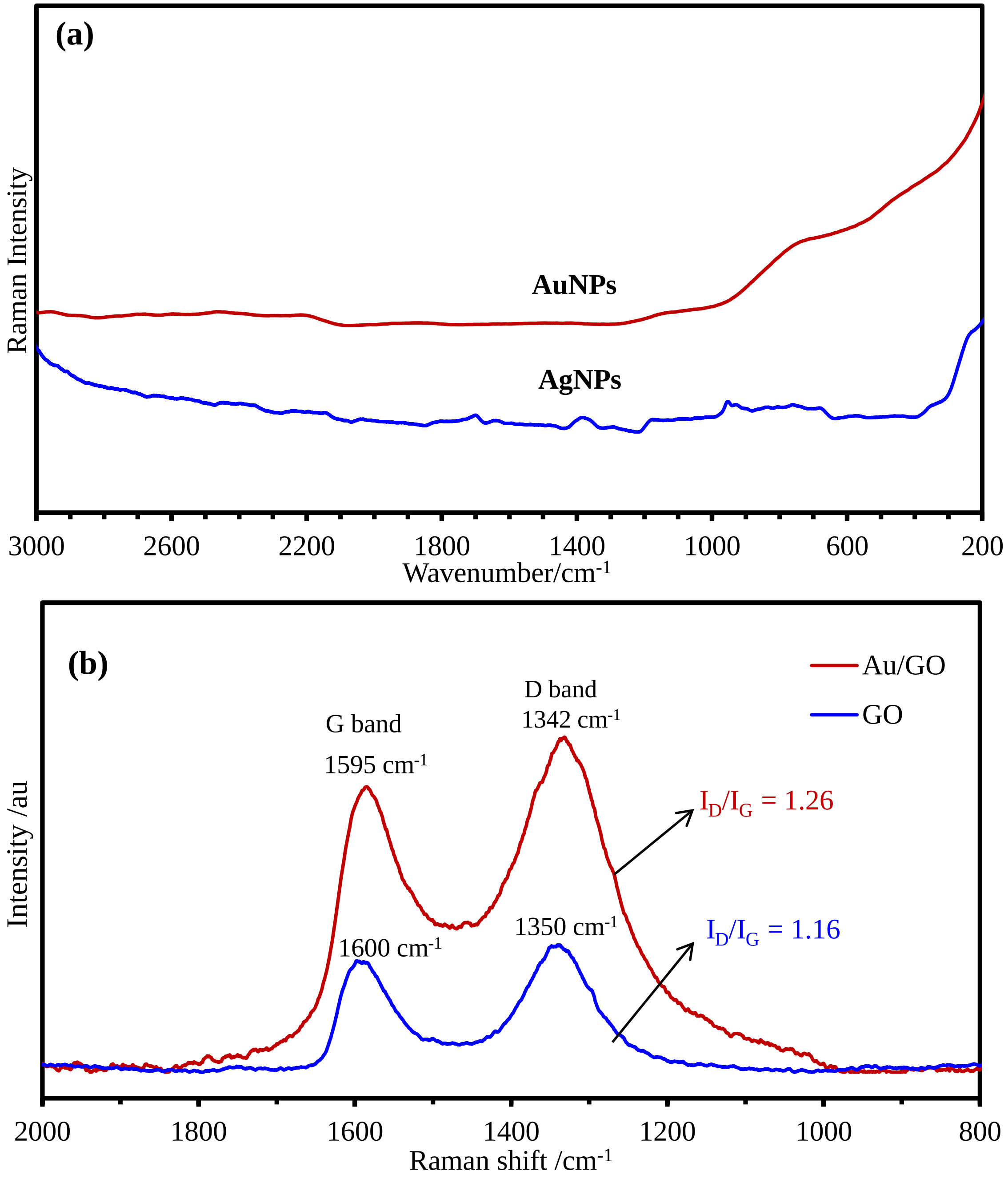

Figure 6.4: (a) Raman spectra of gold, and silver nanoparticles, and (b) Raman spectra of GO, and Au/G nanocomposites.

6.3.1.5. XPS Analysis

XPS is a surface sensitive technique to analyze the chemical composition of the graphene oxide, and graphene oxide- gold nanocomposites. Figure 6.5a shows the XPS survey spectra for GO, and Au/G nanocomposites. The Au 4f peaks (doublet) present in Au/GO indicate a successful deposit of Au NPs on the GO sheets.

The core level C1s spectra of GO and GO/AuNPs are shown in Figure 6.5b, and Figure 6.5c. The attributions of various peaks of C1s core level, and 4f are given in Table 6.1. In case of GO, four prominent peaks are observed in a deconvoluted C1s spectrum. These signals are attributed to carbon atoms in different functional groups, C-C (Csp^2 and Csp^3 at 284.5 eV), C-O (epoxy and hydroxyl, at 286.72 eV) C=O (carbonyl, at 287.8 eV), and O-C=O (carboxylate carbon, at 289.2 eV). However, for GO/Au composite the decrease in intensity of oxygenated functional groups (hydroxyl and epoxy, carbonyl, and carboxylate groups) indicate the removal oxygenated functional groups by the chemical reduction [24,25].

Figure 6.5d shows the XPS spectrum of Au 4f in the form of a doublet ($4f_{7/2}$, and $4f_{5/2}$) for GO/AuNPs. The $4f_{7/2}$, and $4f_{5/2}$ peaks present at 83.3 eV, and at 89.0 eV, respectively. With $\Delta = 3.7$ eV. Which is in very good agreement with literature [26].

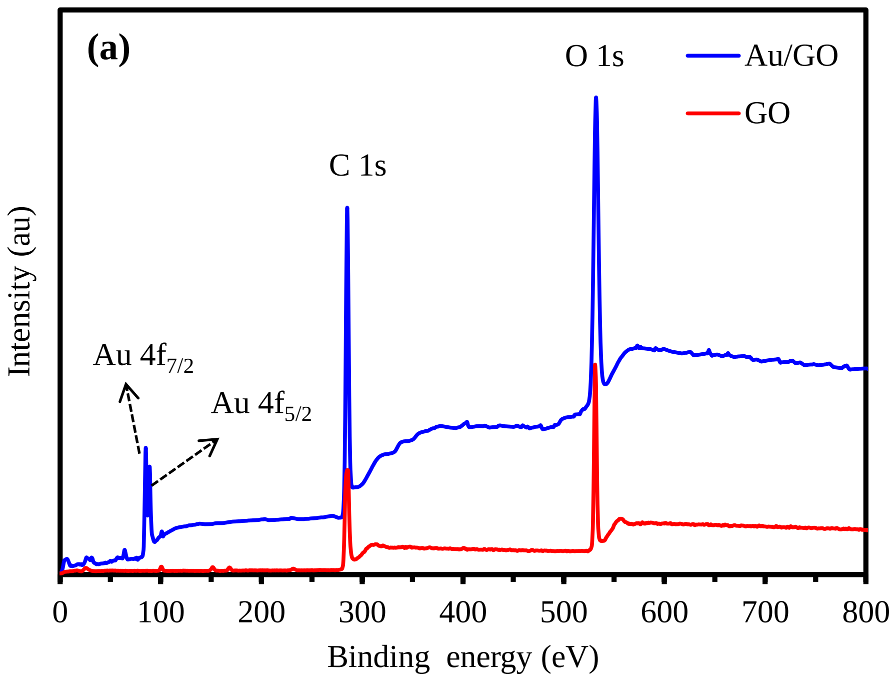
(a)
O 1s
Au/GO
GO
C 1s
Au 4f$_{7/2}$
Au 4f$_{5/2}$
Intensity (au)
0
100
200
300
400
500
600
700
800
Binding energy (eV)

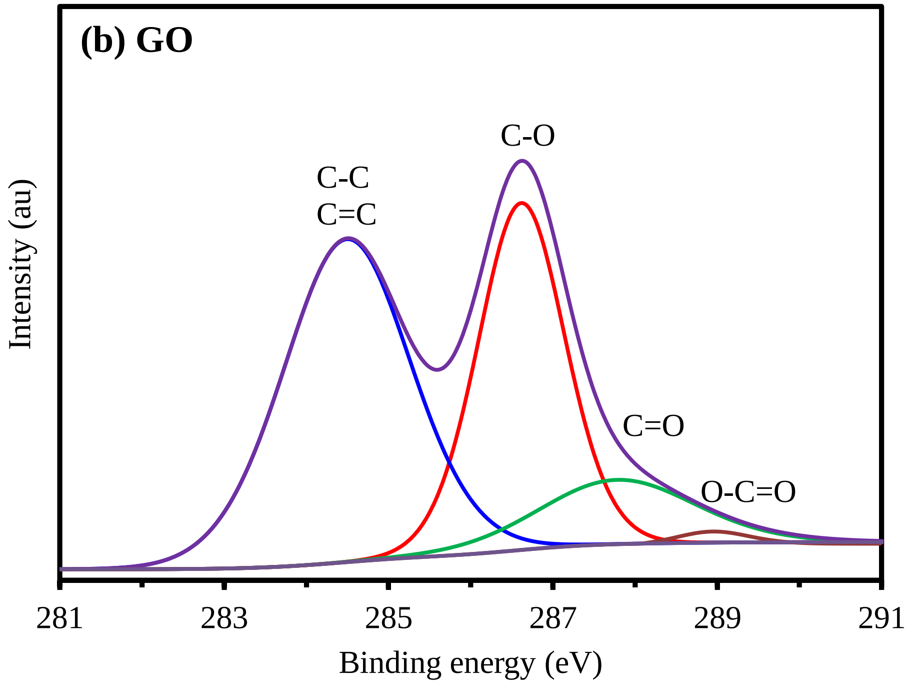
(b) GO
C-O
C-C
C=C
C=O
O-C=O
Intensity (au)
281
283
285
287
289
291
Binding energy (eV)

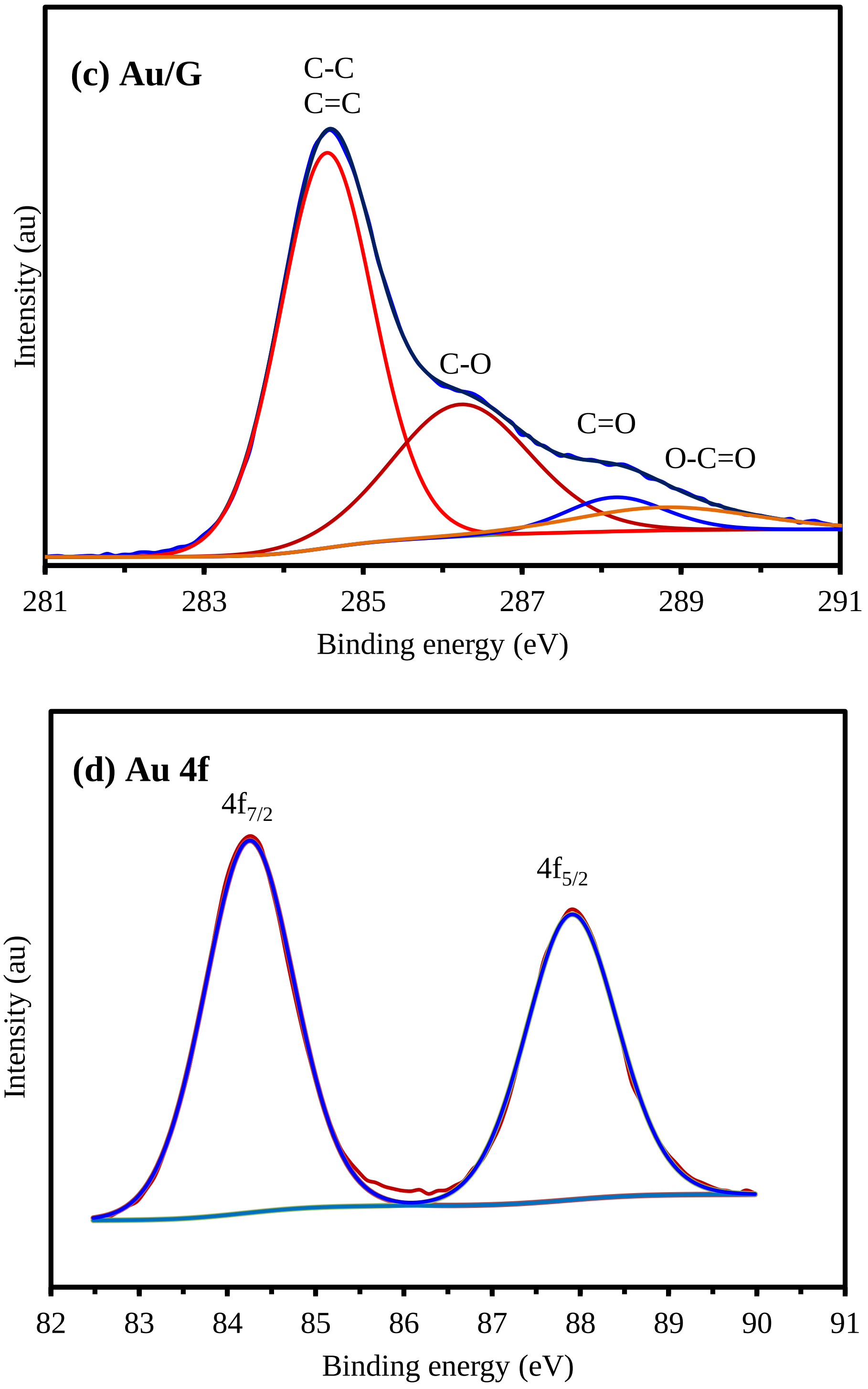

Figure 6.5: (a) XPS survey spectra of GO, and Au/G nanocomposites, (b) the C 1s core level XPS spectra of GO, (c) the C 1s core level XPS spectra of Au/G, and (d) XPS analysis spectra of Au 4f in Au/G.

Table 6.1: XPS data of various core level present in GO, and GO/Au nanocomposites.

Composites	**Peaks**	**BE (eV)**	**Atomic %**	**Bond Type**
Ghraphene Oxide	C1s	284.5	49.76	C-C, and C=C
		286.72	36.39	C-O (epoxy and hydroxyl groups)
		287.8	11.92	C=O (carbonyl groups)
		289.2	1.94	O-C=O (carboxylate carbon groups)
Graphene oxide – Gold nanocomposites	C1s	284.5	58.94	C-C, and C=C
		286.52	24.14	C-O (epoxy and hydroxyl groups)
		288.0	14.41	C=O (carbonyl groups)
		289.1	4.51	O-C=O (carboxylate carbon groups)
	Au 4f	84.3	59.56	$4f_{7/2}$
		89.0	40.44	$4f_{5/2}$

6.3.2. Density Functional Theory (DFT)

6.3.2.1. Molecular geometry of MTZ

The structure of a certain molecule is the first substantial step in the theoretical calculations. The optimized structure of methimazole was determined using the DFT calculations with B3LYP/6-311++G (d, p) basis set, as shown in Figure 6.6 with minimum surface potential energy. All measurements were derived using the Gaussian 09 program. The important parameters of the optimized geometry such as bond length, bond angles, and dihedral angles are summarized in Table 6.2. All-theoretical calculations to the isolated methimazole molecule were performed in the gaseous state while the experimental results were done in the solid state. Therefore, the theoretical parameters of the optimized structure are complementary to the experimental values.

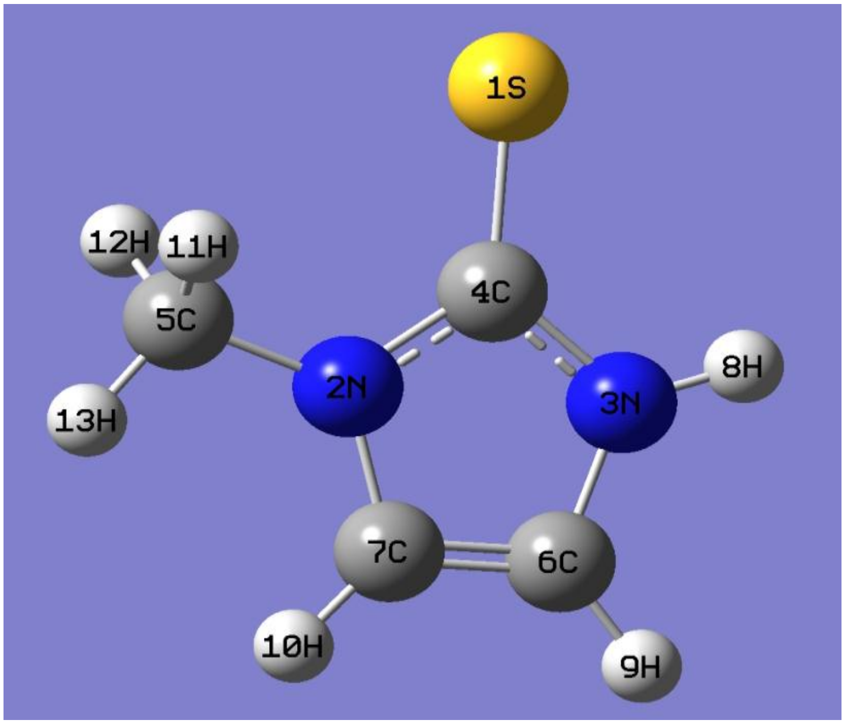

Figure 6.6: The optimized structure of MTZ

Table 6.2: Optimized bond lengths (Å), bond, and dihedral angles (^{0}) of methimazole at the DFT B3LYP/6-311++G(d,p).

Bond lengths (Å)		Bond Angles (^{0})		Dihedral angles (^{0})	
S1-C4	1.676	C4-N2-C5	123.3467	C5-N2-C4-S1	-0.0016
N2-C4	1.375	C4-N2-C7	110.42	C5-N2-C4-N3	180.0006
N2-C5	1.4527	C5-N2-C7	126.2333	C7-N2-C4-S1	179.9801
N2-C7	1.3912	C4-N3-C6	111.4707	C7-N2-C4-N3	-0.0177
N3-C4	1.3727	C4-N3-H8	121.4634	C4-N2-C5-H11	-59.6814
N3-C6	1.3859	C6-N3-H8	127.0658	C4-N2-C5-H12	59.7299
N3-H8	1.0067	S1-C4-N3	128.2274	C4-N2-C5-H13	180.0239
C5-H11	1.091	S1-C4-N2	127.7167	C7-N2-C5-H11	120.3399
C5-H12	1.091	N2-C4-N3	104.056	C7-N2-C5-H12	-120.2488
C5-H13	1.0894	N2-C5-H11	110.1909	C7-N2-C5-H13	0.0453
C6-C7	1.3529	N2-C5-H12	110.1952	C4-N2-C7-C6	0.0074
C6-H9	1.0768	N2-C5-H13	108.7338	C4-N2-C7-H11	-180.0081
C7-H10	1.0772	H11-C5-H12	108.2649	C5-N2-C7-C6	-180.0116
		H11-C5-H13	109.7254	C5-N2-C7-H11	-0.0271
		H12-C5-H13	109.7228	C6-N3-C4-S1	-179.9758
		N3-C6-C7	106.4567	C6-N3-C4-N2	0.0219
		N3-C6-H9	122.6968	H8-N3-C4-S1	-0.0589
		C7-C6-H9	130.8465	H8-N3-C4-N2	-180.0611
		N2-C7-C6	107.5965	C4-N3-C6-C7	-0.0181
		N2-C7-H10	121.9342	C4-N3-C6-H9	180.001
		C6-C7-H10	130.4692	H8-N3-C6-C7	180.0707
				H8-N3-C6-H9	0.0898
				N3-C6-C7-N2	0.0062
				N3-C6-C7-H10	180.0236
				H9-C6-C7-N2	-180.015
				H9-C6-C7-H10	0.0023

6.3.2.2. Vibrational Assignments

The vibration frequency modes of MTZ were calculated through DFT method with B3LYP level and 6-311++G (d, p) basis sets, and the results are summarized in Table 6.3. The FT-IR and Raman spectra of the theoretical and the experimental are shown in Figure 6.7, and Figure 6.8, respectively. The FT-IR and Raman theoretical wavenumbers of the vibration modes were excellently correlated with the experimental modes.

(a) Vibrational Assignment Theoretically by DFT

The FT-IR and Raman theoretically spectra are shown in Figure 6.7. The calculated wavenumber was scaled using the scaling factor 0.961 for frequency region ≥ 2000 cm^{-1}, and scaling factor 0.985 for frequency region < 2000 cm^{-1} [27]. The calculated CH stretching vibrational modes for MTZ is assigned at 3162, 3142, 3022, 2998, 2929cm^{-1} which is corresponding to ν (C7-H), ν (C6-H), ν (C5-H11), ν (C5-H12), and ν (C5-H13). The NH stretching vibrational mode can be assigned at 3531 cm^{-1} in theoretical spectra. The band at 1588 cm^{-1} is corresponding to C=C stretching vibration mode. The C-S stretching vibrational modes were predicted to have four vibrational frequencies, at 1473,1459, 1415 and at 1159 cm^{-1}. The peak at 238 cm^{-1} is attributed to C-S wag mode. The CN stretching was predicted at ten different frequencies as shown in Table 6.3. The N-H in plane bending was assigned at three different frequencies. The NH (CH) mode (out the plane, and in plane) vibration was predicted at three different frequencies, the ring bend (in plane) was predicted three different vibrations, and at one position for ring bend (out plane). The SCN vibration mode was predicted at two different frequencies. These vibrations are in the mix with other vibrational modes (Table 6.3).

(b) Vibrational Assignments Experimentally

Figure 6.8a shows the FT-IR, and Figure 6.8b shows the Raman spectra of the pure MTZ solid sample, which are in agreement with that found in the literature [21]. The FT-IR and Raman experimental mode are in correlation with the calculated results. For example, the C-H stretching mode for methimazole in this study was predicted theoretically at 3162 cm^{-1}, which is in a very good agreement with the experimentally observed IR bands at 3161cm^{-1}, and with the Raman peaks at 3166 cm^{-1} of a previous study [12, 21]. The stretching vibration of S-C at 1415 cm^{-1} in the Raman experimental spectrum, and at 1403 cm^{-1} in the IR experimental spectrum appears at 1410cm^{-1} in the theoretical spectrum. The C=C stretching vibrational theoretically assigned at 1588 cm^{-1} can be assigned at 1578 cm^{-1} in the IR experimental spectrum, and at 1579 cm^{-1} in the Raman experimental spectrum, which is in a good agreement with the reported IR spectra in the literature [12, 15]. The C-N stretching vibrational was predicted at 1315, 1285, 1212, 1159 cm^{-1} in the theoretical spectra, are assigned at 1339, 1274, 1248, 1152 cm^{-1} in the IR experimental spectrum, and were observed at 1342, 1278, 1252, 1156 cm^{-1} in the Raman experimental spectrum, respectively. These are in agreement with the literature [5,21]. The observed N-C-S in- plane bending vibration at 534, and 411 cm^{-1} in the theoretical spectrum appears at (527, and 411) cm^{-1}, and (525, 410) cm^{-1} in the IR and Raman experimental spectrum, respectively. This is in agreement with earlier reported by Chandra and Chowdhury [28].

Figure 6.8c shows the Raman spectrum of the 1.0 M MTZ saturated solution for the 200-3000 cm^{-1} region. The paramount bands observed in the 1.0 M solution of the MTZ are tabulated in Table 6.3. The Raman spectrum is in an agreement with the normal Raman spectrum of the 2-TU solid.

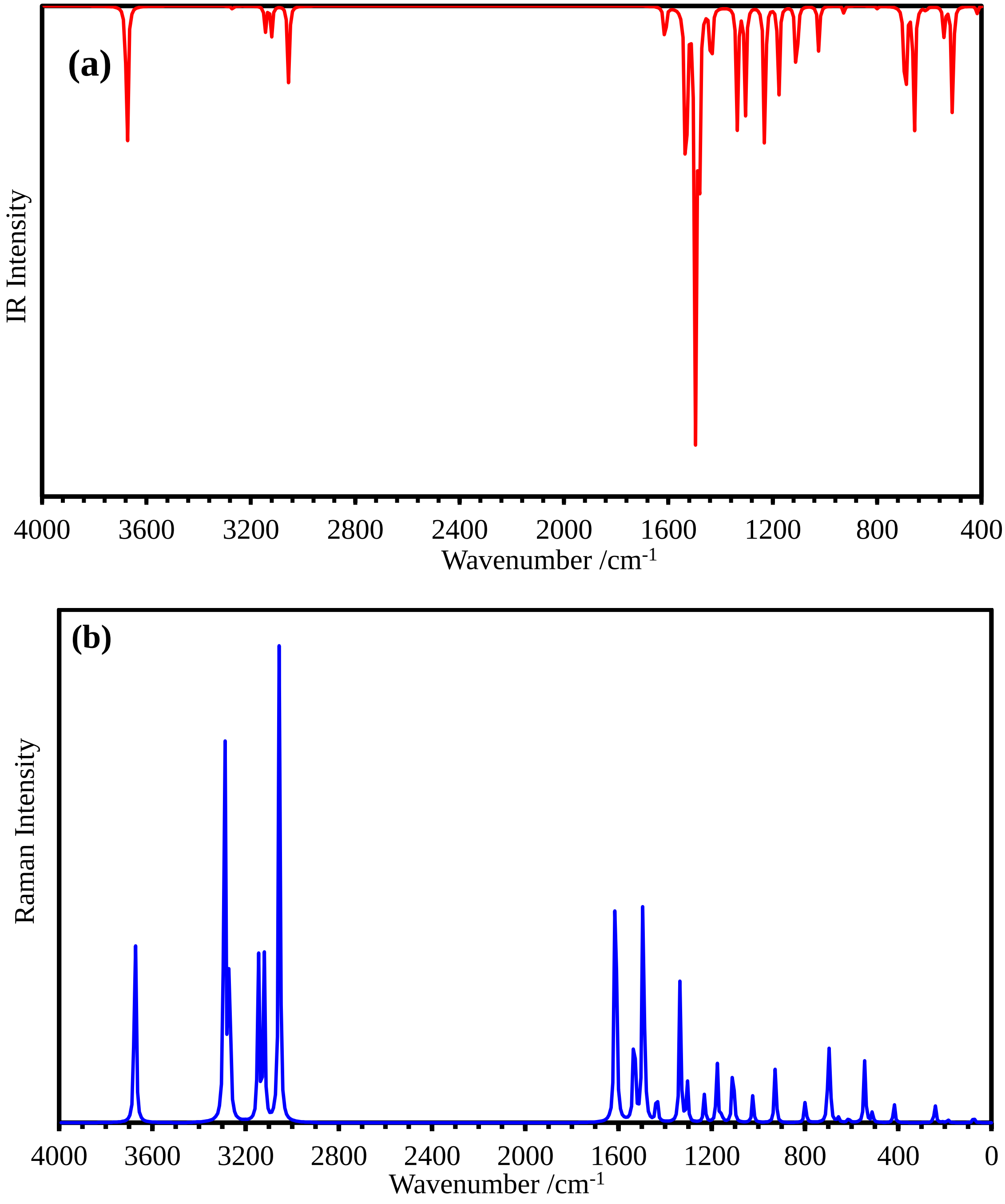

Figure 6.7: Theoretical (a) FT-IR spectrum and (b) Raman spectrum of MTZ

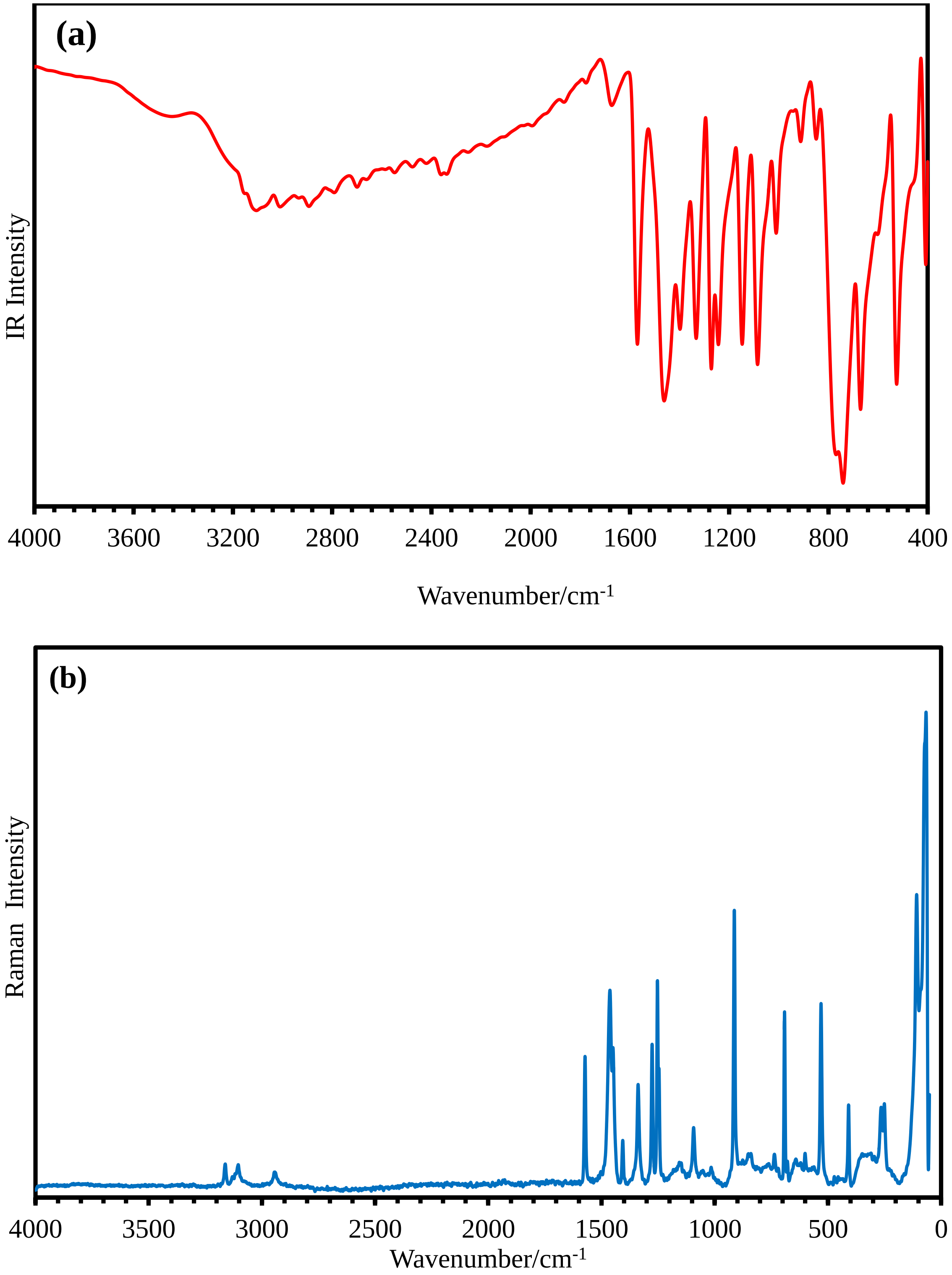
(a)
IR Intensity
4000
3600
3200
2800
2400
2000
1600
1200
800
400
Wavenumber/cm^{-1}
(b)
Raman Intensity
4000
3500
3000
2500
2000
1500
1000
500
0
Wavenumber/cm^{-1}

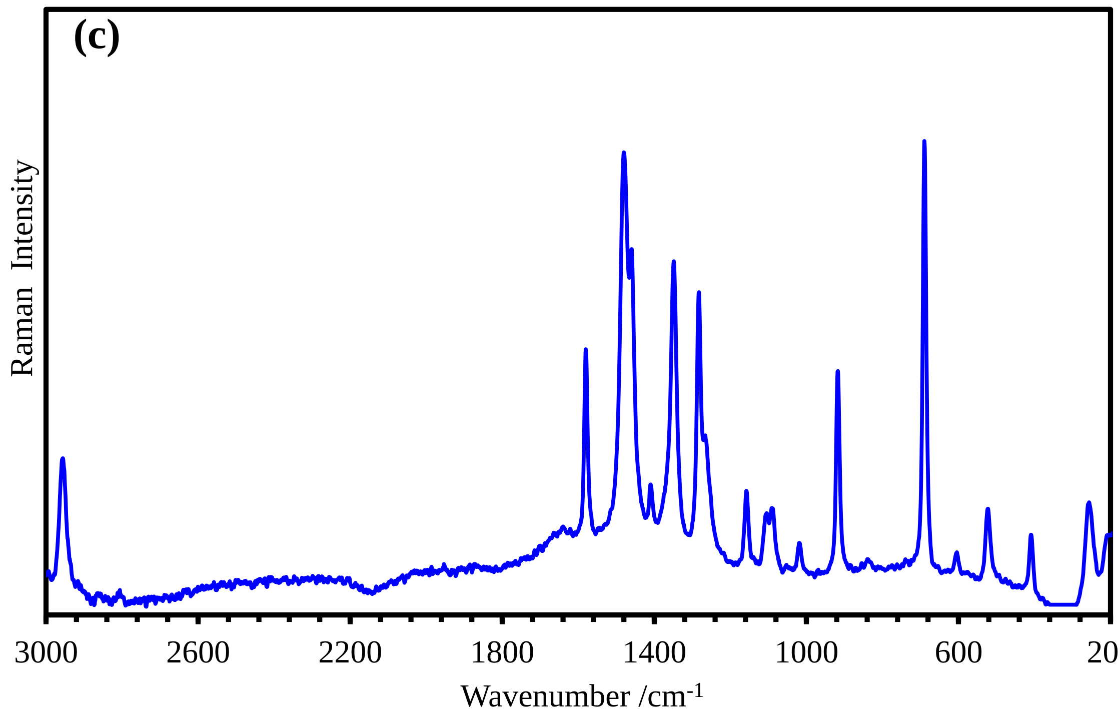

Figure 6.8: (a) Experimental IR spectrum, (b) Raman spectrum of MTZ, and (c) Raman spectrum of 1.0M saturated solution of MTZ

Table 6.3: IR and Raman Experimental and calculated vibrational frequencies (cm^{-1}) of the MTZ using DFT methods.

Calculated (Calc)			Observed (Obs)					
Scaled Freq.	**IR Int.**	**Raman Act.**	**IR**	**Raman**	**Solution**	**SERS**		**Assignment**
						Ag	**Au**	
3531	73.02	80.12						100% ν (N3-H)
3162	0.17	147.43	315 w	3161w	3166 m			97% ν (C7-H)
3142	1.63	60.82	310 w	3105w	3106 vw			98% ν (C6-H)
3022	10.80	50.79	301 w					96% ν (C5-H11)
2999	12.50	49.40						100% ν (C5-H12)
2936	32.91	145.60	2949 vw	2950 m	2960 m	2946 m	2946 m	96% ν (C5-H13)
1588	19.31	74.13	1578 vs	1579 s	1580 m	1571 vw	1571 vw	63% ν (C6=C7), 10%δ (N3-H) bend
1509	108. 5	26.28		1538 vw		1523 m	1522 m	24% ν (N2-C4), 15% ν (C-C) , 38%δ (H11-C-H12) bend
1473	172. 6	40.75						23% ν (S-C4), 14% ν (C4-N) bend, 10%δ (N3-H) bend,

1466	13.57	9.99		1479 vw	1480 vs			72% δ CH_{Me} scissoring
1459	69.16	1.95	1462 vs	1463 vs	1460 vw	1455 m	1456 m	23% ν (S-C4), 14% ν (N3-C4), 12%δ (C-H)bend,
1415	34.51	7.33	1403 m	1410 m	1410 vw	1408 w	1406 w	14% ν (N2-C4), 14% ν (N3-C6),13% ν (S-C4), 30%δ (C- H) bend
1315	51.11	27.72	1339 vs	1342 s	1345 s	1363 vs	1367 vs	32% ν (N2-C4), 11%δ ring bend, 19% δ (C6-N3-H) bend
1285	45.11	7.71	1274 s	1278 m	1281 m	1318 s	1320 s	15% ν (N2-C5), 19%δ N3-H(C6-H) bend, 14% δ ring breathing
1212	60.77	5.70	1248 m	1252 vs	1255 vw	1279 vw	1281 vw	51% ν (N3-C4), 18%δ N3-H(C6-H) bend, 13%δ (C7-H)bend
1159	38.79	11.74	1152 vs	1156 vw	1153 m	1143 m	1146 m	16% ν (N3-C6),16% ν (S-C4), 15% δ (H11-C-H12) rock,
1089	22.75	8.12	1086 vw	1091 m	1088 vw	1092m	1092 m	46% ν (N3-C6), 14%δ (N3-H) bend, 21%δ (C7-H)bend
1013	18.80	4.89	1014 s	1016 m	1017 vw	1030 w	1031 w	15% ring CH bend, 13% δ CH_{Me} bend, 41%δ ring bend,
913	2.99	9.91	913 m	915 vs	916 s	935 m	934 m	12% ν (N2-C4),12% δ N3-H(C6-H) bend , 62%δ ring bend
806	1.13	3.83	818 w	810 vw		836 vw	834 vw	89%γ (H-C6-C7-H) twist
685	5.18	15.17	673 vs	679 vw	684 vs	695 vw	694 vw	25% δ (C7-N2-C5) bend, 15% δ (C4-N2-C5) bend
650	60.37	0.92		643 vw		670 vw	671 vw	47% ring CH bend, 39%γ (N3-C4-N2)
603	2.10	0.82	599 vw	600 vw	602 vw	616 w	619 w	78 %γCN ring bend.
534	13.08	10.72	527 vs	525 m	522 w	500 vs	501 m	53% δ (S-C4-N3) bend, 25% δ (S-C4-N2),
503	46.31	1.66		493 vw		543 vw	545 vw	84% γ (N3- C6-C7)
411	3.33	2.99	411s	410 s	410 m	430 m	432 m	71 %δ (S-C4-N)
238	3.63	3.13		264 m	260 m	281 w	280 w	85% γ (C4-S) wag
207	3.39	0.15		208 vw	209 vw			76% γ ring

6.3.2.3. DFT calculation of MTZ-silver and gold complex

The silver and gold complex of the MTZ conformers were optimized using the DFT method with B3LYP/ GEN basis set. In both cases, the results of the theoretical calculation show the stable structures when the Ag and Au nanoparticles are close and interact with the S, and N atoms, as shown in Figure 6.9.

The agreement between the solid, SERS of MTZ, and the vibrational frequencies of MTZ-Ag, and MTZ-Au complex are calculated through DFT method and are listed in Table 3. The band at 1315 cm^{-1} is shifted to a higher frequency in the calculated values. In the observed experimental case, the band is shifted from 1342 cm^{-1} to 1363 cm^{-1}, and 1367 cm^{-1}, in the MTZ-Ag, and MTZ-Au, respectively. The band at 1285 cm^{-1} is moved to higher wavenumber in the theoretical and is in a very good agreement with the experimental data, which is shifted from 1278 cm^{-1} to 1318 cm^{-1} in the SERS-Ag spectrum, and to 1320 cm^{-1} in the SERS-Au spectrum. The other agreements between the experimental data and the theoretical data are summarized in Table 6.4.

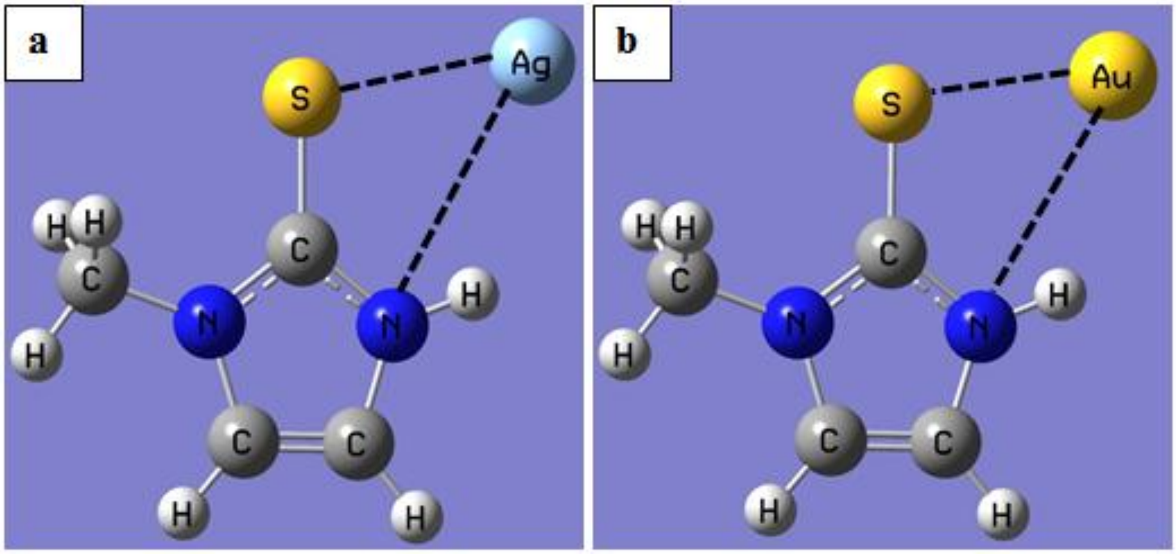

Figure 6.9: The optimized structures of the, (a) MTZ-silver, and (b) MTZ-gold complex

Table 6.4: Experimental Raman shift compared with the calculated Raman shift of MTZ complex

Calculated (Calc)			Observed (Obs)		
MTZ	**MTZ-Ag**	**MTZ-Au**	**Solid**	**SERS Ag**	**SERS Au**
3531	3366	3321			
3162	3166	3167	3161w		
3142	3147	3147	3105w		
3022	3021	3023			
2999	2995	2995			
2936	2932	2932	2950w	2946 m	2946 m
1588	1581	1579	1579s	1571vw	1571 vw
1509	1496	1497	1538 vw	1523 s	1522 s
1473	1467	1471			
1466	1457	1461	1479 vw		
1459	1452	1453	1463 vs	1455 m	1456 m
1415	1411	1412	1410 m	1408 w	1406 w
1315	1328	1328	1342 s	1363 vs	1367 vs
1285	1309	1311	1278 vs	1318 s	1320 s
1212	1237	1239	1252 vs	1279 vw	1281 vw
1159	1150	1151	1156 vw	1143 m	1146 m
1089	1091	1090	1091 m	1092 m	1092 m
1013	1022	1023	1016 m	1030 w	1032 w
913	923	925	915 vs	935 m	934 m
806	818	820	810 vw	836 vw	834 vw
685	699	704	679 vw	695 vw	694 vw
650	667	669	643 vw	670 vw	671 vw
603	623	621	600 m	616 vw	619 vw
534	520	517	525 vs	500 s	501 s
503	569	576	493 vw	543 vw	545 vw
411	421	423	410 s	430 m	432 m
238	251	257	264 m	281 w	280 w
207	220	221	208 vw		

6.3.3. SERS results of MTZ on different nanomaterials

6.3.3.1. SERS spectra of MTZ with Au/NPs and GO/Au composites.

The Figure 6.10a shows the normal Raman spectrum, SERS spectra of the Au/NPs and GO/Au nanocomposites with the 1×0^{-5} M of MTZ. In the GO/AuNPs case, a cleaner Raman spectrum was obtained in a range 300-1800 cm^{-1}, to avoid contaminants are adsorbed on the graphene surface from the atmosphere. On the contrary, for the same concentration of MTZ, the Raman bands with AuNPs much stronger and detectable. The prominent characteristic peaks observed in the SERS spectrum of 1×0^{-5} M MTZ with AuNPs are listed in Table 6.3. A comparison between SERS spectrum and normal Raman spectrum of the MTZ shows that the medium band at 1342 cm^{-1} in the normal Raman spectrum is shifted to a higher wavelength, at 1367 cm^{-1} in the SERS spectrum. This band shows high enhancement factor, which is attributed to the N2-C4 stretching with contributions from ring binding, and C6-N3-H bend (in-plane). The peak at 1278 cm^{-1} in the normal Raman spectrum is observed at 1320 cm^{-1} in the SERS spectrum with small enhancement. This band assigned to the N2-C5 stretching, N3-H (C6-H) bend, and ring breathing. The modes at 1156 and 1091 cm^{-1} in normal Raman Spectrum are shifted to 1146, and 1092 cm^{-1} in the SERS spectrum. These bands are contributed to S-C4, C-N stretching, and N-C-N bend. In addition, the low-intensity band at 1016 cm^{-1} in the normal Raman spectrum assigned to ring CH bend, CH_{Me} bend (in the plane) is shifted to a higher wavelength of 1031 cm^{-1} in SERS spectrum. This band is enhanced by a higher intensity in SERS spectrum. The very weak signal at 600 cm^{-1} in the normal Raman spectrum is shifted to a higher wavelength at 619 cm^{-1} in the SERS spectrum.

This band attributed to the CN ring bend out of the plane, which shows a significant enhancement in SERS spectrum.

6.3.3.2. SERS spectra of MTZ with Ag/NPs

The Figure 6.10b shows the normal Raman spectrum and SERS spectra of the Ag/NPs with the 1×0^{-5} M MTZ. The prominent characteristic peaks observed in the SERS spectrum of 1×0^{-5} M MTZ with AgNPs are listed in Table 6.3. The band at 1342 cm^{-1} in the normal Raman spectrum shifted to 1363 cm^{-1} in the SERS spectrum. This band shows a significant enhancement in SERS spectrum. The bands at 1278, 1156, 1091, 1016, and 600 cm^{-1} in the normal Raman spectrum are shifted to 1318, 1143, 1092, 1030, and 616 cm^{-1}, respectively in the SERS spectrum. These bands are enhanced to higher intensities in SERS spectrum than normal Raman spectrum. The band at 534 cm^{-1} in the normal Raman spectrum is observed at 500 cm^{-1} in the SERS spectrum. This band is attributed to SCN bending and shows a significant enhancement in SERS spectrum.

The enhancement of the intensities of the N-C, S-C, and N-H stretching indicated that the MTZ ring directly interacts with metal nanoparticles through the unpaired electron on the N and S atom. According to the SERS electromagnetic enhancement mechanism [29, 30], and the metal surface selection rules [31]. The groups are very close to the metal surface with a tilted orientation should be more enhanced than the groups are parallel to the metal surface. This is in agreement with our SERS theoretical calculation conducted in this study. These surface selection rules should apply to adsorption on metal nanoparticles with a diameter more than 20Å. However, less enhancement for the smaller particles is expected [32].

From the SERS results, it can be suggested that the SERS of AgNPs was found to yield stronger signals than the AuNPs at the same concentration of an analyte, and the enhancement factors of silver are better than those of gold.

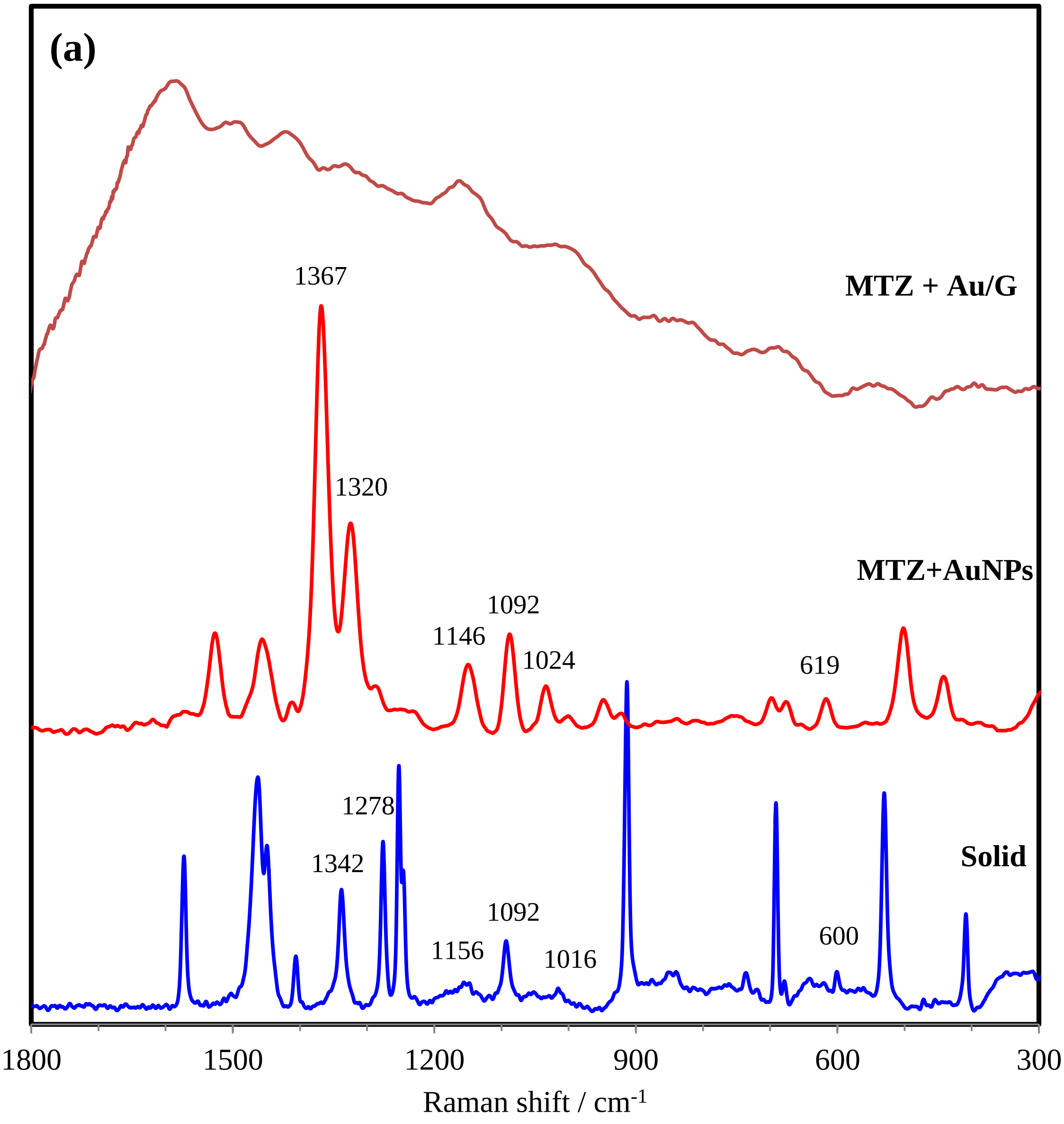

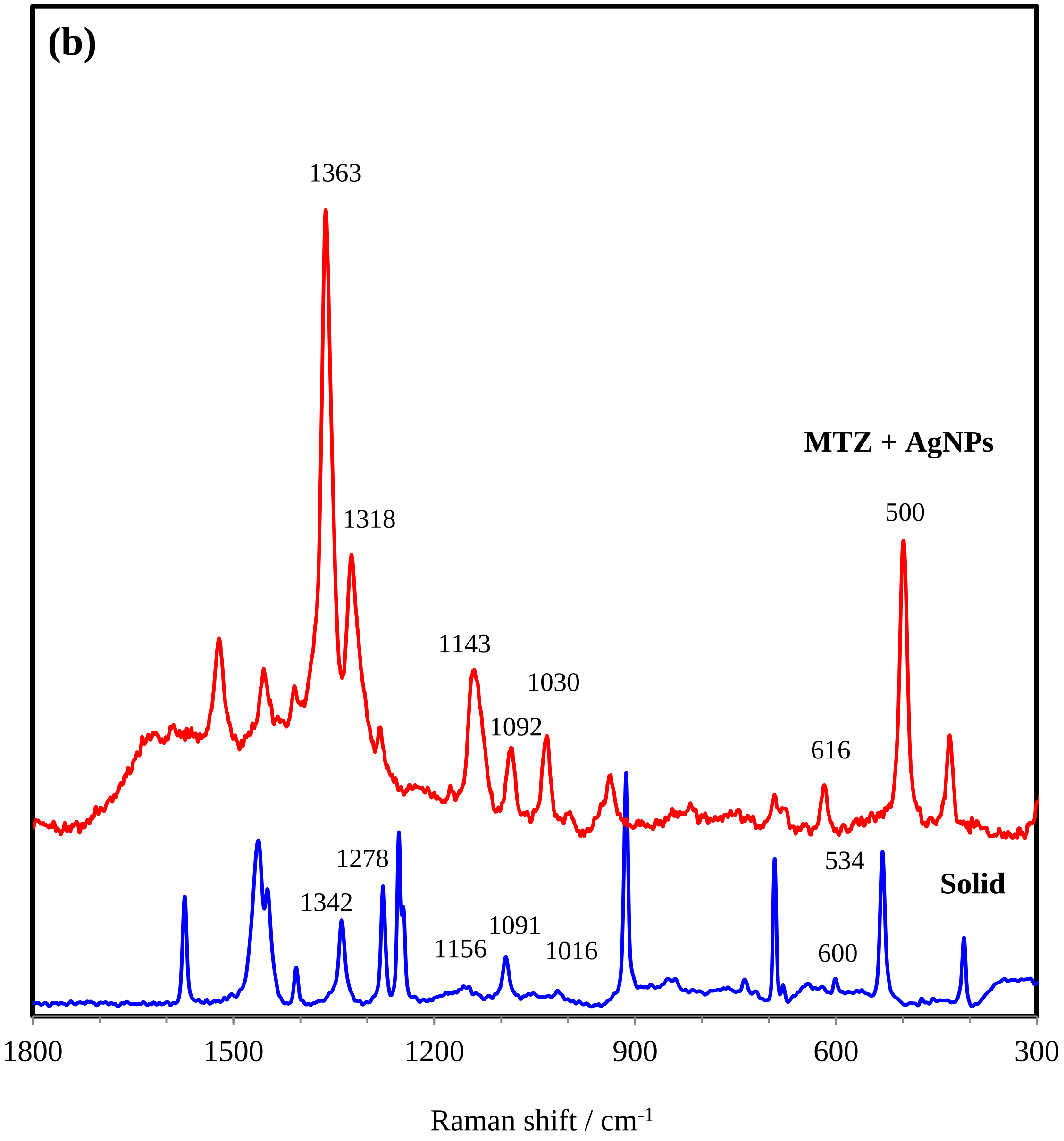

Figure 6.10: (a) SERS spectra of 1×0^{-5} M MTZ with AuNPs, and GO/NPs, (b) SERS spectra of 1×0^{-5} M MTZ with AgNPs. Laser ʎ; 633nm, acquisition time; 30 sec, and objective; 10x.

6.3.3.3. SERS enhancement factor of MTZ

The SERS enhancement factors for the vibrations of MTZ (1×10^{-3} M) on silver and gold colloids to the corresponding band obtained from 1.0 M saturated solution were calculated using the following equation.

$$\mathrm{EFs} = (\delta_{\mathrm{SERS}} \times C_{\mathrm{normal}}) / (\delta_{\mathrm{normal}} \times C_{\mathrm{SERS}})$$

Where δ and C are the Raman mode intensity and sample concentration, respectively. The EFs for the SERS peaks of MTZ on silver and gold colloids are given in Table 6.5. The EFs is not the same for the different MTZ modes, the maximum enhancement was observed at 1342 cm^{-1}.

Table 6.5: SERS enhancement factor of MTZ on gold and silver colloids

Substrate	**Normal Raman spectra (cm^{-1})**	**SERS spectra (cm^{-1})**	**EFs**
Gold colloid	1342	1367	1.0×10^{4}
	1278	1320	1.7×10^{3}
	1156	1146	3.8×10^{3}
	1092	1092	1.8×10^{3}
	1016	1031	2.3×10^{3}
	600	619	1.2×10^{3}
Silver colloid	1342	1363	9.6×10^{4}
	1278	1318	2.2×10^{4}
	1156	1143	4.4×10^{4}
	1092	1092	2.1×10^{4}
	1016	1030	3.4×10^{4}
	600	616	1.4×10^{4}
	534	500	1.8×10^{4}

6.3.3.4. SERS spectra of methimazole at different concentrations

The SERS spectra of MTZ aqueous solution with gold as a substrate at different concentrations are given in Figure 6.11a. The intensities of the SERS spectra increase with an increase in the concentration of MTZ. This suggests that the SERS intensities are proportional to the molecular quantity of MTZ. The highest enhanced band at 1367 cm^{-1} in SERS spectra was selected for creating a qualitative analysis of MTZ. Within the dynamic range, the lowest concentration measured in the SERS analysis of the MTZ solution was 10^{-9} M. Figure 6.11b shows the SERS intensity of the vibration frequency at 1367 cm^{-1} versus the minus logarithm concentration of the MTZ solution. The linear SERS response from 10^{-3} M to 10^{-9} M of MTZ was obtained with a linear coefficient (R^2) of 0.9974.

On the other hand, the Figure 6.12a shows the concentrations dependent SERS spectra of MTZ obtained by using silver nanoparticles. The SERS intensity increases proportionally with increasing the concentrations of the MTZ solution in the range from 10^{-7}M to 10^{-12}M. The highest enhanced band at 1363 cm^{-1} in SERS spectra was selected for creating a quantitative analysis of MTZ. Figure 6.12b shows the calibration curve of MTZ solution with AgNPs. The linear SERS response from 10^{-7} M to 10^{-12} M of MTZ was obtained with a good linear coefficient (R^2) of 0.9989.

The linear equations and correlation coefficients of MTZ with gold and silver substrates are listed in Table 6.6. A good linear correlation between the Raman peak intensities and MTZ concentrations were noted with wide linear working range (LWR) for MTZ with both substrates. However, AgNPs showed lower detection limits.

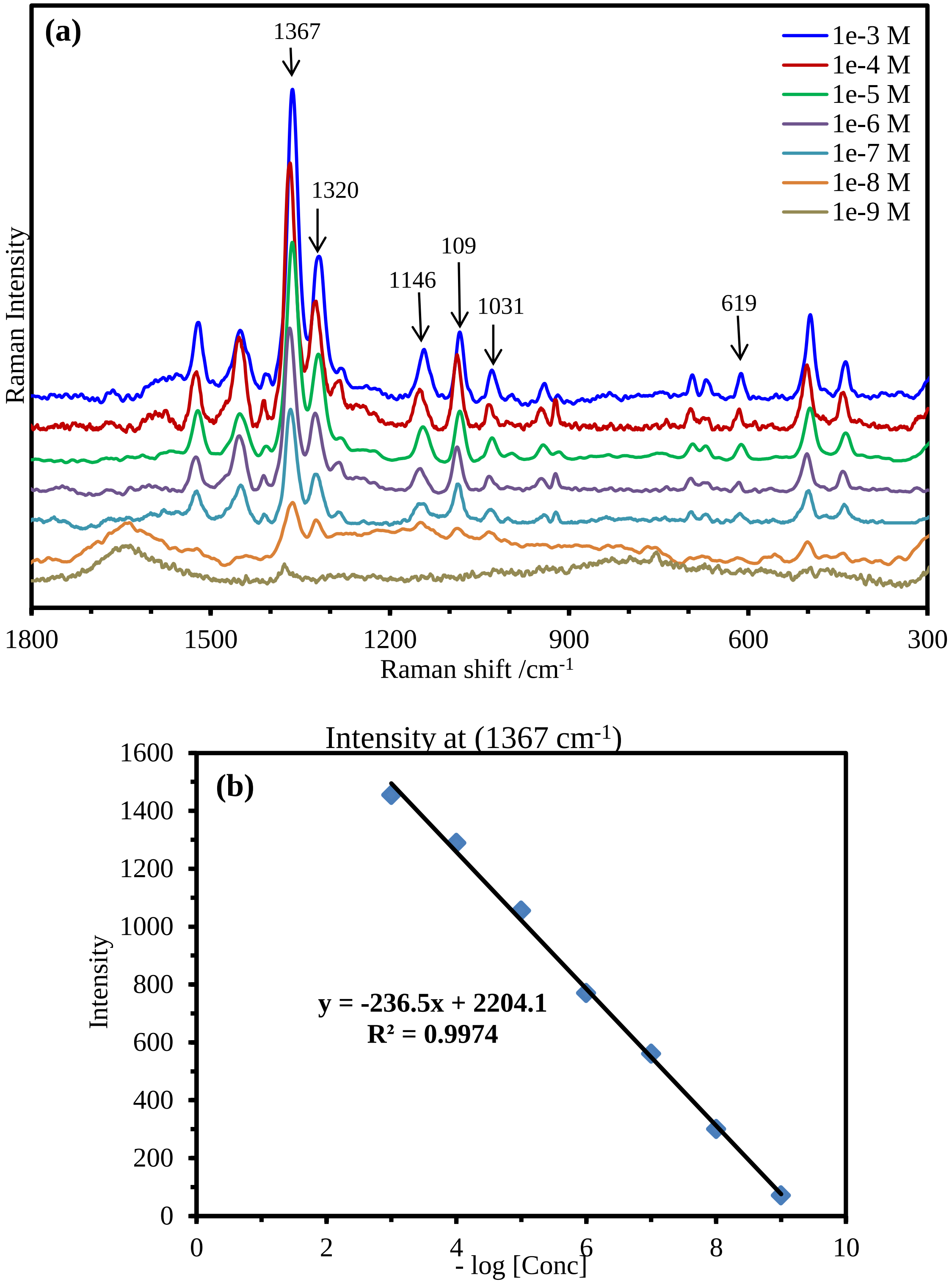

Figure 6.11: (a) SERS spectra of MTZ with different concentration using AuNPs, (b) calibration curve of the band at 1367 cm^{-1} using AuNPs. Laser ʎ=633nm, acquisition time; 30 sec, and objective; 10x.

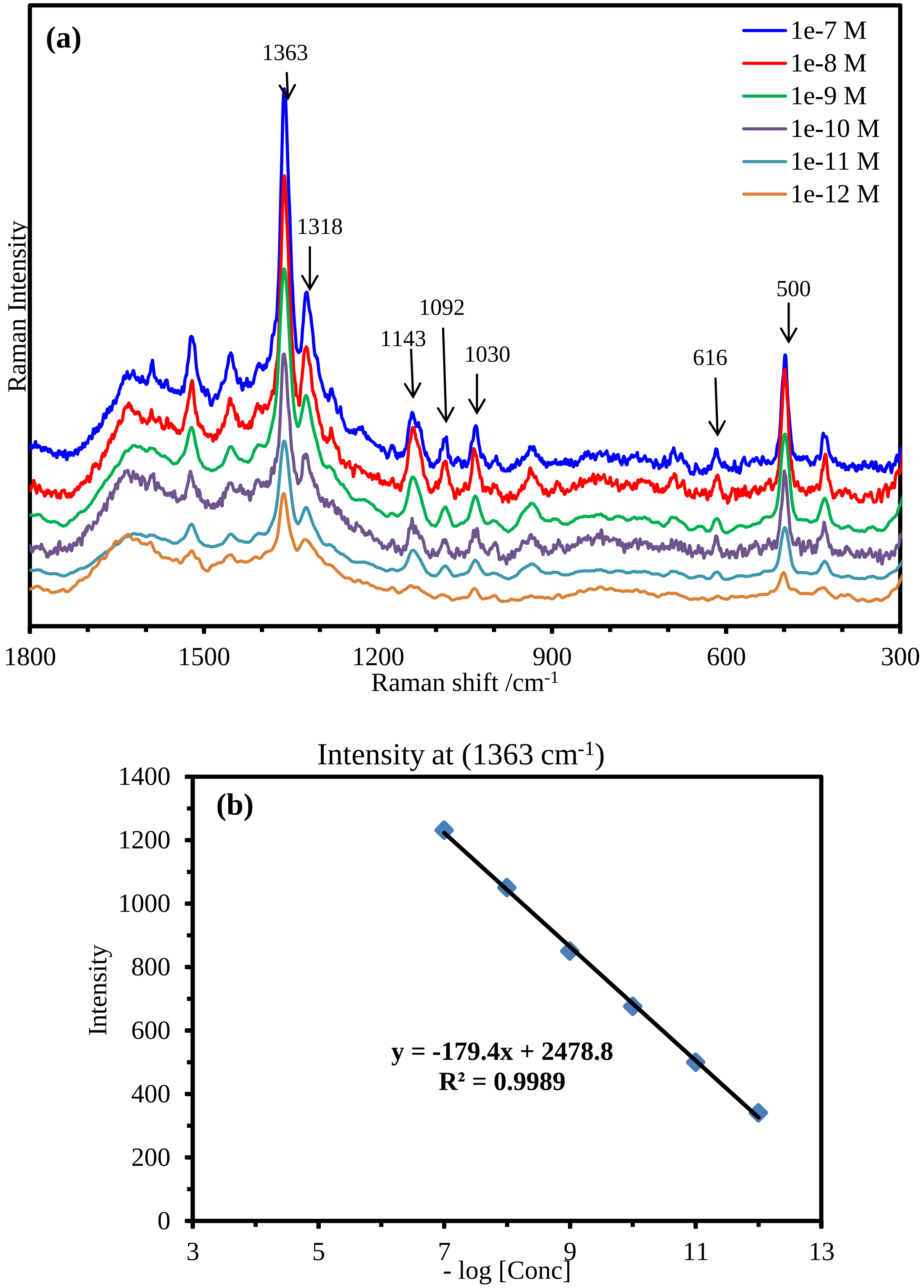

Figure 6.12: (a) SERS spectra of MTZ with different concentration using AgNPs, (b) calibration curve of the band at 1363 cm^{-1}, using AgNPs. Laser ʎ=633nm, acquisition time; 30 sec, and objective; 10x.

Table 6.6: Regression equation between Raman intensities and concentrations of MTZ and their correlation coefficients.

NPs Type	**Raman Peaks**	**Regression Equation**	**R^2**	**Dynamic range (M)**	**SD**	**LOD**
Gold NPs	1367 cm^{-1}	y = - 236.5x + 2204.1	0.9974	$10^{-3} – 10^{-9}$	2.24	$6.08×10^{-10}$
	1320 cm^{-1}	y = - 104.6x + 1018.5	0.9898	$10^{-3} – 10^{-8}$	1.81	$4.24×10^{-10}$
	1146 cm^{-1}	y = -36.486x + 342.5	0.991	$10^{-3} – 10^{-8}$	1.06	$1.01×10^{-9}$
	1092 cm^{-1}	y = - 29.71x + 399.55	0.9713	$10^{-3} – 10^{-8}$	1.13	$1.62×10^{-9}$
Silver NPs	1363 cm^{-1}	y = - 179.4x + 2478.8	0.9989	$10^{-7} – 10^{-12}$	1.58	$5.01×10^{-14}$
	1318 cm^{-1}	y = - 74x + 1093.3	0.9964	$10^{-7} – 10^{-12}$	2.74	$3.4×10^{-14}$
	500 cm^{-1}	y = - 74.8x + 1027	0.9812	$10^{-8} – 10^{-12}$	1.82	$3.8×10^{-13}$

6.4. CONCLUSION

The silver and gold nanoparticles as colloids were prepared by reduction methods with about 60 nm and 10 nm particle size, respectively. The SERS method was exploited to record the vibrational frequencies of MTZ adsorbed on Au and Ag nanoparticles. The optimized conformation and vibrational assignments of MTZ have been carried out using the DFT calculation with B3LYP/6-311++G (d, p) basis set. The vibration assignments and the wavenumber of vibration frequency bands in the theoretical spectra were in agreement with those of the experimental spectra. Most of the bands related to N atom and S atom were apparently enhanced and shifted. These results confirm that methimazole molecules were adsorbed on the silver and gold substrates through probably the lone pair on N and S atoms. The correlation between the methimazole concentration and the SERS signal was linear and of good detection limits. The Ag/NPs showed better linearity and detection limit compared with the Au/NPs.

6.5. REFERENCES

[1] Weetman, A. P.; McGregor, A. M. Clin. Endocrinol.1984, 21, 163-172.

[2] Georg B, Dankwart R. Georg K et al. Clinical Endocrinology. 1998, 49, 451.

[3] Subramanian, R. Lakshminarayanan, V. Corros. Sci. 2002, 44, 535.

[4] J.Y. Sun, C.Y. Zheng, X.L. Xiao…et al. Electroanalysis 2005. 17, 1675.

[5] Xue Liao, Yanhua Chen, Meihong Qin, …et al.Talanta. 2013, 117, 203.

[6] D. L. Poster, M. M. Schantz…et al.. Anal. Bioanalytical Chem. 2006, 4, 859.

[7] Ma P,Liang F, SunY, Jin Y …etal. Microchim Acta. 2013, 180, 1173.

[8] H. C. Camargo, Leslie Au, M. Rycenga…et al. Chem Phys Lett. 2010, 484, 304.

[9] Huanping Yang, Hailong Hu, Zhenhua Ni et al. CARBON. 2013, 62, 422.

[10] Shuang Lin, Wu-Li-Ji Hasi, Xiang Lin, …etal. Anal. Methods. 2015,7, 5289.

[11] Nandita Biswas, Sudhir Kapoor, …et al. Chem. Phys. Lett. 2016, 444, 338.

[12] Rui Zhang, Ying Wen, Na Wang…et al. J. Phys. Chem. B. 2010, 114, 2450.

[13] Lijia Liang, D. Huang, H. Wang …et al. Anal. Chem. 2015, 87 (4), 2504.

[14] Zhenzhen Han, Honglin Liu, Bin Wang…etal. Anal. Chem., 2015, 87 (9), 4821.

[15] Pinyi Ma, F. Liang, Q.Yang…et al. Microchimica Acta. 2014, 181, 975.

[16] Weigao Xua, Xi Linga, Jiaqi Xiaoa et al. PNAS. 2012, 109, 9281.

[17] Siyavash K. Movahed, Mahsa Fakharian …etal.. RSC Adv. 2014, 4, 5243.

[18] An-Wu Xu, Han-Qing Yu, Wen-Gang Qu. J. Mater. Chem. 2012, 22, 20986.

[19] Min Song, LuluYu, and YiminWu. Journal of Nanomaterials. 2012, 1.

[20] Henan Zhang, Deon Hines and Daniel L. Akins. Dalton Trans. 2014, 43, 2670.

[21] Xiaochen Dong, Wei Huang, Peng Chen. Nanoscale Res Lett. 2011, 6, 60.

[22] H. Kang, A. Kulkarni, …et al. Carbon. 2009, 47, 1520.

[23] N. A. Kumar, S. Gambarelli…et al. J. Mater. Chem. A. 2013, 1, 2789.

[24] S. Bhandari, M. Deepa et al. Nanoscale Research Letters. 2011, 6, 424.

[25] D. Zhan, Z. Ni, W. Chen et al. Carbon. 2011, 49, 1362.

[26] Huanping Yang, Weiwei Zhou et al. Journal of Nanotechnology. 2012, 8.

[27] A. A. Al-Saadi, J. Laane. Journal of Molecular Structure. 2007, 830, 46.

[28] S.Chandra, J. Chowdhury…et al. J. Phys. Chem. A. 2012, 116, 10934.

[29] A. D. McFarland, M. A. Young…et al. J. Phys. Chem. B. 2005, 109, 11279.

[30] N. Félidj, J. Aubard, G. Lévi, J. R. Krenn et al. Phys. Rev. B. 2002, 65, 1.

[31] M. Moskovits and J. S. Suh. J. Phys. Chem.1984, 88, 5526.

[32] Robert G. Greenler, D.R. Snider…et al. Surface Science. 1982, 118, 415.

CHAPTER 7

Graphene Dendrimer-Stabilized Silver Nanoparticles for Detection of Methimazole using Surface-Enhanced Raman Scattering with Computational Assignment

7.1. INTRODUCTION

Raman spectroscopy is based on the inelastically scattered photons by molecules. The Raman scattering process is called Stokes scattering when it occurs from the ground vibrational state to higher energy excited vibrational state due to the energy absorption by the molecules. Scattering from the excited states to the ground state is called anti-Stokes scattering. The weak Raman signal hinders its applications in various fields. However, the advances in instrument technology, like surface-enhanced Raman scattering (SERS), have simplified the equipment and substantially reduced the problems [1].

In SERS, the targeted molecules adsorbed from aqueous solution onto nanoparticles that allow for the examination of charge transfer between analyte molecules and substrate metal surface as well as the orientation of the molecules [2]. Other substrates commonly used in SERS analysis are films which include metals on planar surfaces such as glass, quartz, and silicon wafers or nanoparticles embedded surfaces such as silica beads and polystyrene [3, 4]. Films are of high purity and can also be tuned somewhat to appropriate localized surface plasmon resonances by altering parameters such as film thickness and deposition rate, with most thicknesses of metal being between 5-60 nm [5].

SERS substrate of colloidal silver or gold nanoparticles can consistently yield large signal enhancement [6]. There are two mechanisms explaining the enhancements; electromagnetic and chemical enhancement. The first accounts for the enhancements related to the incident electric field. The second accounts for the enhancements related to the polarizability of the molecule and are specific to the chemical interaction between the adsorbed analyte and the metallic surface. Yet a deep understanding of the mechanisms requires more experiments.

Screening the literature, several analytical procedures have been reported for the determination of methimazole (1-methyl-2-mercapto-imidazole, tapazole) termed an antihormone and is widely used in medicine to treat hyperthyroidism. These methods include molecularly imprinted biomimetic sensor [7], fluorescence [8] thin layer chromatography [9], coulometry [10], conductometry [11], and high-performance liquid chromatography with ultraviolet detection [12]. SERS has many advantages for use in drug analysis over other techniques. SERS has the ability to not only improve the sensitivity for those applications already used by Raman while also expanding the potential uses of the method for those that would not be possible without the added sensitivity and limits of detection. SERS has the potential to impact the areas of analytical chemistry, biochemistry, forensics, environmental analysis, and trace analysis. Recently, SERS has been reported as a promising technique for quantitative and qualitative identifications of various targets [13]. Due to its ultra-sensitivity, SERS was used to detect trace organic and inorganic analytes in different media. For example, some organophosphorus compounds, such as methylparathiol and dimethoate, that exist in pesticides were identified at the nanogram level [14]. Due to the fact that water molecules scatter weakly in Raman experiments made SERS technique an attractive choice to conduct useful characterizations of samples [15, 16, 17].

However, SERS does have certain limitations as an analytical technique, many of which are related to the substrate fabrication and properties. SERS requires metal colloid-like silver can possess hotspot within the nanoparticles that achieve extremely high enhancement [18]. However, the agglomeration of the nanoparticles diminishes the enhancement in SERS since it is required to have more nanoparticles to hook the targeted molecules. Using support to load the silver nanoparticles may allow control the agglomeration.

Dendrimers are a new class of polymeric belongings, nanoscale compounds, homogeneous, and a tree like structure. The unique properties of dendrimers make them useful in health industry, pharmaceutical, and materials applications [19]. Dendrimers considered to be one of the most appropriate encapsulating agents for the stabilization of metal NPs due to their large size and the presence of unique three dimensional architectures of the dendrons that prevent leaching of the NPs during the course of the reaction [20]. The (poly) amidoamine (PAMAM) dendrimers are considered the favored for pharmaceutical application due to the regular structure, a large size and chemical versatility [21]. Here in this work, we proposed the use of graphene as a support and the use of a dendrimer to have more nanoparticles linked to its branches. Therefore, we have synthesized graphene linked with dendrimers-stabilized silver nanoparticles to obtain Ag/G dendrimer. The prepared material was evaluated as SERS substrate for methimazole detection.

7.2. EXPRIMENTAL

7.2.1. Chemicals and Materials

Sodium borohydride ($NaBH_4$), product number 63390, was purchased from allied signal. Ethylenediamine (≥ 99.5%), product number 03550, Methyl acrylate (99%), the CAS number 76778, and Thionyl chloride ($SOCl_2$, ≥ 99%), product number 230464**,** were purchased from Sigma-Aldrich.

7.2.2. Synthesis of graphene dendrimer silver composite

The scheme 7.1 shows the preparation steps of dendrimer functionalization with silver. About 0.2 g of the prepared GO compound was dispersed in 20 ml of $SOCl_2$ by sonication in an ultrasound bath for 30 min and stirred for 12 h at 60 ^{o}C and the mixture was filtered. The obtained material was dried overnight at room temperature. Next, 10 ml of ethylenediamine was added to the solid product, the reaction mixture was sonicated for 3 h at 60 ^{o}C, and stirred for another 12 h at room temperature. The solid product was collected by centrifugation at 10000 rpm/min for 10 min and dried overnight at room temperature.

The last solid product was suspended in 10 ml methanol was added dropwise into a 25 ml of 1:4 methyl acrylate - methanol solution under stirring. The reaction mixture was treated in an ultrasonic bath at 60 ^{o}C for 2 hours and stirred for another 12 h at room temperature. The solid product was collected by centrifugation at 10000 rpm/min for 10 min and dried overnight at room temperature. Afterward, the obtained material was immersed in 10 ml methanol, then a mixture of 10 ml of ethylenediamine – methanol in the ratio 1:1 was added at a rate 1 drop/sec to the solution. The solution was placed in an ultrasonic at 50 ^{o}C for 5 h and stirred for another 10 h at room temperature. The solid product was collected by centrifugation and dried overnight at room temperature. The steps were repeated for methyl acrylate and ethylenediamine until reach to GO-G3-PAMAM.

The solid of GO-G3-PAMAM was dispersed in 20 ml de-ionized water by sonication in an ultrasound bath for 10 min. Then, 10 ml of 0.2 M $AgNO_3$ was added dropwise with previously dispersed solid and the mixture was stirred for 1 hour. Then, 10 ml of a freshly prepared solution of $NaBH_4$ was added to the solution and the solution was kept under stirred for another 5 h. Finally, the mixture was filtered, and the obtained material was washed with deionized water for several times. The greenish yellow isolated solid was dried overnight at room temperature. The proposed mechanism of the stabilization of the AgNPs on the GO-G-PAMAM surface is shown in scheme 7.2.

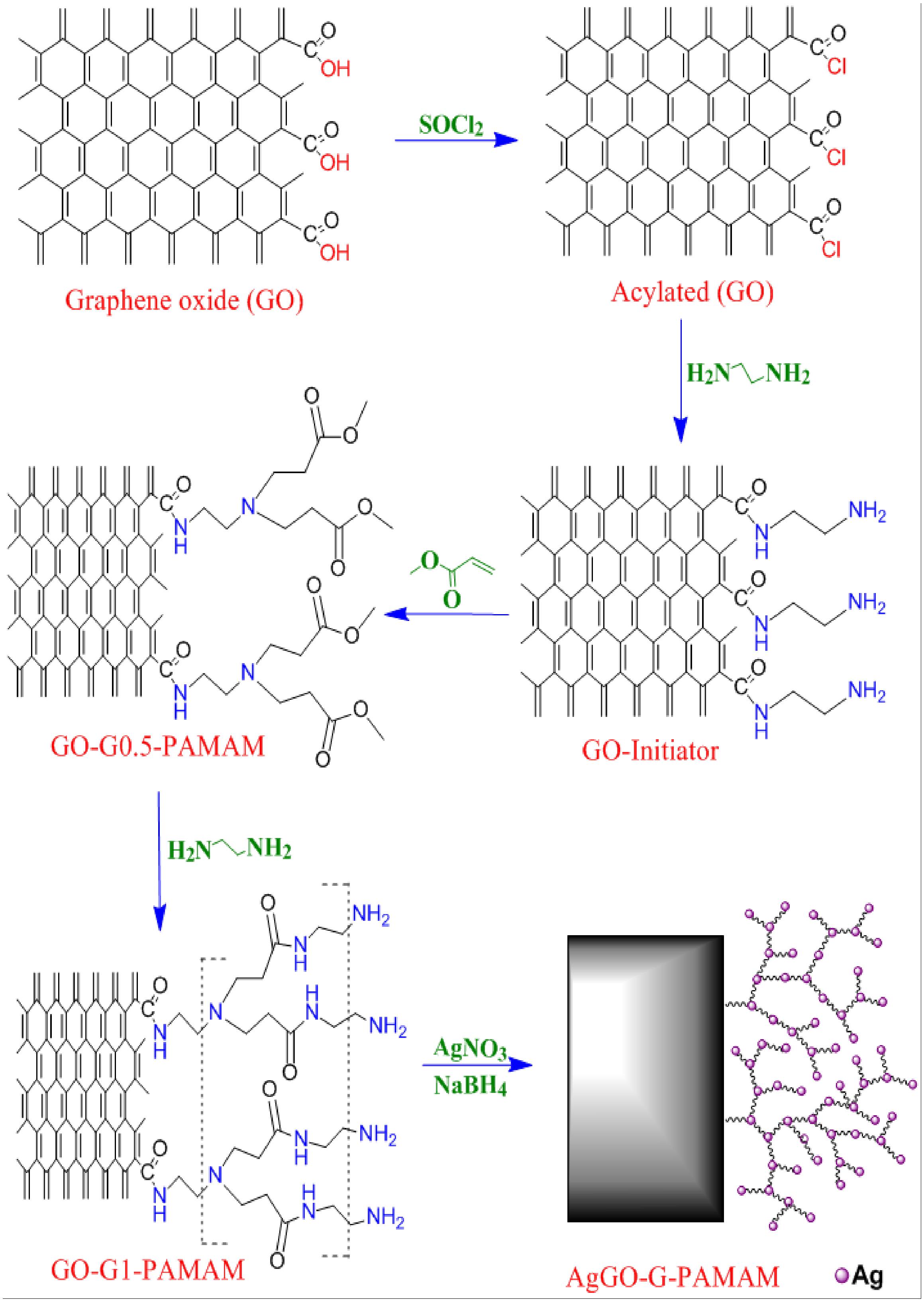

Scheme 7.1: Illustration explaining the synthesis steps of the Ag/G dendrimer.

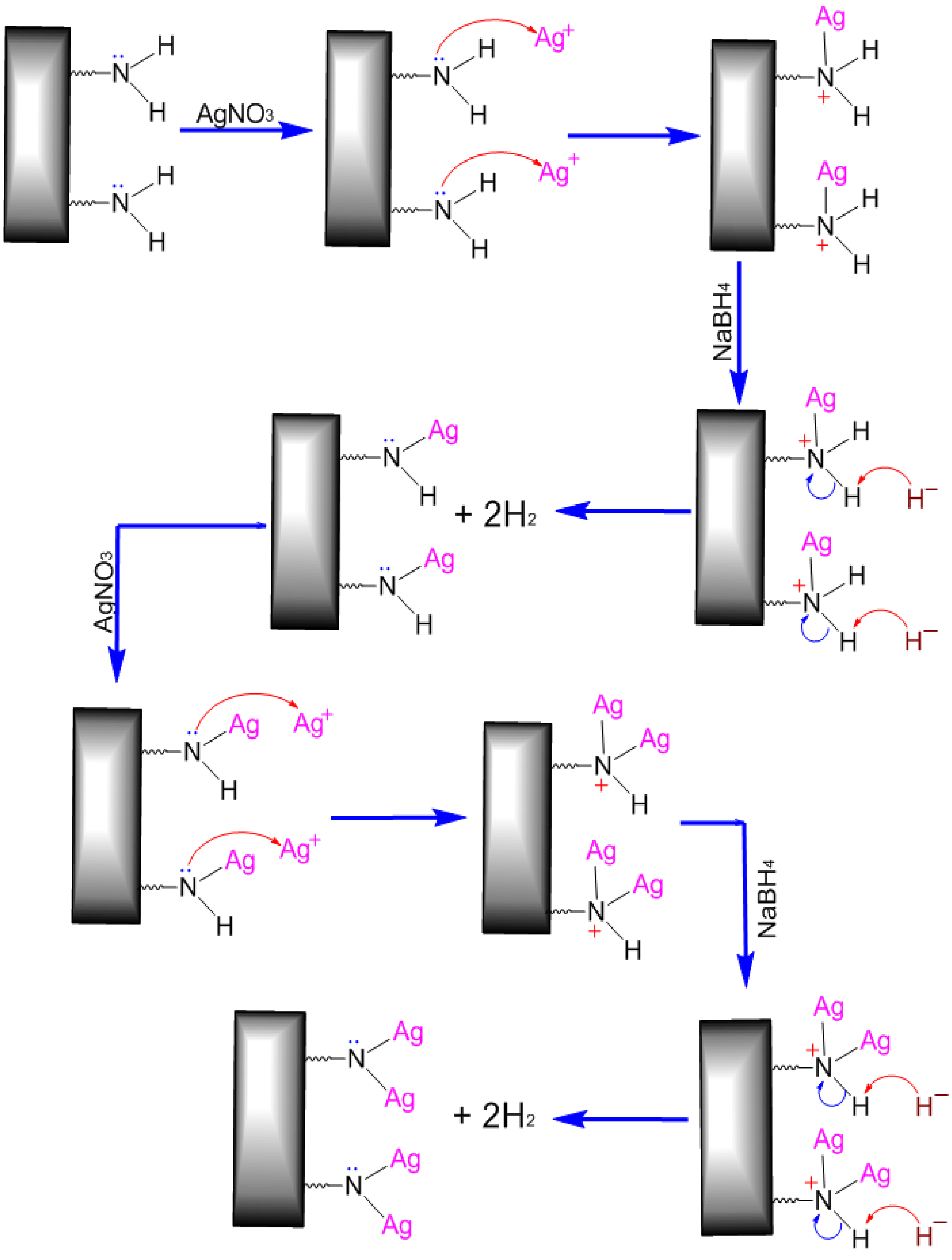

AgGO-PAMAM

Scheme 7.2: Proposed mechanism of the stabilization of the AgNPs on the GO-G-PAMAM for the preparation of Ag/G dendrimer.

7.3. RESULTS AND DISCUSSION

7.3.1. Structure analysis

The ultraviolet-visible spectra of G dendrimer and Ag/G dendrimer are shown in Figure 7.1. The maximum absorption band at 300 nm is attributed to the n-π* electronic transitions of the dendrimer. Moreover, the maximum absorption peak of Ag/G dendrimer is at 400 nm due to Plasmon resonance of Ag/G dendrimer indicating the formation Ag NPs on the surface of the dendrimer.

The FT-IR was employed to confirm the chemical structure of GO and Ag/G dendrimer. Figure 7.2 shows the FTIR spectra of GO and Ag/G dendrimer. The FT-IR spectrum of GO dendrimer shows the weak broadband at ~3418 cm^{-1} corresponding to vibration $NH_{2.}$ The very low-intensity peaks at 2923 cm^{-1}, and at 2854 cm^{-1} are assigned to symmetric and antisymmetric stretching vibration of CH_2, respectively. The band at 1654 and 1324 cm^{-1} are assigned to C=C and C=O, respectively. The FTIR spectrum of Ag/G dendrimer differs from that of GO dendrimer as evidenced by the weakening of the NH_2 band in the range 3350 to 3450 cm^{-1}. It suggests that the silver nanoparticles are stabilized in the GO dendrimer network through this functional group [22]. The disappearance of the peak attributed to C-O at 1324 cm^{-1} in the G/Ag dendrimer spectrum, due to removing the oxygenated functional groups through the heat treatment [21].

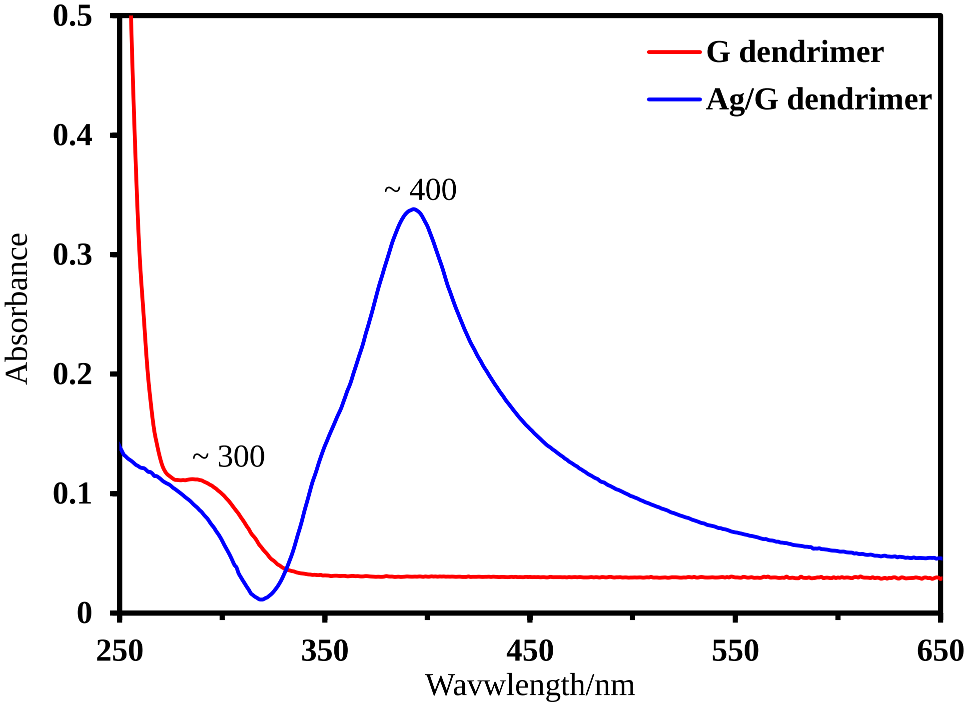

Figure 7.1: UV-Vis absorption spectra of graphene dendrimer and Ag/G dendrimer

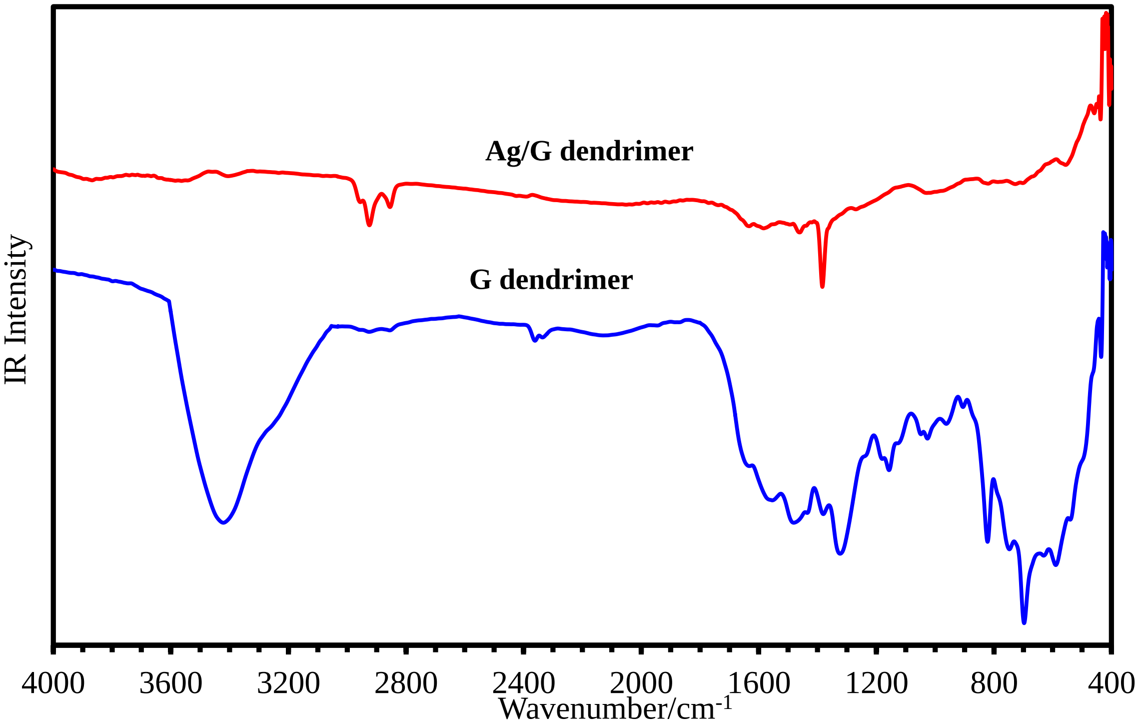

Figure 7.2: FT-IR spectra of G dendrimer and Ag/G dendrimer

The SEM images were taken using the (JSM-6610LV, Scanning Electron Microscope, JEOL) at 20kV acceleration voltage. Figure 7.3a shows the SEM image of G dendrimer. The SEM image of Ag/G dendrimer presented in Figure 7.3b, which indicating the formation Ag NPs on the surface of the G dendrimer with a flower – like structure, it can be seen that the stabilizing AgNPs are almost spherical in shape.

The Raman spectra of GO dendrimer and the G/Ag dendrimer are shown in Figure 7.4. The Raman spectra of all samples displayed two prominent bands. The D band around 1333 cm^{-1}, which is related to disordered carbon sp^3 atoms. The G band around 1598 cm^{-1} is corresponding to order sp^2 carbon atoms [23]. A significant frequency shift (about 27 cm^{-1}) toward a smaller wavenumber of the D-band is found in G/Ag dendrimer compared with the GO (1350 cm^{-1}) indicating a higher level of disorder of the graphene layers and increased numbers of defects [24].

Besides, the intensity ratio of D and G bands (I_D/I_G) increases. The I_D/I_G is used to assess the sp2/sp^3 carbon ratio, a degree of disorder the average size of the sp^2 carbon atoms domains. The ratio values are 1.42 and 1.76 for graphene oxide and Ag/G dendrimers respectively, reflecting the functionalization of the Ag/NPs on the GO dendrimer surfaces [25]. This can be explained by the removing of some oxygen functional groups through reduction process, leading to form high-level fragmentation along the reactive sites of graphene dendrimer [26].

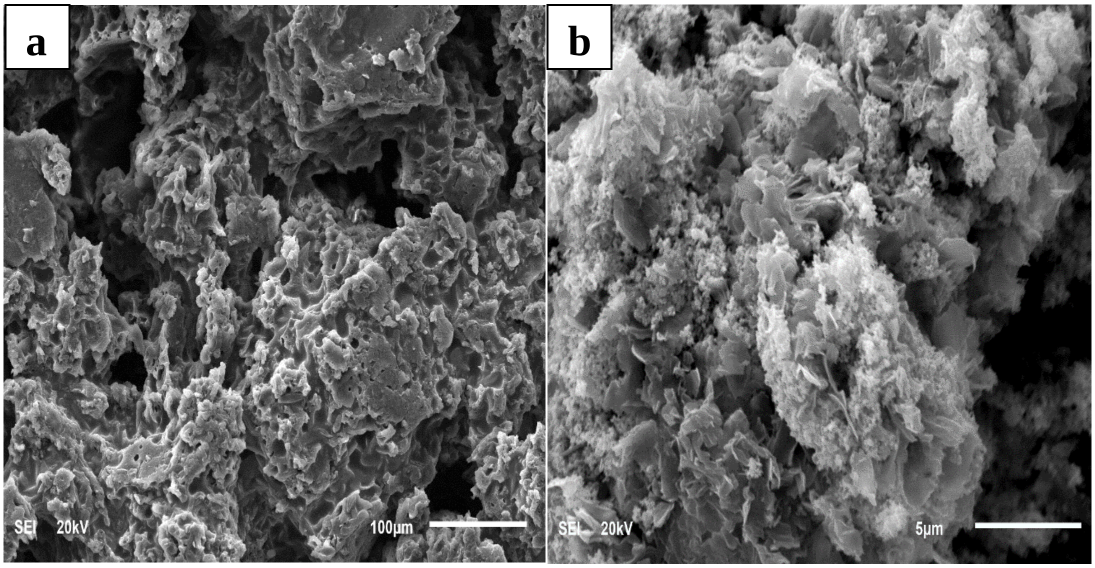

Figure 7.3: Typical SEM images of (a) G dendrimer and (b) Ag/G dendrimer;

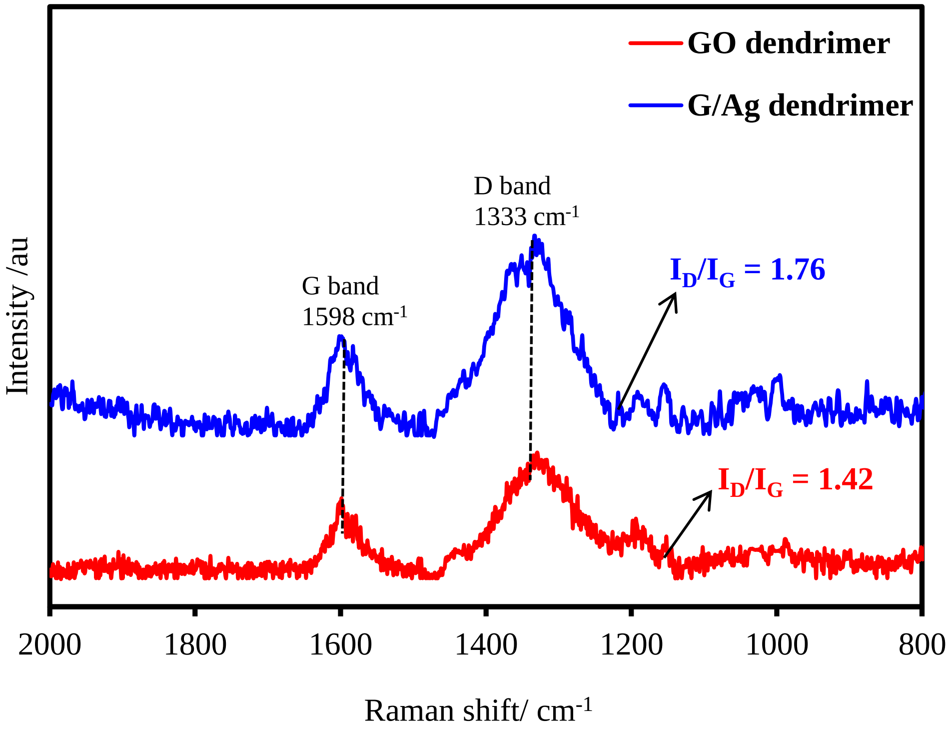

Figure 7.4: Raman spectra of GO and Ag/G dendrimers

7.3.2. Vibrational Assignments

The Theoretical and Experimental vibration frequency modes of MTZ are shown in Table 7.1. The Wavenumbers were calculated through DFT method with B3LYP level and 6-311++G (d, p) basis sets, which excellently correlated with the experimental modes.

Table 7.1: Infrared (IR) and Raman Experimental and calculated vibrational frequencies (cm^{-1}) of the MTZ using DFT methods.

Calculated (Calc) [a]			**Observed (Obs) [b]**				
Scaled Freq.	**IR Int.**	**Raman Act.**	**IR**	**Raman**	**Solution**	**SERS**	**Assignment [c]**
3531	73.02	80.12					100% ν (N3-H)
3162	0.17	147.43	3159w	3161w	3166 m		97% ν (C7-H)
3142	1.63	60.82	3104w	3105w	3106 vw		98% ν (C6-H)
3022	10.80	50.79	3012w				96% ν (C5-H11)
2999	12.50	49.40					100% ν (C5-H12)
2936	32.91	145.60	2949vw	2950 m	2960 m	2945 m	96% ν (C5-H13)
1588	19.31	74.13	1578vs	1579s	1580 m	1567 w	63% ν (C6=C7), 10%δ (N3-H) bend
1509	108.45	26.28		1538 vw		1522 vs	24% ν (N2-C4), 15% ν (C-C) , 38%δ (H11-C-H12)bend
1473	172.66	40.75					23% ν (S-C4), 14% ν (C4-N) bend, 10%δ (N3-H) bend,
1466	13.57	9.99		1479 vw	1480 vs		72% δ CH_{Me} scissoring
1459	69.16	1.95	1462 s	1463 vs	1460 vw	1452 s	23% ν (S-C4), 14% ν (N3-C4), 12%δ (C-H)bend,
1415	34.51	7.33	1403 m	1410 m	1410 vw	1408 w	14% ν (N2-C4), 14% ν (N3-C6), 13% ν (S-C4), 30%δ (C -H)bend
1315	51.11	27.72	1339 vs	1342 s	1345 s	1359 vs	32% ν (N2-C4), 11%δ ring bend, 19% δ C6-N3-H bend

1285	45.11	7.71	1274 s	1278 m	1281 m	1320 s	15% ν (N2-C5), 19%δ N3-H(C6-H) bend, 14% δ ring breathing
1212	60.77	5.70	1248 m	1252 vs	1255 vw	1277 vw	51% ν (N3-C4), 18%δ N3-H(C6-H) bend, 13%δ (C7-H)bend
1159	38.79	11.74	1152 vs	1156 vw	1153 m	1141 m	16% ν (N3-C6),16% ν (S-C4), 15% δ (H11-C-H12) rock,
1089	22.75	8.12	1086vw	1091 m	1088 vw	1090 m	46% ν (N3-C6), 14%δ (N3-H) bend, 21%δ (C7-H)bend
1013	18.80	4.89	1014 s	1016 m	1017 vw	1037 m	15% ring CH bend, 13% δ CH_{Me} bend, 41%δ ring bend,
913	2.99	9.91	913 m	915 vs	916s	937 w	12% ν (N2-C4),12% δ N3-H(C6-H) bend, 62%δ ring bend
806	1.13	3.83	818 w	810 vw		830 vw	89%γ (H-C6-C7-H) twist
685	5.18	15.17	673 vs	679 vw	684 vs	687 w	25% δ (C7-N2-C5) bend, 15% δ (C4-N2-C5) bend
650	60.37	0.92		643 vw		670 vw	47% ring CH bend, 39%γ (N3-C4-N2)
603	2.10	0.82	599 vw	600 vw	602 vw	619 m	78 %γCN ring bend.
534	13.08	10.72	527 vs	525 m	522 w	498 s	53% δ (S-C4-N3) bend, 25% δ (S-C4-N2),
503	46.31	1.66		493 vw			84% γ (N3- C6-C7)
411	3.33	2.99	411 s	410 s	410 m	427 m	71 %δ (S-C4-N)
238	3.63	3.13		264 m	260 m	279 w	85% γ (C4-S) wag
207	3.39	0.15		208 vw	209 vw		76% γ ring

[a] IR intensities and Raman activities are calculated in (km/mole),(Ǎ^{4}/amu) respectively.

[b] vs = very strong; s = strong; m = medium; w = weak; vw = very weak, sh=shoulder.

[c] ν, stretching, vibration; δ, bending in the plane; γ, bending out of the plane.

7.3.3. SERS spectra of MTZ with AgG dendrimer

Figure 7.5 shows the normal Raman spectrum of MTZ and SERS spectrum of the 1×0^{-5}M MTZ with the AgG dendrimer substrate. The prominent characteristic peaks observed in the SERS spectrum of 1×0^{-5}M MTZ AgG dendrimer are listed in Table 7.1. The band at 1342 cm^{-1} in the normal Raman spectrum shifted to 1359 cm^{-1} in the SERS spectrum.This band shows high enhancement factor, which is attributed to the N2-C4 stretching with contributions from ring binding, and C6-N3-H bend (in-plane). The modes at 1538 and 1463 cm^{-1} in the normal Raman spectrum are shifted to 1522, and 1452 cm^{-1}, respectively in the SERS spectrum with significant enhancement. These bands are contributed to S-C, C-N stretching. The bands at 1278, 1156, 1092, 1016, and 600 cm^{-1} in the normal Raman spectrum are shifted to 1320, 1141, 1090, 1037, and 619 cm^{-1}, respectively in the SERS spectrum. These bands are enhanced to higher intensities in SERS spectrum than normal Raman spectrum. The bands at 534 and 410 in the normal Raman spectrum are observed at 498 and 427 cm^{-1}, respectively in the SERS spectrum. These bands are attributed to SCN bending and show a significant enhancement in SERS spectrum.

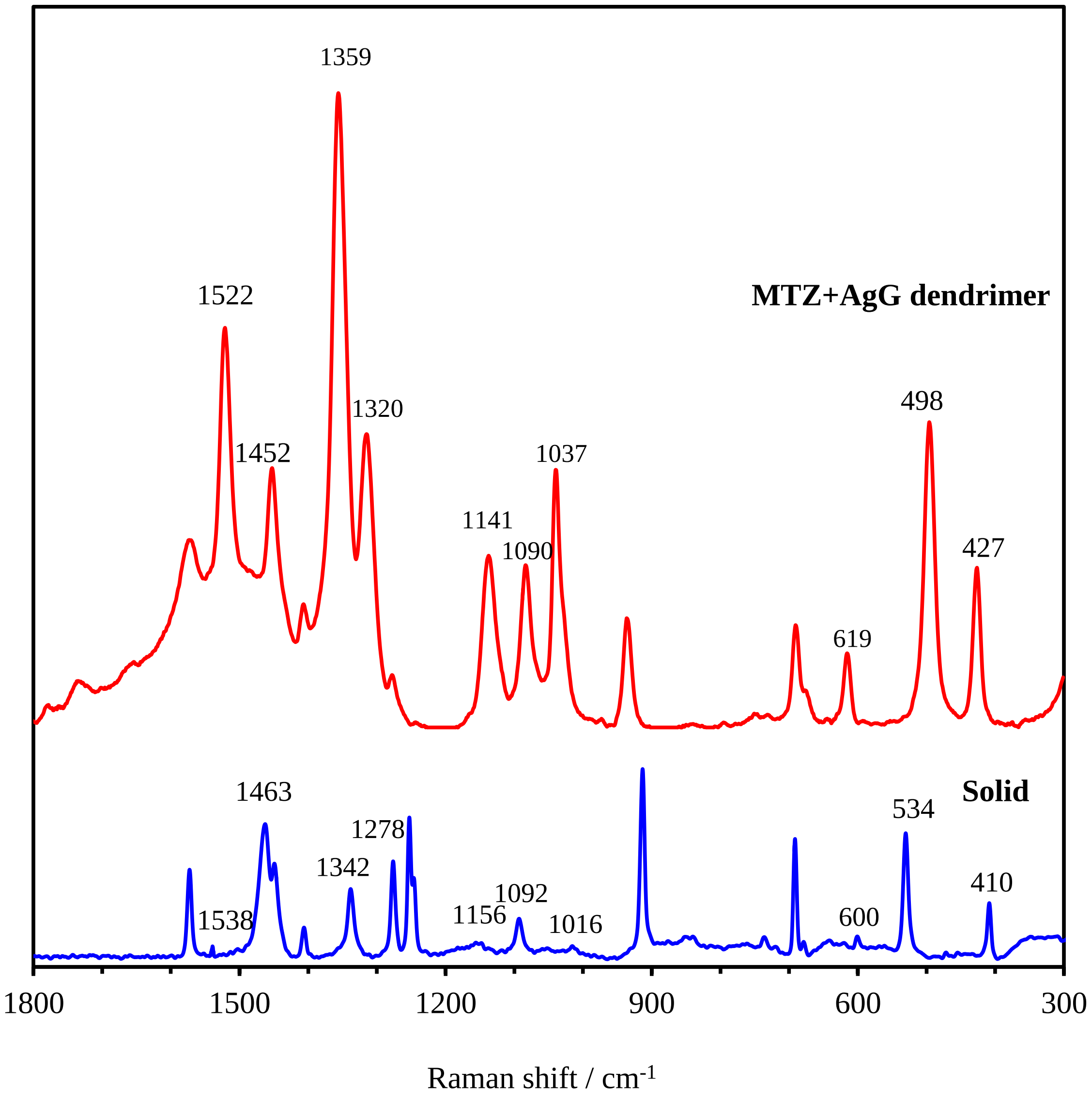

Figure 7.5: Raman spectrum of pure solid MTZ and SERS spectrum of 10^{-5} M MTZ with AgG dendrimer as a substrate, Laser ʎ=633nm, acquisition time; 20 sec, and objective; 50x.

7.3.4. SERS enhancement factor of MTZ with AgG dendrimer

The SERS enhancement factors for the vibrations of MTZ (1×10^{-3} M) on AgG dendrimer to the corresponding band obtained from 1.0 M saturated solution were calculated using the following equation.

$EFs = (\delta_{SERS} \times C_{normal}) / (\delta_{normal} \times C_{SERS})$

Where δ and C are the Raman mode intensity and sample concentration, respectively.

The EFs for the SERS peaks of MTZ on AgG dendrimer are given in Table 7.2. The EFs is not the same for the different MTZ modes, the maximum enhancement was observed at 1342 cm^{-1}.

Table 7.2: SERS enhancement factor of MTZ on AgG dendrimer

Substrate	Normal Raman spectra (cm^{-1})	SERS spectra (cm^{-1})	EFs
Ag/G dendrimer	1538	1522	8.3×10^{4}
	1463	1452	1.1×10^{4}
	1342	1359	1.5×10^{5}
	1278	1320	2.5×10^{4}
	1156	1141	1.0×10^{4}
	1092	1090	2.3×10^{4}
	1016	1037	3.8×10^{4}
	600	619	1.4×10^{4}
	534	498	2.0×10^{4}
	410	427	2.4×10^{4}

7.3.5. SERS spectra of methimazole at different concentrations

The SERS spectra of MTZ aqueous solution with Ag/G dendrimer as a substrate at different concentrations are given in Figure 7.6a. The intensities of the SERS spectra increase with an increase in the concentration of MTZ. This suggests that the SERS intensities are proportional to the molecular quantity of MTZ. The highest enhanced band at 1359 cm^{-1} in SERS spectra was selected for creating a qualitative analysis of MTZ Within the dynamic range, the lowest concentration measured in the SERS analysis of the MTZ solution was 10^{-11} M. Figure 7.6b shows the calibration curve of MTZ solution with AgNPs. The linear SERS response from 10^{-6} M to 10^{-11} M of MTZ was obtained with a good linear coefficient (R^2) of 0.9976.

The linear equations and correlation coefficients of MTZ with Ag/G dendrimer substrate are listed in Table 7.3. A good linear correlation between the Raman peak intensities and MTZ concentrations were noted with wide linear working range (LWR) for MTZ with the substrate.

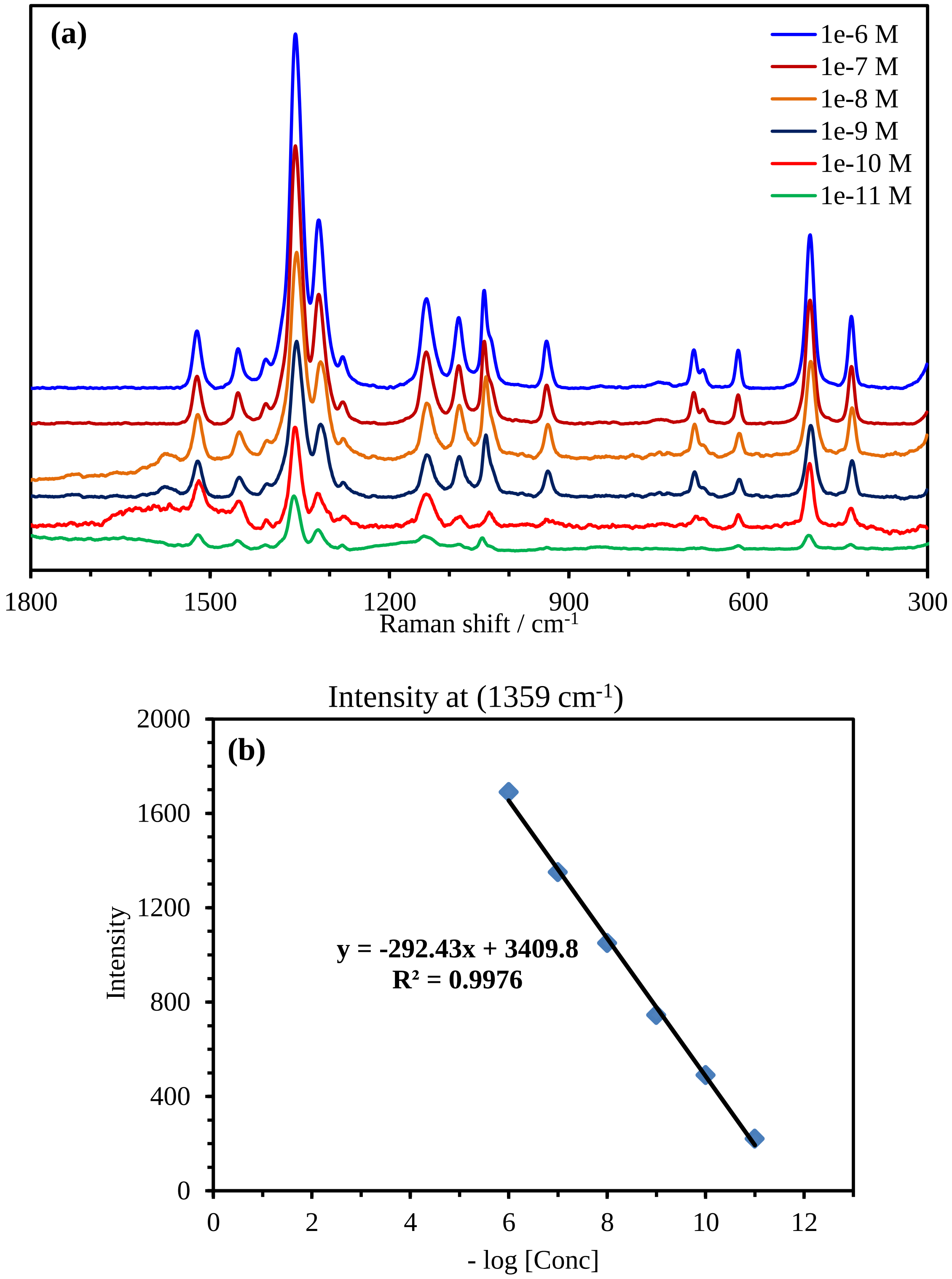

Figure 7.6: (a) SERS spectra of MTZ with different concentration using Ag/G dendrimer, (b) calibration curve of the band at 1359 cm^{-1} using AuNPs. Laser ʎ=633nm, acquisition time; 20 sec, and objective; 50x.

Table 7.3: Regression equation between Raman intensities and concentrations of MTZ and their correlation coefficients.

Raman Peaks	Regression Equation	R^2	Dynamic range (M)	LOD (M)
1359 cm^{-1}	y = - 292.43x + 3409.8	0.9976	$10^{-6} – 10^{-11}$	1.43×10^{-12}
1320 cm^{-1}	y = - 144.97x + 1651.9	0.9921	$10^{-6} – 10^{-11}$	2.67×10^{-12}
498 cm^{-1}	y = - 124.14x + 1479	0.9744	$10^{-6} – 10^{-11}$	3.71×10^{-12}
427 cm^{-1}	y = - 63.771x + 739.39	0.9651	$10^{-6} – 10^{-11}$	0.91×10^{-11}

7.4. CONCLUSION

The graphene dendrimer-stabilized silver nanoparticles were synthesized and characterized by using various techniques including SEM, TEM, FTIR and UV. The SERS method was exploited to record the vibrational frequencies of MTZ adsorbed on graphene dendrimer-stabilized silver nanoparticles. The optimized conformation and vibrational assignments of MTZ have been carried out using the DFT calculation with B3LYP/6-311++G (d, p) basis set. The vibration assignments and the wavenumber of vibration frequency bands in the theoretical spectra were in agreement with those of the experimental spectra. Most of the bands related to N atom and S atom were apparently enhanced and shifted. These results confirm that methimazole molecules were adsorbed on the graphene dendrimer-stabilized silver nanoparticles through probably the lone pair on N and S atoms. The correlation between the MTZ concentration and the SERS signal was linear within a dynamic range of $10^{-8} – 10^{-11}$ and R^2 of 0.9976 and of good detection limits down to 1.43×10^{-12}.

7.5. REFERENCES

[1] Fleischmann. M, Hendra, P. J. Chemical Physics Letters. 1974, 26(2), 166.

[2] Tian, Z. Q., Ren, B. Journal of Physical Chemistry B. 2002, 106(37), 9463.

[3] Vanduyne, R. P., Hulteen, J. C. Journal of Chemical Physics. 1993, 99(3), 2101.

[4] Giesfeldt, K, Connatser, R. M. …et al. Applied Spectroscopy. 2003, 57(11), 1346.

[5] De Jesus, M. A., Giesfeldt, K. S, Sepaniak, M. J. App. Spectro. 2004, 58, 1157.

[6] Reilly, T. H., III, Corbman, J. D, Rowlen, K. L. Anal. Chem. 2007, 79(13), 5078.

[7] M. Pan, Guozhen Fang, Yang Lu, Lingjie Kong, Yukun Yang, Shuo Wang, Sensors and Actuators B: Chemical, Part A. 2015, 207, 588.

[8] L. Farzampour, M. Amjadi, Journal of Luminescence. 2014, 155, 226.

[9] M. Aletrari, P. Kanari, D. Partassides, E. Loizou. Journal of Pharmaceutical and Biomedical Analysis. 1998, 16, 785.

[10] K. Nikolic, K. Velasevic. Pharmazie. 1987, 42, 698.

[11] A. Berka, K. Velasevic, K. Nikolic. Pharmazie.1989, 44, 499.

[12] G. Moretti, P. Betto, P. Cammarata, F. Fracassi, M. Giambenedetti, A. Borghese. Journal of Chromatography: Biomedical Applications. 1993, 616, 291.

[13] R. S. Golightly, W. E. Doering, M. J. Natan. ACS Nano. 2009, 3, 2859.

[14] Szymanski, H. A. Plenum Press, Buffalo, NY, 1967.

[15] O. Peron, E. Rinnert, M. Lehaitre, P. Crassous. Talanta. 2009, 79, 199.

[16] Y. Kitahama, Y. Tanaka, T. Itoh, Y. Ozaki. Chem. Lett. 2009, 38, 54.

[17] R. J. Stokes, E. McBride, C. G. Wilson…etal. App. Spectrosc. 2008, 62, 371.

[18] Aroca, R. F., Alvarez-Puebla, R. A., Pieczonka, N., Sanchez-Cortez, S. and Garcia- Ramos, J. V. Advances in Colloid and Interface Science. 2005, 116(1-3), 45.

[19] E. Abbasi1 , S.F. Aval1, Abolfazl A…et al. Nan. Res. Lett. 2014, 9, 247..

[20] Yijun Jiang and Qiuming Gao. J. Am. Chem. Soc. 2006, 128, 716.

[21] R. Rajesh, S. S.Kumar, R. Venkatesan. New J. Chem. 2014, 38, 1551.

[22] Jianfeng Shen, Yizhe Hu, Min Shi…etal. J. Phys. Chem. C. 2010, 114, 1498.

[23] Sarkar, S.; Bekyarova, E…et al. J. Am. Chem. Soc. 2011, 133, 3324.

[24] Nguyen Thi Lan, Do Thi Chi , Ngo Xuan Dinh, Nguyen Duy Hung, Hoang Lan, Pham Anh Tuan, Le Hong Thang…et al. Journal of Alloys and Compounds. 2014, 615, 843.

[25] M. Fang, K. Wang, H. Lu, Y. Yang and S. Nutt, J. Mater. Chem., 2009, 19, 7098.

[26] Huang Lin-jun, Wang Yan-xin, Tang Jian-guo, Wang Yao, Liu Ji-xian, Jiao Ji-qing, Wang Wei. Int. J. Electrochem. Sci. 2016, 11, 398.

VITAE

Name **:** Mutasem Mohammad Al-Shalalfeh

Nationality **:** Palestinian

Date of Birth **:**3/24/1991

Email **:** mshalalfeh91@gmail.com

Address **:** King Fahd of Petroleum and Minerals, Dhahran,

Saudi Arabia

Academic Background **:** Received my B.Sc. in Chemistry from Birzeit University (BZU), Ramallah, West Bank, Palestine in May 2013.

: Earned the M.S. degree in nanomaterials chemistry from KFUPM in April, 2016.

A co-author of the following publication:

1. **Mutasem M. Al-Shalalfeh**, Manzar Sohail, Tawfik A. Saleh, Md. Abdul Aziz. "Electrochemical Investigation of Gold Nanoparticles-Modified Glassy Carbon Electrode and its Application for Ketoconazole Determination**". Revised.**

2. **Mutasem M. Al-Shalalfeh**, Tawfik A. Saleh, Abdulaziz A. Al-Saadi. " Spherical Silver nanoparticles as SERS substrate for enhanced detection of ketoconazole". **Revised.**
3. **Mutasem M. Al-Shalalfeh**, Tawfik A. Saleh, Abdulaziz A. Al-Saadi. "Silver Colloid and Film substrates in Surface-enhanced Raman scattering for 2-Thiouracil Detection". **Under Review.**
4. Tawfik A. Saleh, **Mutasem M. Al-Shalalfeh**, M.I.M. Wazeer, Abdulaziz A. Al-Saad. Silver Nanoparticle-Decorated Graphene: A substrate for Surface enhanced Raman scattering based Detection of 2-Thiouracil ". **Under Review**.
5. **Mutasem M. Al-Shalalfeh**, Tawfik A. Saleh, Abdulaziz A. Al-Saadi." Surface-enhanced Raman scattering based on colloidal Ag and Au nanoparticles for detection of methimazole". **To be submitted.**
6. **Mutasem M. Al-Shalalfeh**, Tawfik A. Saleh, Abdulaziz A. Al-Saadi. "Graphene Dendrimer-stabilized silver nanoparticles for detection of methimazole using Surface-enhanced Raman scattering with computational assignment". **To be submitted.**